2013

The VHE gamma-ray spectra of several hard-spectrum blazars from long-term observations with the VERITAS telescope array

Arun Sreenivasan Madhavan
Iowa State University

The VHE γ-ray spectra of several hard-spectrum blazars from long-term observations with the VERITAS telescope array

by

Arun Madhavan

A dissertation submitted to the graduate faculty

in partial fulfillment of the requirements for the degree of

DOCTOR OF PHILOSOPHY

Major: Physics

Program of Study Committee:

Frank Krennrich, Major Professor

Amanda Weinstein

John Lajoie

Charles Kerton

Xiaoqing Wu

Iowa State University

Ames, Iowa

2013

DEDICATION

This dissertation is dedicated to Olde Main Brewing Company, and to the fine beers which have made this work possible.

TABLE OF CONTENTS

LIST OF TABLES

LIST OF FIGURES

ACKNOWLEDGEMENTS

This dissertation, though written over a period of only a few months, is the final product of the last six and a half years I've spent at Iowa State University. It's been tough at times, but I'd say it was definitely worth the effort. As is the case with any contribution to science, this work would have been impossible without the help of many colleagues and friends.

First, I'd like to thank my advisor Frank Krennrich. Frank is a meticulous physicist who carefully inspects every aspect of a scientific experiment and doesn't let me use any analysis technique that I don't fully understand. This isn't any easy process, but it means that I can vouch for every data point that I plot, and that I can always explain how I obtained my results. Even when occupied with the time-consuming duties of being department chair, Frank has been able to go over this dissertation with a fine-toothed comb and root out all ambiguity and incorrectness. If anything's left, it's definitely my fault for missing it. More than anyone, Frank has taught me how to be an experimental physicist, and this is a skill set that I'll rely on throughout my career.

I would also like to thank Amanda Weinstein, who at times has been a second advisor for my graduate work. Amanda basically knows everything about the VERITAS experiment, from the trigger hardware to the guts of the analysis chain, and on many occasions I've relied on her explanations of how all of this stuff fits together. If not for some in-depth conversations with her about the camera trigger, I'd probably have never figured out how to fix that jitter correction problem. On a shift when we both happened to be observing together (with me as czar!), she prevented me from breaking T3. I thank her for not letting me ruin a perfectly good telescope. On a side note, I would also like to thank her for putting up with my science fiction affinity. It surprises me that we never got into a Star Trek vs. Stargate argument.

I thank the rest of my committee as well, who have been a fun and helpful group of physicists during my graduate work. John Lajoie regularly indulges my fascination with nuclear reactions,

and is a fellow Trekkie with whom I've had many conversations on our mutual dislike of the new Star Trek films. Charles Kerton is a highly knowledgable astronomer who has helped me to put my work into its proper context. I also have a sneaking suspicion that he wrote the problem on the department qualifying exam that put me above the pass line, so for this I also thank him. Xiaoqing Wu did a great job introducing me to atmospheric physics, which I now think about whenever working out a problem on air shower physics. And Ed Yu, while not actually on my committee, has always been amenable to hanging out with me and giving me practical advice on getting through graduate school.

There are several current and former members of the ISU gamma-ray group who have been of great help over the past few years. Asif, who was my officemate for three years, got me started on VERITAS data analysis and taught me how to do the various other day-to-day computing tasks that are essential to all astrophysicists. Even after moving on to a postdoc, he's always replied to my emails to give me important scientific and career insights. Tomo Nagai, though far removed from the classroom, nonetheless went through classical mechanics problems with me the summer that I was studying for my Ph.D. qualifier. Matt Orr has bailed me out more times than I can remember. Some examples include going over my collaboration meeting talks with me, teaching me about the theory of our field, and explaining the guts of the ANL trigger. I'd also like to thank my fellow graduate student Josh Cardenzana. He's pretty much the only one with whom I could make gamma-ray small talk at physics parties. And finally there's Hugh Dickinson and Jon "Eisch-man" Eisch, who in addition to their considerable research expertise are pretty awesome to hang out with after work.

None of my work would have been possible without the members of the VERITAS collaboration, who have been a great bunch of colleagues and coworkers. I would like to thank Sagar Godambe and Anna Cannon, who made my first observing shift a blast. Sagar gave me several backyard astronomy lessons during our breaks from the VERITAS control room. And while it's unfortunate that we missed an observing day due to rain, I'm glad for the opportunity we had to sit around the Ridge Dorm and watch a movie which Anna assured us was representative of life in the Irish countryside. I would also like to thank Drs. Gareth Hughes and Dave Staszak, who tolerated my obsession with attaining the title of "doctor," all while they were dealing

with the stress of being VERITAS czar. Speaking of titles, I also thank Herr Prof. Dr. Rer. Nat. Dipl. Physiker Nepomuk Otte. In addition to teaching me the proper title with which to address a German professor, Nepomuk's sense of humor definitely made up for the Arizona summer heat in which we were upgrading the cameras. For the record, I do feel mildly guilty that I spent most of the upgrade in an air conditioned trailer while the pixel folks were on top of a platform just a few feet away.

And then there are my numerous friends from the physics department, who had absolutely nothing to do with my research work, but without whom graduate school would have been very boring. Blomberg, who was one of my first friends in Ames, introduced me to the importance of Wednesday nights at the bar. Suyog, ever the philosopher, always reminded me that physics is cool. Gus, on the other hand, reminded me that RoboCop is cool, and if this physics thing doesn't work out I hope he'll go into business with me building a cyborg. Thank you also to Suffian, Milap, Andres, William, and the rest of the Olde Main crowd. A special thanks to Alyssa and Liz, who were my study buddies at Olde Main as I wrote much of this dissertation.

I would like to thank my family for everything the past few years. Besides the usual moral support stuff, they've helped in more practical and/or fun ways. My brother, being of a similarly scientific background, has corrected two memos and a conference proceeding for me. My dad often cites episodes of *Star Trek: The Next Generation* to remind me why physics is cool. And my mom...well, she does the usual mom stuff and tells everyone that I'm a rocket scientist. I frequently object to this definition of my work in astrophysics, of course to no avail. Finally I thank Sapna, who puts up with me even though she cares nothing for either astrophysics or Star Trek. Apparently I do have a few endearing traits!

ABSTRACT

Analysis is presented on VERITAS observations of the very high energy γ-ray spectra of five high frequency peaked BL Lac objects over a range of redshifts. Each object has an unusually hard intrinsic GeV spectrum, and is expected to produce TeV γ-ray emission into the optically-thick regime of the universe's diffuse extragalactic background light (EBL). Hard spectrum HBLs have recently emerged as an effective tool for measurement of the EBL spectrum, due to extinction of γ-ray signals from blazars via the pair production interaction $\gamma_{TeV}\gamma_{EBL} \rightarrow e^{+}e^{-}$. The VERITAS collaboration has approved long term observations on several of these sources, with the specific intent of studying their spectra to probe for absorption features resulting from these interactions. An introduction to the field of particle astrophysics is presented, followed by an overview of the EBL and its relation to the evolution of the universe. The VERITAS γ-ray telescope is described in detail, followed by a full overview of the analysis techniques used to derive γ-ray spectra from VERITAS data. The analyses of the blazars themselves are presented, followed by a discussion of their application to further constraints of the EBL. Each blazar is de-absorbed with an assumed EBL spectrum. In each case the intrinsic TeV spectrum is consistent with lower-energy γ-ray emission in the optically-thin regime of the EBL.

CHAPTER 1. INTRODUCTION TO PARTICLE ASTROPHYSICS

1.1 High Energy Astrophysical Emission

Ever since the discovery of cosmic rays by the balloon experiments of Victor Hess in 1912, the question of the origin of high energy astrophysical particles has been an open topic of inquiry to astronomers. The early 20th century sabbaticw many rapid advancements in the field of particle physics. Ernest Rutherford's absorption experiments had resulted in the discovery of an early "particle zoo" consisting of massive α-particles, penetrating β-particles, and γ-rays. Since Hess's first observation of high energy astrophysical particles, it has been discovered that particles including protons, electrons, positrons, heavier nuclei, and high energy γ-rays are constantly bombarding the earth from all directions. Many of these particles have energies of over a 10^{12} electron volts (eV). Some particles have been observed with energies on the order of 10^{20} eV (Gaisser, 1990).

Since the first discoveries of elementary particles, high energy physicists have sought to build accelerators capable of colliding fundamental particles at higher and higher energies so as to probe the internal structure of protons and neutrons, as well as to produce more exotic particles which are thought to have also existed in the primordial soup of the Big Bang. At the present, the world's most powerful particle accelerator, the Large Hadron Collider, is capable of accelerating protons to center of mass energies of 14 TeV. Yet it would seem that nature is capable of accelerating fundamental particles to far greater energies. This begs the question of what physical phenomena are capable of performing such a feat.

The particle physicist produces beams of high energy radiation in a controlled setting, and seeks to study the interactions of such particles by observing their exotic decay products. The particle astrophysicist, on the other hand, returns to the world of protons, electrons, and

photons, but asks where high energy astrophysical particles come from, and how we can use them to elucidate the underlying physics of the cosmic accelerators that produce them.

1.1.1 Cosmic rays

When astrophysicists refer to cosmic rays, we typically mean to speak of high energy hadrons and leptons that pass through the interstellar medium. At lower energies, protons are the most abundant of these particles, but heavier nuclei are present at higher energies (Seo et al., 2004). Cosmic rays also include electrons (Evenson, 1998) and positrons (Aguilar et al, 2013). Since their initial discovery, the energy spectrum of cosmic rays has been measured over a wide range of energies, from 10^9 eV to 10^{20} eV. Figure 1.1 shows a compilation of cosmic ray spectra from various experiments, adapted by W. Hanlon[1] from Swordy (2001). Like many astrophysical phenomena, the cosmic ray spectrum is described by a power law, $\Phi(E) = N_0 E^{\Gamma}$, with $\Gamma \approx -2.7$. The cosmic ray spectrum contains two important features, commonly referred to as the "knee" and the "ankle." At the knee around 10^{15} eV, the cosmic ray spectrum softens from -2.7 to -3.1 (Amenomori et al, 2008). At the ankle around 10^{18} eV, the spectrum again hardens[2]. Cosmic rays are not the principle topic of this work and thus will not be discussed in greater detail. However it is noteworthy that sites of cosmic ray acceleration are thought to also produce γ-ray emission, and thus the study of cosmic rays are of scientific interest to many γ-ray astrophysicists. As noted by Renaud (2009), shell-type supernova remnants and pulsar wind nebulae in the center of our galaxy are candidate sources for the origin cosmic rays up to the knee.

1.1.2 Astrophysical γ-rays

γ-rays comprise the highest frequency band of the electromagnetic spectrum. Electromagnetic radiation above 10^{19} Hz, or $\sim$100 keV is typically classified as γ-radiation. Astrophysical γ-rays are subdivided into two bands: high energy (HE) γ-rays between 30 MeV and 100 GeV,

[1] http://www.physics.utah.edu/$\sim$whanlon/spectrum.html

[2] We often refer to "soft" and "hard" spectra. These relative terms refer to spectra with smaller and larger spectral indices. For a power law spectrum of the form $\Phi(E) = N_0 E^{-\Gamma}$, $-\Gamma$ is the spectral index, and represents the slope of the spectrum on a log-log plot. Many energy spectra in astrophysics are not described by single power laws, but rather by piecewise smooth power laws.

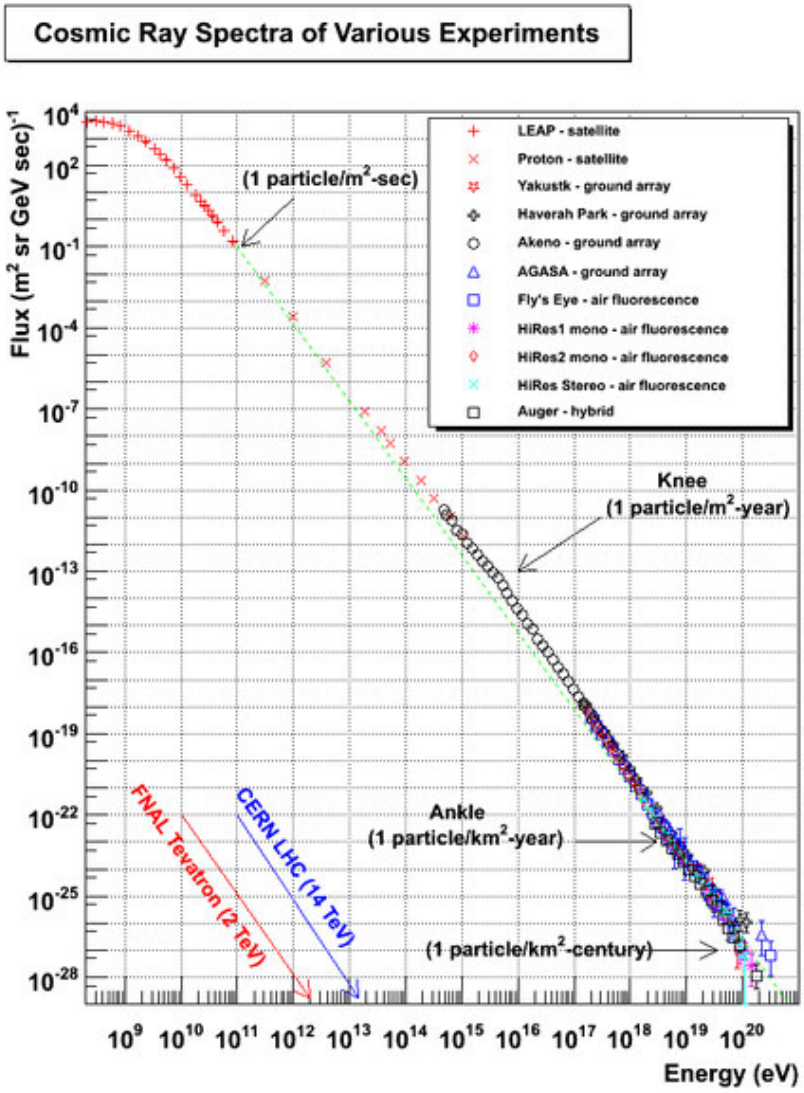

Figure 1.1 *A summary of cosmic ray spectra from various experiments. At lower energies the spectrum has a spectral index of -2.7. This spectrum softens at the "knee" around* 10^{15} *eV, then hardens at the "ankle" around* 10^{18} *eV.*

and very high energy (VHE) γ-rays between 100 GeV and 100 TeV. This distinction is made based on the differing detection techniques used to study radiation in these two energy bands.

Much of the universe's radiation is thermal in nature; that is, it is generated by a body's heat content. γ-rays, however, are typically produced by non-thermal processes. Astrophysical γ-rays are typically emitted due to processes such as proton-proton collisions and inverse Compton scattering of electrons. The production of γ-radiation requires the presence of very high energy charged particles. It is for this reason that sources of γ-rays are often referred to as cosmic accelerators. Whereas high energy physicists use known interactions of particles in a man-made accelerator to study new physics from exotic decay modes, particle astrophysicists use well known interaction and decay processes to study astrophysical populations of particles via their γ-radiation, which passes to earth unimpeded by magnetic fields as would the charged particles which produce them.

γ-ray astronomy has historical roots in attempts to use satellite-based observatories to detect the γ-ray emission from terrestrial detonations of nuclear bombs. However, one of the first reliable surveys of the γ-ray sky was conducted by the Energetic Gamma-Ray Experiment Telescope (EGRET). EGRET was a satellite experiment launched in 1991, and surveyed HE γ-rays in the regime of 30 MeV to 20 GeV. Hartman et al. (1999) counts 271 point sources of γ-rays detected by EGRET, in addition to a diffuse γ-ray component both from our own galaxy as well as from extragalactic space. The energy regime explored by EGRET was later extended by the Large Area Telescope (LAT) onboard the Fermi satellite. The Fermi Gamma-Ray Space Telescope, launched in 2008, is able to detect γ-rays from 20 MeV to beyond 300 GeV (see Baldini (2011)). Fermi detected 1451 point sources in its first year catalog, greatly improving on EGRET's exploration of the HE band of γ-rays.

In 1989, the first VHE point source of γ-rays, namely the Crab Nebula, was detected by the Whipple Collaboration (Weekes, 1989). In the past two decades since this milestone discovery, VHE γ-ray astronomy has rapidly evolved from an arcane branch of physics into an essential component of astronomical research. At the time of this work's composition, there are 145 known sources of VHE γ-rays, as shown in Figure 1.2 (referenced from http://tevcat.uchicago.edu). Figure 1.2 also illustrates the diffuse HE γ-ray background de-

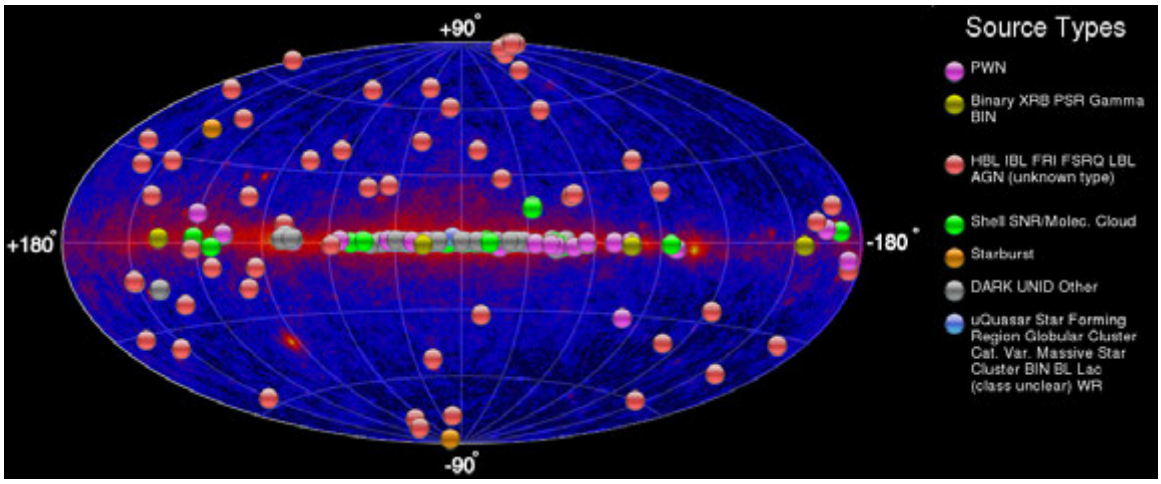

Figure 1.2 *Skymap of resolved sources of VHE γ-rays, superimposed over the diffuse HE γ-ray background as seen by the Fermi Gamma-Ray Space Telescope. From: http://tevcat.uchicago.edu.*

tected by Fermi, which consists of a galactic component due to interactions of high energy cosmic rays with matter and radiation fields, as well as an isotropic extragalactic background from unresolved sources (Baldini, 2011).

1.1.3 Sources of Astrophysical High Energy Particles

The universe is replete with violent environments in which particles are accelerated to high energies. Here we briefly survey some galactic sources of high energy particles, namely supernova remnants, pulsars, and binary systems, before moving onto active galaxies, which are the major focus of this work.

1.1.3.1 Supernova remnants

Near the end of their life cycles, sufficiently massive stars will undergo a core collapse and violently explode as supernovae, releasing on the order of 10^{46}W in neutrino emission over a very short time span (Woosley and Janka, 2005). The resulting pressure wave exceeds the local sound speed and creates an expanding shock front of magnetized plasma that sweeps up gas from the interstellar medium. This shock front is thought to act as a mechanism for the

acceleration of charged particles via diffusive shock acceleration (often referred to as 1st order Fermi acceleration). A review of the process is provided by Malkov and Drury (2001); the basic idea of diffusive shock acceleration is that charged particles gain kinetic energy by bouncing between converging upstream and downstream regions of the flow. As Gaisser (1990) explains, diffusive shock acceleration allows for macroscopic kinetic energy from the shock front to be transferred to the microscopic charged particles.

The blast wave from a supernova, which we refer to as a supernova remnant (SNR) expands very quickly when compared to an astronomical time scale. The Crab Nebula, one of the most famous and well studied objects in astronomy, is the remnant of a supernova observed by Chinese astronomers in 1054; in less than a thousand years it has grown to a diameter of approximately 11 light years. SNRs in our own galaxy are commonly thought to be the source of galactic cosmic rays. This view, however, has been called into question by Butt (2009).

As explained in Drury et al. (1994), supernova remnants can accelerate protons so as to produce γ-rays via the mechanism,

$$p + p \rightarrow \pi^0 + \text{other products} \tag{1.1}$$

$$\pi^0 \rightarrow \gamma + \gamma \tag{1.2}$$

γ-rays with multi-TeV energies have been observed from SNRs. For example, the VERITAS γ-ray telescope has observed Tycho's Supernova Remnant (see Figure 1.3), the relic of a supernova from the year 1572 (Acciari et al., 2011). VERITAS was able to observe γ-rays as energetic as 10 TeV from the remnant. γ-ray emission from the remnant may be the result of interactions between accelerated particles in the supernova shock front and target particles in a nearby carbon monoxide cloud. As Figure 1.2 shows, the galactic plane contains many SNRs that have been detected in TeV γ-rays.

Although SNRs are spoken of generically in this context, astronomers typically distinguish between shell-type SNRs in which the the star at the center of the remnant no longer exists, and other types of SNRs such as pulsar wind nebulae. Tycho's SNR is an example of a shell-type

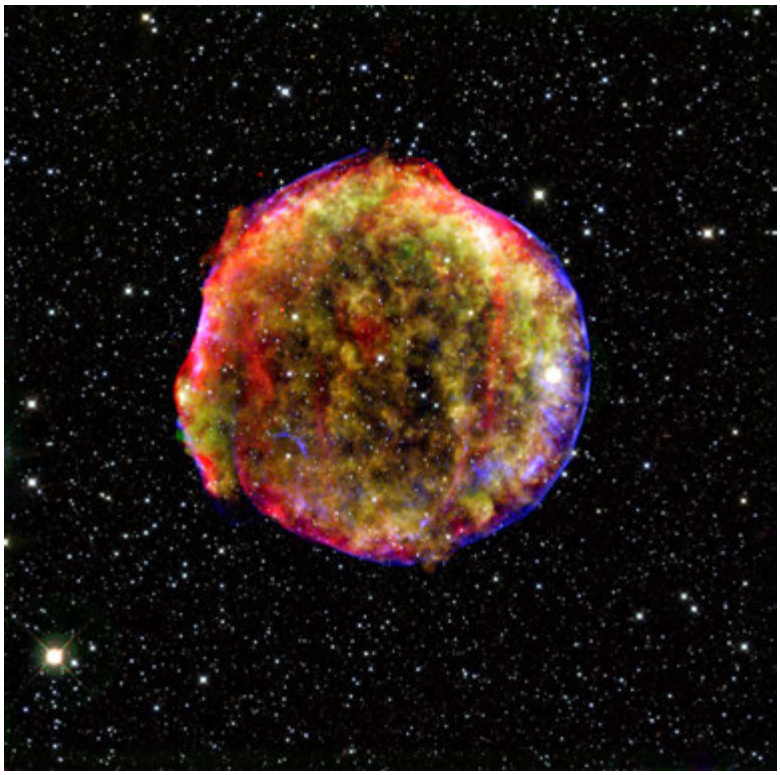

Figure 1.3 *Tycho's Supernova Remnant, a shell-type SNR from 1572. The source was detected by VERITAS with γ-ray emission extending to 10 TeV (Acciari et al., 2011). The observed γ-ray emission may come from hadronic interactions between the shock front and a nearby CO cloud. [Credit: NASA/MPIA/Calar Alto Observatory, Oliver Krause et al.]*

SNR, whereas the Crab Nebula is a pulsar wind nebula.

1.1.3.2 Pulsars and pulsar wind nebulae

Following a core-collapse supernova, it is possible for gravitational pressure to overcome the outward pressure of electron degeneracy, resulting in neutronization of the stellar remnant. Neutron stars possess strong magnetic fields, charged particles are accelerated along the field lines, resulting in beams of particle radiation (as well as resulting electromagnetic radiation) along a neutron star's magnetic axis. When the magnetic axis is displaced from the spin axis, and points toward earth at some point during the neutron star's rotation, it is possible to detect pulsed radiation; hence these stars are referred to as pulsars. Pulsars have moments of inertia on the order of 10^{38} kg $\cdot$ m^2, and typically have rotation rates on the order of 0.5 s (Lorimer,

2008). There are, however, pulsars with much faster rotation rates. For example the Crab Nebula contains a pulsar with a period of 33 ms.

Pulsar wind nebulae are a special case of SNRs in which the pulsar from the supernova core-collapse still exists at the center of the remnant. As described by Hester (2008), pulsars produce winds of electrons and positrons which are confined by the SNR ejecta into which they expand. This wind of electrons and positrons is accelerated by the pulsar to very high energies, approximately 1 PeV in the case of the Crab Nebula. High energy electrons which interact with the SNR shock front can gyrate in local magnetic field lines and emit synchrotron radiation. Those same electrons can inverse Compton scatter either background photons or their own synchrotron photon field, thus converting lower energy photons to GeV and TeV γ-rays.

1.1.3.3 Binary systems

A binary system (in the context of high energy astrophysics) consists of a compact object such as a neutron star or pulsar and a larger star orbiting around a common center of mass. There are two potential mechanisms for electromagnetic emission from a binary system. In one scenario, the companion star can accrete mass onto the compact object; the interaction of charged particles with the compact object's magnetic field results in a pair of jets of high energy electrons, similar to emission from an active galactic nucleus (see Section 1.2). These electrons would then become constrained by magnetic fields, and inverse Compton scatter background photons to higher energies. Alternatively, another scenario suggests that if the compact object is a pulsar, then the shock interface between the pulsar wind and equatorial disk or wind of the companion star can serve as a mechanism for acceleration of charged particles. Given a sufficient number of background photons, accelerated electrons can inverse Compton scatter these photons to higher energies.

γ-ray emitting binary systems are extremely rare. One example is the binary system LS I +61 303, detected by the VERITAS telescope array with a VHE flux of 15% to 20% of the Crab Nebula[3] flux (Acciari et al., 2008). To date only three γ-ray binary systems have been

[3]As will be discussed at length, the Crab Nebula is one of the most strong and stable sources of VHE γ-rays, and is thus used as a benchmark for comparison to other sources.

detected: LS I +61 303 (Acciari et al., 2008), PSR B1259-63 (Aharonian et al., 2005a), and LS 5039 (Aharonian et al., 2005b).

1.2 Active Galactic Nuclei

Active galactic nuclei are by far the most ubiquitous source of detectable γ-rays from outside of the galaxy. As described by Kitchin (2006), active galaxies are defined by both the presence of a central, supermassive black hole (SMBH), and an abundance of material (e.g. stars, planets, gas, and dust) to be consumed by the black hole via accretion. Unlike a normal galaxy in which the bulk of observed emission comes from starlight, in an active galaxy most of the emission is a result of non-thermal processes. The high energy processes in an active galaxy take place in a small region around the central SMBH, therefore we typically refer to these objects as active galactic nuclei (AGNs). The SMBHs in the center of AGNs allow for gravitational potential energy to be transformed into radiation - via accretion - both efficiently, and within a small volume (Blandford, 1991).

The activity in an AGN is thought to be powered by the accretion of matter onto the SMBH. Kitchin (2006) lists the following characteristics of AGNs.

- A very high luminosity within the radio, infrared, UV, or X-ray regimes
- Strong optical emission lines
- Visible ejecta from the nucleus in the form of a pair of opposing jets
- Radio lobes located up to 1 Mly from the AGN, created by ejecta that has been deposited into extragalactic space

It should be noted that not all of these characteristics are present in all AGNs. Urry and Padovani (1995) make a distinction between two types of AGN known as flat spectrum radio quasars (FSRQs) and BL Lacertae (BL Lac) objects: while FSRQs exhibit strong emission absorption or emission lines, BL Lacs lack this feature.

AGNs are also characterized by luminosity variability, which can be very rapid due to the small size of the region in which accretion occurs. While many AGNs vary their luminosity over

the course of months or even years, much smaller timescales are possible. For example, day scale variation was observed in the AGN Mrk501 by Catanese et al. (1997) and in 1ES1218+304 by Acciari et al. (2010). Variability on the order of 100s of seconds was observed in the AGN PKS2155-304 by Aharonian et al. (2007).

The jets exhibited by AGNs, which arise due to the accretion of matter onto the central SMBH, consist of relativistic plasma (see Marscher et al. (2002) and Acciari et al. (2009)). Indeed, AGNs are capable of accelerating particles to energies exceeding a TeV. AGN jets are thus an excellent laboratory for studying high energy particle interactions in an astrophysical setting. The jet phenomenon is perhaps best illustrated by M87. M87 is an elliptical galaxy located at a redshift of $z = 0.0043$, and Macchetto et al. (1997) classify it as an AGN. M87 is a unique object in that the plasma jet, which is at an angle to the observer, is visible and elucidates detailed structure including broadening from its origin at the nucleus. Figure 1.4 shows a composite image.

1.2.1 Classification of AGN and blazars

As mentioned above, AGNs are subdivided into classifications. The observed properties of an AGN depend strongly on the angle at which they are viewed. Because of this, historically AGN were classified as various types of astrophysical objects, and only later were they unified as a single type of phenomenon viewed from different angles. Figure 1.5 illustrates the structure of an AGN and various classifications associated with different viewing angles. When viewed at a large angle to the jet, the regions of the AGN further from the SMBH are visible. Narrow line emission is detectable from slow-moving ionized gas, as is the radio emission from the lobes at the ends of the relativistic jets. These galaxies are referred to as Type 2 Seyfert Galaxies. Viewing an AGN at a smaller angle to the jet elucidates the inner region of the nucleus. Here, ionized gas orbits the SMBH at a high speed, and Doppler broadening of spectral lines creates a broad line region. When the broad line region is visible we refer to the galaxy as a Type 1 Seyfert. At small angles to the jet, the beamed electromagnetic emission from the jet particles dominates and we refer to the object as a blazar.

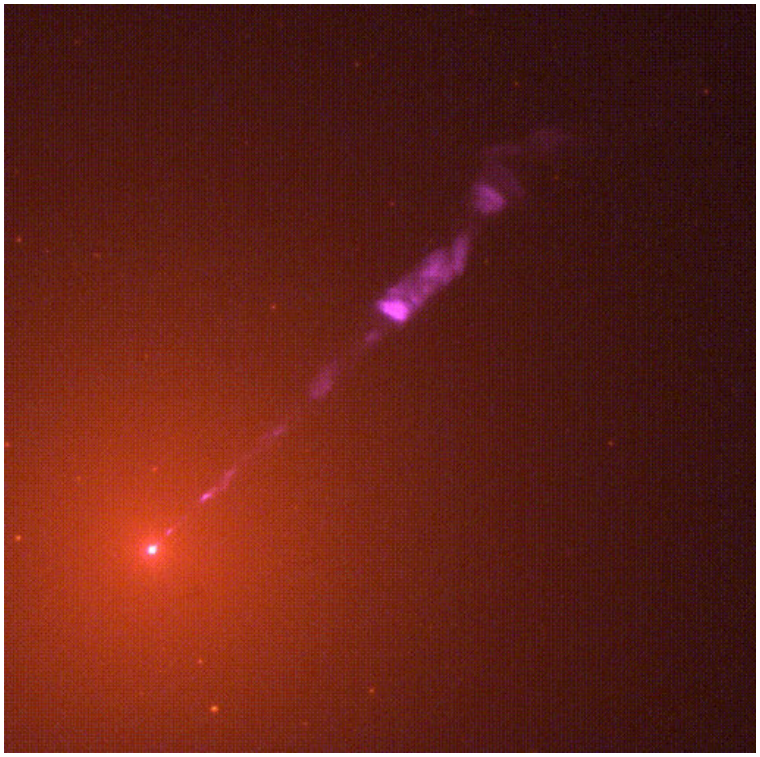

Figure 1.4 *Stacked image of M87 from HST WFPC2 images taken at approximately 290 and 800 nm. The jet extends to about 5 kly from the core. Photo credit: John Biretta.*

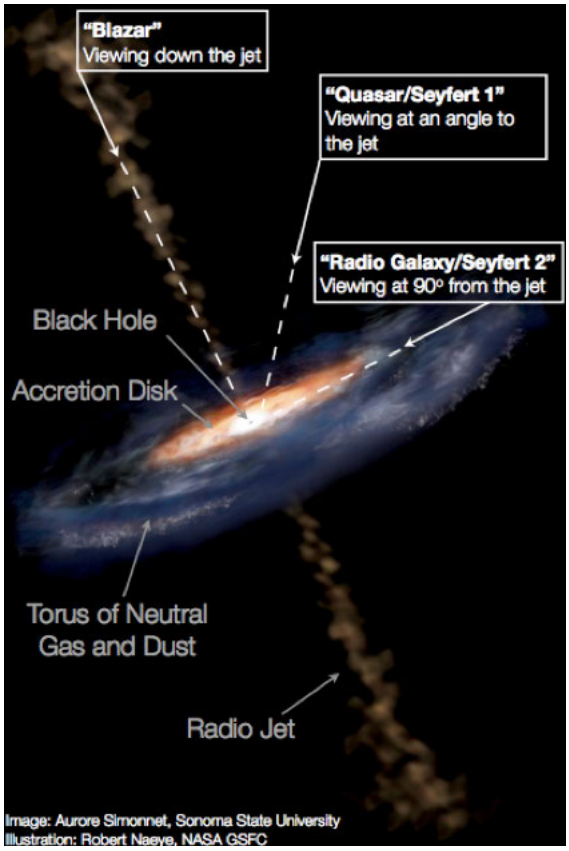

Figure 1.5 *Artist's conception of an AGN with examples of viewing angle-dependent classification.*

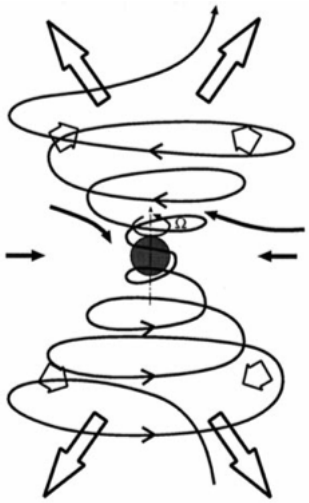

Figure 1.6 *Schematic diagram depicting the MHD acceleration and collimation model. Magnetized and rotating inflow toward a compact object (solid arrows) winds the magnetic field lines into a rotating helical coil called a torsional Alfvén wave train (TAWT). Magnetocentrifugal forces expel some of the material along the field lines and magnetic pressure and pinching forces (short open arrows) further lift and collimate it into a jet outflow (long open arrows). (Diagram and caption taken from Meier et al. (2001)).*

1.3 The Blazar Class of AGNs

A small fraction of AGNs have relativistic jets which are oriented within a small angle of the line of sight; these objects are referred to as blazars. Any electromagnetic radiation produced by the jet particles will be relativistically beamed along the jet axis. If the AGN is a blazar, this relativistically beamed radiation will often outshine the starlight from the galaxy itself. Because the analysis of VHE γ-rays from blazars is the major theme of this work, the properties of blazars will be outlined in some detail.

1.3.1 Jet production

The environment in the nucleus of an active galaxy contains not only the strong gravitational field of the central SMBH, but strong magnetic fields as well. While many viable models exist to explain the AGN jet phenomenon, the leading theory is that the production of the relativistic jets from AGNs is governed by magnetohydrodynamics. The specific details of

this production are still an open question. However, the computational model of Meier et al. (2001) suggests that the differential rotation in the accretion process creates a magnetic coil, as shown in Figure 1.6. This coil expels and pinches some of the infalling matter. This process is sufficient to accelerate charged particles to high energies. Diffusive shock acceleration, facilitated by a sufficiently strong magnetic field, is capable of accelerating charged particles to relativistic γ factors of $\sim$20. The dependence of the jet on infalling matter also explains the phenomenon of blazar flares. The high energy particles in the jet generate electromagnetic radiation (mechanisms for this are described below). Blazars often enter brief high states in which the flux of their emission increases. This is often due to a spontaneous injection of additional matter from the accretion disk, which produces more high energy particles, and thus a greater flux of electromagnetic radiation.

The multiwavelength spectra of blazars has a characteristic double-peaked structure. An example from observations of the blazar Markarian 421 is shown in Figure 1.7. The first peak in a blazar spectral energy distribution (SED) is usually attributed to synchrotron emission from the local electron population, while the second peak is thought to be generated by inverse Compton scattering of ambient photons off of these same electrons. It is also possible, however, that the second peak originates from the decay of pions produced by proton interactions.

1.3.2 γ-ray emission

The origin of the γ-ray emission from blazars is an open subject of inquiry in particle astrophysics, and it is likely that no single model is applicable to all AGNs. However, it is currently believed that the highest energy emission in all blazars can be attributed to either a hadronic or leptonic emission mechanism. Both models are briefly reviewed below.

Hadronic mechanism

Pohl and Schlickeiser (2000) have shown that any protons produced in an AGN jet are capable of being accelerated to energies as high as 10^{18} eV by sweeping up ambient material. Hadronic models invoke interactions of these high energy protons to explain the production of high energy photons. We can reasonably assume that AGN jets are comprised of proton-

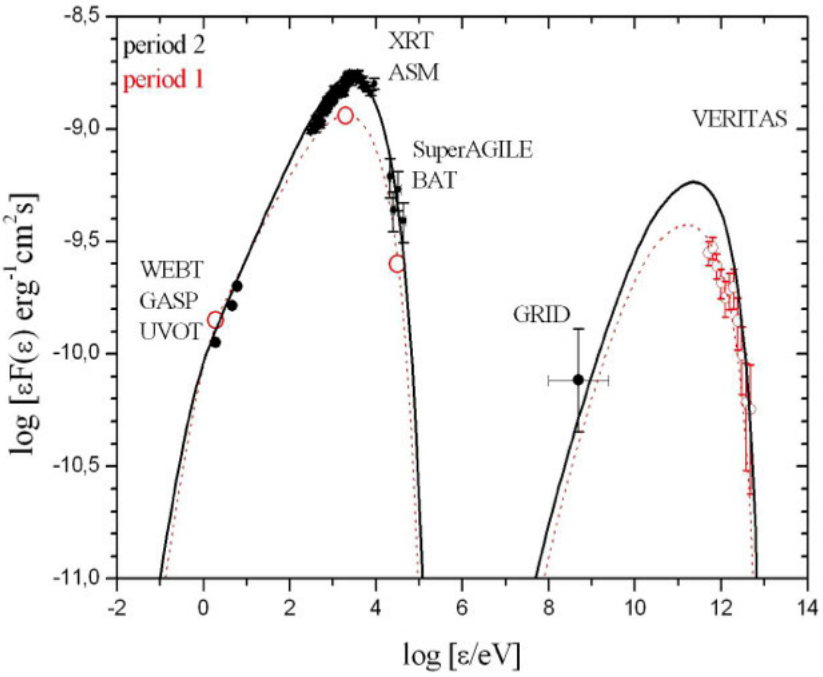

Figure 1.7 *Multiband spectrum of the blazar Markarian 421, observed with multiple instruments during lower and higher states. Note the two peaks, which correspond to synchrotron emission, and inverse Compton scattering. The fit comes from a one-zone Synchrotron Self-Compton emission model. This double-peaked spectrum is characteristic of blazars. Taken from Donnarumma et al. (2009).*

electron plasma. Protons are almost 2,000 times heavier than electrons, and therefore do not undergo significant magnetic deflection or suffer greatly from synchrotron losses. Any protons which exceed a certain threshold are capable of $p - \gamma$ photo-pion production against the soft photon field in the emission region (Böttcher, 2013). Two channels are shown in Equations 1.3 and 1.4.

$$p + \gamma \rightarrow p + \pi^0 \tag{1.3}$$

$$p + \gamma \rightarrow p + \pi^{\pm} \tag{1.4}$$

The neutral pions quickly decay into γ-rays. The charged pions under go the decay shown in Equation 1.5

$$\pi^{\pm} \rightarrow \mu^{\pm} \rightarrow e^{\pm} \tag{1.5}$$

The electrons then produce a cascade of γ-ray photons in a process identical to the electromagnetic atmospheric showers described in Section 3.1. This is known as a proton-induced cascade because protons are the initiating particles. Additional γ-ray emission comes from synchrotron radiation from the photo-pion decay products of the charged pions

Leptonic mechanism

In the leptonic emission model, seed photons in the emission region are inverse Compton scattered to higher energies. The electrons necessary for this process are the very synchrotron electrons which produce the first blazar peak; these electrons are constrained in the jet by the ambient magnetic field, and are available to upscatter background photons. The ability of inverse Compton scattering, which is a quantum electrodynamic process, to produce higher energy photons is illustrated by the inverse Compton scattering formula. If a photon of energy E scatters off an electron with relativistic factor[4] γ, then, the scattered energy is given by E_s.

[4]Here, $\gamma = \frac{1}{\sqrt{1-\frac{v^2}{c^2}}}$

$$E_s = \begin{cases} \gamma^2 E & E/m_e c^2 << \frac{1}{\gamma} \quad \text{Thomson Regime} \\ \frac{1}{2}\gamma E & E/m_e c^2 >> \frac{1}{\gamma} \quad \text{Klein} - \text{Nishina Regime} \end{cases}$$

For sufficiently low photon energies (with respect to the synchrotron electrons), the scattered γ-ray energy increases as the square of the electron energy.[5]

The mathematical description of inverse Compton scattering explains how lower-energy photons can be upscattered to HE and VHE energies. The origin of these lower-energy photons, however, also requires a physical explanation. While external sources of photons can be invoked, the Synchrotron Self-Compton (SSC) model. Bloom and Marscher (1996) explains correlations between synchrotron flares and TeV flares. In the "one zone" SSC model, it is assumed that synchrotron emission and inverse Compton scattering occur within the same emission region. The synchrotron electrons thus upscatter their own emitted photons to VHE energies. If an AGN injects additional electrons into its jet, resulting in a synchrotron flare, this model predicts that observers should see a contemporaneous high energy flare. This model does not, however, explain so-called orphan flares, in which an increased flux in VHE emission is not accompanied by an increased flux at lower energies (see Kusonose and Takahara (2006) for a treatment of orphan flare modeling).

1.3.3 Blazar spectral classification

Because the peak energy/frequency of a blazar's synchrotron peak is a proxy for the energy of particles in the jet, it is clear that the synchrotron and inverse Compton peaks should be correlated. We thus expect blazars with high-frequency synchrotron peaks to produce VHE γ-ray emission at higher energies such that they may be visible to γ-ray telescopes. BL Lac objects are often classified by the location of their synchrotron peaks in νF_ν representation: low-frequency peaked (LBLs), intermediate-frequency peaked (IBLs), and high-frequency peaked (HBL) BL Lac objects. The classification scheme is rough, but generally LBLs are taken as objects with synchrotron peaks in the submillimeter to infrared wavelengths, while HBLs are classified as having a synchrotron peak in the UV to X-ray regime. Albert et al. (2006)

[5] Particle energy is proportional to the γ-factor, $E = \gamma m_0 c^2$

observes that at least in the case of HBLs, blazars are expected to produce a roughly equivalent luminosity of γ-ray emission as synchrotron.

γ-rays from blazars that traverse large distances through extragalactic space do not do so unimpeded. A diffuse photon field known as the extragalactic background light permeates extragalactic space, and photons from this radiation field can interact with γ-ray photons so as to absorb them. Thus, γ-ray emitting blazars can act as a probe of this diffuse radiation field. While the question of blazar emission mechanisms is of great scientific importance to astrophysicists, blazars are also important tools for probing the space between our own galaxy, and distant sources of γ-rays. Therefore we now turn to the topic of the extragalactic background light, and the utility of blazars in studying it.

CHAPTER 2. INDIRECT PROBES OF THE EXTRAGALACTIC BACKGROUND LIGHT

One of the principle motivations of this work is the study of the extragalactic background light (EBL). The EBL is a diffuse cosmological radiation field consisting of all light emitted into extragalactic space since the epoch of recombination (Orr et al., 2011)[1]. Major sources of the EBl include nuclear energy releases, mid-infrared light from accretion processes, and light from early structure formation. The EBL thus encodes important information about the structure formation and stellar evolution history of the universe, and is a fundamental cosmological quantity (Dwek and Krennrich, 2012). The EBL is analogous to its more well-known "cousin," the cosmic microwave background (CMB), which probes physics at the surface of last scattering (Kashlinsky, 2005).

As described by Orr et al. (2011), the EBL has proven difficult to observe directly at most wavelengths, due to the foreground emission of the zodiacal light. In Section 2.4, we describe an indirect detection technique involving the analysis of distant, hard spectrum blazars. Gould and Schréder (1967) describe the attenuation of high energy spectra by ambient photon gases; the effect of the EBL on spectra obtained from distant blazars can be used to indirectly measure the spectrum of the EBL.

2.1 Origin and Spectrum of the EBL

The spectral energy distribution of the EBL is double-peaked, as shown in the summary of EBL studies in Figure 2.1. The near infrared (NIR) peak at $\sim$1 μm corresponds to energy releases from the formation of heavy elements in stellar nucleosynthesis. This ultraviolet and optical light was absorbed by dust and polycyclic aromatic hydrocarbons, then re-radiated at

[1]For the purposes of this work, we define the EBL as the diffuse radiation in the regime of 1μm to 1 mm.

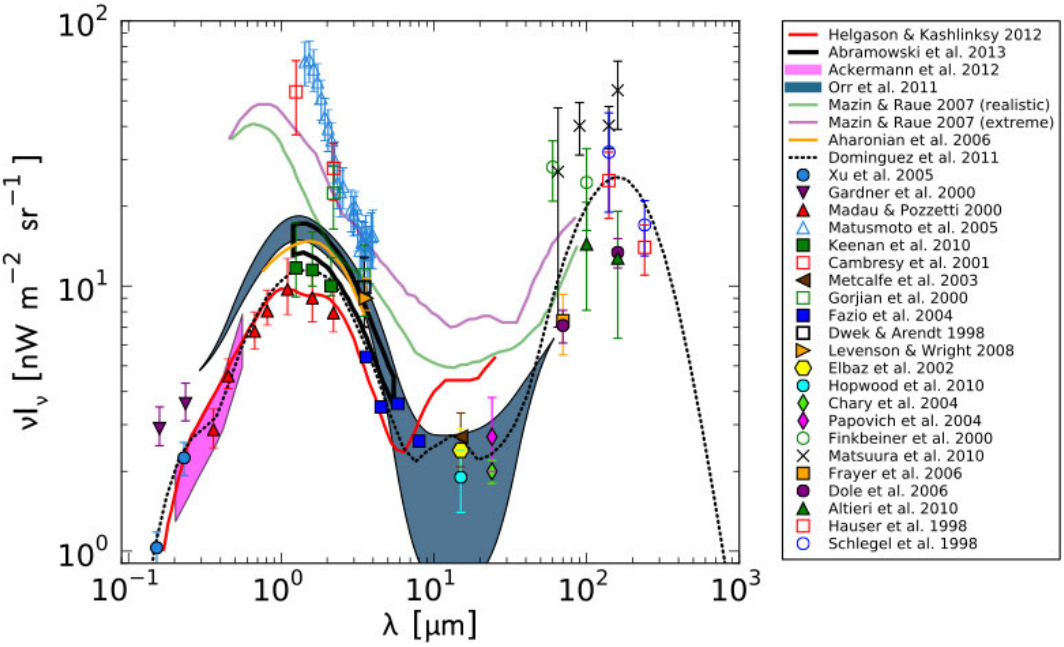

Figure 2.1 *EBL scenarios from models and measurements. Notice that while the flux of the EBL (both absolute flux and relative flux of peaks and troughs) varies, the locations of the peaks and troughs remains roughly constant. Probes of the EBL in this work focus on constraining the free parameters, specifically the absolute flux of the EBL, and the relative flux of the 1.6 μm and 10 μm fluxes. Plot taken from Krennrich and Orr (2013).*

infrared wavelengths to produce the far-infrared (MIR and FIR) emission, peaking at ∼100 μm. As noted by Dwek and Krennrich (2012), X-ray emission from AGN can be degraded and re-radiated at IR wavelengths, and it is estimated that 15% of the EBL's intensity at 24 μm is due to this emission.

The absolute intensity of the EBL is also an important quantity which elucidates the star formation history of the universe. Horiuchi et al. (2013) work backwards, using current estimates of the EBL intensity to estimate the cosmic star formation history of the universe (i.e. supernova rates).

2.2 Theoretical EBL Models

Hauser and Dwek (1998) note that the total EBL intensity is a measurement of the bolomet-

ric luminosity of the universe. In order to account for both peaks of the EBL's spectral energy distribution (SED), theoretical models must account for the NIR emission from galaxies, the MIR and FIR emission from the dust content of galaxies, and redistribution of energy from cosmic expansion. Dominguez et al. (2011) describes four theoretical approaches to constructing an EBL model:

1. **Forward evolution:** Assumptions are made about the initial cosmological state of the universe. The system is evolved forward in time using semi-analytic models of galaxy formation to predict the current spectrum of the EBL.

2. **Backward evolution:** Information about current galaxy populations is used to evolve the universe backward in time.

3. **Evolution of galaxy populations, inferred over a range of redshifts:** Galaxy evolution is inferred using some observational quantity, such as the star formation rate density of the universe.

4. **Evolution of galaxy populations from direct observations:** Galaxy populations are observed over a range of redshifts that contribute significantly to the EBL.

Furthermore, because the EBL consists of light from all times after last scattering, the effect of cosmic expansion is significant. The expansion of the universe has shifted the spectrum of the EBL and redistributed light to longer wavelengths.

In this work, the backward evolution EBL model of Dominguez et al. (2011), as well as the empirical fit derived by Orr et al. (2011) will be used to remove the effects of the EBL from γ-ray spectra.

2.2.1 Contributions to the EBL

The short-wavelength component of the EBL in the UV, optical, and NIR regime is produced mainly by direct emission from galaxies, and is a good proxy for the stellar component of galactic emission in the early universe (Kashlinsky, 2005). Most of the stellar component of the EBL is emitted by massive stars that end their lives as core collapse supernovae, and therefore the

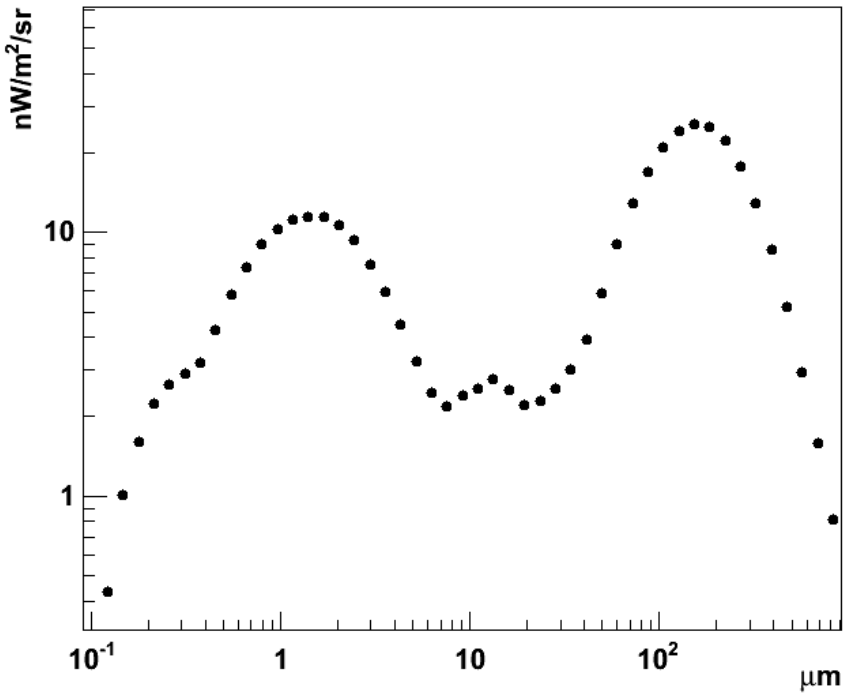

Figure 2.2 *The backward evolution EBL spectrum of ?) at a redshift of z=0.*

total intensity of the EBL (including the thermally reprocessed light at longer wavelengths) can be used to derive an estimate of the universe's supernova rate and resulting flux of supernova neutrinos (Dwek and Krennrich, 2012). The stellar component of the EBL is therefore an important tool in understanding and constraining stellar evolution models.

The far infrared contributions to the EBL come from thermal emission by dust; the thermal energy originally comes from heating by starlight. As stated by Dwek (1998), dust is produced in a variety of environments ranging from quiescent stellar outflows to explosive ejecta such as novae and supernovae. Upon injection into the ISM, dust particles are subjected to various physical processes causing evaporation. Dust is also grown in the ISM, in part by the accretion of ambient gas particles. At mid-IR wavelengths, the EBL emission originates from thermal radiation by polycyclic aromatic hydrocarbons and small grains which have been transiently heated to $T = 200\,K$. This thermally-reprocessed emission represents roughly 50% of the light from stars in the optical and UV regimes (Chary et al., 2001). This reprocessing is an important

consideration for galaxy evolution models: because optical and UV light are redistributed to longer wavelengths, it necessarily means that star formation rates derived from optical/UV galaxy luminosities will represent a lower limit.

2.3 Direct EBL Measurements

Direct measurements of the EBL are possible at longer wavelengths, where foreground emission is minimal. At wavelengths above 125 μm, the solar system's zodiacal light contributes only a small fraction of observed emission (Fixen et al., 1998). Such measurements have been made by two instruments on the Cosmic Background Explorer (COBE) satellite.

Aboard COBE are two devices capable of measuring EBL intensities: DIRBE and FIRAS. As Kashlinsky (2005) observes, mutually consistent direct detections of the FIR band of the EBL have been made by DIRBE and FIRAS. DIRBE (Diffuse Infrared Background Experiment) is designed to image the sky in ten photometric bands from 1.25 to 240 μm (Schlegel, 1998). Schlegel (1998) reports EBL spectral intensities of 32 ± 13 and 17 ± 4 $\frac{\text{nW}}{\text{m}^2 \cdot \text{sr}}$ at 140 and 240 μm respectively, at the 95% confidence level. Analysis of the DIRBE data by Hauser et al. (1998) gives 25 ± 7 and 14 ± 3 $\frac{\text{nW}}{\text{m}^2 \cdot \text{sr}}$, respectively, at these wavelengths.

The analysis of Hauser et al. (1998) was performed by selecting a portion of the sky with high galactic and ecliptic latitude, and removing various sources of foreground emission. Figure 2.3 shows the strength of the zodiacal foreground with respect to the EBL spectrum. A 3 σ detection as well as isotropy in the region of the sky sampled was required to claim an EBL detection, and only the data points at 140 and 240 μm met this criterion.

The Far Infrared Absolute Spectrophotometer (FIRAS) measures the spectrum of the FIR portion of the cosmic infrared background, as well as the cosmic microwave background (Fixen et al., 1998). Fixen et al. (1998) reports an EBL spectrum between 125 and 2000 μm of $I_\nu = 1.3 \pm 0.4 \times 10^{-5} \left(\frac{\nu}{\nu_0}\right)^{0.64 \pm 0.12} P_\nu\left(18.5 \pm 1.2\text{K}\right)$, where $\nu_0 = 2.4 \cdot 10^{12}\,\text{Hz}$ and $P_\nu\left(T\right)$ is a blackbody spectrum. They note that this is consistent with the spectral intensities derived from the DIRBE analysis. This spectrum corresponds to an integral EBL intensity between 5 and 80 cm^{-1} of 14 $\frac{\text{nW}}{\text{m}^2 \cdot \text{sr}}$, and comprises 20% of the estimated energy release from stellar nucleosynthesis over the course of the universe's history.

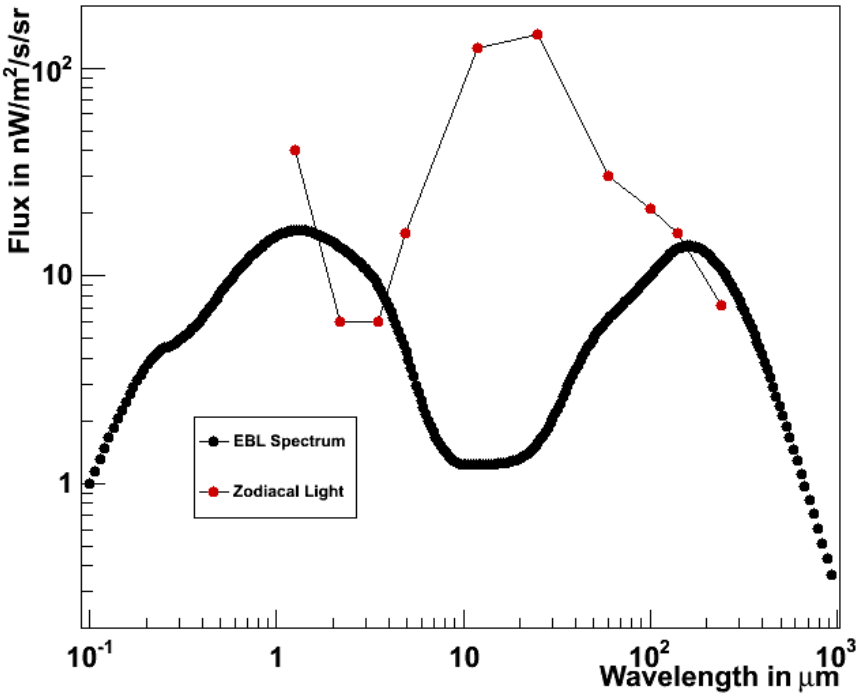

Figure 2.3 *EBL spectrum from Orr et al. (2011), shown along with the zodiacal foreground seen by DIRBE. The relative strengths of the two radiation fields illustrates the difficulty in directly measuring the mid-IR portion of the EBL.*

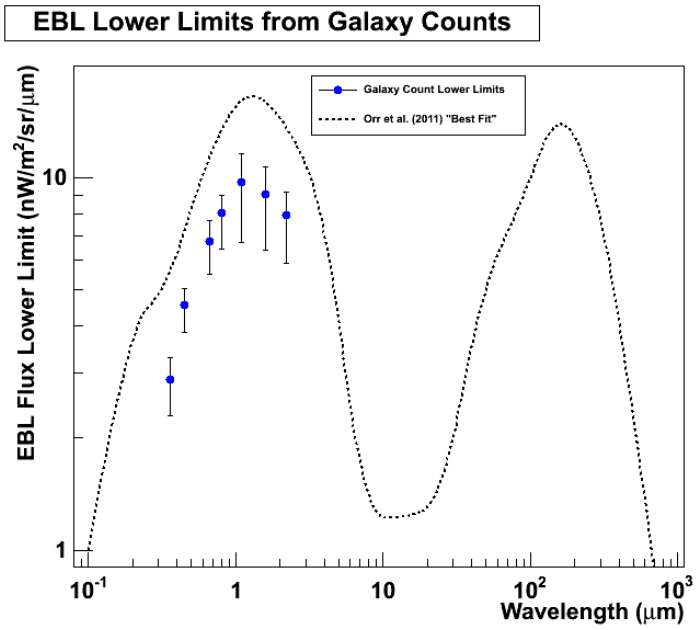

Figure 2.4 *EBL fluxes derived from galaxy counts Madau and Pozzetti (2000), compared with the EBL SED derived in Orr et al. (2011). Because galactic light is only one contributor to the flux of the EBL, these data points serve as lower limits on the actual SED of the EBL.*

It is also possible to place lower limits on the shorter wavelength component of the EBL by making direct measurements of starlight. The UV/Optical/NIR portion of the EBL is comprised of the composite emission from galaxies. Because the galactic contribution comes ultimately from stellar nucleosynthesis, most of this emission is produced by hydrogen fusion. Lower limits on this portion of the EBL flux have been obtained from galaxy counts. Madau and Pozzetti (2000) employ a technique using data from the Hubble Deep Field. Here, 425 objects were observed over a $50 \times 50\,\mathrm{arcsec}^2$ area of the sky. Luminosities were calculated at wavelengths ranging from 0.25μm to 2.2μm. These luminosities correspond to integrated starlight from galaxies in the field of view, and represent lower limits on the flux of the EBL in the NIR regime. The results are shown in Figure 2.4, along with a comparison to an EBL SED measured from γ-ray data (this technique is described in Section 2.4).

2.4 EBL Extinction of TeV γ-rays

With the advent of current generation ground- and space-based γ-ray telescopes, it now possible to sample the spectra of distant blazars over a wide range of energies from the GeV to multi-TeV regime. The EBL absorbs a detectable fraction of TeV photons, thus making it possible for us to probe the EBL by searching for absorption features in the spectra of these blazars.

2.4.1 $\gamma\gamma$ Pair production

Gould and Schréder (1967) describe in detail the process of $\gamma\gamma$ pair production, as well as absorption probabilities for high energy photons traversing cosmic distances. Here, we derive the opacity of the EBL to a γ-ray photon from a distant blazar. Opacity τ is defined as per the usual astrophysical meaning, in which an emitted spectrum with flux $F(\nu)$ will be observed as $F(\nu)\, e^{-\tau(\nu)}$

We begin with the cross-section for this interaction. The cross-section for the pair production interaction $\gamma\gamma \rightarrow e^+e^-$ has been calculated by Breit and Wheeler (1934), and is given by Equation 2.1.

$$\sigma_{\gamma\gamma}(E_\gamma, \epsilon, \mu) = \frac{3}{16}\sigma_t^2 \left(1-\beta^2\right)\left[2\beta\left(\beta^2-2\right) + \left(3-\beta^4\right)\ln\frac{1+\beta}{1-\beta}\right] \tag{2.1}$$

Here, σ_t is the Thompson cross-section, and we define $\beta = \sqrt{1-\frac{\epsilon th}{\epsilon}}$, where ϵ_{th} is the energy threshold for pair production ($\epsilon = \frac{E}{c}$ is used to represent energy in natural units). The cross-section is maximized at $\beta = 0.70$. Equation 2.2 gives the wavelength of the maximal cross-section as a function of γ-ray energy.

$$\frac{\lambda_{max}}{\mu m} \approx 1.24\frac{E_\gamma}{TeV} \tag{2.2}$$

The linear dependence of the cross-section maximum on γ-ray energy is important because it implies that longer wavelengths of the EBL absorb higher energy gamma rays. We now derive this relation explicitly. We model the EBL as a Bose gas with energy-dependent photon density $n_\epsilon(\epsilon, z)$, where ϵ is the EBL photon energy and z is the redshift at which the EBL is

being sampled. The spectral energy distribution of the EBL is typically specified in terms of νI_ν, with the unit of $\frac{nW}{m^2 sr}$ being a convenient unit of choice (though choice of units is of course irrelevant to this derivation). The relation between the EBL photon density and the spectral energy is given by Equation 2.3.

$$\epsilon^2 n_\epsilon(\epsilon, z) = \left(\frac{4\pi}{c}\right) \nu I_\nu \tag{2.3}$$

The EBL is a cosmological radiation field, and we must therefore transform the photon energy so as to account for cosmological expansion. We therefore let $\epsilon' = (1+z)\epsilon$. Next, photon number conservation is invoked. The number of photons at redshift z between energy ϵ' and $\epsilon' + d\epsilon'$ is equal to the number of photons at redshift zero between energy ϵ and $\epsilon + d\epsilon$, as described by Equation 2.4.

$$n_\epsilon\left(\epsilon', z\right) d\epsilon' = (1+z)^3 n_\epsilon(\epsilon, 0)\, d\epsilon \tag{2.4}$$

A minimal amount of algebra gives the number density to flux relation shown in Equation 2.5.

$$n_\epsilon\left(\epsilon', z\right) d\epsilon' = (1+z)^4 \frac{4\pi}{c} \frac{\nu I_\nu(\nu, 0)}{\epsilon'^2} d\epsilon' \tag{2.5}$$

We note that the minimum threshold energy for a pair production interaction between a γ-ray photon and an EBL photon incident at an angle θ is given by Equation 2.6[2].

$$\epsilon_{th}(\epsilon_\gamma, \mu) = \frac{2m_e^2}{\epsilon_\gamma (1 - \cos(\theta))} \tag{2.6}$$

We also require the following redshift, distance relation from cosmology, given in Equation 2.7.

$$\frac{dl}{dz} = \frac{c}{(1+z) H_0} \frac{1}{\sqrt{\left[(1+z)^2 (\Omega_m z + 1) + z(2+z)\right] \left[(1+z^2)\Omega_r - \Omega_\Lambda\right]}} \tag{2.7}$$

[2]This can be derived from conservation of 4-momentum

Here the density parameters Ω_m, Ω_r, and Ω_Λ are ratios of the density of matter, radiation, and the cosmological constant (respectively) to the critical density of the universe. H_0 refers to the current value of the Hubble Parameter, also known as the Hubble Constant. Equation 2.7 can be integrated between zero and z_0 to obtain the physical distance to any given redshift z_0.

In order to derive the integrated opacity from a photon gas, we must evaluate the triple integral in Equation 2.8.

$$\tau_\gamma\left(E_\gamma, z\right) = \int_0^z \int_{-1}^{1} \int_{\epsilon'_{th}}^{\infty} \frac{dl}{dz} \frac{1-\mu}{2} n_\epsilon\left(\epsilon', z\right) \sigma_{\gamma\gamma}\left(E'_\gamma, \epsilon', \mu\right) \mathrm{d}\epsilon' \, \mathrm{d}\mu \, \mathrm{d}z' \tag{2.8}$$

Here we have made the substitution $\mu = \cos(\theta)$. By substituting 2.7, 2.5, and 2.1 into the integrand in 2.8, the opacity can be evaluated by numerical integration. Equation 2.5 of course requires an input EBL spectrum. For illustrative purposes, the "best fit" model of Orr et al. (2011) has been used to calculate optical depths. Figure 2.5 shows the optical depth vs. γ-ray energy relation for several redshifts. Note that while sources at larger redshifts see a greater opacity, the overall shape of the curve does not change. Note also that there is always a flattening of the opacity between ~1 and 10 TeV. This flattening, which arises from the sharp downturn in the EBL intensity between 1 and 10 μm is an important feature which can be exploited when using blazar spectra to probe the EBL, since it will cause a break in the shape of an intrinsic power law spectrum between 1 and 10 TeV. It is thus possible to search the spectra of TeV-emitting blazars for this feature, and to place constraints on the SED of the EBL.

2.5 TeV Spectral Variations Due to Extinction of AGN γ-ray Signals

The EBL is capable of extincting photons of differing energies to different extents, thus producing characteristic features in the spectra of γ-ray sources. In principle, if we know the intrinsic spectrum of a source, we can use features in the spectrum to probe the EBL. This technique was proposed by Gould and Schréder (1967), who calculated the opacity of the universe to high energy photons for a variety of background photon gases and specifically noted

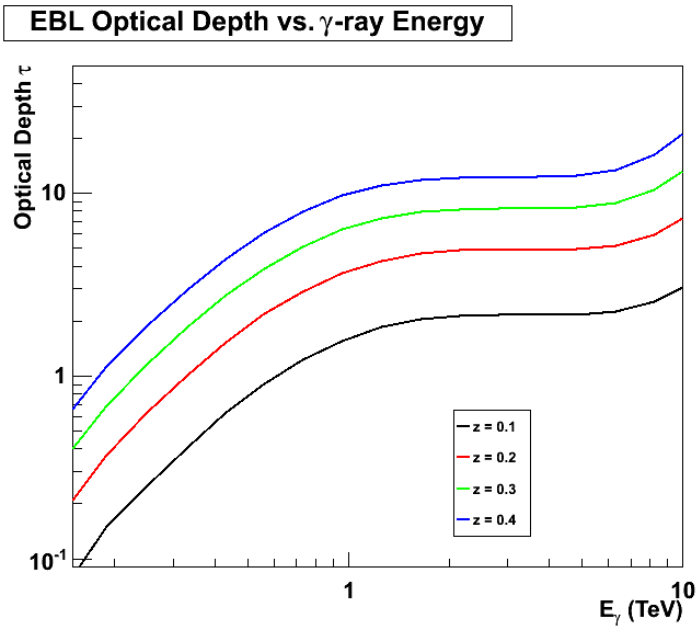

Figure 2.5 *EBL opacities for several source redshifts. The SED of Orr et al. (2013) was used to calculate these opacities.*

that the detection of γ-rays in the 1 to 10 TeV regime would be of great value in determining the universe's optical photon density and testing cosmological models. The advent of new γ-ray detectors has made this technique a viable option for probing the EBL. One of the early uses of this technique was by Stecker and De Jager (1993), who used γ-ray data from space-based instruments along with ground-based TeV detectors to place upper limits on the NIR band of the EBL spectrum. γ-rays from the blazar Mrk 421 (redshift $z = 0.03$) were studied using data taken from the EGRET γ-ray satellite, as well as ground-based data from the Whipple 10 m experiment. The multiband spectrum of Mrk 421 was produced using spectral points between 50 MeV and 2 GeV taken from EGRET data (Lin et al., 1992) as well Whipple data extending to 3 TeV (Mohanty et al., 1993). When fit with power law spectra, the spectral indices in the two regimes were consistent, with the EGRET team reporting a result of Γ = -1.96 $\pm$ 0.14 in the GeV regime and Whipple reporting Γ = -2.25 $\pm$ 0.19_{stat} $\pm$ 0.3_{sys}. The 2σ upper limit placed on the integral EBL spectrum in the 1-5 μm regime was approximately 10 $\frac{\mathrm{nW}}{\mathrm{m}^2 \cdot \mathrm{sr}}$

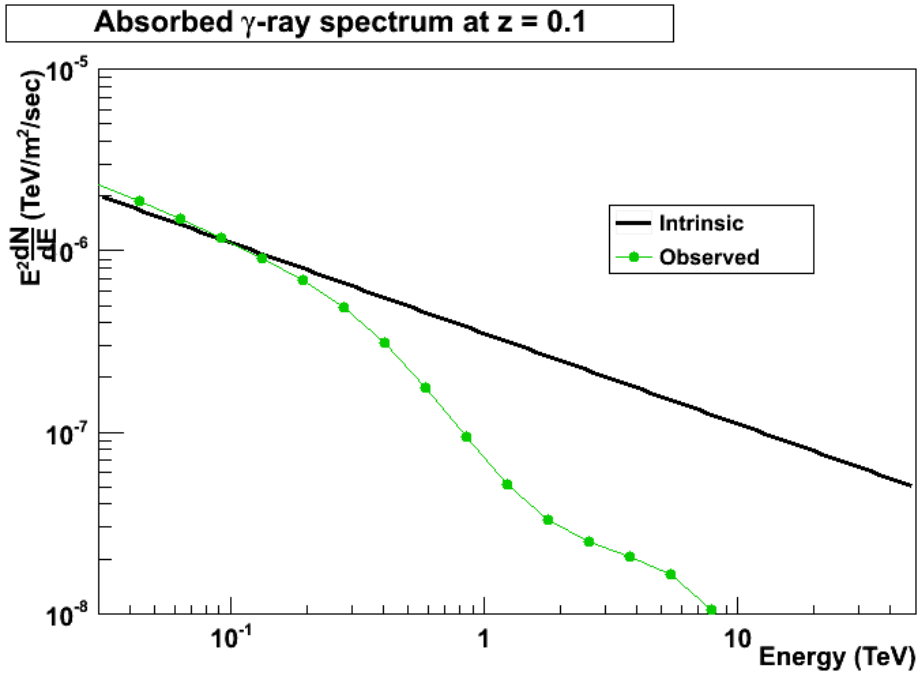

Figure 2.6 *Spectral variation from an intrinsic power law source. A power law function was absorbed with the opacity resulting from a γ-ray signal traversing a redshift of z=0.1 through an EBL with the SED derived from Orr et al. (2013).*

2.6 Existing Constraints from γ-ray Observations of TeV-emitting Blazars

As Dwek and Krennrich (2005) observe, TeV-emitting blazars afford us the opportunity to probe the EBL. There are a number of available methods for using the EBL's opacity to TeV γ-rays to constrain the spectrum of the EBL. However, such techniques are limited by our lack of knowledge concerning the intrinsic spectra of TeV-emitting sources. Even if we make no assumption of the intrinsic TeV emission of the source, a parameter space of EBL scenarios can be explored. Each scenario can then be tested against blazar data. We can thus use γ-ray observations of blazars to place upper limits on the EBL flux.

The blazars Mrk 421 ($z = 0.03$) and Mrk 501 ($z = 0.03$) have often been used as means to constrain the EBL by the method of γ-ray spectral variations. Biller (1998) used both sources to place upper limits on the IR portion of the EBL between 1 and 30 μm. Both sources pose challenges in any EBL study because of their rapid short-term variability and intrinsic spectral curvature. To calculate upper limits, the blazar spectra were allowed to take on any shape softer than E^{-2}. The EBL spectrum was allowed to take on any value provided that 1.) upper limits imposed by previous experiments were satisfied and 2.) EBL attenuation does not alter the observed spectral shape outside of the bounds initially imposed by the data. The resulting upper limits were two orders of magnitude more restrictive than those imposed by DIRBE. Mrk 501 has also been used by Funk (1998) to constrain the EBL. Here, Mrk 501 was assumed to obey a strict power law into the multi-TeV regime. Between the energy ranges of 1 to 400 μm, an *ansatz* was made for the EBL spectrum based on two separate models. The energy density of the EBL at 40 μm was constrained at less than 1.1×10^{-3}eV/cm^3. Another study by Dwek and Krennrich (2005) also employed Mrk 421 and Mrk 501. Here, both spectra were de-absorbed with various models of the EBL, and ruled out models which exhibited a statistically significant rise at these energies. This provided an EBL flux upper limit of 15 $\frac{\mathrm{nW}}{\mathrm{m}^2\cdot\mathrm{sr}}$ at 60 μm. Figure 2.7 provides a summary - compiled by Dwek and Krennrich (2012) - of limits imposed on the EBL by γ-ray observations of blazars.

Improved probes of intrinsic blazar spectra were made possible with the 2008 launch of the Fermi Gamma-Ray Space Telescope. Fermi measures γ-rays in the regime of 100 MeV to

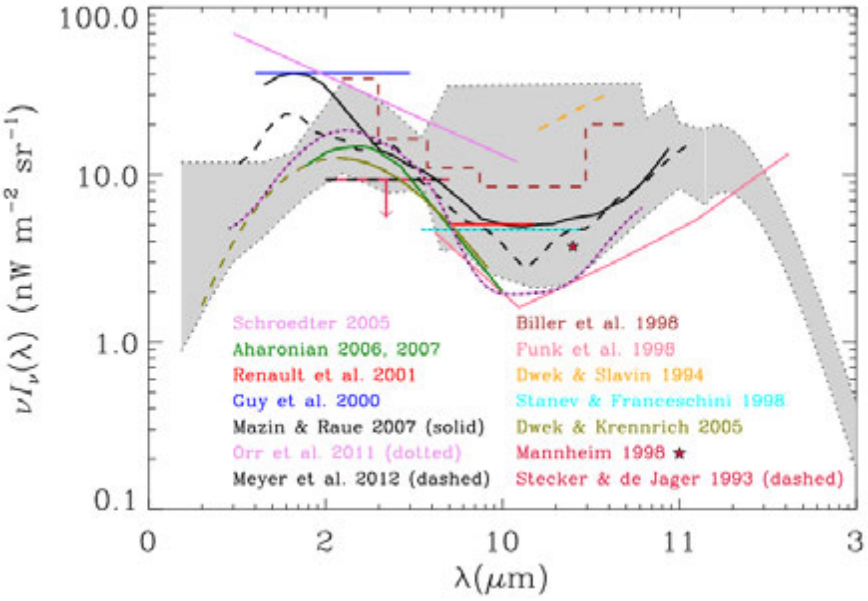

Figure 2.7 *Limits on the EBL imposed by γ-ray observations of blazars. Taken from Dwek and Krennrich (2005)*

beyond 100 GeV. At these energies, EBL absorption is minimal. This means that blazar spectra measured by Fermi are good proxies for intrinsic blazar spectral shapes at TeV energies (barring TeV absorption by some other means). In the study by Orr et al. (2011), a selected parameter space of EBL models were used to de-absorb the spectra of several distant blazars, and models which provided TeV spectra that were inconsistent with the Fermi spectra were ruled out. Additionally, Orr et al. (2011) made use of TeV spectra taken from current generation IACT instruments, which provide sufficient energy resolution to detect the sorts of spectral variations illustrated in Figure 2.6. In particular, spectral breaks were examined near the $\sim$1 TeV flux, where flattening of the opacity is expected to cause a change in the shapes of blazar spectra. Using this "TeV spectral break" method, additional constraints were placed on the spectrum of the EBL. These constraints were used to derive the "best fit" SED shown in Figure 2.4.

Table 2.1 List of hard spectrum blazars analyzed in this work. Shown here is each source's redshift, the HE spectrum from Fermi data, and the VHE spectrum from analysis presented in this work.

Source	Redshift	Γ_{HE}	Γ_{VHE}
RGBJ0710+591	0.125	-1.53±0.12	-2.64±0.24
H1426+428	0.129	-1.32±0.12	-2.55±0.21
1ES0229+200	0.140	-1.36±0.25	-2.81±0.19
1ES1218+304	0.182	-1.72±0.07	-3.12±0.05
1ES0414+009	0.287	-1.98±0.15	-4.64±0.90

2.7 The Use of Hard Spectrum HBL Objects in Probes of the EBL

The EBL opacities shown in Figure 2.5, and the resulting spectral variation on a model power law shown in Figure 2.6 illustrate that in order to effectively probe the EBL it is advantageous to study blazars whose spectra extend far into the optically thick regime of the EBL, i.e. where $\tau > 1$. The opacity of the EBL causes an overall decrease in the absolute flux of TeV emission. It is also effective to probe beyond 1.3 TeV, where the downturn in the EBL spectrum at 1.6 μm causes a flattening of the EBL's opacity to γ-rays. This flattening leads to variations in the shape of the TeV spectra.

Among HBLs, a class of sources known as hard-spectrum blazars has emerged which exhibit significant emission at relatively high energies. These blazars are so-named because their (assumed) intrinsic emission spectra are unusually hard.

Table 2.1 gives a list of hard-spectrum blazars that will be analyzed in this work, along with their intrinsic emission spectral index (assumed to be well-represented by the HE spectra derived by the Fermi satellite), and the VHE spectral index. These blazars are listed in order of increasing redshift, and we note that sources located at greater distance tend to have softer spectra, as expected due to increased EBL absorption. The intrinsic spectra, on the other hand, appear to not be correlated with redshift and are all especially hard.

The importance of these objects and of their spectral analysis to EBL studies motivates the preparation of a robust technique for detecting and analyzing γ-rays from blazar sources. We thus turn to the development of γ-ray astronomy, the ground-based method of detecting

VHE γ-rays, and the design and implementation of an analysis chain for performing spectral analysis.

CHAPTER 3. GROUND BASED γ-RAY ASTRONOMY

3.1 Air Showers

The earth's atmosphere is constantly bombarded by high energy γ-ray and cosmic ray particles. Many of these particles interact with atmospheric nuclei to create secondary products. Often, these products can induce further interactions, resulting in a cascade of particles that can penetrate deep into the atmosphere. We refer to these particle cascades as extensive air showers. An air shower begins with a single particle interacting at the top of the atmosphere, which multiplies into more particles at successive generations, peaks at some maximum value, and then reduces in number until falling below some threshold for particle production (Gaisser, 1990).

While the creation of these air showers makes direct detection of γ-rays on the ground impossible, it makes indirect detection possible by observing the showers. The use of the atmosphere as a component in a particle detector is more effective for the detection of TeV γ-rays than space-based observatories. The flux of γ-rays from the Crab Nebula above 1 TeV is approximately 7 photons per square meter per year[1]. However, the Fermi γ-ray space telescope has an effective collection area of less than 1 square meter above 100 GeV (Rando, 2009), which would make detection of TeV γ-rays from space impractical even if the instrument's high energy coverage extended into the TeV regime. The earth's atmosphere, on the other hand, provides a much larger surface area for absorbing γ-rays, as well as a much greater column depth for absorbing very high energy particles. By using the atmosphere to absorb γ-rays, it is possible to detect astrophysical γ-ray sources well into the multi-TeV regime.

[1]This can be easily derived from Aharonian et al. (2006), which reports a measurement of the > 1 TeV flux of the Crab Nebula as $2.26 \pm 0.08_{\text{stat}} \cdot 10^{-7} \frac{\text{photons}}{\text{m}^2 \cdot \text{second}}$

3.1.1 γ-ray induced electromagnetic cascades

γ-rays incident upon the atmosphere initiate *electromagnetic* cascades, so-called because the secondaries interact via the electromagnetic force. A sufficiently energetic[2] γ-ray that enters the atmosphere will interact with the intense Coulomb field of a nucleus to produce an electron/positron pair (typically both referred to as "electrons" for these purposes). Both particles are then deflected by atmospheric nuclei to produce bremsstrahlung photons; the average distance over which a bremsstrahlung photon is produced is the particle's radiation length (and is equal to the radiation length for e^+e^- pair production). The bremsstrahlung photons produce more electrons, and the cascade continues until the current generation of electrons has an energy of about 80 MeV (Gaisser, 1990), at which point ionization losses dominate. The electromagnetic cascade can be approximated by the Heitler toy model, as shown in Figure 3.1. Although Monte Carlo simulations can be used to model electromagnetic cascades in much finer detail, the Heitler toy model can nonetheless be used to easily estimate properties of an air shower such as the number of generations of particles produced for a given primary γ-ray energy, the number of particles in any generation, the size of the shower, etc.

3.1.2 Hadronic cascades

As discussed in Section 1.1.1, the chemical composition of the cosmic ray spectrum in the TeV regime is dominated by protons. Although many types of cosmic ray particles interact with the earth's atmosphere, cosmic ray protons are by far the most important source of atmospheric particle cascades, and thus form the principle background seen by a ground-based γ-ray telescope. Proton-induced cascades are referred to as *hadronic* because they produce baryons and mesons that interact via the strong force. As shown in Figure 3.2, an incident proton will interact with an atmospheric nucleus to create charged and neutral pions. The neutral pion quickly decays into a pair of γ-rays and produces an electromagnetic cascade via the process depicted in 3.1. The charged pions produce their own sub-showers and eventually decay into muons, and eventually into electrons and neutrinos. The atmospheric nucleus also leaves behind its spallation products.

[2]Because the mass of an electron is 511 keV, the minimum energy for this process is 1.022 MeV

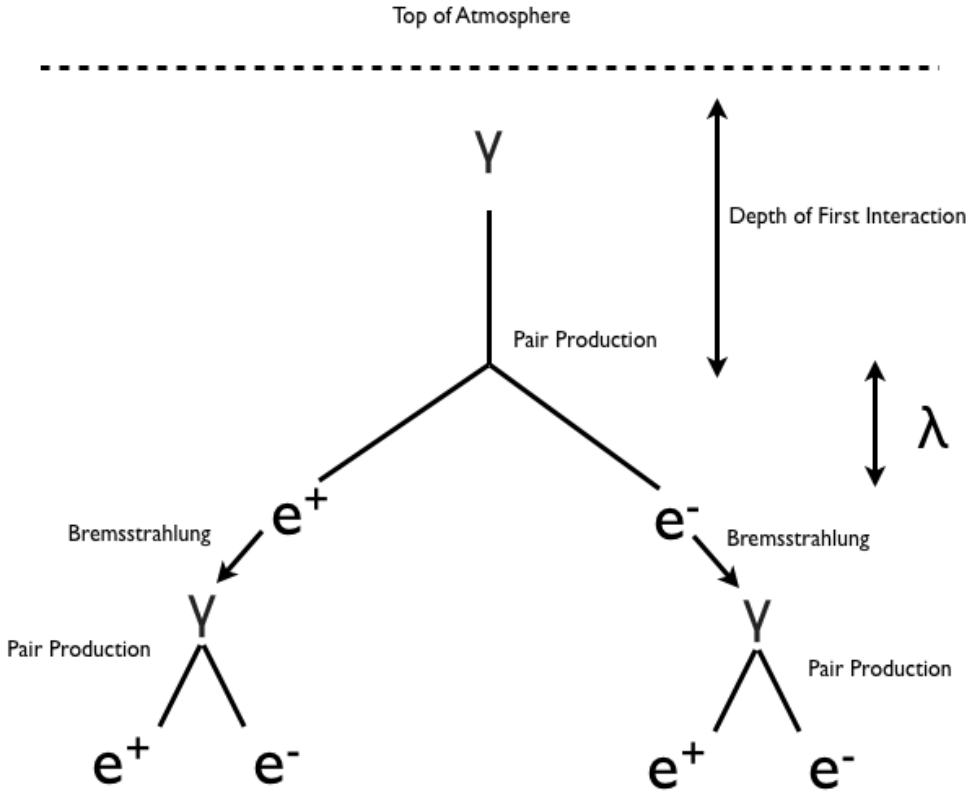

Figure 3.1 *A diagram of the Heitler toy model. This is a rough approximation of the development of an extensive air shower. The radiation length λ is identical for bremsstrahlung losses and pair production.*

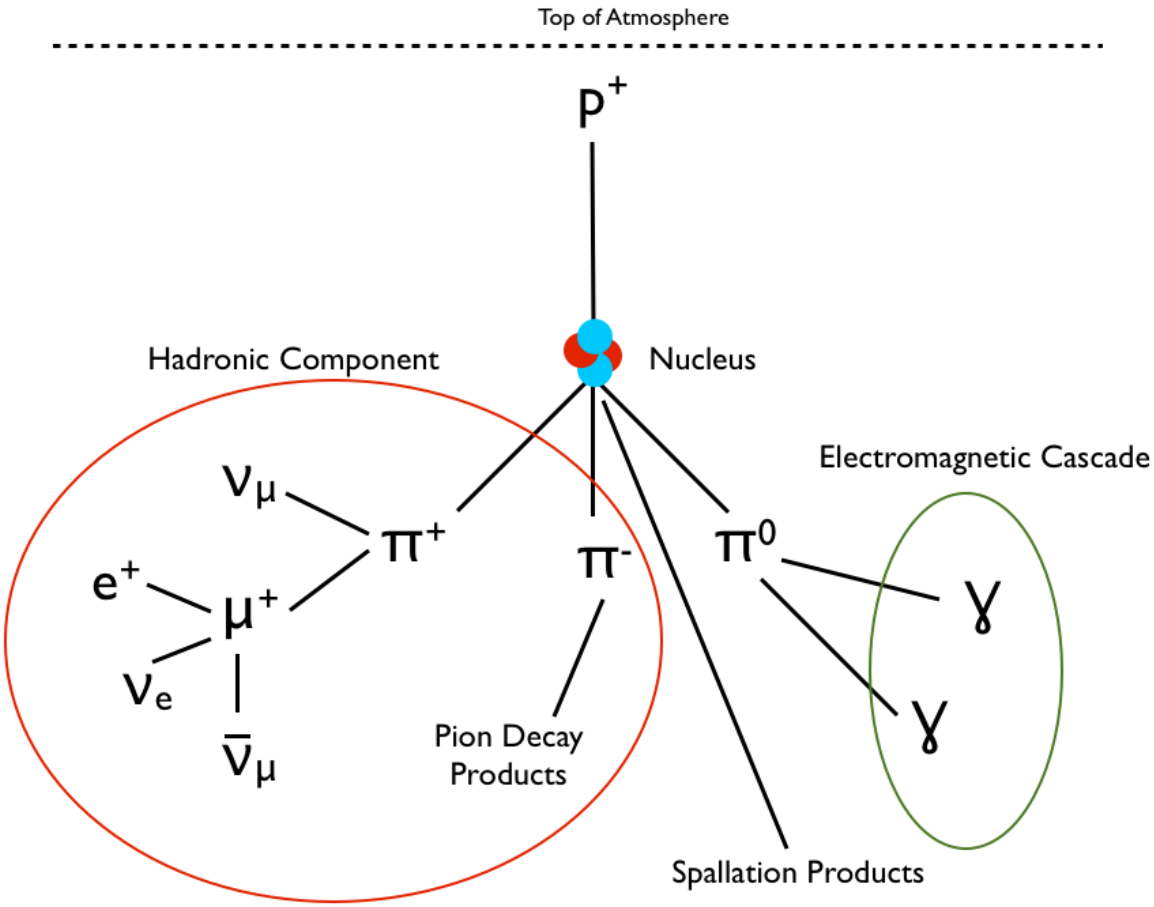

Figure 3.2 *The cascade induced by a proton incident on the earth's atmosphere. In addition to the electromagnetic component, there are additional products due to spallation of the nuclear target as well as the decay of charged pions.*

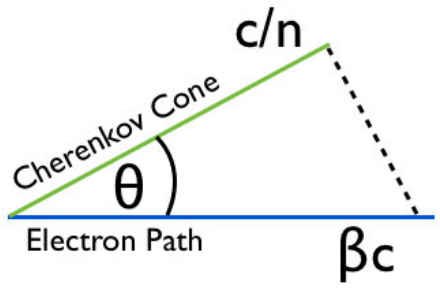

Figure 3.3 *Geometric construction to derive the Cherenkov angle from a single emitting electron.*

3.1.3 Cherenkov light from air showers

The earth's atmosphere has an altitude-dependent index of refraction which retards the speed of light such that the high energy electrons from a particle cascade travel faster than the propagation speed of light. This causes brief flashes of optical and ultraviolet radation. As early as 1934, P.A. Cherenkov reported the discovery of "feeble visible radiation emitted by pure liquids under the action of fast electrons." This radiation was soon termed Cherenkov light, and its emission was explained quantitatively by Frank and Tamm (1937). Cherenkov radiation is produced when a charged particle traverses a dielectric faster than the material's light propagation speed. As a particle traverses the medium, its charge causes nearby atoms to depolarize. When returning to their ground states, they release electric dipole radiation. Normally this light would interfere destructively and no net radiation would be produced. However, when the disturbance of atomic electrons propagates at a superluminal speed, the resulting light interferes constructively and produces radiation.

As described in Section 3.2, Cherenkov radiation can be exploited to use the earth's atmosphere as a calorimeter and detect astrophysical γ-rays. In order to demonstrate the efficacy of this technique, we derive the spectrum of radiation from particles in an air shower.

A single relativistic electron moving at some speed βc emits its Cherenkov radiation in a cone. We refer to the opening angle of this cone as the Cherenkov angle. If we draw the velocity vector of the electron and the Cherenkov wavefront, the geometric construction shown in Figure 3.3 can be used to easily derive the Cherenkov angle,

$$\cos(\theta) = \frac{1}{\beta n}. \tag{3.1}$$

The maximum Cherenkov angle is found by minimizing the cosine function, i.e. by setting $\beta = 1$. Thus,

$$\theta_{max} = \cos^{-1}\left(\frac{1}{n}\right) \tag{3.2}$$

We can also derive the minimum energy threshold for Cherenkov emission. Given a charged particle with speed $v = \frac{c}{n}$, the relativistic gamma-factor is $\gamma = \frac{1}{\sqrt{1-\frac{1^2}{n^2}}}$. The relativistic kinetic energy, $E_{min} = \gamma_{min} m_0 c^2$ (where m_0 is the particle's rest mass) is given by Equation 3.3.

$$E_{min} = \frac{m_0 c^2}{\sqrt{1-\frac{1^2}{n^2}}} \tag{3.3}$$

Note that because n is a function of altitude in the atmosphere, this threshold will likewise vary. Grieder (2010) gives the dependence of the atmospheric refractive index as a function of atmospheric column depth X and temperature T in Equation 3.4,

$$n(X,T) = 1.0 + 0.00029\left(\frac{X}{1030\text{g/cm}^2}\right)\left(\frac{273.2K}{\text{T}}\right) \tag{3.4}$$

We next require the relation for energy losses due to Cherenkov emission. The energy emitted by a charged particle in a dielectric medium per unit length per unit frequency has been derived by Frank and Tamm (1937). The differential relation is given Equation 3.5,

$$dE = \frac{q^2}{c^2}\left(1 - \frac{1}{\beta^2 n(\omega)^2}\right)\omega \text{d}\omega \text{d}l \tag{3.5}$$

Here q refers to the electronic charge (or the charge of whatever relativistic particle is being considered). Equation 3.5 implies that the Cherenkov energy loss is proportional to the frequency of radiation. It is also helpful to express the energy loss function per unit wavelength. We note that,

$$\omega = \frac{2\pi c}{\lambda} \tag{3.6}$$

and

$$\mathrm{d}\omega = -\frac{2\pi c}{\lambda^2}\mathrm{d}\lambda. \tag{3.7}$$

Therefore,

$$\omega\mathrm{d}\omega = -\frac{4\pi c^2}{\lambda^3}\mathrm{d}\lambda \tag{3.8}$$

Therefore the differential energy loss in wavelength is proportional to $\frac{1}{\lambda^3}$.

Using the conversion invoked in Grieder (2010), we can transform Equation 3.5 into the differential photon number density.

$$\frac{\mathrm{d}N_{ph}}{\mathrm{d}l\mathrm{d}\lambda} = \frac{2\pi\alpha}{\lambda^2}\left(1 - \frac{1}{\beta^2 n\left(\lambda\right)^2}\right) \tag{3.9}$$

Here α is the fine structure constant. We now note that the differential column depth $\mathrm{d}X = \rho\mathrm{d}l$. So Equation 3.9 implies that,

$$\frac{\mathrm{d}N_{ph}}{\mathrm{d}l\mathrm{d}X} \propto \frac{1}{\lambda^2}\frac{1}{\rho} \tag{3.10}$$

The dependence of the Cherenkov spectrum on the inverse square of wavelength explains why Cherenkov radiation is dominated by shorter wavelengths and typically has a bluish hue. Indeed, the bulk of Cherenkov radiation from air showers is emitted at shortwave optical frequencies. A superluminal electron traveling in air at sea level produces about 30 photons per meter between 350 and 500 nm. Jelly (1958) notes that the distribution of Cherenkov photon density in frequency is,

$$\frac{\mathrm{d}N_{ph}}{\mathrm{d}l\mathrm{d}\omega} = \text{const.} \tag{3.11}$$

The fact that a charged, superluminal particle will produce a constant number of Chernekov photons per unit length per unit frequency is the very property that makes the earth's atmosphere an effective calorimeter. Incoming particles with higher energies traverse greater distances, because they can experience more energy losses before reaching the Cherenkov threshold

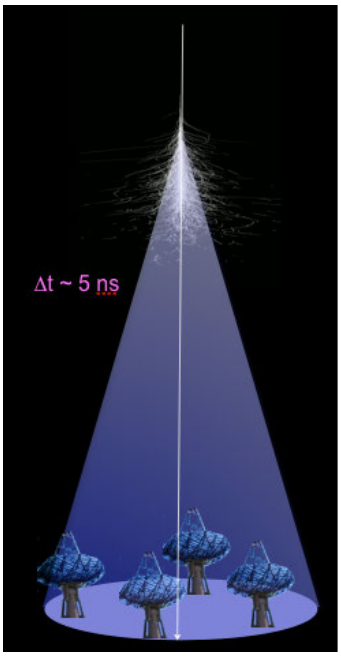

Figure 3.4 *A cartoon diagram of the total Cherenkov emission from an air shower. IACT telescopes have a large effective area because their ability to detect γ-rays is limited by the much larger size of the light pool.*

given in Equation 3.3. Thus, there is a relationship between an incoming particle's energy and the observed flux of photons, and this observed flux can be used to estimate particle energies.

An air shower consists of many particles moving at superluminal speeds. Because the particles in an air shower come from an initial primary interaction by an astrophysical particle with the atmosphere, higher energy primaries will produce higher energy secondary particles, and the showers will penetrate deeper into the atmosphere. The brightness of a shower in Cherenkov emission scales with the energy of the primary initiator. The composite emission from an air shower is beamed to the ground in a pool, as shown in Figure 3.4. It is thus possible to detect the air shower by placing a detector anywhere within the resulting light pool.

3.1.4 The Cherenkov light pool

An approximate distribution of the radially-dependent density of Cherenkov light pools from air showers is given by Greisen (1960). For a shower with N electrons in a medium with

Molière radius[3] r_1, an empirical analytic function describes the density of Cherenkov photons. As shown in Equation 3.12,

$$\rho\left(N, r\right) = \frac{0.4N}{r_1^2}\left(\frac{r_1}{r}\right)\left(\frac{r_1}{r+r_1}\right)^{3.26}\left(1+\frac{r}{11.4r_1}\right) \tag{3.12}$$

Greisen (1960) notes that without the final term, Equation 3.12 is (to first approximation) a special case of the Nishimura-Kamata-Greisen functions, a family of functions which describe the radial density of electrons from air showers. The last term is included to account for the fact that at large distances from the shower axis, the particle density drops as $\sim \frac{1}{r^3}$.

As an example, we can consider a shower initiated by a γ-ray with energy 100 GeV. The method described in Section A.2 can be used to show that the Heitler toy model predicts that shower maximum will occur after about 10 radiation lengths in the atmosphere. Assuming that each electron in the particle cascade produces two more, this results in about 1028 particles at the shower maximum. Greisen (1960) observes that at sea level, the Molière radius of the atmosphere is 79 m. If we use a Moliére radius of 79 meters, then Equation 3.12 gives us the photon density curve shown in Figure 3.5.

Monte Carlo simulations provide a better picture of the resulting Cherenkov light pool from an air shower. A plot of Cherenkov photon densities on the ground resulting from 50 GeV and 100 GeV γ-rays is shown in Figure 3.6. Ten showers were averaged in each case to smooth over statistical fluctuations. The ground has been simulated at an atmospheric depth of 888.8 gm/cm^2, corresponding to the Mount Hopkins basecamp where the VERITAS array is located.

The shape of these curves can be understood from the physics at work in the development of showers and emission of Cherenkov radiation. A simulated image of a shower from a 100 GeV γ-ray is shown in Figure 3.9 on the left-hand side. Photons from the center of the light pool out to approximately 100 m comes from electrons with small scattering angles to the axis of the shower.

The peak of the light pool at 120 meters is a focusing effect from the changing index of refraction of the atmosphere as a function of atmospheric depth. Let us consider the case of

[3]The Molière radius a constant of a material describing the characteristic transverse deflection of electrons in an electromagnetic shower. In this context, it describes the lateral size of an air shower.

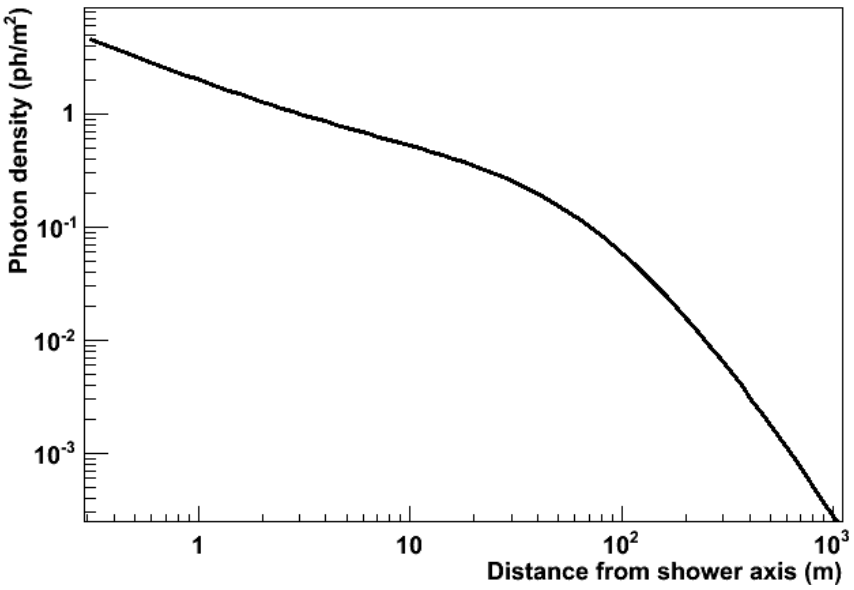

Figure 3.5 *Plot of Equation 3.12. This curve provides an analytic approximation of the lateral distribution of Cherenkov photons on the ground resulting from an atmospheric shower.*

superluminal electrons at an altitude of 11 km (a common shower maximum for air showers). Here the depth of the atmosphere is 230 gm/cm^2. It we assume a temperature of 230 K and use Equation 3.4, we find that the index of refraction is n = 1.00005. Equation 3.2 then gives the maximum Cherenkov angle as $\theta_{max} = 0.58°$. At sea level, the atmospheric depth is approximately 1000 gm/cm^2. If we consider superluminal electrons on the ground (again assuming a temperature of 293 K), the maximum Cherenkov angle is now 1.36°. The Cherenkov angle increases as a function of atmospheric depth. We therefore expect that the distribution of Cherenkov photons on the ground from an air shower will not be uniform. Photons produced deeper in the atmosphere will be emitted at wider angles to their emitting particles, leading to a buildup of photons in certain regions on the ground. This effect creates the 120 m peak.

The halo of the light pool is an effect of multiple scattering. Superluminal electrons in the atmosphere are deflected by atmospheric nuclei via the Coulomb interaction. When an electron experiences a large number (typically more than ∼20) of scattering interactions, we refer to the process as multiple scattering and may treat it statistically. Multiple scattering causes some particles in a cascade to scatter at large angles to the shower core. Their Cherenkov light can

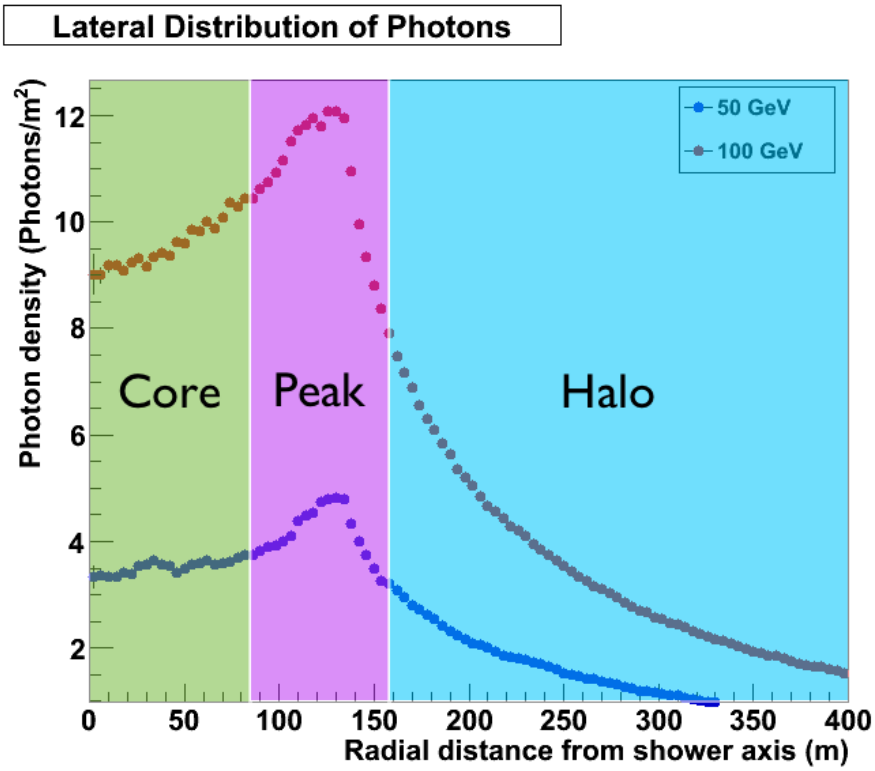

Figure 3.6 *Radial photon density plots from Monte Carlo simulations of 50 GeV and 100 GeV γ-rays. Curves were produced from averages of 10 showers in order to average over statistical fluctuations. Notice that the photon density of the light pool scales with the energy of the initiating γ-ray. The light out to 100 meters comes from the core of the shower. The peak at 120 meters is a focusing effect of the changing index of refraction of the air, resulting in a changing Cherenkov angle. The halo consists of Cherenkov emission from electrons at large scattering angles to the shower core.*

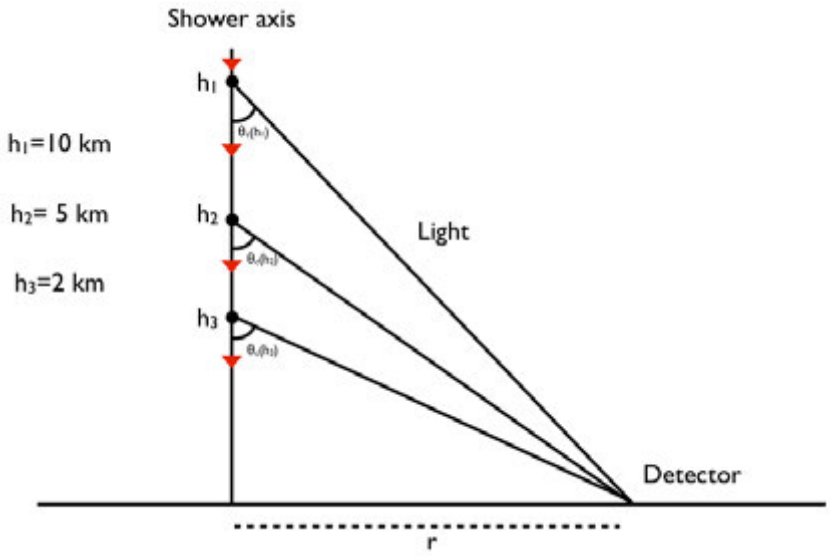

Figure 3.7 *A model one dimensional shower which illustrates the time dispersion of Cherenkov light from an air shower. Light from different portions of the shower traverse different path lengths, and thus reach the detector at different times. Adapted from Hillas (1982).*

fall outside of the 120 meters peak, resulting in a halo around the central light pool.

This characteristic structure of the Cherenkov light pool plays an important role in the design of ground-based γ-ray telescopes. Light pools from air showers have a characteristic core radius of about 120 meters (for an observatory at an atmospheric depth of 888.8 gm/cm^2; this value changes for observatories located at different heights). In the case of atmospheric Cherenkov experiments consisting of more than one telescope, it is advantageous to detect showers with two or more telescopes so as to view the shower from multiple angles. Therefore, Cherenkov telescope arrays are typically built with telescope spacings of less than 120 meters, so as to improve the chance of multiple telescope triggers on the same shower.

3.1.5 Time dispersion of Cherenkov light

Because air showers are often detected via their Cherenkov light, it is important to understand the time dispersion of the light pools so as to design appropriate detectors. Arrival time differences between Cherenkov photons from different regions of an air shower are treated by Hillas (1982). Figure 3.7 provides a one-dimensional model of an air shower, as treated by

Hillas. The arrival time of Cherenkov photons from an emitting electron at height h is given by $\Delta t = \frac{h}{v} - \frac{h_2 - h_1}{c}$, where the second term accounts for the light travel time across the length of the shower. Because $v = \frac{c}{n}$, $\Delta t = \frac{nh}{c} - \frac{h_2 - h_1}{c}$. However, to account for the changing index of refraction of the air, we must perform the integral in Equation 3.13.

$$\Delta t = \frac{1}{c} \int_{h_1}^{h_2} (n - 1)\, \mathrm{d}h \tag{3.13}$$

As an example, we calculate the time dispersion of the Cherenkov photons from an air shower injected at an altitude of 20 km, which maintains an electromagnetic cascade until an altitude of 1.3 km. We assume an exponential model to describe the atmospheric refractivity, as shown in Equation 3.14. The value of n_0 can easily be extracted from Equation 3.4 ($n_0 = 0.00029$), and we may use a typical atmospheric scale height of $h_0 = 7600m$.

$$n = 1 + n_0 e^{-\frac{h}{h_0}} \tag{3.14}$$

The time dispersion in this model air shower is then,

$$\Delta t = \frac{1}{c} \int_{1.3\,\mathrm{km}}^{20\,\mathrm{km}} 0.00029 e^{-\frac{h}{7600\mathrm{km}}}\, \mathrm{d}h = 5.7\,\mathrm{ns} \tag{3.15}$$

This estimate agrees very well with experimental data. In observed light pools from air showers, time dispersions between 1 and 10 nanoseconds are typically observed. Figure 3.8 shows the distribution of time dispersions from a 20 minute exposure of a VERITAS camera to the Crab Nebula, with γ/hadron cuts applied (no background subtraction has been performed; this distribution consists largely of γ-rays with a small amount of cosmic ray contamination). All events have time dispersions similar to the value derived from the model air shower.

3.1.6 Distinguishing γ-ray showers from hadronic showers

The vast majority of air showers are induced by cosmic rays. Because γ-ray astrophysicists are interested in the rarer photon-induced showers, it is important to distinguish the two types of showers.

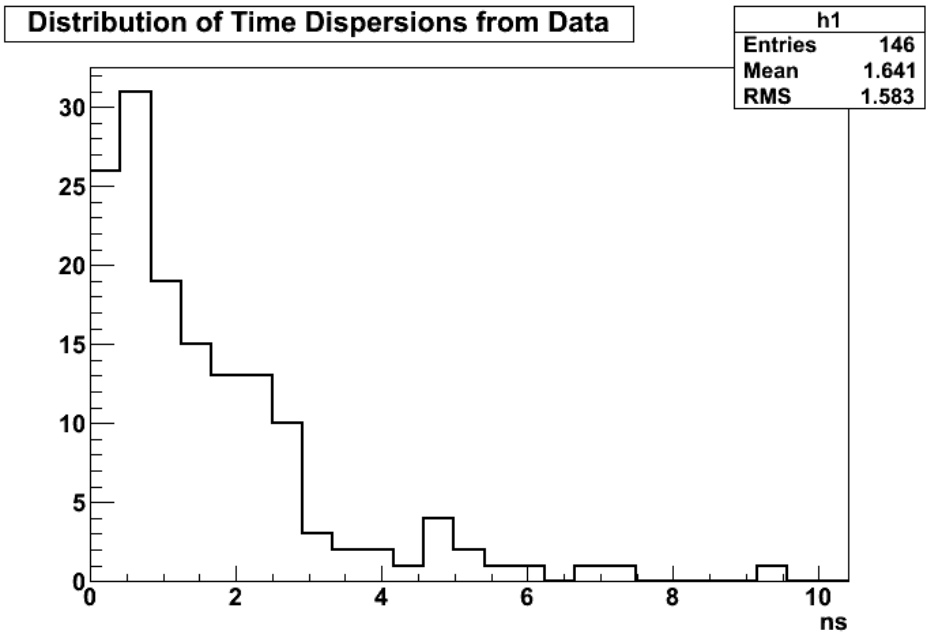

Figure 3.8 *Distribution of event time dispersions from a 20 minute exposure of a VERITAS camera to the Crab Nebula. γ/hadron separation cuts have been applied, but no background subtraction has been performed. Time dispersions as large as the value calculated in Equation 3.15 (which is an extreme example) are indeed seen in data.*

Figure 3.9 illustrates the structural difference between particle cascades induced by γ-ray and protons. Whereas γ-ray cascades tend to collimate along the shower axis, the particle tracks from proton cascades exhibit a greater lateral spread. This differences arises from the differing physics at work in electromagnetic and hadronic interactions. Jelly and Porter (1963) explain that hadronic interactions, such as those in a proton-induced cascade, impart a large transverse momentum to their secondary particles. This produces the lateral spread in proton cascades with respect to γ-ray showers.

We expect the lateral distribution of shower particles in γ-ray and proton cascades to affect their distribution of Cherenkov light on the ground. Figure 3.10 shows the Cherenkov light pool for a simulated 200 GeV γ-ray and proton, respectively. Whereas the γ-ray produces a well-defined and compact light pool, the proton's light pool is asymmetric and does not have a single, well-defined boundary. Multiple photon density maxima can be seen due to the hadronic sub-showers. This difference in the Cherenkov photon distribution between γ-ray and cosmic ray showers is instrumental in identifying and separating the cosmic ray background from astrophysical γ-ray observations. See Section 4.8.1 for details on the use of the differing shower physics between γ-rays and hadrons in suppressing the cosmic ray background.

3.2 The imaging atmospheric Cherenkov technique

The imaging atmospheric Cherenkov technique (IACT) is a method of detecting γ-rays by taking advantage of the electromagnetic cascade described in Section 3.1. Essentially the earth's atmosphere is used as a fully active electromagnetic calorimeter. Whereas air shower arrays sample the cascade particles directly, IACT experiments detect them via their Cherenkov radiation on the ground. As shown in Figure 3.10, a typical Cherenkov light pool at a detection altitude of 1400 m has a radius of approximately 130 m, and thus a surface area of $\pi \cdot (130m)^2 \approx 53,000m^2$. By placing a Cherenkov light detector in this light pool, it is possible to obtain information about the shower that produced the light pool, and thus about the primary γ-ray itself.

The IACT technique does not merely refer to detection of γ-ray showers, but to *imaging* of these showers. By using a camera consisting of an array of many photodetector pixels, it is

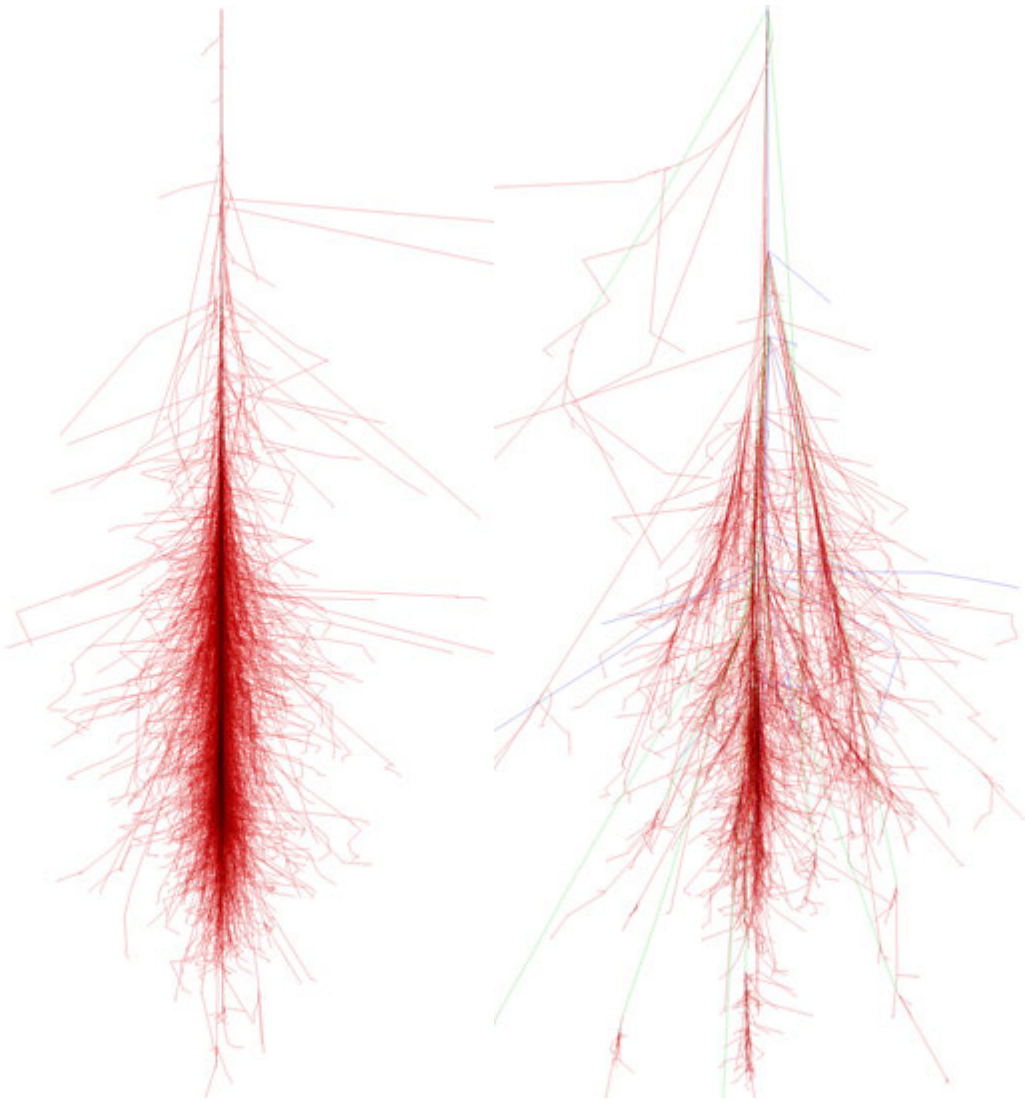

Figure 3.9 *Particle cascades from a 100 GeV photon-induced shower (left) and a 100 GeV proton-induced shower (right). The red tracks represent electrons or positrons, the green tracks muons, and the blue tracks pions. Note that the photon-induced cascade is more compact along the shower axis. These showers were simulated with the Corsika package.*

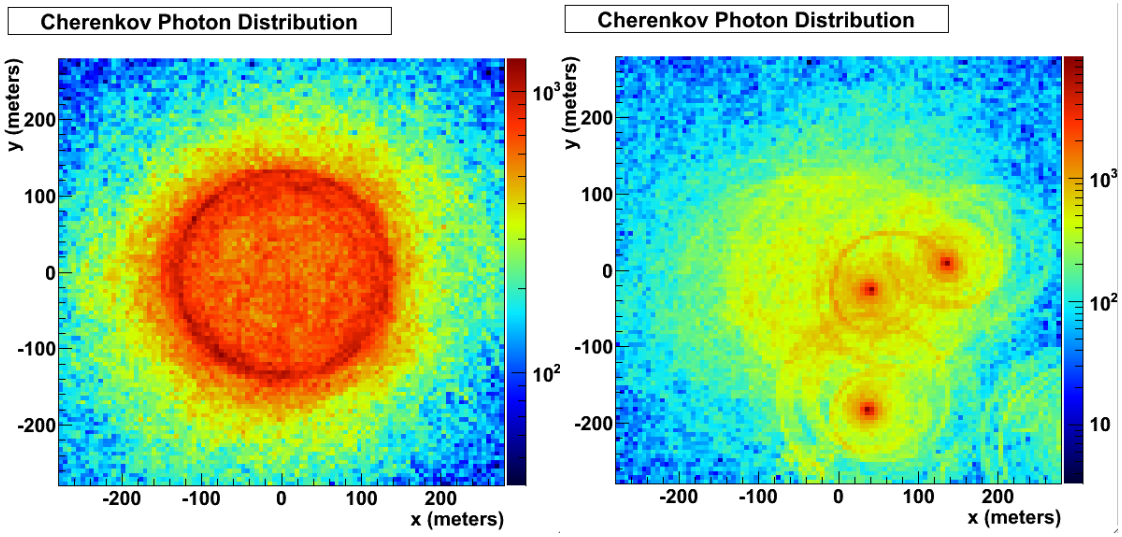

Figure 3.10 *Distribution of Cherenkov photons on the ground due to an electromagnetic cascade from a γ-ray (left) and a proton (right), from Monte Carlo simulations. The color scale represents photon density in arbitrary units. Both primary particles were incident on the earth's atmosphere with an energy of 200 GeV with a direction parallel to the zenith, and an impact location at the center of the coordinate system. The Cherenkov photons from the γ-ray are more symmetric about the impact axis than those from the proton, due to the smaller transverse momentum of the secondary particles.*

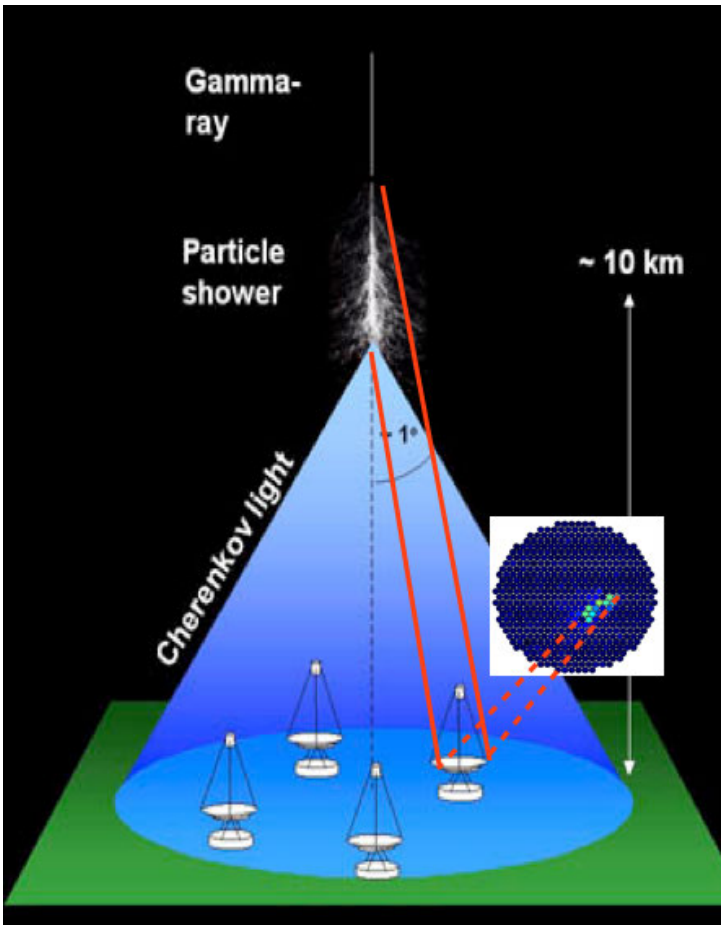

Figure 3.11 *Air showers, due to their collimation, produce elliptical images in cameras on the ground. The camera image is an off-axis projection of the particle cascade.*

possible to produce a projection of the air shower in the plane of the camera. These projections have an elliptical structure (see Figure 3.11); their major axes represent the longitudinal development of the shower. In the coordinate system of the camera, the major axes of Cherenkov images also point towards the origin of the initiating γ-ray on the sky.

Second generation IACT telescopes such as the Whipple 10 m experiment (Weekes, 1989) used a single telescope to image γ-ray showers. By deploying multiple telescopes in an array, it is possible to perform *stereoscopic* imaging to improve angular resolution. An IACT array operates by pointing all telescopes at a single γ-ray source. The recorded camera images from a single shower are overlaid, as shown in Figure 3.12. Because each image major axis points to

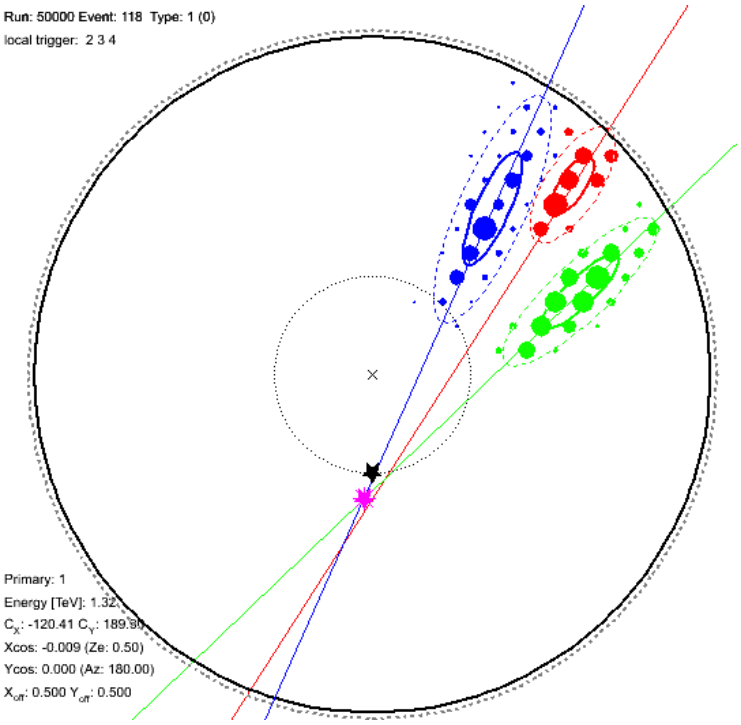

Figure 3.12 *The stereoscopic imaging technique uses the geometric information contained in the elliptical structure of Cherenkov images to reconstruct shower directions.*

the γ-ray primary, pairs of images can be used to locate the particle direction on the sky by parallax.

Currently operating IACT arrays include HESS (Aharonian et al., 2006), MAGIC-II (Moralejo, 2009), and VERITAS (Holder, 2011).

3.3 VERITAS

The **V**ery **E**nergetic **R**adiation **I**maging **T**elescope **A**rray **S**ystem (VERITAS) is an array of four gamma-ray telescopes located at Fred Lawrence Whipple Observatory, approximately 50 miles from Tucson, Arizona. Four-telescope operation of the array began in the spring of 2007. Telescope 1 was moved in the summer of 2009 to increase the sensitivity of the array[4]. Currently the array is a square shape with an approximate side length of 100 m (see Figure

[4]The initial location of T1 was a temporary measure. The experiment was intended to be constructed at the Kitt Peak observatory, but delays related to the site permit required that VERITAS be completed at the basecamp of Whipple observatory, thus requiring a relocation of T1

Figure 3.13 *The VERITAS array, located at the foot of Mount Hopkins in Arizona. This image was taken after relocating T1 in the summer of 2009.*

3.13). The instrument is sensitive to gamma-rays between 100 GeV and 30 TeV. [5]

3.3.1 Telescopes and optics

The pedestal of each VERITAS telescope suspends the optical support structure (OSS) for the instrument's reflector and quad arms to support the camera box. The telescope itself employs an alt-azimuth drive for rotation about two mutually perpendicular axes at approximately corresponding to altitude (elevation) and azimuth. Typical observations are conducted between elevations of 25 and 85 degrees and across all azimuth angles; and the alt-az drive slews at approximately 1°/sec in azimuth and 0.5°/sec in elevation. A counterweight is constructed on the rear of each reflector in order to balance the telescope. The multi-faceted reflectors themselves are modeled after the design described in Davies and Cotton (1957). The surface of each of the 350 mirror facets is spherical and identical, with a focal length of 12 m. The aperture of the full dish is likewise 12 m. This design is advantageous over a single parabolic reflector because it compensates against off-axis aberrations and thus provides a better optical performance at the edge of the field of view. As noted by Cogan (2004), this design is also

[5]The range of detectable energies is dependent not only on the instrument hardware but also on source strength, spectrum, and observation. For example, a simulated spectrum of 50 million gamma-rays with an index of -2.0 at a 20 degree zenith angle will trigger a nonzero number of 50 TeV events that pass all quality and gamma/hadron cuts.

advantageous because the construction from multiple small mirrors avoids the gravitational slumping associated with a single large dish, and is cost effective because it allows for the replacement of individual mirrors. The most significant disadvantage of the Davies-Cotton design is that it is not isochronous. That is, the global curvature of the dish introduces a spread into the arrival times of coincident photons.

3.3.2 Cameras

The focal plane of the VERITAS cameras, shown in Figure 3.15, covers a 3.5° field of view on the sky. Each VERITAS camera contains 499 photomultiplier tubes (PMTs). Prior to the July 2012 upgrade, the PMTs were Photonis XP 2970/02 ten-dynode devices with a bi-alkali photocathode. The pixels were sensitive in the approximate range of 270 nm to 550 nm, and had a peak quantum efficiency of approximately 20%.

IACT cameras use PMTs rather than CCDs because of the rapid response time required to detect Cherenkov flashes. The Cherenkov light from an air shower has a typical time dispersion of a few ns (as demonstrated in Section 3.1.5). A PMT can produce secondary photoelectric emission followed by multiplied statistics with a sub-nanosecond rise time after a photon strikes the photocathode.

Each PMT is attached to a base containing a preamplifier which amplifies the output signal strength by 6.6. Each base provides a high voltage connection, a "charge injection" cable which can carry diagnostic pulses that mimic a PMT response to photons, a cable to supply power to the preamplifier and measure the PMT anode current, and a BNC signal cable which carries the output of the PMT to the data acquisition system (see diagram in Figure 3.16). The application of high voltage (typically ∼1000 V during nightly observations) results in a PMT gain of 2×10^5 (Le Bohec and Sleege, 2004). A 50 meter signal cable with a 75 Ω impedance carries the PMT signal to the data acquisition system. The entire amplification chain is shown in Figure 3.22.

In July 2012, the camera PMTs were replaced in all four telescopes with Hamamatsu R10560 photomultipliers. These devices feature an improvement in peak quantum efficiency (Figure 3.14) and a faster response to photoelectrons (Figure 3.17, see Section 3.3.3.1 for a description

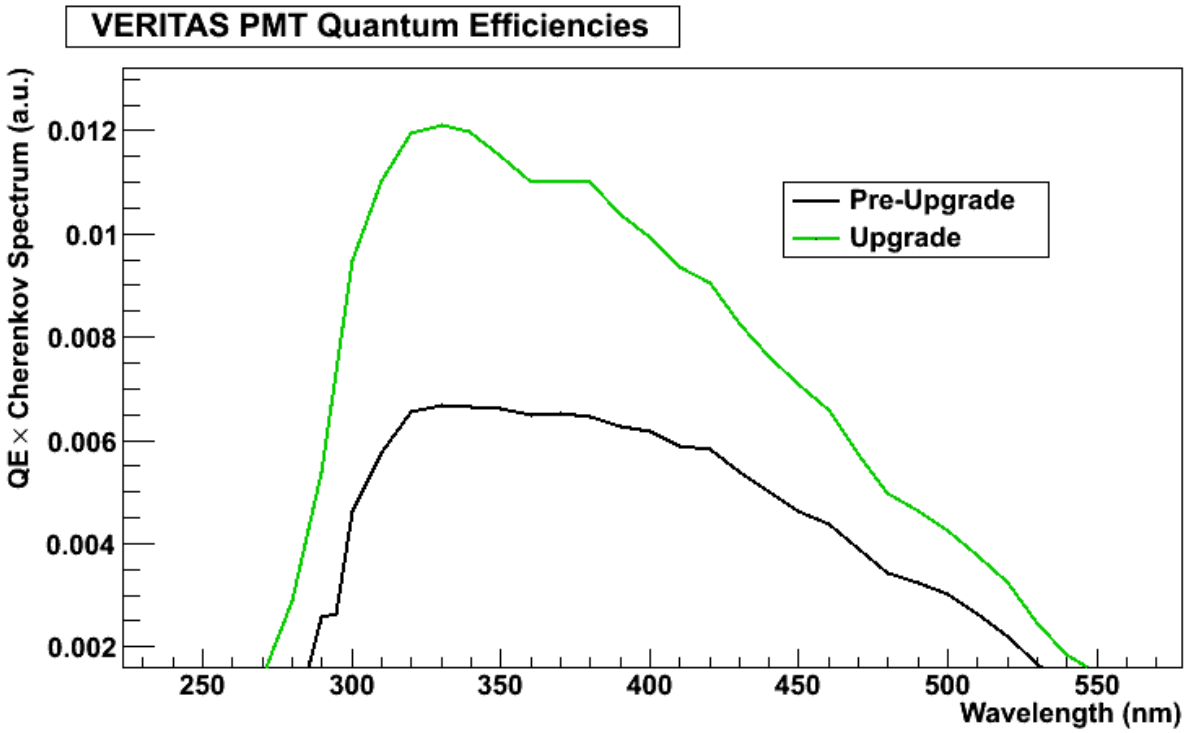

Figure 3.14 *The quantum efficiency of VERITAS pixels as a function of wavelength. These curves include the effects of atmospheric extinction and the shape of the Chernekov spectrum. Each curve is an average of many pixel measurements, and were incorporated into the detector model used in the Monte Carlo simulations.*

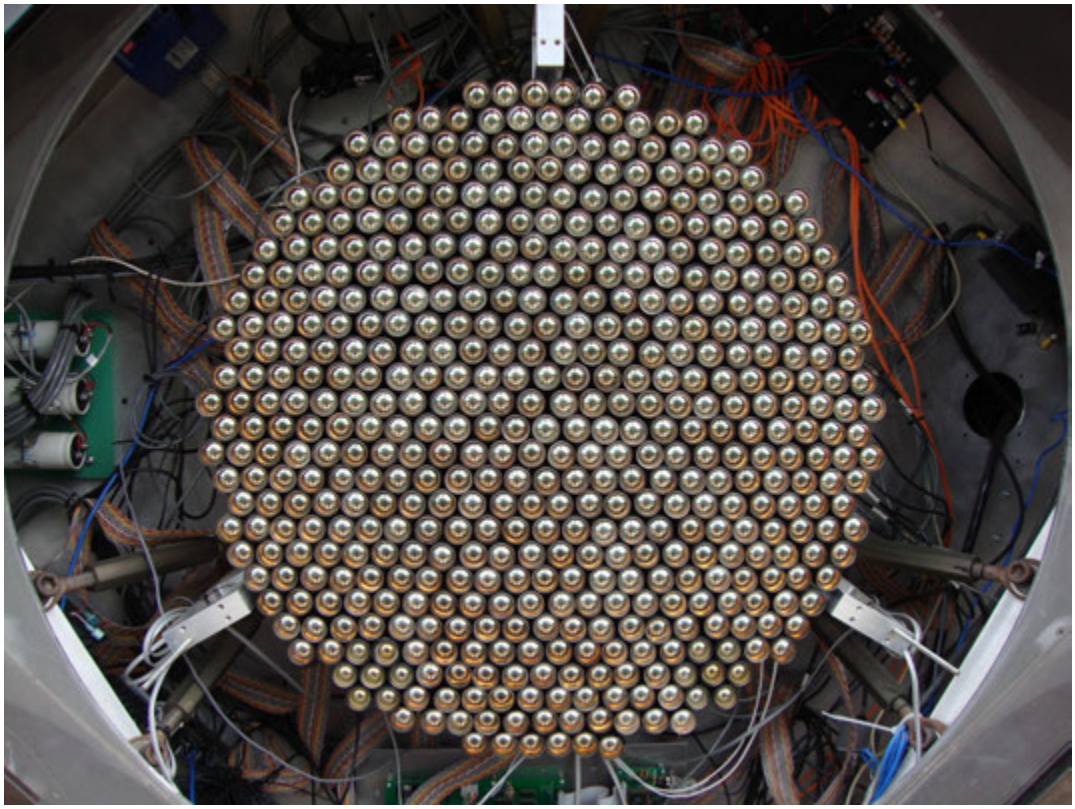

Figure 3.15 *The focal plane of a VERITAS camera before the 2012 upgrade. The light cones, which are placed over the PMTs during nightly observations, have been removed in this image.*

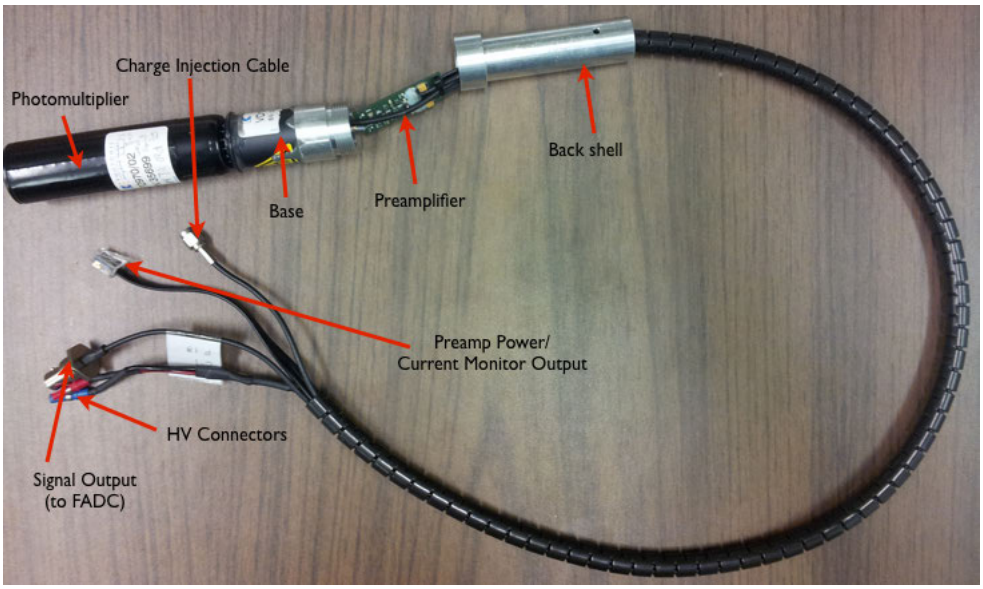

Figure 3.16 *The components of a pre-upgrade VERITAS pixel. The upgrade pixels were designed according to the same configuration.*

of the pixel signal output). Otte et al. (2011) reports an improvement of 35% photon yield over the pre-upgrade pixels. A pre-upgrade pixel is shown in Figure 3.19. An upgrade pixel is shown in Figure 3.20.

3.3.3 Data acquisition and trigger system

The night sky provides a large flux of photons from various sources such as the starfield, the disk of the galaxy, and terrestrial sources (for observations taken from Whipple Observatory this includes a glow from nearby Tucson and Nogales). These sources of photons are collectively referred to as the night sky background (NSB). VERITAS conducts observations during partial moon illumination, and moonlight provides a flux of photons in addition to the NSB. The typical NSB flux taken at zenith and integrated from 300 to 600 nm is about 3.2 $\cdot 10^{12}$ photons/m^2/sec/sr (Mirzoyan, 1994). If we assume a telescope throughput[6] of $\sim$10%[7], this

[6]We define throughput as the fraction of light from an air shower that passes through the detector into the data acquisition system.

[7]The actual value of the telescope throughput depends on atmospheric extinction, the mirror reflectivity, the PMT quantum efficiency, and the lightcone reflectivity. Although 10% is a reasonable first approximation, the actual throughput of the telescopes can be determined by measuring these quantities. Throughput measurements are also possible via analysis of muon data taken at zenith.

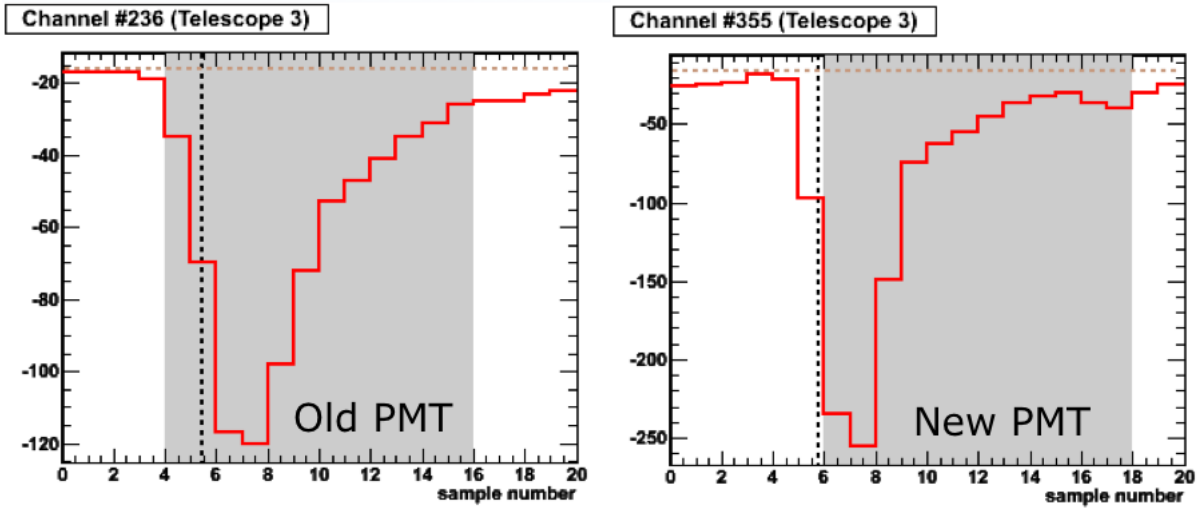

Figure 3.17 *Comparison of FADC pulses from a pre-upgrade pixel and an upgrade pixel. The narrower pulse width in the new pixels allows VERITAS analysts to better isolate Cherenkov pulses from the NSB, thus reducing the instrument's low-energy threshold. (Images taken from Dave Kieda, VERITAS winter collaboration meeting 2012.)*

corresponds to 320 photoelectrons/m^2/ns/sr. This value varies with the telescope zenith angle, the density of the starfield, and phase of the moon, as well as the angle of the telescope to the moon, thus the VERITAS calibration and simulations working group models the detector using a range of NSB values ranging from 100 to 870 photoelectrons/m^2/ns/sr.

As an illustration, we estimate the flux of photons incident on a single pixel due to a typical dark sky NSB of 150 photons/m^2/ns/sr. The VERITAS PMTs each cover 0.148 degrees of the sky. The corresponding solid angle can be found by integrating $\int\int \mathrm{d}\Omega = \int_0^{2\pi}\int_0^{\theta_0} \sin(\theta)\,\mathrm{d}\theta\mathrm{d}\phi$. We must also multiply the NSB flux by the area of the reflector (which has a diameter of 10 m), and divide by the number of pixels (under the crude assumption that each pixel is equally exposed to the NSB). So,

$$\text{single pixel flux } (\Phi) = (\text{nsb flux}) \times (\text{PMT solid angle}) \times (\text{reflector area}) \tag{3.16}$$

Numerically, this is equal to,

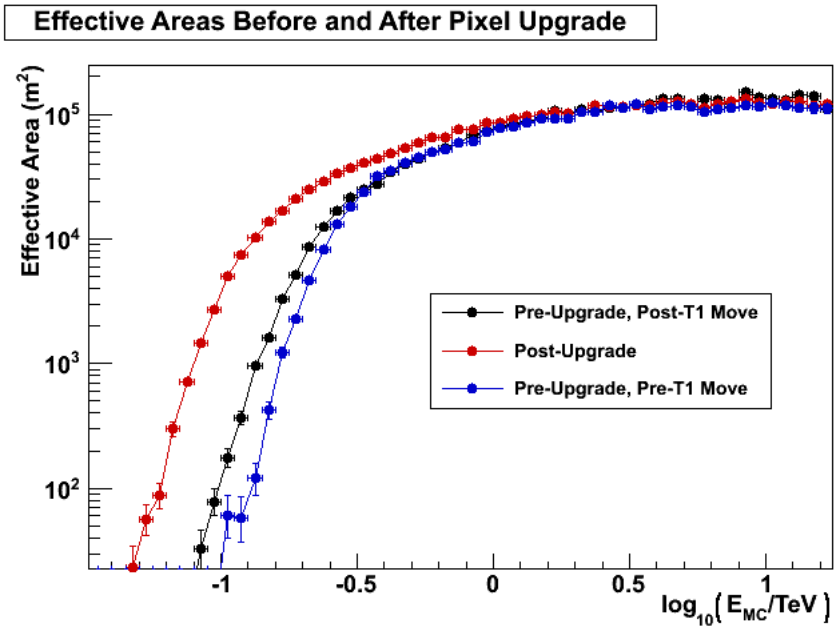

Figure 3.18 *The effective collection area of the VERITAS array before the T1 relocation, after the T1 relocation, and after the VERITAS II trigger and camera upgrades, derived from a simulated spectrum of γ-rays with an index of -2.0 at a zenith angle of 20 degrees, azimuth angle of 0 degrees (East), and an NSB level of 200 p.e./m^2/sec/sr. Both pre-upgrade curves were derived from simulations which included an accurate model of the Leeds L2 trigger which operated in each telescope until November 2011. This trigger exhibited trigger inefficiencies not originally anticipated from the specifications of the hardware. Note that each improvement increases the effective area of the array to lower energy events.*

Figure 3.19 *A Photonis XP 2970/02 pixel. These pixels comprised the VERITAS photodetector system from the beginning of operations until the summer of 2012.*

Figure 3.20 *A pixel from the upgraded VERITAS II cameras.*

$$\Phi = 150 \frac{\text{p.e.}}{\text{m}^2 \text{ns sr}} \times \int_0^{2\pi} \int_0^{0.148^\circ \frac{\pi}{180^\circ}} \sin(\theta)\, \mathrm{d}\theta \mathrm{d}\phi \times \pi \left(\frac{10m}{2}\right)^2 \approx 0.25\, \text{p.e./ns} \tag{3.17}$$

We can obtain a second estimate of the single pixel NSB from current seen by a PMT. During standard observations, pixel currents typically range from 5 to 10 μA. It is reasonable to assume that,

$$\Phi = \text{current} \times \frac{1}{\text{electron charge}} \times \frac{1}{\text{PMT gain}} \tag{3.18}$$

This gives an estimated NSB flux of,

$$\Phi = 7\mu\text{A} \left(\frac{1\,\text{s}}{10^9\,\text{ns}}\right) \left(\frac{1}{2 \cdot 10^5}\right) \approx 0.22\,\text{p.e./ns} \tag{3.19}$$

The flux of the NSB is large enough that recording all data would overwhelm the data acquisition system and cause the detector to miss most air showers. In order to reject the NSB and record Cherenkov images (including images from gamma-ray induced cascades), VERITAS employs a data acquisition system and a three-level trigger. Each PMT's signal is split into two copies. One is sent to the data acquisition system, and one to the trigger. Whenever all three trigger levels are exceeded within a set of time constraints, the data acquisition system records the signal output of the PMTs.

3.3.3.1 VDAQ

VERITAS data is recorded using a VME Data Acquisition system (VDAQ), as described in Hays (2007). The data is only recorded to disk when an event passes all three levels of triggering. A schematic of the data acquisition chain is shown in Figure 3.21.

Each telescope trailer houses five VME crates. One of these crates is an auxiliary crate which houses a clock trigger module and a GPS clock for recording event timestamps. The other four crates contain custom-built 500 MHz flash analog-to-digital converter (FADC) boards. A single FADC board can accept inputs from up to ten PMTs, and each crate houses 13 boards. Each FADC samples the PMT signal every two nanoseconds and stores the data in a buffer until a trigger decision is made. The PMT response to photoelectrons produces a characteristic trace in

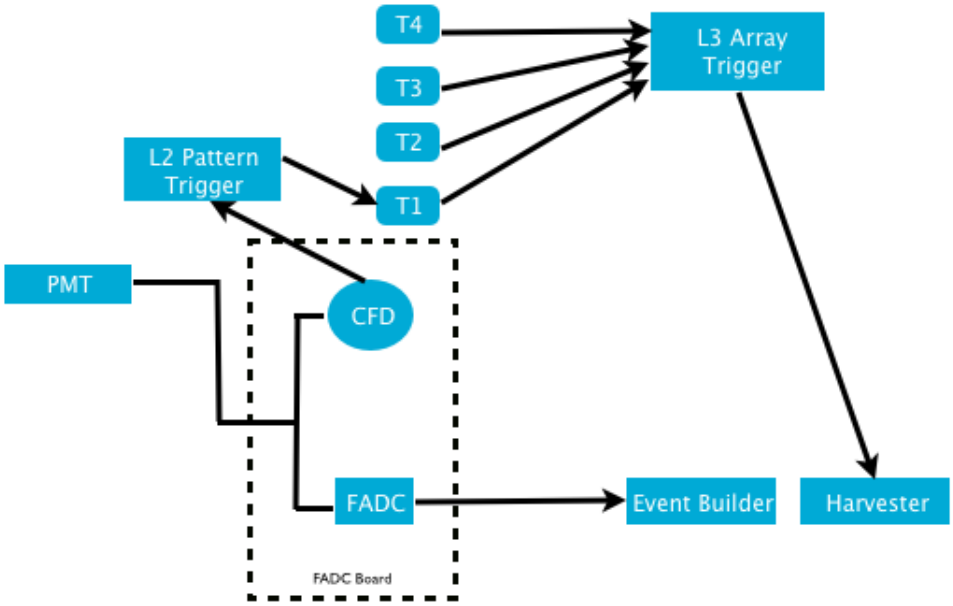

Figure 3.21 *Schematic of the VERITAS Data Acquisition System (VDAQ).*

the FADC. Shown in Figure 3.23 is a pixel's FADC trace from approximately 70 photoelectrons. The response of the FADCs is measured in digital counts; one digital count corresponds to a PMT signal of 7.81 mV.

Figure 3.22 illustrates the sources of amplification between the photocathode and FADC. We can use Ohm's Law to estimate the voltage at the FADC due to a single photoelectron, noting that Le Bohec and Sleege (2004) gives the single p.e. pulse width as 5 ns. We begin by calculating the current,

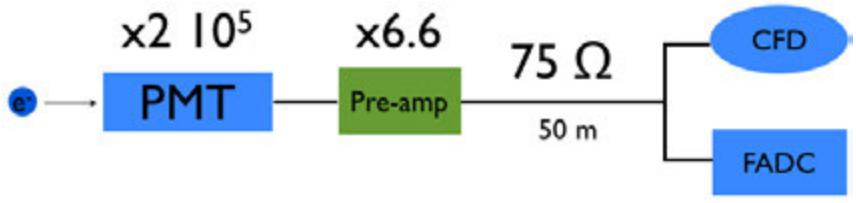

Figure 3.22 *Stages of amplification chain from the PMT to the data acquisition system.*

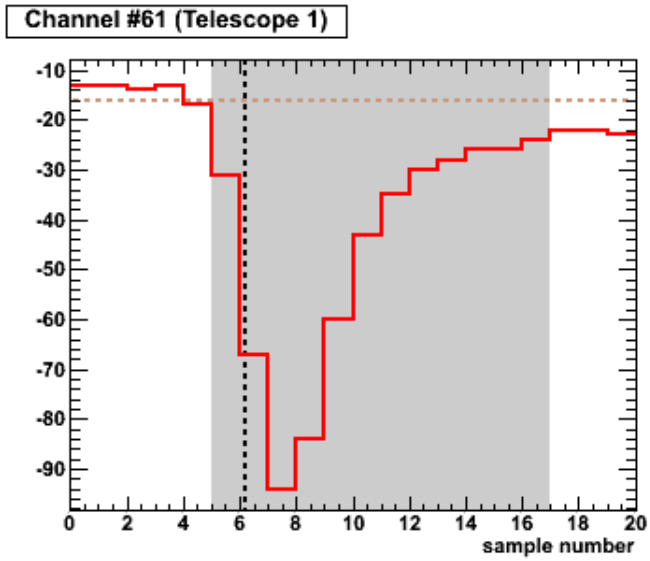

Figure 3.23 *The FADC trace from a pixel in a Cherenkov image. The trace integral is 357.73 digital counts, which corresponds to 71 photoelectrons assuming a dc/p.e. ratio of 5. This particular trace was taken from a Crab Nebula run prior to the upgrade (run 53734). The dashed horizontal line indicates the pedestal, the dashed vertical line indicates the half-max (also referred to as t_0), and the shaded area is the region of signal extraction determined by the offline analysis.*

$$\frac{\mathrm{dQ}}{\mathrm{dt}} = \frac{1.6 \cdot 10^{-19}\,\mathrm{C} \cdot 2 \cdot 10^{5}}{5\,\mathrm{ns}} \tag{3.20}$$

$$\mathrm{I_{PMT}} = 0.64 \cdot 10^{-5}\mathrm{A} \tag{3.21}$$

$$\mathrm{I_{Amp}} = 4.22 \cdot 10^{-5}\mathrm{A} \tag{3.22}$$

$$\mathrm{V} = \mathrm{I_{Amp}R} = 4.22 \cdot 10^{-5} \cdot 75\Omega = 3.2\mathrm{mV} \tag{3.23}$$

This estimate produces a result on the same order of magnitude as the 7.81 mV/dc conversion factor which characterizes the FADCs, and shows that the FADC readout should indeed be sensitive to a small number of photoelectrons.

3.3.3.2 Level 1: CFD triggers and rate feedback

The first tier of triggering occurs at the single pixel level and filters out single photoelectrons from the NSB, as well as pileups of multiple NSP photoelectrons. This level 1 trigger employs a constant fraction discriminator (CFD) which is housed on the same board as the FADCs. Each CFD splits the input signal in two, delays and inverts one of the pulses, scales the other pulse down by some factor, and then adds the two signals (Vassiliev, 2003). If this sum exceeds some preset CFD threshold, a level 1 trigger is recorded. CFDs are advantageous over simple threshold triggers because they discriminate based on pulse risetime as well as threshold. Prior to the pixel upgrade, the telescopes typically operated with a CFD threshold of 50 mV. Post-upgrade data is taken with a threshold of 45 mV. VERITAS furthermore implements a rate feedback trigger (RFB) to dynamically increase the CFD threshold as the trigger rates increase. The RFB is set to a nominal value of 60 mV/MHz.

The nominal CFD threshold corresponds to an FADC threshold of,

$$\frac{50\text{mV}}{7.81\text{mV/digital count}} = 6.4\text{digital counts} \tag{3.24}$$

Using Equation 3.23, we can estimate that two photoelectrons from a Cherenkov shower can trigger the CFD. From data analysis, it can be shown that the effective pixel threshold after folding in the effects of the additional two tiers of triggering is in fact closer to 7 photoelectrons.

3.3.3.3 Level 2: pattern selection trigger

Though the first level of triggering ensures that single photoelectrons do not trigger the telescope, it is possible for two or more photoelectrons from the NSB to arrive in a sufficiently short time window to cause a single pixel to send a CFD trigger. To filter out these NSB triggers, a second tier of triggering is necessary to select for Cherenkov photons. The level 2 pattern selection trigger (PST) is a camera-level trigger that takes advantage of the the short time dispersion of Cherenkov photons from air showers to select for these events against NSB photons. Whereas NSB photons in neighboring pixels are uncorrelated and arrive at the camera at random times, the Cherenkov photons from an air shower spread out over multiple pixels.

The PST returns a positive decision when any three contiguous pixels send a CFD trigger within a specified coincidence window (this value is typically set to 6 ns). This is referred to as a threefold coincidence.

The original VERITAS PST was designed at the University of Leeds, and is described briefly in Bradbury et al. (2002). The Leeds L2 is organized into overlapping strips of 59 pixels (the exception is the central strip, which only covers 19 pixels and has a hexagonal shape), as shown in Figure 3.24. Each strip corresponds to a PST module in the L2 crate. The strips are set up in three different orientations on the camera; an example is shown in Figure 3.24. Each module is further divided into overlapping hexagonal patches of 19 pixels. The PST modules contain a lookup table for each patch which specifies every combination of CFD triggers that correspond to three contiguous pixels. Because the strips corresponding to the PST modules also overlap, it is possible to determine the fired pixels from overlapping strips. We can thus deterimine any coincident CFD triggers of three contiguous pixels on the camera. The outer ring of pixels is excluded from the pattern trigger.

In November 2011, Argonne National Lab and Iowa State University commissioned a new L2 trigger which employs Xilinx Virtex-5 FPGAs with a clock frequency of 400 MHz. The ANL/ISU trigger splits the camera into three sectors (shown in Figure 3.25). The CFD outputs of the camera pixels are routed into one of the three L1.5 boards corresponding to each of the sectors. Each L1.5 board contains a hardware lookup table specifying every combination of threefold coincidences within the sector; a trigger decision from any L1.5 board will result in an L2 trigger. In order to account for threefold coincidences that span multiple sectors, each sector includes one row of pixels that is also contained in the adjacent sector.[8] The ANL/ISU L2 trigger is able to operate at shorter coincidence windows of as little as 3 ns, thus suppressing additional NSB photons with respect to the Leeds L2.

Additionally, the installation of the ANL/ISU trigger exposed a previously unknown inefficiency in the Leeds trigger. This trigger inefficiency was not predicted based on the system's

[8]This method accounts for most threefold coincidences that overlap sectors, but there remains a very small class of coincidence sets that will not cause an electronic trigger. Because there are approximately only 30 such threefold coincidences, failure to model the effect in simulations is unlikely to have any noticeable effect on the analysis of VERITAS data.

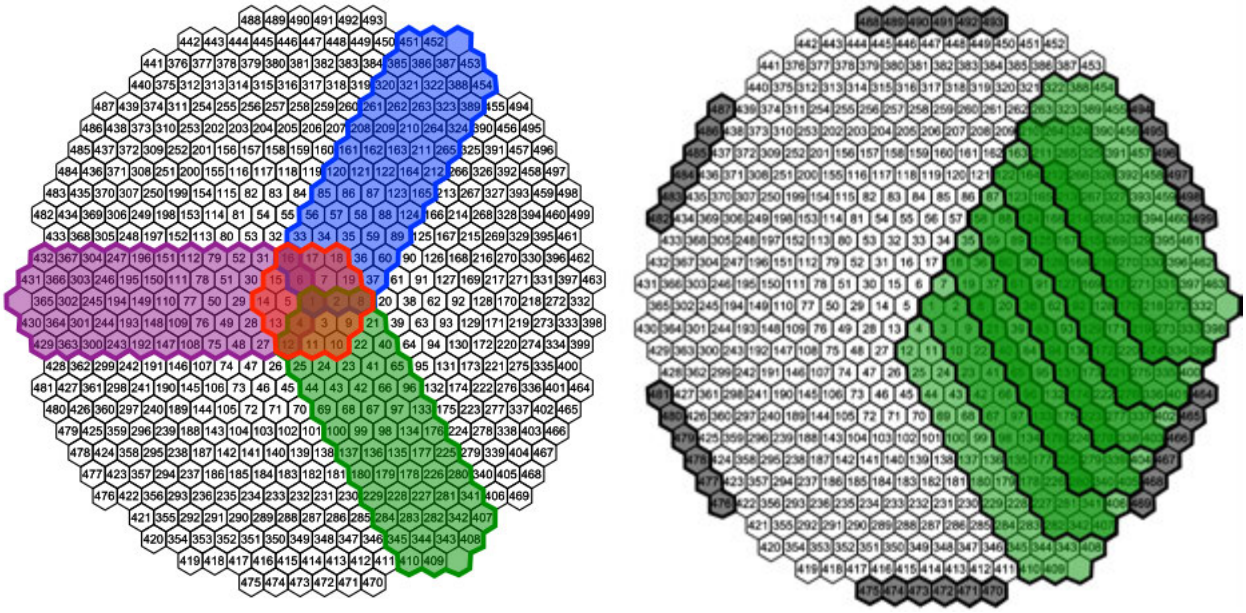

Figure 3.24 *Left: Three possible module orientations. The red area indicates the central module, which consists of only 19 pixels. Right: Several overlapping modules with a single orientation. Note that the outer ring of pixels (shaded gray) do not participate in the pattern trigger decision.*

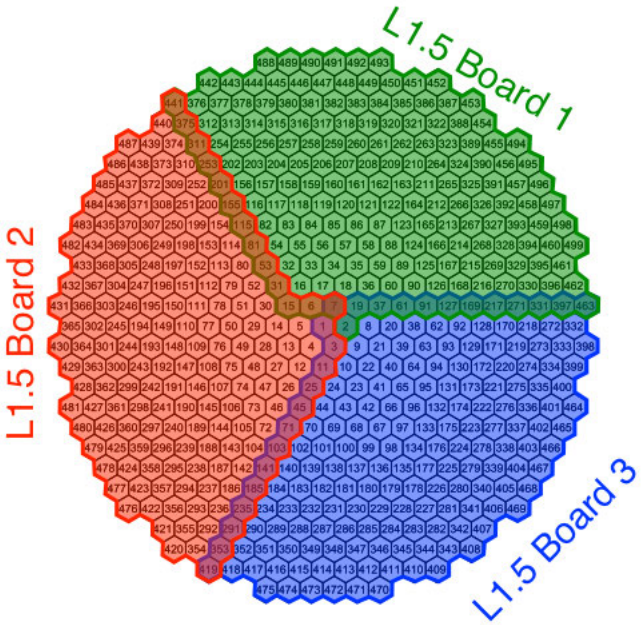

Figure 3.25 *The three sectors of the ANL/ISU trigger.*

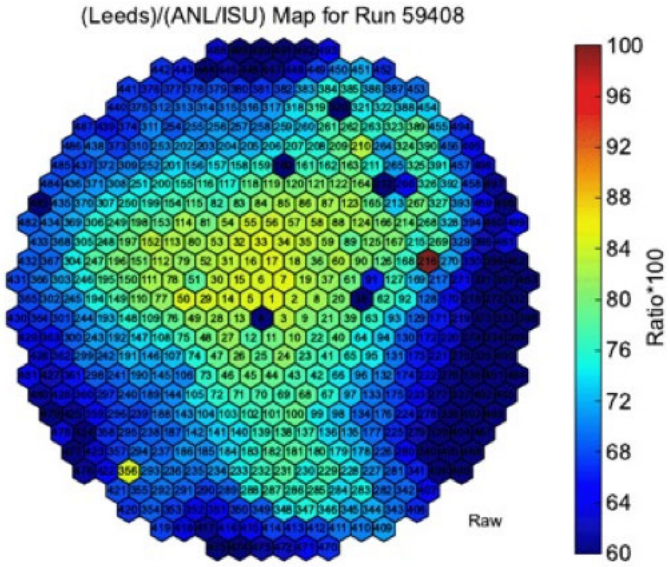

Figure 3.26 *Pixel participation map constructed from a data run with the ANL/ISU trigger, with the Leeds trigger operating in parasitic mode.*

design specifications, and thus would have been difficult to model until comparisons were made with the performance of the ANL/ISU trigger[9]. During the installation of the ANL/ISU trigger, several runs were taken with both L2 triggers in the system. One trigger was used to send the actual signal used to make a trigger decision, while the other trigger produced a boolean which was recorded to file, but not used by any other hardware component. These runs are referred to as *parasitic* data runs, with the latter trigger operating in parasitic mode. Parasitic runs were analyzed by creating pixel participation maps. In a pixel participation map, the value assigned to each channel is defined as the number of CFD triggers over the run for which events contain trigger bits from both triggers divided by the number of CFD counts over the run where at least the primary trigger bit is present. If both triggers function with equal efficiency, the map should be uniform, and every pixel should have a value of 1. When taking parasitic runs with the ANL/ISU trigger operating as the primary trigger, a non-uniform pixel participation map was found, as shown in Figure 3.26.

[9]At the time of this work's composition, the fundamental hardware cause of this trigger inefficiency is unknown.

3.3.3.4 Level 3: array trigger

Though the pattern trigger filters out most of the NSB, it does not eliminate most of the cosmic ray background, or the contribution of Cherenkov light from local particles. Certain low energy cosmic rays can trigger single telescopes (see Figure 3.10). Furthermore, cosmic ray protons incident on the earth's atmosphere create secondary muons, which reach the ground in spite of their short lifetime via relativistic time dilation. When passing through the radius of a reflector, they produce a ring of Cherenkov light that reaches the camera. Because these Cherenkov photons arrive within a short time of one another, they tend to pass the L2 trigger criterion. A muon image is shown in Figure 3.27. In addition to increasing the deadtime of the detector, muon rings hinder gamma-ray detections because muons with large impact parameters appear similar to images from gamma-ray induced showers.[10] Because muons interact with single telescopes, muon events are unlikely to be correlated across cameras. γ-ray induced air showers, however, develop sufficiently far above the array that Cherenkov photons from a single shower will arrive at the cameras within a short time interval. The array trigger has the following purposes:

- Ability to reduction the CFD threshold and thus energy threshold
- Cosmic ray shower and NSB rejection
- Muon rejection

L3 imposes the requirement that at least two telescopes send level 2 triggers within a coincidence window of 50 ns. However, this technique is complicated by pointing-dependence of the relative Cherenkov photon arrival times from air showers. For example, a shower that arrives from zenith can be expected to deposit its Cherenkov light across all telescopes within a short time interval. However, the Cherenkov front from a shower that arrives at a large zenith angle will have varying arrival times at the four telescopes. To account for this effect, the level 3 trigger incorporates a pulse delay module (PDM), described in Weinstein (2007). The PDM

[10] The effect comes from the camera essentially zooming in on a portion of the ring to the point that it resembles a line. Gamma-ray induced showers are likewise elongated and compact. Thus, any muons with large impact parameters that pass the trigger and selection cuts become part of the irreducible background.

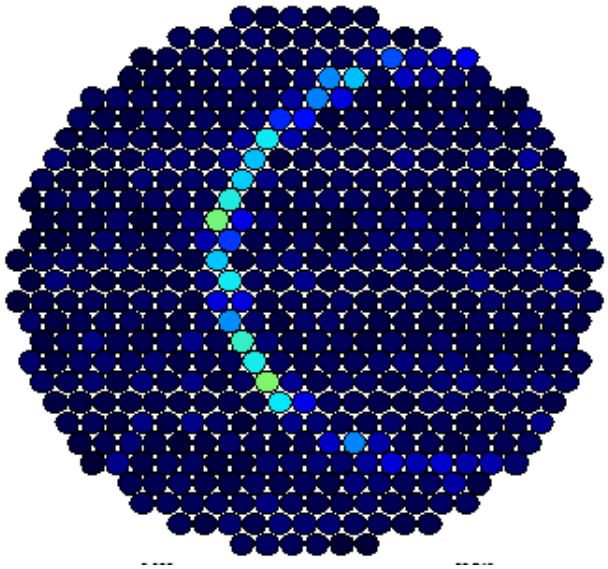

Figure 3.27 *A portion of a ring from the Cherenkov emission of a local muon. Muon images can pass image cleaning cuts and would constitute a large fraction of recorded events if the array-level trigger did not suppress them. This particular muon appeared concurrently with a small Cherenkov shower image in another telescope.*

calculates the expected L2 trigger delay times between telescopes based on the array pointing, and applies them every five seconds. The PDM also accounts for fixed delay times due to optical fiber and cable lengths.

Because the array trigger allows for a lower CFD threshold, it is important to determine an appropriate CFD setting before conducting observations. VERITAS observers perform bias curve measurements multiple times over the course of a dark run. A bias curve is produced by observing the night sky with a high CFD threshold, and then dynamically reducing this threshold while measuring the array trigger rate and L2 rates. Below some minimum threshold, the L3 rate will dramatically increase due to the cosmic ray background. By identifying this inflection point it is possible to set the CFD threshold sufficiently high that these additional cosmic ray triggers are not introduced into the data stream. An example bias curve is shown in Figure 3.28.

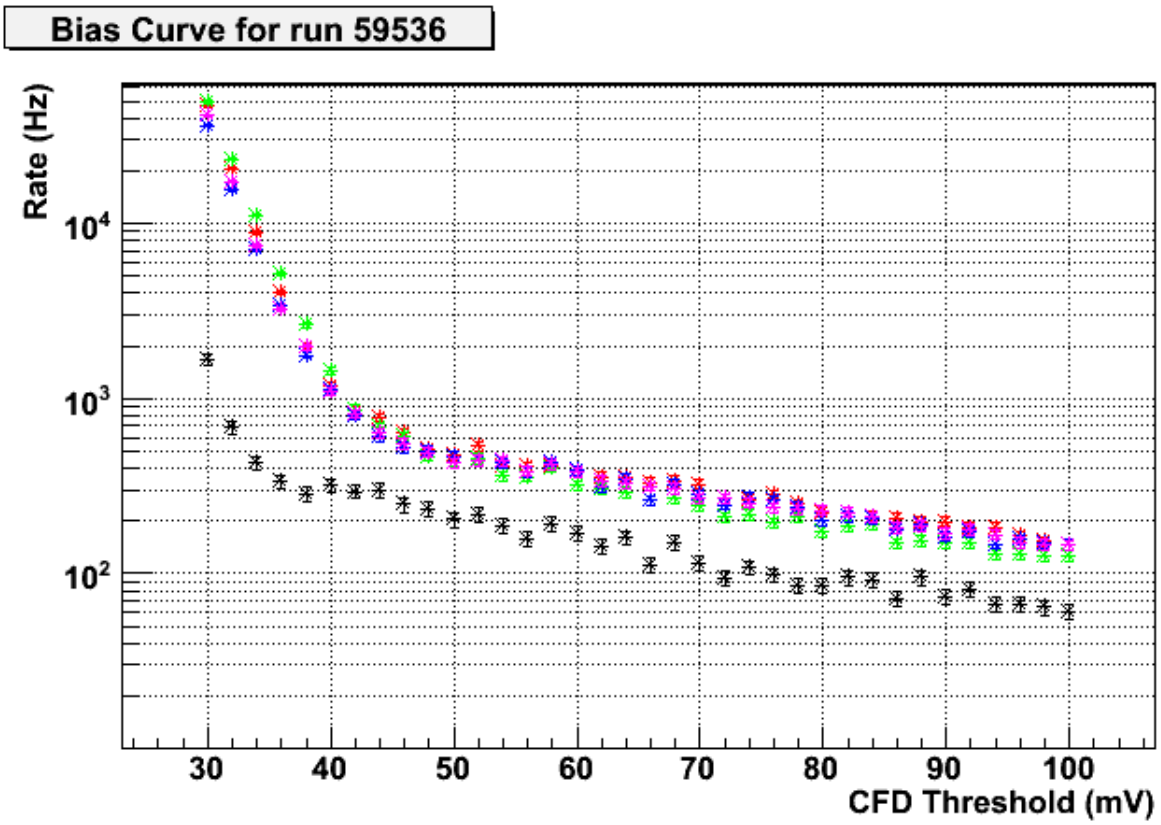

Figure 3.28 *A bias curve taken on December 29, 2011, after the commissioning of the ANL/ISU pattern trigger, and prior to the VERITAS II camera upgrade. The L2 rates for T1 (red), T2, (green), T3 (blue), and T4 (purple) are shown, as well as the array trigger rate (black). The inflection point in the array rate indicates the minimum allowable CFD threshold that can be set for observations. Standard observations during this array configuration were taken with a CFD threshold of 50 mV.*

3.3.4 Observations

VERITAS observations are performed nightly during the fall, winter, and spring of each year. The monsoons in Arizona prevent summer observations, therefore this time is instead used to perform maintenance and upgrade work on the instrument. Because the camera photomultiplier tubes are extremely sensitive to light and could easily be damaged by overexposure, observations are only performed after astronomical twilight and are coordinated with the phase of the moon. The observing year is divided into several dark runs, two to three week periods during which the moon is either not in the sky during observations, or is only partially illuminated. Originally VERITAS did not operate during bright moon periods. Currently, however, observations are performed during partial moon illumination with a reduced HV (typically $\sim$81% of standard settings) applied to the PMTs and during bright moonlight with the installation of camera UV filters (Holder, 2011). PMT currents are measured by the camera current monitors, and are displayed to observers with a special software utility. Observation settings are dictated by these currents, as well as the current illumination of the moon.

3.3.4.1 Data runs

Exposures are taken in short time intervals called data runs. Two basic observing modes are possible. Most commonly, sources are observed in wobble mode, with the source displaced 0.5° from the putative source location so that analysts can easily obtain a background estimate using the reflected regions method of analysis (see Berge (2007)). On occasion, sources will also be observed in ON/OFF mode, similar to the Whipple procedure described in Weekes (1989). Here, the putative source is observed on-axis for a certain period of time, and then observations are taken on a dark region of the sky with no known γ-ray source so as to obtain a background estimate.

Typically, runs are taken in twenty minute intervals. When observing in wobble mode, a single wobble offset is used over the course of the run; the next run is taken at a new wobble offset[11], and observers attempt to maintain a uniform wobble balance (though in principle this

[11]For simplicity only the directions North, South, East, and West are used as wobble offsets, but any wobble direction could be chosen without changing the simulation or analysis procedure. It is crucial, however, to maintain an offset of 0.5°, since different offset angles require new simulations. VERITAS occasionally observes

is not necessary). After the camera upgrade in the summer of 2012, observers began taking data runs in 30 minute intervals.

3.3.4.2 Calibration runs

The camera PMTs are non-identical, and thus calibration runs must be taken to flatfield the camera, i.e. to account for these variations. The two most significant sources of PMT-to-PMT variation are signal delays due to cable length differences between pixels, and gain variations between PMTs. The latter is largely accounted for by adjusting the HV applied to each pixel. However both sources of variation can be accounted for in the data analysis by illuminating the camera with a uniform source of light. Differences in photon arrival times can then be attributed to cable length delays, and differences in light exposure can be attributed to gain variations. These can then be corrected across the camera.

In principle, calibration runs could be taken once or twice per dark run. However, it is advantageous to take calibration runs as often as possible to track the aging of the cameras by looking for variations in the gains of the camera PMTs; calibration runs are also very straightforward to perform. Observers therefore take a calibration run at some point every night. Originally, these runs were taken with a pulsed laser attached to the quad arms of each camera, which emitted very stable light output that could be expanded to illuminate the entire camera, and the L3 trigger was externally triggered concurrently with the laser. Currently, calibration runs are taken with an LED flasher containing seven LEDs (shown in Figure 3.29). The flasher is advantageous because different numbers of LEDs can be illuminated so as to calculate gain variations in the camera over a variety of light levels. Like the laser, the LED flasher is pulsed concurrently with an external trigger to the L3. However, different numbers of LEDs are lit with every pulse; the flasher cycles from zero lit LEDs to all seven[12]. Flasher runs provide identical calibration information as the laser. However, flasher runs can be used to perform various other calibration studies (e.g. tests of the linearity of the system when varying light levels). Additionally, the flasher is cheaper than a laser, more robust, and more easily

sources sources at different offset angles, and this requires analysts to use another library of simulations.

[12]Individual LEDs are *not* identical, however this is irrelevant to the calculation of relative gains and timing offsets.

Figure 3.29 *An example of the LED flashers currently used to take VERITAS calibration runs.*

replacable.

CHAPTER 4. ANALYSIS OF VERITAS γ-RAY DATA

The principle goal of γ-ray data analysis is to derive information of astronomical interest, including γ-ray sky maps, energy spectra, and light curves. The VDAQ system (see 3.3.3.1) stores γ-ray data in the VERITAS Bank Format (VBF). VBF binary files are written to disk by VDAQ during observations and stored for later offline analysis. A single VBF file from a data run (typically 20 minutes of observation time prior to the camera upgrade, and 30 minutes afterwards) consists of many packets. The first is a header containing such information as the source observed, the run start and end time, the pointing of the telescopes in right ascension and declination, and list of telescopes participating in the observation. Following the header, the VBF file includes one packet for each recorded event, which states the event type (calibration, pedestal, Cherenkov from L3, etc.), status of the L2 trigger in each telescope, array event index, and event timestamp. These packets also contain information on every participating telescope pixel including the status of the CFD trigger and the full FADC trace. VBF files from simulated data contain the same information[1], as well as simulation parameters such as γ-ray energy and shower arrival direction. This raw detector data is processed through a data analysis chain in order to derive physical information about the γ-ray emission of the observed source.

Tests on a Calibration Source

It is important to test any analysis chain on a set of real data in which the expected result is already known. The Crab Nebula provides an excellent calibration source for this purpose, because it is one of the best-studied sources in all of astronomy. The Crab is the strongest

[1]Certain entries, such as the source location and event timestamps are meaningless, and thus filled with arbitrary values.

source of steady VHE γ-rays in the night sky, and was the first source detected with the IACT technique in 1989 (Weekes, 1989). In γ-ray astrophysics, the Crab Nebula has long been regarded as *the* standard for calibration of new detectors, although recent detections of flaring in the MeV-GeV band (Abdo et al., 2011) have called into question the Crab's status as a "standard candle." Contemporaneous TeV data have not detected flux variability or spectral variability (Aliu at al, 2013b), and therefore the Crab retains its importance as a strong and stable source of γ-ray emission. Whenever developing a new analysis technique in VHE γ-ray astronomy, the first test on real data should always be performed using observations of the Crab Nebula. In order to test and demonstrate the VERITAS data analysis chain, a sample of 6.8 hours of observations on the Crab Nebula was analyzed. All data were taken between December 2011 and February 2012; this was after the relocation of T1 and subsequent L2 trigger upgrade, but prior to the camera upgrade.

4.1 Simulation of Atmospheric Cherenkov Showers

An important aspect of IACT experiments is that Monte Carlo simulations play an essential role in the analysis of detector data. In this way, an IACT array resembles an accelerator-based or cosmic-ray detector experiment. Standard VERITAS simulation packages model particle cascades from γ-ray particles incident on the earth's atmosphere, as well as the production of Cherenkov radiation from the cascade particles. A full simulation of the detector is also performed, including ray-tracing of Cherenkov light from the telescope mirrors to the cameras, and the production of FADC traces from the resulting photoelectrons. Monte Carlo simulations used to simulate and verify the detector response to γ-rays. With regards to analysis of IACT observations, Monte Carlo simulations also play the following three roles in the analysis chain of γ-ray data:

- Measurement of γ-ray event energy
- Calculation of γ-ray detector efficiencies and cuts
- Determination of the energy-dependent effective collection area of the instrument ("spectral unfolding")

In order to derive γ-ray energy spectra, we must accurately measure the energy of each γ-ray that initiates an observed particle cascade. To that end, we simulate the response of the VERITAS detector to a spectrum of γ-ray showers over a range of energies, process the data through the analysis chain, and correlate certain analysis parameters with the simulated γ-ray energies. We then derive functions from these correlations, and use them to estimate energies on an event-by-event basis.

As described in Section 3.1.6, γ-rays and hadrons produce cascades which result in different distributions of Cherenkov photons on the ground. When analyzing data, image shapes from each event are compared to the shapes of γ-ray showers simulated under similar observation parameters (specifically the zenith and azimuth angles of the observation, and the level of the NSB). From this comparison it is possible to determine how closely each event resembles a γ-ray shower, and then retain or reject it accordingly.

When deriving a γ-ray spectrum, we must account for the non-uniform response of the atmosphere and detector in energy-space. For example, low-energy showers are fainter and thus have a lower probability of triggering the array, as well as a higher probability of being incorrectly reconstructed. Certain analysis-level cuts also have an energy-dependent efficiency When simulating a spectrum of γ-rays, the total number of events incident upon the detector is known, and it is thus possible to determine the fraction of events in each energy range that pass the trigger criteria and all cuts, as well as the fraction of mis-reconstructed events in each energy bin (sometimes referred to as "leakage events"). These energy-dependent fractions can then be applied to real data to derive the spectrum of γ-rays incident at the top of the atmosphere. See Section 4.9.3 for details on the process of spectral unfolding.

4.1.1 VERITAS Collaboration Standard Simulations

The VERITAS Offline Analysis Working Group (OAWG) produces γ-ray simulations for general use by the collaboration in analyzing data. Electromagnetic cascades and their resulting Cherenkov radiation are simulated using the CORSIKA package. Simulation of the VERITAS detector is performed by the GrISUdet package. GrISUdet is a detector simulation package developed by Grinnell College, Iowa State University, and the University of Utah.

Simulations are generated over a power law spectrum $\frac{dN}{dE} = \Phi_0 \, (E/E_0)^{\Gamma}$ with Γ=-2.0[2] between energies of 30 GeV and 50 TeV. Simulations are performed at zenith angles of 0, 20, 30, 35, 40, 45, and 50 degrees. Each γ-ray is directed at a random azimuth. An atmospheric profile is used to model the development of the electromagnetic cascade, as well as the atmospheric extinction of Cherenkov radiation. In order to increase processing time and reduce disk usage, only Cherenkov photons that arrive close to the telescopes are saved. The detector simulation includes such information the telescope optics, reflectivity, throughput, camera geometry, photodetector quantum efficiency curve, and single p.e. pulse shape. A simple FADC threshold trigger is used in place of the CFDs, however GrISUdet includes a full simulation of the pattern and array triggers.

Three detector simulations must be performed for the various epochs of the array: pre-T1 move, post-T1 move, and post-upgrade. However, the simulation of electromagnetic cascades is independent of the detector configuration and can thus be performed once. The OAWG simulates a five telescope array for the purposes of generating Cherenkov photons; both T1 locations are used as inputs. Afterwards, three detector simulations can be performed using the same Cherenkov photon simulations. For a spectrum of γ-rays with index -2.0 from 30 GeV to 50 TeV, thrown uniformly within a radius of 750 meters of the center of the telescope coordinate system, only about 1% of simulated photons will trigger the array. Non-triggering events are nonetheless saved, because this information is essential in deriving the instrument response functions needed to perform spectral unfolding.

Large photon statistics are needed to produce the analysis tools used in data analysis. Therefore the OAWG simulates 50 million γ-ray showers at each non-zero zenith angle, and 20 million showers from the zenith[3].

As described in 3.3.4, VERITAS does not typically observe sources on-axis, rather sources

[2]This spectrum is harder than most known γ-ray sources. The choice of spectral index is made so as to achieve sufficient statistics at higher energies, as it is always possible to re-weight simulations to a softer index when necessary.

[3]The array's trigger efficiency depends on the density of Cherenkov photons on the ground. Cascades arriving from larger zenith angles traverse a greater column depth of atmosphere, and therefore produce their Cherenkov emission from further away, thus having the effect of raising the telescope's energy threshold. The fraction of simulated events which trigger the array drops with zenith angle θ as $cos^2(\theta)$, therefore it is reasonable to simulate fewer photons at zenith. In principle the simulations could be more finely tuned by increasing the number of simulated photons at each successive zenith angle.

Table 4.1 Simulated FADC configuration used in the GrISUdet detector model.

Quantity	Value
Voltage/dc	7.84 mV/dc
Pedestal	20/16/16 dc
Dynamic Range	255 dc
Readout Window	24/20/16 samp.
Start of Trace	7 samp.

Table 4.2 Simulated trigger configuration used in the GrISUdet detector model.

Quantity	Value
"CFD" Threshold	60/80 mV
L2 Coinc. Window	5 ns
N-fold coinc.	3 pixels
Telescope coinc.	2 tel.
L3 coinc.	50 ns

are typically observed with the telescope pointing displaced from the source location by 0.5 degrees. Thus, the detector simulations are performed with the same offset between shower direction and telescope pointing. Many galactic sources, however, are close enough to be resolvable, and cover an area of the sky larger than the VERITAS PSF[4] (see Figure 4.1 for an example source, taken from Acciari et al. (2009a)). Here emission does not come from a single point, and reconstructed γ-ray showers are not necessarily covered by the simulated offset. In order to analyze extended sources, γ-ray simulations are also generated at offset angles between 0 and 2 degrees.

Because observations are conducted under a variety of sky brightness conditions (e.g. diffuse levels of light from the ground, light from different starfields, and different moon phases), a proper modeling of the NSB is also essential when generating simulations. To reduce processing time, simulations are generated without any NSB or even injected pedestal. The pedestal and NSB are added in the analysis.

[4]PSF refers to the point spread function. This is the spatial distribution of light seen by a telescope due to a point-source.

Table 4.3 Pixel electronics values used in the GrISUdet detector model.

Quantity	Value
PMT Gain	$1.975/2.025 \cdot 10^5$
Impedence	2722Ω

Tables 4.1, 4.2, and 4.3 provide the simulated configurations of the electronic components in the FADC, trigger, and pixels. Entries with two values indicate different parameters before and after the pixel upgrade. Entries with three values indicate different parameters before the T1 relocation, after the T1 relocation, and after the pixel upgrade.

4.1.2 Special Leeds L2 Simulations

As described in Section 3.3.3.3, the VERITAS level 2 trigger designed by Leeds University was replaced in November 2011 by Argonne National Lab and Iowa State University. It was later discovered that the Leeds L2 hardware contained hardware-level inefficiencies that were not properly modeled in the simulations. This inefficiency creates systematic features in γ-ray energy spectra (see Section 4.10.7 for details). In order to correct for these features, the GrISUdet simulation code was modified to reflect this hardware inefficiency, and a special round of simulations was generated at the Minnesota Supercomputing Institute. There are 30 million showers were generated at zenith, and 65 million showers were generated at zenith angles of 20, 30, 35, 40, 45, and 50 degrees[5]. Because these simulations were only used to analyze the Crab nebula and the blazars described in this work, only the 0.5 degree offset angle was simulated.

4.2 Analysis Chain and Outline of VEGAS

The VERITAS Collaboration has produced several software packages which are used for the analysis of data. These packages implement very similar algorithms to derive the same astronomical quantities of interest (sky maps, energy spectra, etc.). Independent analysis of the same data through separate analysis chains allows analysts to elucidate any possible errors in

[5]The increased number of showers with respect to the OAWG simulations was necessary because the trigger inefficiency reduces the number of showers that pass all three trigger criteria

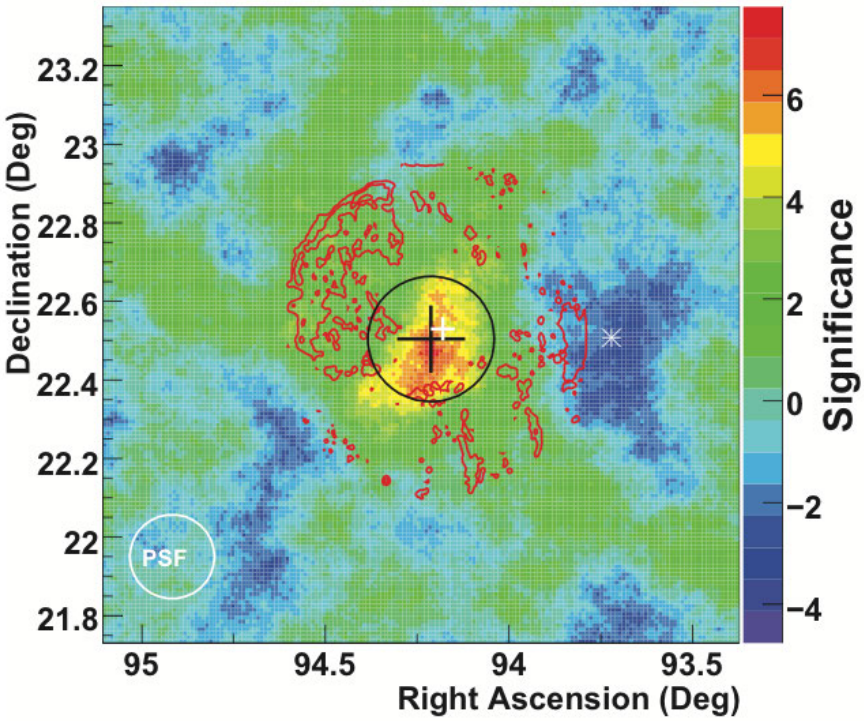

Figure 4.1 *Skymap of IC443. The emission region is sufficiently extended to be resolved to within the instrument's PSF.*

the processing or interpretation of data. The two software packages used most frequently in the VERITAS collaboration are the **VE**RITAS **G**amma-Ray **A**nalysis **S**uite (VEGAS) and EventDisplay. All analyses described in this work are performed with VEGAS, however EventDisplay uses an almost identical analysis chain. Because the two packages are developed independently, analysis results derived from one package can be cross-checked with the other. The VEGAS analysis chain is graphically depicted in Figure 4.2.

In order to analyze data, it is first necessary to analyze γ-ray simulations. The analysis chains for simulations and data are similar, however they are treated differently at certain points to account for differences between simulated γ-rays and real data. Simulations and real data have the following differences:

- Simulations have no event timestamps. Therefore any time dependent quantities such as fluxes, energy spectra[6], and light curves cannot be calculated.

- Although simulated events are distributed over various zenith angles and azimuths, they are always assumed to come from the same RA/Dec location in the sky coordinate system (we arbitrarily choose (RA, Dec) = (0, 0). The detector simulation always assumes that the telescopes are pointing at the source location (or at an angle to the source, in the case of wobble observations).

- When observing real sources in wobble mode, the source location rotates about the telescope pointing over the course of the observations (due to the rotation of the sky with respect to the earth). Whereas real data must be de-rotated to account for this, no de-rotation is necessary for simulations.

- γ-ray simulations have no background by definition. Real data, on the other hand, is dominated by background. To illustrate this, note that a data run taken on the Crab Nebula at an $\sim 11^\circ$ angle to the zenith contains approximately 270,000 events. However, the number of excess events detected after background subtraction and cuts is only 0.08%

[6]It certainly is possible, and diagnostically useful, to calculate time integrated energy spectra. In practice VEGAS simply assigns simulated data runs a meaningless exposure time. Time integrated energy spectra are typically calculated by analysts to confirm that VEGAS can accurately reconstruct a simulated energy spectrum.

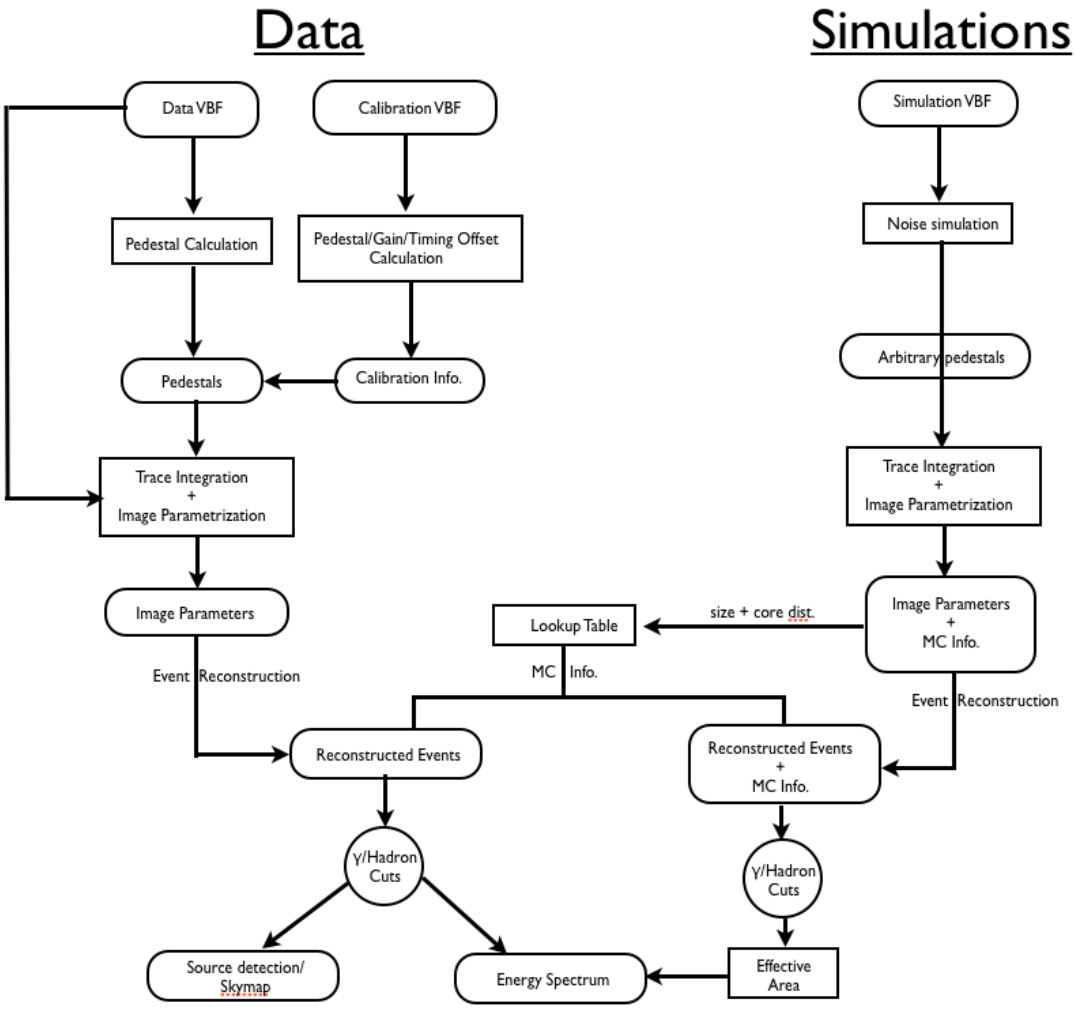

Figure 4.2 *Schematic of the VERITAS analysis chain employed in the VEGAS suite. Other analysis packages differ slightly, but implement essentially the same set of algorithms.*

of the total number of events detected. Therefore while background subtraction is not performed on simulations, it is an essential step in the analysis of data.

VEGAS consists of six stages. Stages 1 and 2 involve calibration and analysis of FADC traces from the raw VBF data. Stages 4 through 6 successively analyze and reduce the data to produce physically meaningful quantities of interest. The following list describes the analysis of real data:

Stage 1 (calibration runs) Calculation of relative gains between pixels, and relative timing offsets (due to differing cable lengths)

Stage 1 (data runs) Calculation of FADC pedestals for later subtraction, and calculation of pedestal standard deviations (often referred to as *pedvars*). Pedvars are directly related to the flux of the NSB, and are calculated over three minute intervals. Traces are corrected for FADC jitter.

Stage 2 Calculation of Cherenkov photon counts in individual pixels via FADC trace integration. Pedestals from stage 1 are applied and subtracted, and pedvars are used to calculate signal-to-noise ratios. Timing offset calculations are applied prior to trace integration, and relative gains are applied afterwards.

Stage 3 Calculation of the Hillas parameters (see Section 4.6) from stage 2 photon count information. In more recent versions of the code, stage 3 has been integrated into stage 2, and only the Hillas parameters are saved to file.

Stage 4 Image de-rotation, calculation of shower-level parameters (e.g. core location, shower maximum, direction reconstruction), and energy reconstruction. **This is the first point at which information from the simulations is used in data analysis**.

Stage 5 Application of γ/hadron separation cuts.

Stage 6 Background subtraction, sky map generation, and use of energy response curves in spectral energy unfolding.

The analysis of simulations proceeds as described above, but with the following differences.

- The pixels are assumed to be identical, therefore no relative gain or timing offset calculation is performed
- Special NSB simulations are used to randomly add noise to FADC traces in stage 1. No jitter correction is performed.
- Stage 2 assumes all pedestals to be identical.
- Stage 4 performs no image de-rotation.

4.3 Analysis of Calibration Runs

As described in 3.3.4.2, nightly calibration runs are taken to account for differences in PMT gain variations and differences in signal cable lengths. Calibration runs taken prior to the 2009/2010 observing season were performed with a pulsed laser, while runs taken after November 2009 were performed with an LED flasher. The analysis of both types of calibration runs is similar, and in either case VEGAS produces identical analysis products. The goal of calibration analysis is to calculate the *relative gains* and *timing offsets* of each camera pixel.

Relative gains are calculated under the assumption that the laser/flasher uniformly exposes the camera to light. Because each pixel receives the same number of photons from the laser or flasher, differences in the output signal from each pixel can be attributed to variations in the absolute gains, quantum efficiencies, and collection efficiencies between pixels; these gains are normalized, hence they are termed "relative" gains. The normalization is done on an event-by-event basis, so that in the case of runs taken with the LED flasher the gains can be averaged over a wide range of light intensities. The amount of charge deposited into each pixel is calculated by evaluating the definite integral of the trace. See Section 4.4 for details on this procedure[7]. A distribution of charges and relative gains is shown in Figure 4.3.

[7]The signal from the laser or flasher is much higher than the PMT response to single or even double photoelectrons. Therefore the trace is integrated over the entire readout window, instead of using any specialized technique to isolate the laser or flasher signal from NSB photons.

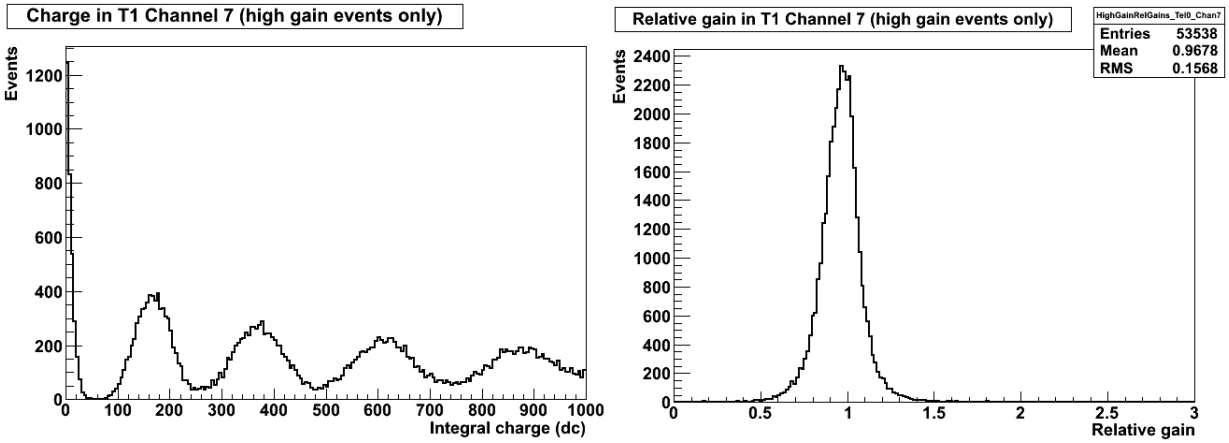

Figure 4.3 *Left: Distribution of charges in a single pixel from events in a calibration run. The presence of multiple peaks is because this run was performed with the LED flasher, which pulses at multiple light intensity levels. Right: Distribution of relative gains from the same calibration run. The mean of the distribution is used in the analysis.*

Timing offsets are calculated under the assumption that laser or flasher photons have a negligible time dispersion across the camera. The arrival time of photons at each pixel is calculated by evaluating the half-maximum of the leading edge of the signal from the FADC trace. Each pixel's photon arrival times are binned on an event-by-event basis, and the mean of the distribution is used to correct for timing offset variations in later stages of the analysis. See an example distribution of photon arrival times in Figure 4.4.

4.4 FADC Trace Integration

In order to analyze images of γ-ray showers, we must first calculate the amount of Cherenkov light in each pixel on an event-by-event basis. This information is obtained from the PMT responses to photoelectrons, i.e. the FADC traces. The amount of charge deposited into a PMT by photoelectrons is proportional to the definite integral of the pixel's FADC trace over the time window for which signal is being received. In principle we could integrate over the entire trace, however this would defeat the purpose of employing FADCs. An FADC is advantageous over a simple charge integrator because we can reject NSB photons by selectively

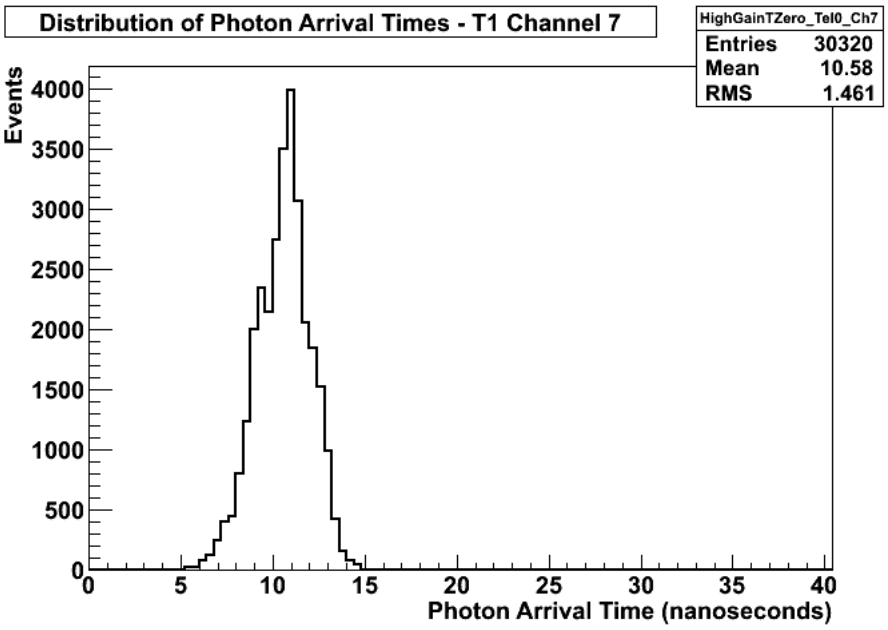

Figure 4.4 *Distribution of timing offsets in a single pixel from a flasher run. The mean of this distribution is used in analysis.*

choosing our region of integration. Figure 4.5 shows an FADC trace from Cherenkov data, with the appropriate region of integration selected. By calculating the definite integral of the trace over this region, we can compute the number of photoelectrons in the pixel.

The integral number of digital counts under the trace can be related to the physical number of photoelectrons through lab tests. It is possible to expose a pixel in a lab to a small light level and create an event-by-event distribution of the integral charge. Such a distribution is shown in Figure 4.6. The pixel will often trigger on noise, creating a peak corresponding to the pedestal, or quiescent response. A second peak is produced from the pixel's response to single photoelectrons. The location of this peak is the value of the FADC trace's definite integral due to a single photoelectron. This so-called "dc-to-p.e. ratio" need not be calculated when analyzing data. It is, however, necessary in the production of simulations so as to produce an accurate simulated FADC trace from the photons incident upon each pixel.

The obvious challenge in FADC trace integration is location of the appropriate region of integration. It is desirable to accurately locate the FADC trace from Cherenkov photons and

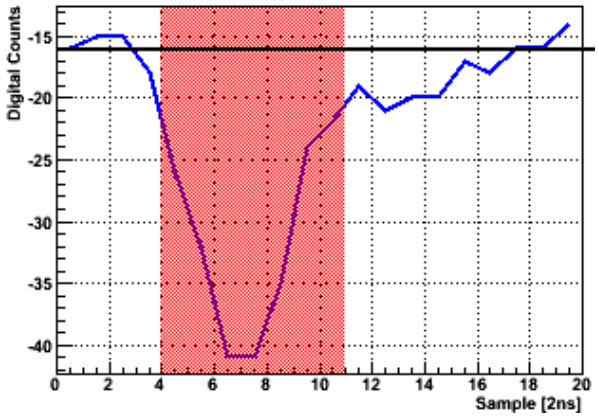

Figure 4.5 *An FADC trace from photoelectrons as viewed in vaDisplay, the VEGAS event display. The solid black line represents the injected pedestal (the signal input to the FADC even in the absence of an external signal from the PMT), and the light red region represents the region of integration.*

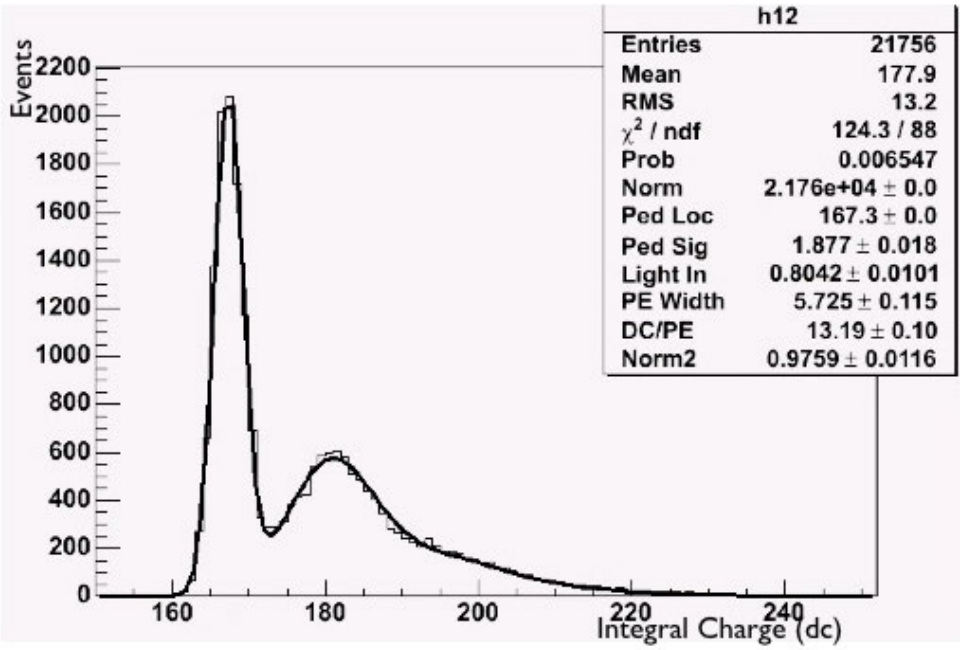

Figure 4.6 *Distribution of charge in a PMT from a single photoelectron lab test. The larger peak represents the PMT pedestal, and the smaller curve is due to single photoelectrons.*

integrate over as small a region as possible so as to extract the Cherenkov signal while rejecting as much of the NSB as possible. Ideally, an FADC trace is integrated beginning approximately at the half-max of the trace's leading edge (we term this the trace's t_0), and continues for a number of samples corresponding to the approximate width of the pulse (VEGAS currently uses 7 time samples, or 14 nanoseconds). An average 20 minute observation produces over 200,000 events. With 4 telescopes and 499 pixels per telescope, there are approximately 400 million FADC traces in every data run. Therefore it is necessary to devise a robust trace integration algorithm which can reliably locate each trace's t_0. One's ability to locate the t_0 is hindered by three effects: timing offset due to differing cable length between pixels, jitter from the FADC crates[8], and time gradient due to the angle between the Cherenkov front and the face of the camera. The problem of timing offset is easily solved via analysis of a calibration run. The latter two issues require specialized techniques.

4.4.1 Jitter Correction

FADC jitter refers to the fact that when traces are read into the DAQ's `eventbuilder` system, each of a given telescope's four FADC crates may not have stopped at the same time, and thus the time samples between crates may not be comparable. In order to align FADC traces across crates, the pattern trigger sends a signal to each crate upon receiving an L3 trigger. Figure 4.7 shows the time-averaged L2 trace from each of the four crates in telescope 1 from a 20 minute data run.

It is impossible to compare the L2 traces between crates to perform a jitter alignment, because no individual channel can be guaranteed to not suffer from FADC jitter. However we can assume that on average, electronic jitter will be Gaussian distributed[9]. Figure 4.8 shows the distribution of L2 pulse arrival times in a particular FADC crate from a Cherenkov data run. When analyzing a calibration or data run, stage 2 performs an initial event loop over a run's first 10,000 events to construct such a distribution and determine the average pulse arrival

[8] Jitter refers to the fact that when the trigger system instructs a readout of the FADCs, individual crates stop on different samples. This shifts isochronous pulses from separate crates to different positions in the readout window. Usually, jitter introduces a time shift of $\sim$2 samples.

[9] This is not an entirely accurate assumption, but turns out to be sufficient for a proper L2 correction

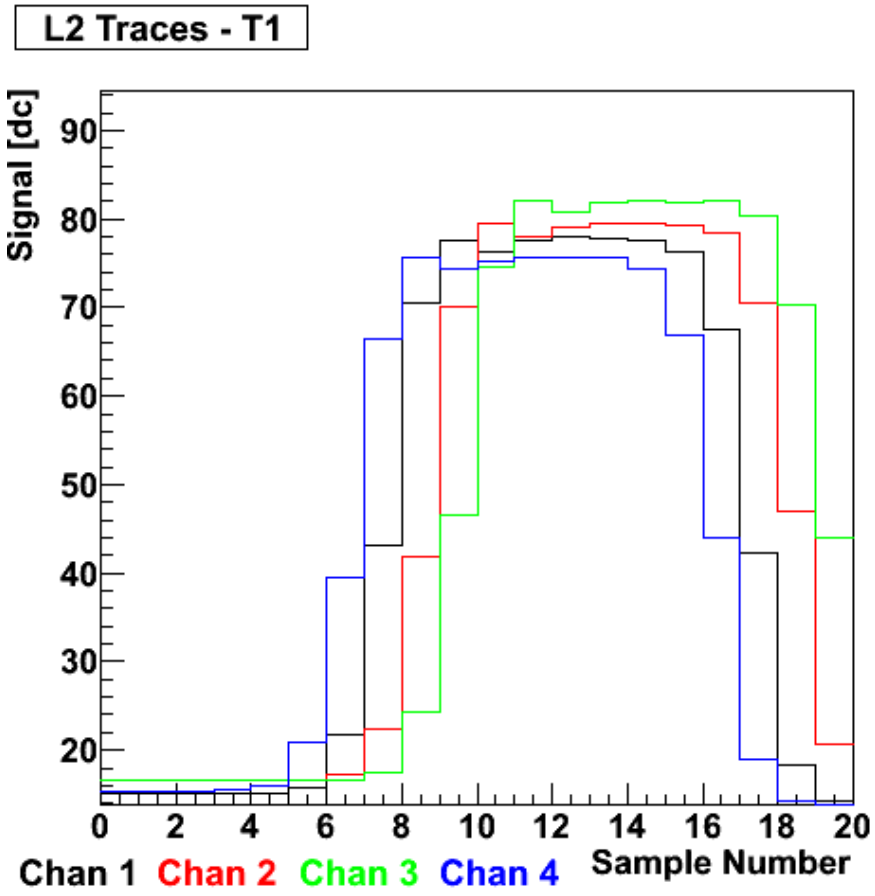

Figure 4.7 *Time averaged L2 traces in telescope 1 from a 20 minute data run.*

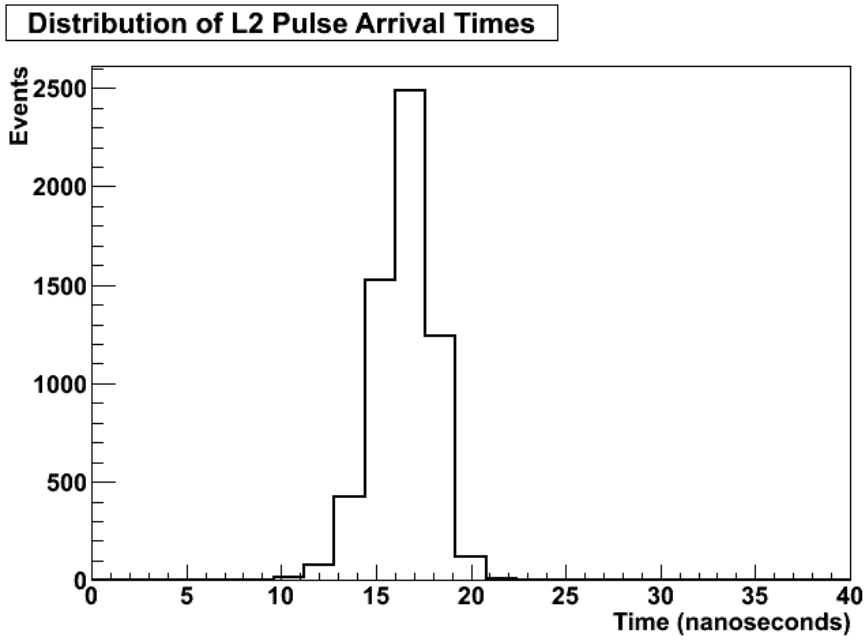

Figure 4.8 *The distribution of L2 pulse arrival times. Each individual pulse is compared to the mean of this distribution to determine the event-by-event jitter.*

time in each crate, and then compare's each L2 pulse arrival time to this average value on an event-by-event basis so as to estimate the electronics jitter in each crate from each event. This technique was implemented by the author, and has been shown to strongly affect the shape of γ-ray spectra derived by VEGAS.

4.4.2 Doublepass method of correction for the Cherenkov time gradient

Cherenkov fronts almost always make an angle to the camera plane. Therefore there is an approximately linear gradient in the photon arrival times. VERITAS FADCs allow for calculation of this gradient by measuring the t_0's of pulses from photoelectrons, which effectively correspond to these photon arrival times. In principle, each trace's t_0 could be used to define its appropriate region for integration. However, this would amplify the amount of charge integrated from pixels containing noise. Instead, the author has implemented a doublepass method of trace integration in VEGAS. In the first pass, each trace is integrated over the entire FADC readout window, excluding the first and last two samples. The integral charges

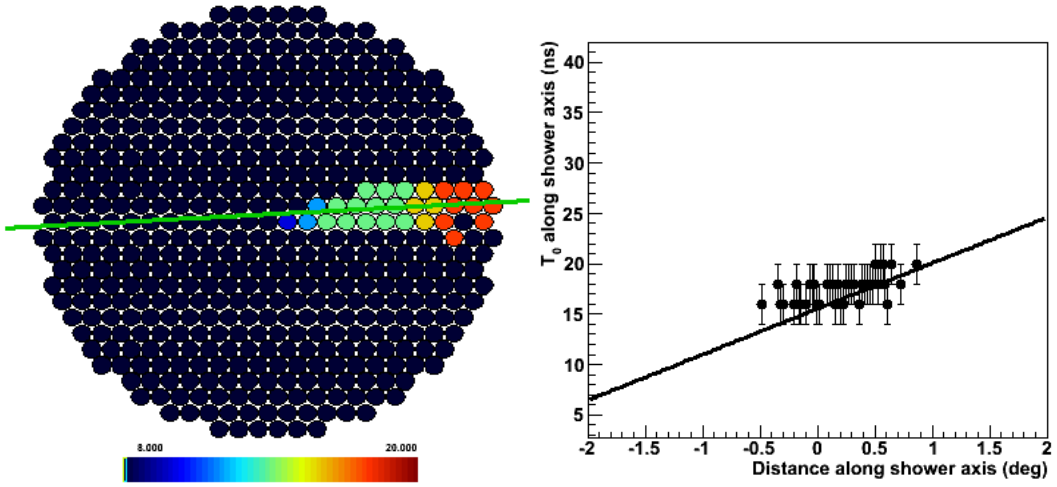

Figure 4.9 *Camera map of photon arrival times in nanoseconds from a simulated γ-ray (left). The resulting time profile plot of photon arrival time vs. distance along the image major axis, with the image centroid defined as 0 deg (right).*

from the pixels are used to construct an image of the Cherenkov light. An abbreviated version of the image parameterization algorithm described in Section 4.6 is used to calculate the major axis (which corresponds to the shower axis) and centroid of each image. Next, a time profile plot is constructed, in which each pixel's photon arrival time is plotted against its distance along the shower axis with respect to the centroid[10]. A time gradient map and time profile plot are shown in Figure 4.9.

The time profile is fit to a first-degree polynomial to derive the image's time gradient. Next, a re-integration of the traces is performed using the time gradient to predict the location of each trace's t_0 and set the integration region appropriately. Because the trace t_0's are not directly used, this method will not bias the trace integrals of noise pixels to higher values.

4.5 Image Cleaning

After completing the trace integrations for an event, it is necessary to clean each telescopes images to remove noise pixels. Figure 4.10 shows a Cherenkov image before and after the removal of these pixels. After the trace integrations for a given event are performed, each pixel's

[10]Noise pixels are largely excluded from this plot by cutting any pixel with a charge/pedvar ratio below 2.5

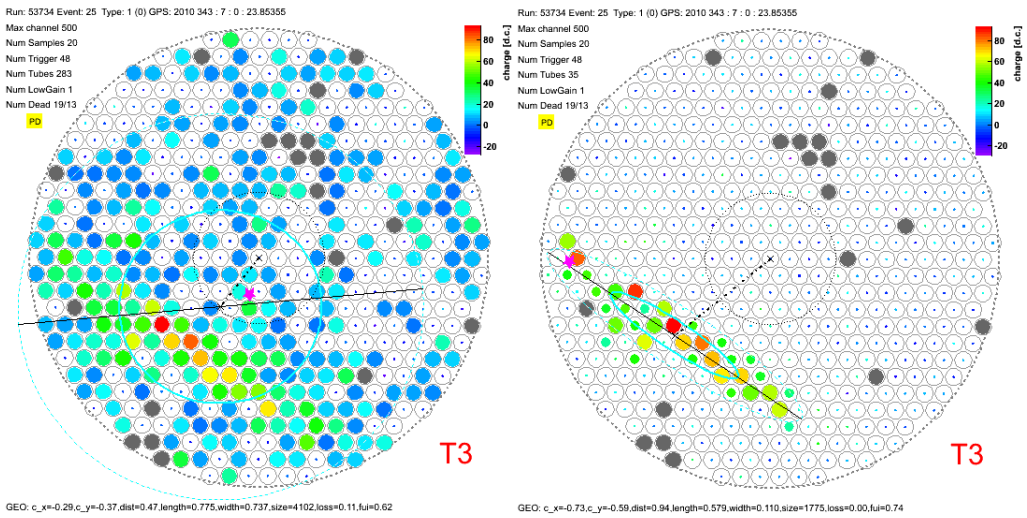

Figure 4.10 *A raw image without cleaning cuts (left). A cleaned Cherenkov image (right).*

integral charge can be divided by the pixel pedvar[11] from the event's timeslice to obtain a signal-to-noise ratio. This ratio is equal to the number of standard deviations between the integral charge and the NSB. However, this information is not sufficient to separate the Cherenkov image from the NSB. A typical Cherenkov image consists of a bright core - corresponding to the core of the electromagnetic cascade where the particle density is highest - surrounded by a dim halo. Pixels in the halo, which contain Cherenkov light, may nonetheless not be significantly above the NSB. VEGAS uses a two-step image cleaning process which retains light from both the core and the halo.

1. Define *image pixels* as pixels with a charge that is 5 σ above the background, and *border pixels* as pixels with a charge that is 2.5 σ above the background.

2. Retain all image pixels, as well as border pixels that are adjacent to image pixels, and remove the rest.

Once a shower image has been cleaned, it accurately represents the projection of the cascade on the camera plane and can be analyzed.

[11] The standard deviation of the pedestal distribution.

4.6 Calculation of the Hillas Parameters

In order to analyze an air shower, camera images must be quantified with a set of variables which fully describe the relevant details of the shower. γ-ray induced showers could in principle be fit to 2D Gaussians or ellipses, however fitting algorithms are costly in terms of computation time[12]. The most common method of quantifying a shower image is the Hillas parameterization (see Hillas (1985)). The first three moments of each image are calculated and used to derive several variables including:

size: The sum of the trace integrals in each participating pixel. This is a measure of the number of photons deposited onto the camera by the source.

length: The semi-major axis of the image. This represents the longitudinal development of the shower.

width: The semi-minor axis of the image. This represents the lateral profile of the shower.

Centroid: The x and y coordinates of the image centroid in the field of view.

dist: The distance of the image centroid from the center of the field of view.

phi: The angle between the semi-major axis of the image and the x-axis of the camera coordinate system. Represents the direction of the shower axis.

The Hillas parameters are used to locate the direction of each shower on the sky, as well as its impact location on the ground (see Section 4.7). Furthermore, the parameters *length* and *width* are scaled by simulated showers and used to establish selection cuts to remove the hadronic background (see sections 4.7.1 and 4.8.1).

4.7 Event Reconstruction

After parameterizing shower images in each telescope, stereoscopic reconstruction is used to locate the arrival direction of each shower, and its impact location in the plane of the

[12]The OAWG has recently developed a stage 3 algorithm that fits each image to a 2D Gaussian. This technique will eventually become a standard VERITAS analysis technique, but was not used in this work.

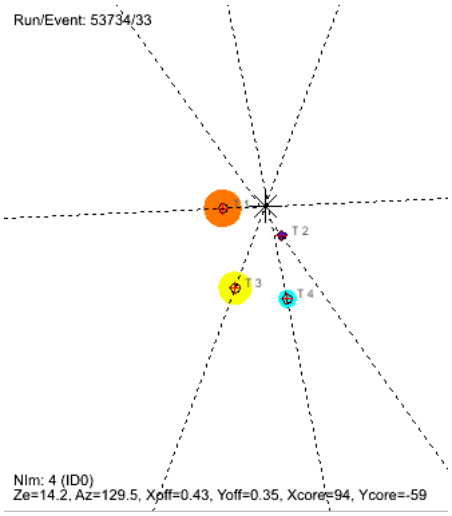

Figure 4.11 *Core reconstruction from an event with 4 participating telescopes after image cleaning cuts.*

telescope mirrors[13]. The major axis of each shower image represents the projection of the cascade's longitudinal development on the camera plane, and thus points back to the location of the initiating γ-ray direction on the sky. Individual images are placed in the same field of view, and pairs of shower images can thus be used to reconstruct the γ-ray shower's arrival direction, as depicted in Figure 3.12. Often, three or even four telescopes record images that survive cleaning cuts (the event shown in Figure 3.12 is reconstructed from three images). In this case, intersection points from each pair of images is used to provide as precise a direction reconstruction as possible, using an algorithm which minimizes the perpendicular distance of the reconstructed direction to the line joining each pair of intersection points.

To reconstruct a cascade's impact location in the plane of the telescope mirrors, the same algorithm as above is employed, but instead of overlaying images in the same field of view, each image is placed at the location of its telescope. In this case, the intersection of the images' major axes represent the cascade's impact location.

[13]This information can be combined with the telescope pointing to also locate shower impact locations on the ground

4.7.1 Lookup Tables and Reconstruction of Event Energy, Length, and Width

In order to reconstruct the energy of a γ-ray shower and filter out hadronic events, it is necessary to compare event information to γ-ray simulations. However, it would be impractical to access simulated γ-ray events directly. Furthermore, individual showers are affected by statistical fluctuations (e.g. depth of the first interaction), and thus it is more helpful to compare each event to average values from simulations. This is accomplished by producing lookup tables. A lookup table is a two-dimensional histogram, produced for a single telescope, which plots the median value of parameters from a set of simulations, binned in size and shower core distance. In the current VERITAS data analysis, lookup tables are produced for energy, *length*, and *width*. Energy lookup tables are used to estimate the energies of showers from real data. Length and width tables are used to compare the measured Hillas parameters from real data to the expected values from simulations, and thus establish cuts to suppress the hadronic background. Individual lookup tables are produced for each simulated zenith angle and noise level. Because simulations are performed with randomized azimuth angles, azimuths are divided into 45 bins. Figure 4.12 shows an example energy lookup table.

Energy lookup tables are used to reconstruct the energies of individual γ-ray showers. The distribution of Cherenkov photons on the ground due to an air shower, as shown in Figure 3.4, implies that a γ-ray shower's energy is a function of its measured size and core distance from the telescope. More energetic primary γ-rays produce more extensive cascades, and thus a greater number of Cherenkov photons on the ground. However, Figure 3.10 shows that the photon density on the ground varies radially with distance from the core of the shower's impact location. Therefore we must use both a shower's *size* and core distance when estimating energies. Image *size* is obtained directly from the Hillas parameterization, and the shower's core location (and thus distance from each telescope) is measured from the stereoscopic reconstruction[14]. Energies could be reconstructed by simply selecting the median energy corresponding to each event's *size* and shower core distance, however this would cause all events in a single *size*, distance bin to return precisely the same energy. Instead, linear interpolation is used to account for

[14]When filling a lookup table, Monte Carlo core locations are used instead of reconstructed values, to avoid placing poorly-reconstructed events in the wrong bin.

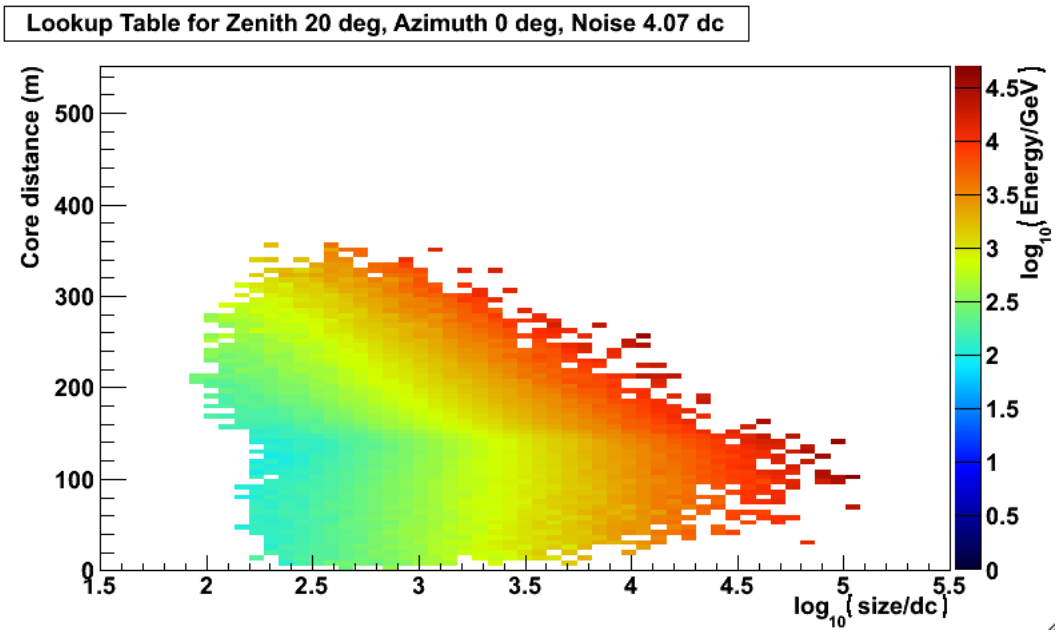

Figure 4.12 *An energy lookup table, derived from simulations. Each bin gives the median energy from simulations as a function of size and core distance. VEGAS also stores the standard deviation of energies in each bin and the number of events.*

the event's position within the bin. Estimated energies from all four telescopes are averaged in order to finally obtain the shower's reconstructed energy. Because zenith angles and noise levels are continuous parameters as opposed to the discrete values used in simulations, energy reconstruction is done using the lookup tables using the zenith and noise values closest to the actual observation parameter, and the results are averaged using linear interpolation.

The *length* and *width* tables are used to define the *mean scaled parameters*, which are used in suppression of the hadronic background. During event reconstruction, *length* and *width* are scaled with the simulations; the "scaled length" and "scaled width" are defined as follows:

$$MSL = \frac{1}{N_{tel}} \sum_{i=1}^{N_{tel}} \frac{length_i}{< length_i >_{MC}} \qquad MSW = \frac{1}{N_{tel}} \sum_{i=1}^{N_{tel}} \frac{width_i}{< width_i >_{MC}}. \tag{4.1}$$

The median *length* and *width* values used in Equation 4.1 are interpolated over zenith angle and noise level, using the same algorithm employed in the energy reconstruction. The mean scaled parameters MSL and MSW essentially describe how the shape of a Cherenkov image

compares to a γ-ray simulated at the same zenith angle, azimuth, and noise level. Cuts can be made on these two parameters to suppress the hadronic background, as described in Section 4.8.1.

4.7.2 Coordinate De-rotation

Because the VERITAS cameras use altitude-azimuth tracking, the star field rotates about the pointing position over the course of an observation. This is unimportant in the case of on-axis observations of point sources. But when observing an extended source on-axis, or when in wobble mode, the source itself rotates in the camera plane. Therefore when reconstructing shower directions, VEGAS implements a special class to convert the elevation and azimuth of each shower to right ascension and declination, correcting for this rotation.

4.8 Sky Analysis

After reconstructing each event, it is necessary to separate the γ-ray signal from the comparatively larger hadronic background. Two methods are used to filter the γ-ray signal from the background. First, selection cuts are used to greatly reduce the background. Second, the distribution of remaining background events is subtracted from the distribution of signal events.

4.8.1 Gamma/Hadron Separation

Due to the differences between the structures of electromagnetic and hadronic showers, the shapes of Cherenkov showers can be used to separate γ-rays from hadronic images. However, image shapes are also affected by observation parameters, especially the zenith angle of observations. Thus the mean scaled parameters (defined in Equation 4.1) are instead used to distinguish signal from background, because they compare data to simulated γ-rays and eliminate variations arising from observation parameters. Figure 4.13 shows the distributions of mean scaled length and width from events reconstructed within signal and background rings, taken from the analysis of Crab Nebula data sample. ON and OFF distributions were subtracted to obtain the excess distributions, and this excess was compared to reconstructed simulations.

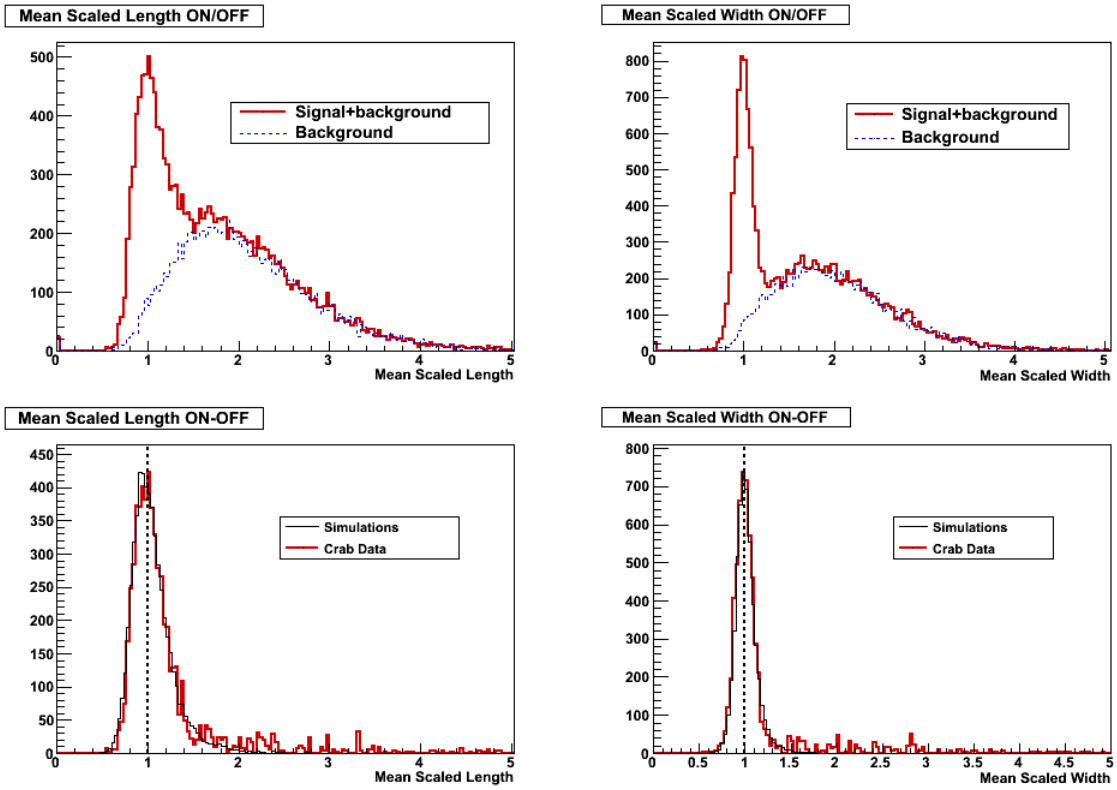

Figure 4.13 *Distributions of mean scaled length and width from several wobble runs taken on the Crab Nebula. One ring was used to obtain the background estimates. The background subtracted data agree well with distributions from simulations. These distributions demonstrate that the mean scaled parameters are extremely effective at separating γ-rays from the hadronic background.*

Cuts on mean scaled length and width have proven to be extremely effective in γ/hadron separation. Analysts typically retain only events with $0.05 < \mathrm{MSL} < 1.30$ and $0.05 < \mathrm{MSW} < 1.15$. These cuts eliminate 98% of the hadronic background whilst retaining 78% of the signal. These cuts are applied by stage 5 of VEGAS[15].

[15]The cuts specified here were used in version 2.3.0. of VEGAS. The OAWG regularly optimizes cuts when introducing a new version of VEGAS or a new set of MC simulations. Optimization is performed by carrying out several analyses of the Crab Nebula while exploring cut parameters in multivariate space, and the cuts specified here change from time to time. These cuts, however, were used in all analyses in this work.

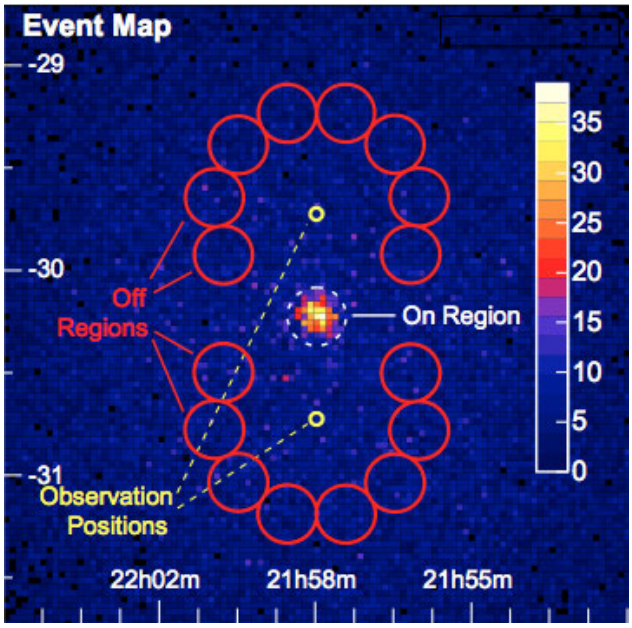

Figure 4.14 *The radial acceptance function of a γ-ray telescope for several different zenith angles of observation after applying standard γ/hadron separation cuts. Taken from Berge (2007) For arrays of multiple IACTs, these curves also depend on the azimuth of the observed source.*

4.8.2 Wobble Analysis

The VERITAS instrument has a radially-dependent response to the isotropic cosmic ray background (see Figure 4.15). By taking observations with the source displaced from the center of the field of view, any other point in the field of view equidistant from the pointing position can be sampled for a background estimate. Data can thus be analyzed using the reflected regions model Berge (2007). Shown in Figure 4.14 is an event sky map illustrating the wobble method (this map was produced after γ/hadron separation, described in Section 4.8.1).

A single ON ring is used to determine the event count estimate from the source location. In principle, a single OFF ring is sufficient to determine the background estimate, however VEGAS averages the background estimates from six background rings. Any background ring encompassing a bright star or another γ-ray source in the field of view is excluded from the background estimate. The use of multiple OFF rings is also advantageous because an accurate background estimate can be made even when the field of view contains many exclusion regions.

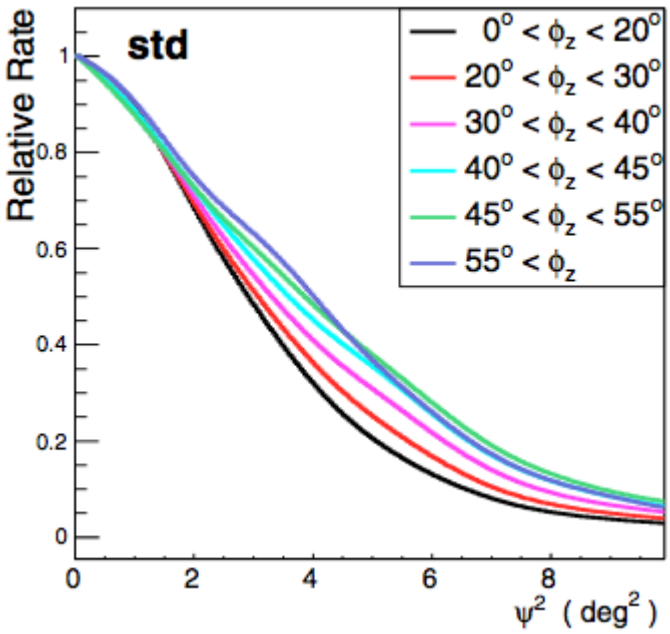

Figure 4.15 *The radial acceptance function of a γ-ray telescope for several different zenith angles of observation after applying standard γ/hadron separation cuts. Taken from Berge (2007).*

It is important to use a signal ring that is sufficiently large to cover the entire source, but not too large so as to cover a large region of background and thus reduce the sensitivity of the analysis. For most point sources, a ring size of 0.1° in radius suffices. For sources with soft spectra, a larger ring of 0.118° is used to account for the larger PSF of low-energy events[16].

4.8.3 Background Subtraction

Despite the efficacy of γ/hadron separation, an irreducible background remains after applying selection cuts. This background cannot be removed directly so as to classify individual events as γ-rays. However, it is possible to make distributions of parameters of interest and subtract so as to obtain the signal distribution. One important parameter distribution of interest is the angular displacement of events from the putative source location. If a γ-ray source is indeed present at the observation position, we expect to see an excess of events above the

[16]Lower energy events produce cascades with fewer electrons, and thus a lesser number of images pass cleaning cuts and are able to participate in event reconstruction. The direction reconstruction from these events is therefore less precise.

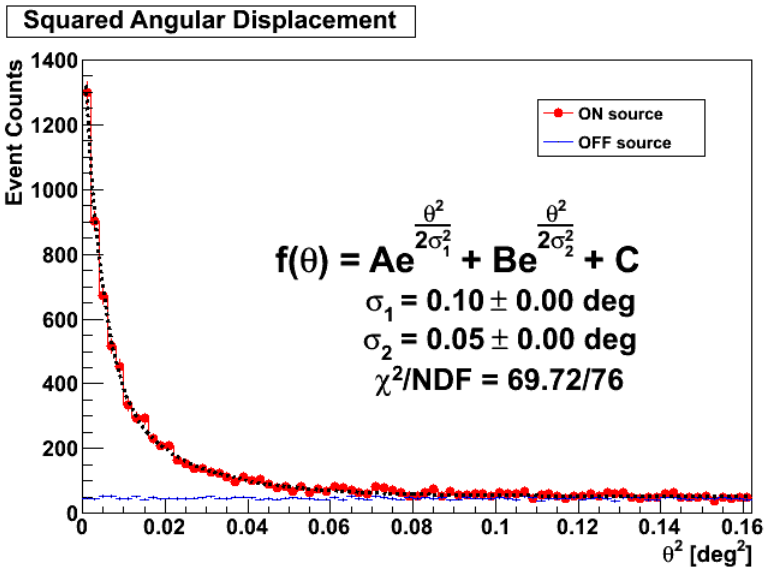

Figure 4.16 *Squared angular displacement of events with respect to the source location of the Crab Nebula. Derived from 6.8 hours of Crab observations taken between December 2011 and February 2012. OFF counts have been corrected for the multiplicity of background rings. The distribution of ON counts was fit to a double exponential function with a constant offset.*

background close to an angular displacement of 0°. In practice, we plot the distribution of *squared* angular displacement of events with respect to the center of the ON and OFF rings, averaging over the number of OFF rings. Figure 4.16 shows distributions of events in squared angular displacement after applying γ/hadron separation cuts to the Crab Nebula data sample. A double exponential function model of the PSF was used to fit the ON distribution. Events are plotted beyond the size of the ON and OFF rings for diagnostic purposes, but in all other parts of the analysis these events are cut.

Despite the very small fraction of γ-rays contained in the set of triggered events - VERITAS triggers about $\sim$25 γ-rays per minute during Crab observations taken close to zenith while the typical L3 rate prior to the camera upgrade was about 300 Hz - it is nonetheless possible to see a clear excess of γ-rays over the cosmic ray background by plotting the distribution of event counts in squared angular displacement.

4.8.4 Calculation of Event Rates and Detection Significance

When studying any γ-ray source, it is always important to obtain the rate of excess events in the ON ring, as well as the statistical significance of the detection. The excess event rate can be obtained by simply subtracting the background estimate from the number of counts in the ON ring, and dividing by the livetime of the observation. We define a parameter α such that the number of excess events in the detection is given by,

$$N_{excess} = N_{ON} = \alpha N_{OFF} \tag{4.2}$$

The rate is given by $R_\gamma = N_{excess}/t$ where t is the lifetime of the observation. When estimating the background using the reflected regions model using n background rings (Section 4.8.2), this parameter is simply given by $\alpha = 1/n$, i.e. the background estimate is the mathematical average of the number of counts inside each OFF ring. When using other background estimation techniques (e.g. the ring background model), α must take into account the relative angular sizes of the ON and OFF regions, as well as the acceptance function of the instrument. Berge (2007) gives a generalized description of the α parameter.

It is important to properly interpret the event excess rate. This number is an *analysis* rate and does not correspond to the physical flux of γ-rays against the atmosphere. For example, a VEGAS analysis of Crab Nebula observations taken near 20 degrees to the zenith gives a γ-ray rate of 7.8 events per minute against a background of 0.6 events per minute. These quantities can be changed by altering the size of the ON and OFF rings or changing the γ/hadron cuts. The analysis rates will also be lower for observations taken at larger zenith angles, because particle cascades traverse a greater column depth, more Cherenkov light from air showers is extincted by the atmosphere, and fewer showers trigger the array and pass all cuts. In order to derive the physical flux of γ-rays, it is necessary to unfold the effective area of the detector (see Section 4.9.2), which accounts for effects from the cuts, the size of the ON and OFF rings, and observation parameters such as zenith angle, azimuth, and noise level.

The significance of a γ-ray detection can be calculated by the Li and Ma formula from Li and Ma (1983). The Li and Ma formula is used to calculate the statistical significance of a

detection as a function of the α parameter and the number of ON and OFF counts.

$$\sigma = \sqrt{2}\sqrt{N_{ON}\ ln\left[\frac{1+\alpha}{\alpha}\left(\frac{N_{ON}}{N_{ON}+N_{OFF}}\right)\right] + N_{OFF}\ ln\left[(1+\alpha)\left(\frac{N_{ON}}{N_{ON}+N_{OFF}}\right)\right]} \quad (4.3)$$

4.8.4.1 Cut Optimization

Statistical significance is an extremely important quantity of interest when observing sources for the purpose of discovery. The VERITAS collaboration requires at least two independent analyses to each obtain a 5σ or greater result in order to claim detection of a new γ-ray source. In principle the simplest way to increase a source's detection significance is to observe the source for as many hours as possible. Because observation hours are often in short supply, it is advantageous for analysts to preferentially select a set of cuts that maximize detection significance. The OAWG regularly performs multiple analyses on a predetermined sample of Crab Nebular runs, exploring the parameter space of cuts to arrive at a cut set which maximizes the detection significance on the run sample. The Crab Nebula is used to create optimized sets of cuts for moderate and hard spectrum sources. For soft spectrum sources, the blazar PG1553+113 is used instead, because it is a very bright source with a soft spectrum (Γ ∼-4.0).

4.9 Spectral Analysis

Spectral analysis refers to the calculation of differential γ-ray fluxes as a function of energy. Spectral analysis is essential to the scientific study of many sources including blazars, and is a central topic of this work.

To first order, the vast majority of VHE γ-ray sources emit spectra which can be characterized by power law functions[17] of the form $F(E) = F_0\left(\frac{E}{E_0}\right)^{-\Gamma}$. As described in Section 4.1.1, the simulation event energies are drawn from a power law spectrum.

The primary obstacle in spectral reconstruction is to account for the energy-dependent effective area of the detector. Figure 4.17 shows the distribution of reconstructed energies

[17]This is an approximation, and is not the most ideal model. The brightest γ-ray source, the Crab Nebula, emits a spectrum which is better fit by a logarithmic parabolic function. However, in this work, power laws suffice for obtaining important scientific results.

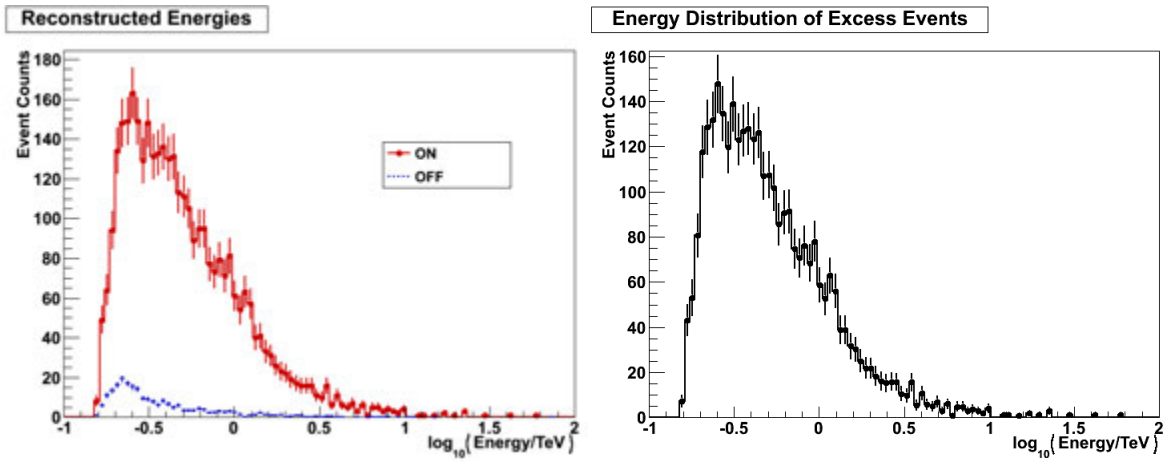

Figure 4.17 *Energy histograms from 6.8 hours of Crab Nebula observations. Left: Distribution of reconstructed energies for events in the ON and OFF regions. OFF distribution was corrected for multiplicity of background rings. Right: Background subtracted distribution of reconstructed energies.*

obtained from the Crab Nebula data sample. The shape of this distribution is determined by three factors: the spectrum of γ-rays incident at the top of the atmosphere, the energy-dependent response of the atmosphere and detector, and the energy resolution of the detector. In order to reconstruct the physical spectrum of γ-rays, it is necessary to account for the latter two effects. This process is referred to as "spectral unfolding," because we are essentially deconvolving or unfolding all detector effects from the γ-ray spectrum.

4.9.1 Calculation of Energy Resolution and Bias

Energy estimation via lookup tables is never perfect. An analysis of a set of monoenergetic, simulated events (using the procedure described in Section 4.7.1) will produce a distribution of reconstructed energies. Figure 4.18 shows a distribution of the the logarithm of the fractional difference between reconstructed and true energies for a set of simulations after standard γ/hadron cuts, fit with a Gaussian[18]. The mean of the distribution is offset from 0, and has a finite width. We refer to the mean as the energy bias, and the width as the energy resolution.

[18]Note from the fit probability that the detector's energy resolution function is not truly Gaussian. For the purpose of modifying effective areas, however, we assume a Gaussian structure to the energy resolution function.

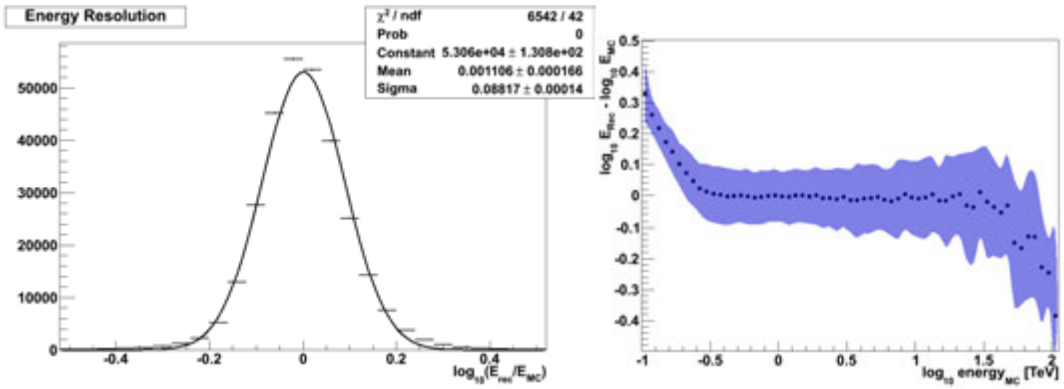

Figure 4.18 *Left: Energy resolution plot for simulations at 20° zenith and 0° azimuth angle, fit with a Gaussian. Right: Energy bias plot, derived from simulations performed at a zenith angle of 20° and azimuth angle of 0°, with a night sky noise level corresponding to a pedestal variance of 6.42 dc. The simulated detector reflects the array after the T1 relocation and trigger upgrade, prior to the camera upgrade. The blue band represents the energy resolution in each particular energy bin, and is not a statistical error.*

Figure 4.18 also shows the energy bias and resolution as a function of energy. The bias is very large at low and high energies, but there is a "sweet spot" between approximately 150 GeV and 30 TeV where the absolute value of the energy bias is less than 20%. The bias itself is corrected by modifying the detector effective area (see Section 4.9.3), however a proper measurement of the energy resolution in each energy bin is crucial to spectral analysis because it tells us the minimum resolvable width of a spectral feature. When binning the final spectrum, flux points should be spaced with a width approximately corresponding to the detector's energy resolution.

4.9.2 Effective Areas

IACT arrays have an energy-dependent effective collection area, or "effective area" which characterizes the efficiency of the detector and the area over which the array is sensitive to γ-rays. The effective area in any simulated energy bin is equal to the number of thrown events in the bin which trigger the array and pass all cuts divided by the number of thrown events in the bin, multiplied by the area on the ground over which simulated events were thrown,

$$A(E_{MC}) = \frac{N_{post-cuts}(E_{MC})}{N_{thrown}(E_{MC})} \cdot \pi R^2_{thrown} \tag{4.4}$$

We typically throw showers over a radius of R_{thrown} = 750m, because this exceeds the array's ability to detect γ-ray events. The trigger criterion accounts for all effects of the atmosphere and detector. Cuts, however, are specific to the source being studied (e.g. an analyst may choose a larger ring size when studying a soft spectrum blazar to contain the low energy events, which have a larger PSF). Therefore it is necessary to produce a new effective area from simulations when choosing a new cut set. Effective area calculations are done from pure γ-ray simulations, and therefore do not account for any effects from the cosmic ray background.

Figure 4.19 shows an effective area derived from simulations performed at a 20° zenith angle and 0° azimuth angle, with a night sky noise level corresponding to a pedestal variance of 6.42 dc. Much like the distribution of reconstructed energies in Figure 4.17, the effective area rises sharply at low energies. The distribution of reconstructed energies from real data is a product of the source spectrum (again, usually a power law of the form $F(E) = F_0 \left(\frac{E}{E_0}\right)^{\Gamma}$) and the detector effective area. The effective area itself is independent of the spectral shape of the observed source, however when generating the curve from simulations, it is nonetheless important to obtain sufficient high-energy statistics to accurately calculate the effective area at these energies. This is another reason for our choice of simulating γ-ray spectra using a power law with a hard spectral index of Γ =-2.0.

4.9.3 Spectral Unfolding

In order to unfold a γ-ray spectrum from the observed distribution of reconstructed energies, we must divide this distribution by the effective area. However, this procedure is complicated by two issues. First, effective areas are derived using true energies from Monte Carlo events, whereas the distribution of energies from observational data is obviously available only in terms of reconstructed energies. This is important because events often migrate between energy bins when being reconstructed. Thus, an event with a true energy in bin i may be reconstructed with a slightly different energy, thus placing it in bin j. Unlike the calculation of true effective area, this effect *is* dependent on the spectral shape of the source being studied. Secondly, while effective areas are derived for a specific combination of zenith angle, azimuth angle, and noise level, each event triggered in real data has a different combination of parameters.

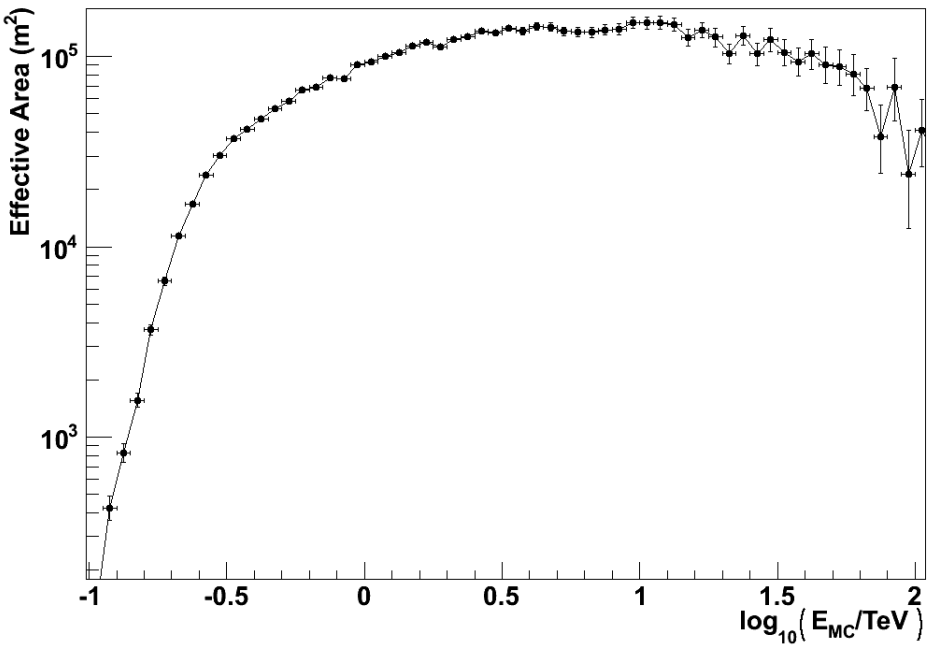

Figure 4.19 *Monte Carlo effective area for simulations produced at 20° zenith angle, 90° azimuth angle, and a noise level corresponding to a pedvar of 5.77 dc.*

To solve the first problem, a modified effective area is created by essentially smearing the distribution of triggered, post-cuts events in each energy bin. During the analysis of real data, the analyst specifies the spectrum of the source being studied. Since most sources are power laws, this is implemented by simply specifying the assumed power law of the source being studied[19]. The simulations are then re-weighted "on the fly" according to the new spectral function. A *migration matrix* M_{ij} is defined to keep track of the number of events in each bin i which migrate into bin j. The distribution of post-cut events from simulations is then transformed into the space of reconstructed energy by smearing each energy bin using the known fraction of mis-reconstructed events in each energy bin, given by the migration matrix. This procedure also corrects for biases in the energy reconstruction. Analysts will often redo the last stage of the analysis and input the spectral index obtained from the first analysis as the assumed spectral index. For power law functions, the measured spectral index should converge

[19]This technique is obviously inadequate for sources with parabolic spectra or exponential cutoffs. Newer versions of VEGAS therefore support the input of non-power law functions.

within two or three iterations of this procedure.

The second problem of spectral unfolding is solved using the same technique employed when estimating energies. While almost no observed events will exactly match the parameter space of simulated zenith angles and noise levels (which are simulated discretely), effective areas can be extracted for the closest zeniths and noise levels, and then interpolated. In principle it is possible to create a single average effective area curve for the data set being analyzed, and then simply divide the excess distribution of reconstructed energies by this curve to obtain the spectrum. In practice, VEGAS creates distributions of $\frac{1}{A_i}$ vs. E_i for both ON and OFF events, where A_i is the effective area for event i and E_i is the reconstructed energy for event i, and the OFF distribution is weighted by α. Each distribution can be thought to represent the "γ-ray flux" of events in the ON and OFF regions, though in reality these intermediate distributions are mathematical tools with no physical meaning. By subtracting these distributions we obtain the spectrum histogram. The flux points themselves are then placed by applying the mean value theorem to the assumed spectral function, as per the method described in Lafferty and Wyatt (1995).

4.9.4 Light Curves

Light curves are an important tool for studying sources with variable emission, such as blazars. A light curve is a plot of source flux as a function of time, and is typically given in terms of Modified Julian Date. During a VEGAS stage 6 analysis, event timestamps, energies, and effective areas are saved to file. The energies and effective areas are used to calculate fluxes in each time bin. Fluxes are corrected for detector deadtime, and can then be plotted as a function of time. The choice of time bin width is chosen by the analyst based on the source's strength. In the case of a source with flux strength equal to 8% of the Crab Nebula flux, it is possible to use bins with as small a width as one day (Acciari et al., 2010).

4.10 Spectral analysis of the Crab Nebula

The VEGAS analysis chain described in this work was applied to the spectral analysis of the Crab Nebula. As mentioned earlier, the Crab Nebula is the calibration candle of all VHE

γ-ray astrophysicists because it provides a strong flux with a very stable spectrum. The Crab Nebula, also referred to as Messier 1, is the remnant of a supernova from the year 1054, and houses a pulsar with a period of 33 milliseconds. Even before the Whipple detection of the Crab in 1989, the observation of polarized radio, optical, and X-ray emission from the nebula confirmed that synchrotron radiation was responsible for the observed emission (Weekes, 1989). The rotational energy of the Crab Pulsar is carried away via a relativistic wind of electrons and positrons; these high energy particles may be accelerated by the pulsar's termination shock and interact with the ambient synchrotron electrons via inverse Compton scattering to produce VHE γ-rays (Aharonian et al., 2006). VERITAS regularly observes the Crab Nebula not only for scientific purposes, but also because these data are useful in calibrating the instrument after new hardware upgrades or when testing new analysis techniques. Here, we derive the VHE γ-ray spectrum of the Crab Nebula's continuum emission and compare to other results in order to demonstrate the reliability of the VEGAS analysis package.

We also derive the Crab Nebula spectrum using data taken specifically from the 2010-2011 observing season using special simulations in order to verify the accuracy of the trigger model used to produce the special Leeds simulations (see Section 4.1.2).

4.10.1 Data Sample

The data sample used for our calibration analysis consists of 6.8 hours of observation after correcting for detector deadtime (no time cuts were applied). Data were taken in the 2011-2012 observing season with all four telescopes in the array. The runlist is shown on table 4.4.

Runs are quality-checked based on nightly diagnostic plots of the Hillas parameters and other variables of interest produced at McGill University, the L3 rates, FIR curves, and observer reports. The 2011-2012 observing season was chosen for this study because all data used here were taken after the L2 trigger upgrade, but prior to the camera upgrade. Therefore the Crab spectrum can be studied without studying effects from the Leeds trigger inefficiency or accounting for any inaccuracies in the detector model used after the camera upgrade[20].

[20]The detector model for the simulations used in the analysis of 2011-2012 data was created in November 2010, and has been studied thoroughly at this point.

Table 4.4 Selected 4-telescope Runs for 2011-2012 Crab Nebula Analysis.

Date	Run	Flasher Run
20111226	59410	59427
20111227	59451	59436
20111229	59521	59534
20111229	59522	59534
20111229	59523	59534
20111230	59562	59561
20111230	59563	59561
20120118	59822	59833
20120118	59823	59833
20120118	59824	59833
20120121	59921	59939
20120219	60434	60454
20120219	60435	60454
20120219	60436	60454
20120219	60438	60454
20120222	60517	60533
20120222	60520	60533
20120222	60521	60533
20120225	60608	60625
20120225	60612	60625
20120225	60613	60625
20120225	60614	60625

4.10.2 Data/Monte Carlo Comparison

Before deriving the spectrum, comparisons were performed between the Crab Nebula data and the OAWG simulations from which the lookup tables and effective areas were produced. The Hillas parameters length, width, and size (defined in Section 4.6) were compared, as were the mean scaled parameters. The simulations are generated with a spectral index of Γ = -2.0, while the spectral index of the VHE emission of the Crab Nebula is approximately Γ =-2.5. Therefore a probability function was used to re-weight the simulations, selectively discarding simulated events so that the final dataset has a spectral index of Γ = -2.5. The simulations consist purely of γ-rays, and it is trivial to generate the necessary parameter distributions. The data, however, consists almost entirely of cosmic rays. This background must be subtracted

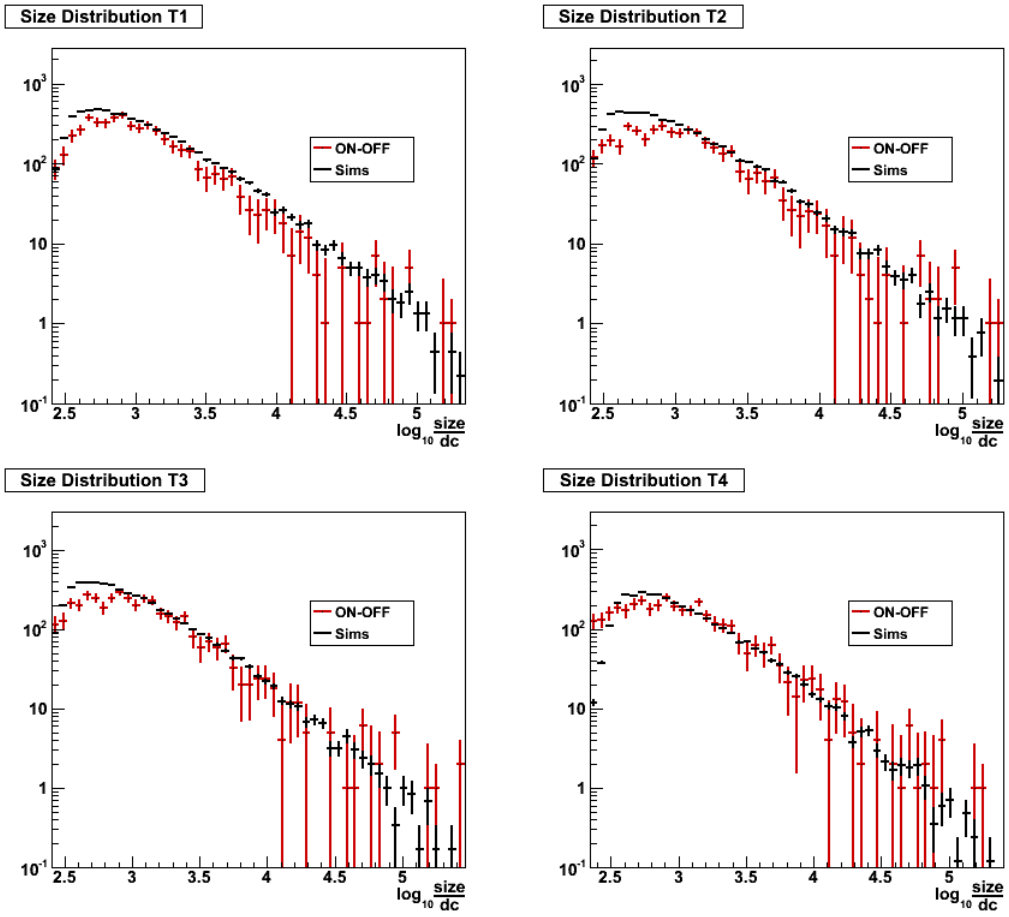

Figure 4.20 *Size distributions from the OAWG simulations and background subtracted Crab Nebula data.*

before doing a data/Monte Carlo comparison.

A simplified wobble analysis was performed on the Crab Nebula data using only one background ring. ON and OFF rings with a more generous radius of 0.13° were used to obtain the source and background data, and the hadronic background was not suppressed. Distributions from data were compared to 20° simulations because this value is closest to the mean zenith angle of the Crab Nebula data sample. Because the simulations contain many more γ-ray events than the excess obtained from the Crab Nebula, simulation distributions were rescaled by integral area. Hillas parameter comparisons are shown in figures 4.20, 4.21, and 4.22. The mean scaled parameters are shown in Figure 4.13.

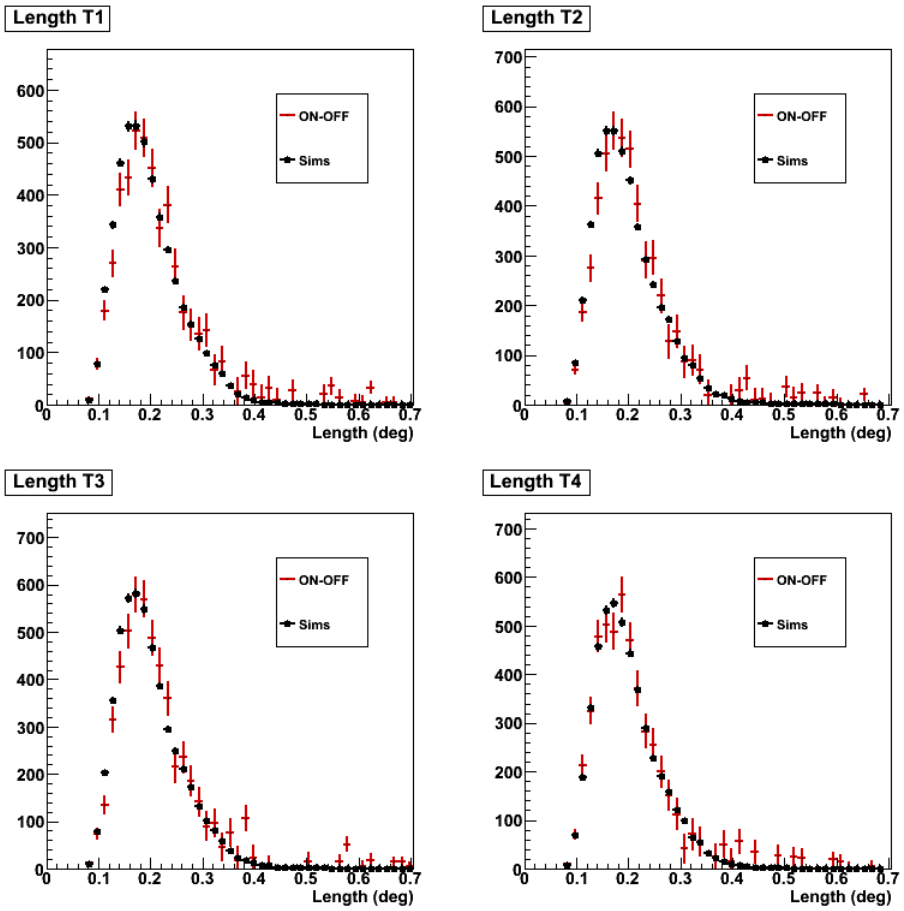

Figure 4.21 *Width distributions from the OAWG simulations and background subtracted Crab Nebula data.*

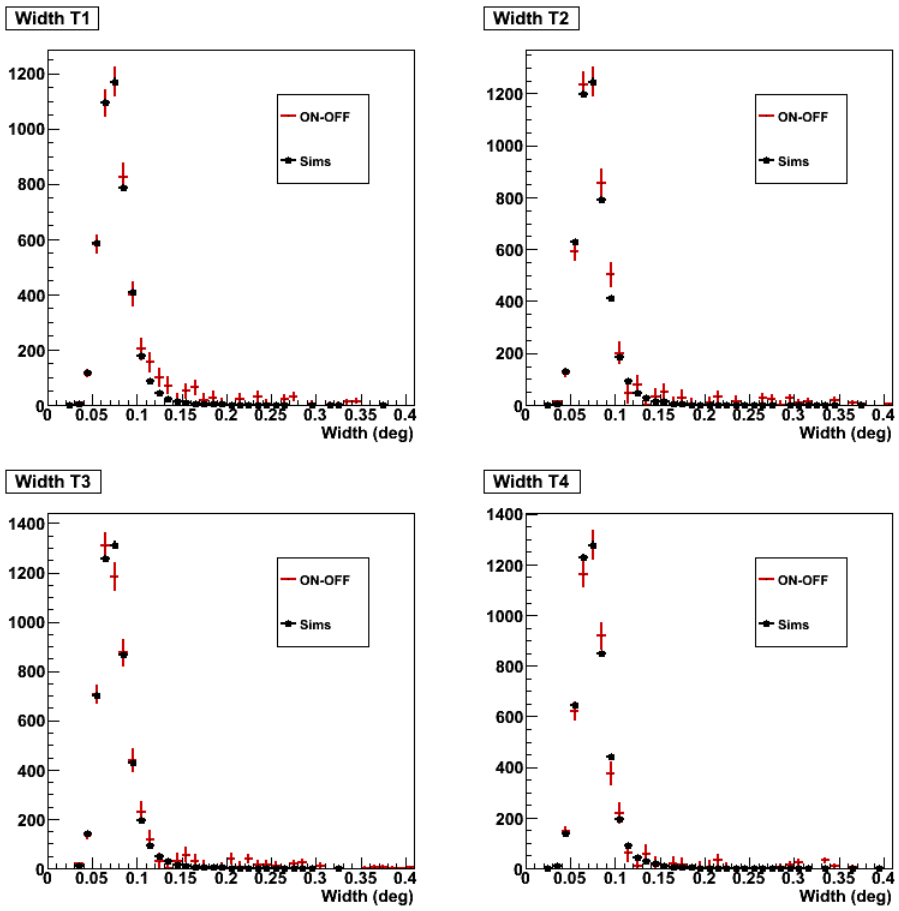

Figure 4.22 *Width distributions from the OAWG simulations and background subtracted Crab Nebula data.*

Table 4.5 Results from the 2011-2012 Crab Nebula Analysis.

ON	3846 events
OFF (total)	1379 events
Significance	95σ
Signal rate	$8.9\pm 0.2\gamma$/min
Background rate	0.6 events/min
Excess	3603.6 events
Exposure time	406.6 min

The simulations resemble the background subtracted data, and demonstrate that the OAWG simulations are a good model of the instrument. Identical plots were produced for the Leeds simulations and compared to a Crab data sample taken with the Leeds trigger. The detector model used for the Leeds simulation is identical to the OAWG model, save for the trigger inefficiency simulation, therefore no greater degree of data/MC disagreement was expected.

4.10.3 Analysis of the 2011-2012 Data Sample

Figure 4.16 shows the distribution of events in squared angular displacement from events with respect to the centers of the ON and OFF rings from the Crab Nebula analysis; events are plotted even outside the ring radius up to a distance of 0.16°, and the OFF distribution is corrected for the multiplicity of background rings. Table 4.5 provides several analysis parameters from the stage 6 sky analysis (note that the OFF counts quoted here are a sum of events in all six rings). VEGAS includes a catalog of bright stars and γ-ray sources, and by default excludes these from all background estimates. Even the observed source itself (in this case the Crab) is excluded out to a radius of 0.4°. Source exclusion is important not only for sky analysis, but also spectral analysis, where the background distribution of reconstructed energies must be evaluated and subtracted without any γ-ray contamination.

4.10.4 Spectrum from the 2011-2012 Data Sample

The spectrum of the Crab Nebula was reconstructed between 220 GeV and 10 TeV. A power law fit gives,

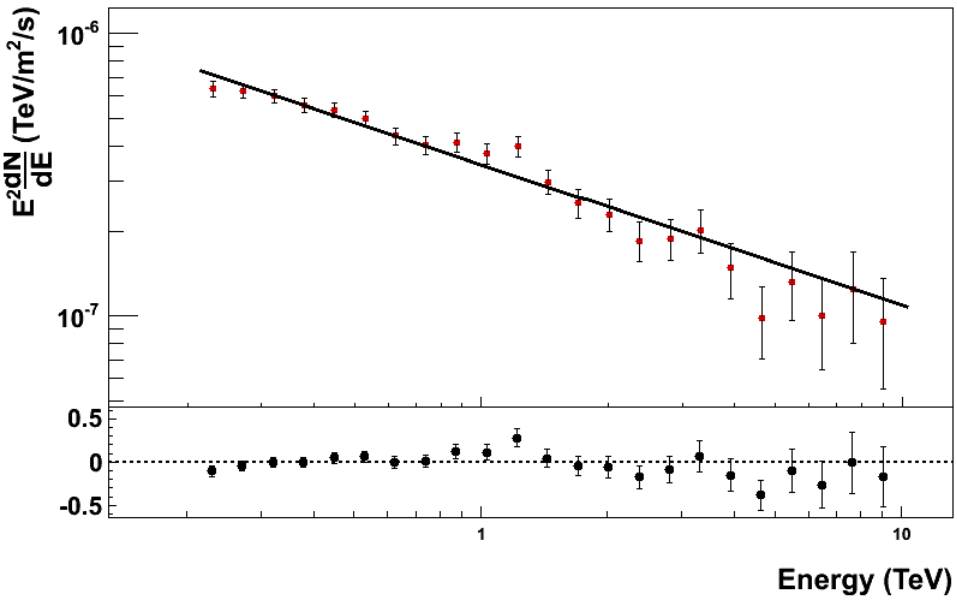

Figure 4.23 *Spectrum of the Crab Nebula from 2011-2012 data taken with the ANL/ISU trigger.*

$$\Phi(\mathrm{E}) = (3.43 \pm 0.08) \cdot 10^{-7} \frac{\mathrm{ph}}{\mathrm{m}^2 \cdot \mathrm{s} \cdot \mathrm{TeV}} \left(\frac{\mathrm{E}}{1\ \mathrm{TeV}} \right)^{-2.50 \pm 0.02} \tag{4.5}$$

This function fits the data with $\chi^2 = 25.48$, and 21 degrees of freedom. This corresponds to a fit probability of 22.7%. The cuts applied in the analysis of both simulations and data are shown in table 4.6. The spectral points from this analysis are provided in table 4.7, with fluxes given in units of ph/m$^2 \cdot$ s $\cdot$ TeV. Figure 4.24 and table 4.8 show the Crab results reported by the Whipple (Mohanty et al., 1998), HESS (Aharonian et al., 2006), and MAGIC collaborations (Zanin et al., 2011). The Whipple collaboration fit their spectrum with a power law of the same form as Equation 4.5. The HESS collaboration fit the Crab spectrum with a function of the form $\Phi(E) = \Phi_0 \left(\frac{E}{1TeV}\right)^{-\Gamma} \cdot e^{-\frac{E}{E_c}}$. The MAGIC collaboration fit their spectrum with a logarithmic parabolic function of the form $\Phi(E) = \Phi_0 \left(\frac{E}{1TeV}\right)^{-\Gamma - \alpha log_{10}\left(\frac{E}{1\mathrm{TeV}}\right)}$. The values of Φ_0 are given in table 4.8 is expressed in units of $10^{-7} \frac{\mathrm{ph}}{\mathrm{m}^2 \cdot \mathrm{s} \cdot \mathrm{TeV}}$, and the cutoff energy E_c is expressed in TeV.

Figure 4.25 shows the multiband γ-ray spectrum of the Crab Nebula from combined Fermi and VERITAS data. The Fermi spectrum (taken from Abdo et al. (2010)) reveals the tail end of the γ-ray synchrotron emission as well as the GeV inverse Compton emission. The

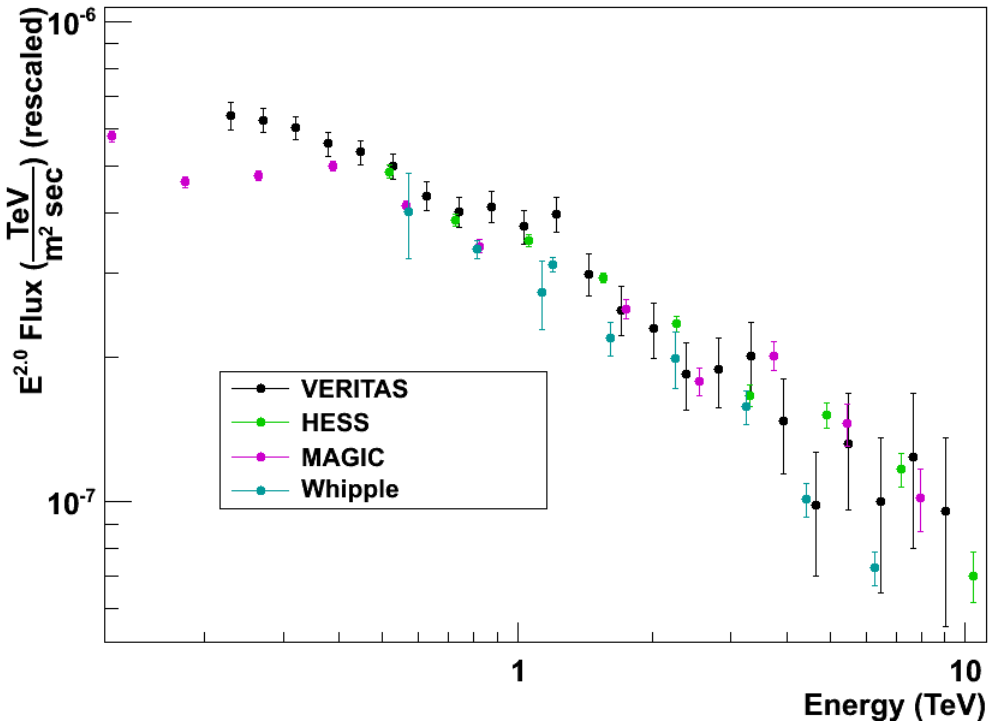

Figure 4.24 *Crab Nebula spectra from the MAGIC (Zanin et al., 2011), HESS (Aharonian et al., 2006), and Whipple (Hillas et al., 1998) experiments are shown along with the spectrum from this work. Fits from publications are shown in table 4.8.*

Table 4.6 Crab Nebula analysis cuts.

Stage 4 quality cuts	size>400 dc	dist<1.43°	ntubes≥5
Stage 6 selection cuts	0.05<MSL<1.3	0.05<MSW<1.15	ring size = 0.1°

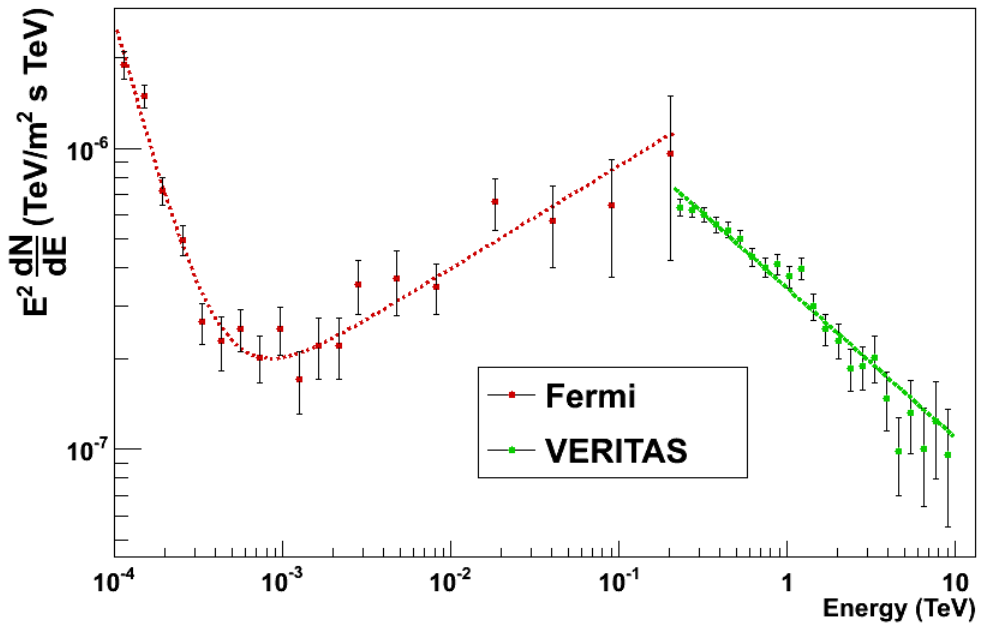

Figure 4.25 *Combined Fermi and VERITAS spectral energy distribution of the Crab. Fermi spectrum has been fit with a double power law between 100 MeV and 300 GeV. Fermi data taken from (Abdo, A.A. et al., 2009).*

Fermi spectrum was fit with a double power law function between 100 MeV and 300 GeV. The synchrotron spectral index is $\Gamma_{sync} = -3.99 \pm 0.12$, and the inverse Compton spectral index is $\Gamma_{IC} = -1.64 \pm 0.05$. Fermi data was taken from (Abdo et al., 2009).

4.10.5 Systematic Uncertainties

Systematic uncertainties were derived on the flux normalization and spectral index of the Crab Nebula. Three sources of systematic uncertainty were considered: throughput, γ/hadron cut efficiency, and the γ-ray PSF of the instrument.

Throughput: The throughput is a product of all photon losses including atmospheric ex-

Table 4.7 Flux Points from Crab Analysis.

Energy (TeV)	Flux	Error on Flux
0.2296	$1.21 \cdot 10^{-5}$	7.97e-7
0.2713	$8.48 \cdot 10^{-6}$	4.9e-7
0.3206	$5.84 \cdot 10^{-6}$	3.25e-7
0.3789	$3.88 \cdot 10^{-6}$	2.22e-7
0.4477	$2.67 \cdot 10^{-6}$	1.56e-7
0.5291	$1.79 \cdot 10^{-6}$	1.09e-7
0.6252	$1.11 \cdot 10^{-6}$	$7.49 \cdot 10^{-8}$
0.7388	$7.37 \cdot 10^{-7}$	$5.32 \cdot 10^{-8}$
0.873	$5.4 \cdot 10^{-7}$	$4.04 \cdot 10^{-8}$
1.032	$3.52 \cdot 10^{-7}$	$2.87 \cdot 10^{-8}$
1.219	$2.68 \cdot 10^{-7}$	$2.2 \cdot 10^{-8}$
1.44	$1.44 \cdot 10^{-7}$	$1.45 \cdot 10^{-8}$
1.702	$8.67 \cdot 10^{-8}$	$1.02 \cdot 10^{-8}$
2.011	$5.67 \cdot 10^{-8}$	$7.45 \cdot 10^{-9}$
2.377	$3.27 \cdot 10^{-8}$	$5.23 \cdot 10^{-9}$
2.809	$2.39 \cdot 10^{-8}$	$3.93 \cdot 10^{-9}$
3.319	$1.83 \cdot 10^{-8}$	$3.18 \cdot 10^{-9}$
3.922	$9.6 \cdot 10^{-9}$	$2.16 \cdot 10^{-9}$
4.634	$4.6 \cdot 10^{-9}$	$1.33 \cdot 10^{-9}$
5.476	$4.42 \cdot 10^{-9}$	$1.21 \cdot 10^{-9}$
6.471	$2.40 \cdot 10^{-9}$	$8.59 \cdot 10^{-10}$
7.647	$2.12 \cdot 10^{-9}$	$7.53 \cdot 10^{-10}$
9.036	$1.17 \cdot 10^{-9}$	$4.95 \cdot 10^{-10}$

tinction of Cherenkov radiation, mirror reflectivity, light cone reflectivity, and PMT quantum efficiency. Incorrect modeling of any of these quantities will contribute to the throughput systematic uncertainty. The *size* parameter scales linearly with light collection. A total throughput uncertainty of 20% was assumed[21], and two additional analyses were performed on the Crab. In each case, the size of all events was scaled up and down (respectively) by a factor of 20% prior to estimating the event energy, and a new spectrum was derived using the same lookup tables and effective areas used in standard analysis.

Cut efficiency: By definition, the peak of the mean scaled length and width parameters

[21] This number is not arbitrary. The OAWG arrives at this value by taking the quadrature sum of the individual uncertainties from each source of photon loss.

Table 4.8 Crab Nebula analysis results from other experiments.

Experiment	Function	Φ_0	Γ	α	E_c
Whipple	Power Law	3.60 ± 0.17	-2.49 ± 0.06	n/a/	n/a
HESS	Exp. Cutoff	3.76 ± 0.07	-2.39 ± 0.03	n/a/	14.3 ± 2.1
MAGIC	Parabolic	3.27 ± 0.03	-2.40 ± 0.01	-0.15 ± 0.01	n/a

Table 4.9 Systematic shifts in spectrum parameters.

	Φ_0 min	Φ_0 max	Γ min	Γ max
Size	2.40	3.96	2.44	2.59
MSL	3.08	3.42	2.49	2.52
MSW	3.06	3.42	2.51	2.52
Ring	3.39	3.45	2.50	2.50

from reconstructed simulations will always occur at 1. Any discrepancy in the data is due to a systematic error in the simulations' ability to model the data. The fractional difference between the peaks of the MSL and MSW parameters and their simulation values was used to arrive at uncertainties in these cut parameters. We arrived at an MSL difference of 5% and an MSW difference of 2.5%. The γ/hadron cuts were varied by these amounts, and four additional analyses were performed.

γ-ray PSF: The ring size used to obtain ON and OFF distributions is chosen based on the PSF of the instrument. In order to calculate the systematic uncertainty in this parameter, a single gaussian function was fit to the θ^2 distribution of the Crab, and the error on the fit was used to vary the ring size in the final stage of the analysis. The ring size was varied by 0.001°, and two additional analyses were performed.

Table 4.9 shows the spectral fit results from each analysis. The value of Φ_0 is given in units of $10^{-7} \frac{ph}{m^2 \cdot sec \cdot TeV}$ The maximum deviation from the standard analysis result is taken to be the systematic uncertainty. We see that the throughput dominates the systematic uncertainty in the spectral fit. The final result for the Crab Nebula spectrum is given by Equation 4.6.

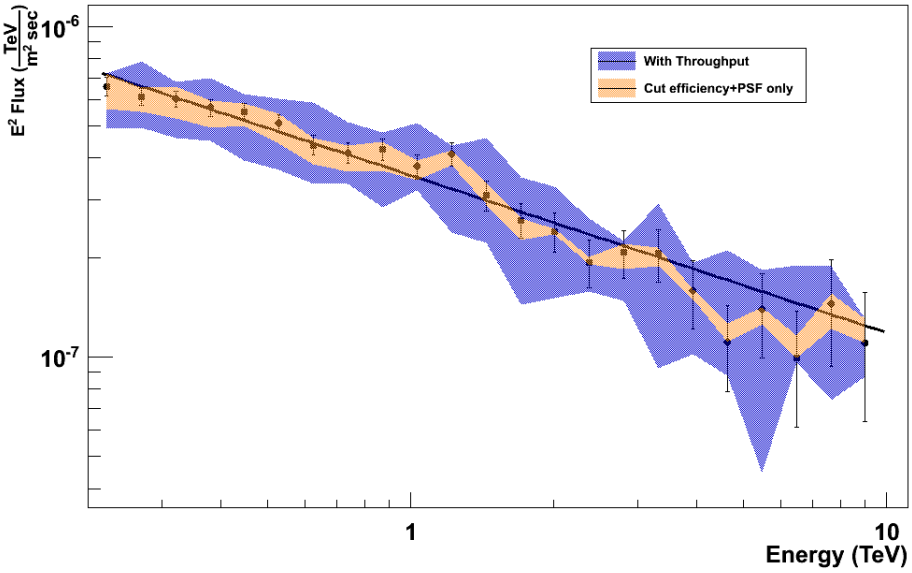

Figure 4.26 *Systematic error band on the spectrum of the Crab Nebula. Simple linear interpretation is used to determine the values on the band between data points. The throughput uncertainty contributes the dominant systematic.*

$$\Phi(\mathrm{E}) = \left(3.43 \pm 0.08_{\mathrm{stat}}\,(+0.53 - 1.03)_{\mathrm{sys}}\right) \cdot 10^{-7} \frac{\mathrm{ph}}{\mathrm{m}^2 \cdot \mathrm{s} \cdot \mathrm{TeV}} \left(\frac{\mathrm{E}}{1\ \mathrm{TeV}}\right)^{-2.50 \pm 0.02_{\mathrm{stat}}(+0.09-0.06)_{\mathrm{sys}}} \tag{4.6}$$

An error band was calculated on a point-by-point basis, and is shown in Figure 4.26.

4.10.6 Soft Cuts Analysis for Low Energy Reconstruction

It is often necessary to study the spectra of γ-ray sources near the VERITAS low-energy threshold. To that end, a set of "soft" cuts is used in spectral reconstruction to derive spectra at lower energies. Here, the size cut is relaxed to 200 dc (400 dc for data taken after the upgrade) in order to accept the smaller images produced by lower energy showers. The ring size used in sky analysis is expanded from 0.1° to 0.1732° in order to collect additional events from lower energy showers, which are often reconstructed at larger angular displacements due to the poorer PSF at low energies. These values are derived by the OAWG using an identical optimization procedure to the one described in Section 4.8.1. Soft cuts analysis accepts additional low energy

Table 4.10 Results from the 2011-2012 Crab Nebula "Soft Cuts" Analysis.

ON	9736 events
OFF (total)	2576.1 events
Significance	94σ
Signal rate	$17.6\pm 0.25\gamma$/min
Background rate	6.3 events/min
Excess	7159.9 events
Exposure time	406.6 min

events at the expense of reducing the analysis sensitivity by introducing additional background events into the analysis[22].

A soft cuts analysis was performed on the Crab Nebula dataset listed in table 4.4. The results of this analysis are listed in table 4.10. Figure 4.27 gives the distribution of events in squared angular displacement, and the spectrum is shown in Figure 4.28

This spectrum is fit by Equation 4.7 with $\chi^2 = 20.86$, and 24 degrees of freedom

$$\Phi(\mathrm{E}) = (3.49 \pm 0.07) \cdot 10^{-7} \frac{\mathrm{ph}}{\mathrm{m}^2 \cdot \mathrm{s} \cdot \mathrm{TeV}} \left(\frac{\mathrm{E}}{1\ \mathrm{TeV}} \right)^{-2.43\pm0.01} \tag{4.7}$$

This result is well within the systematic uncertainties derived earlier, and demonstrates that with a proper understanding systematics, a soft cuts analysis can reproduce the results of standard analysis while reconstructing spectra at lower energies. The analysis spectral points are provided in table 4.11. Fluxes are given in units of $\mathrm{ph/m^2 \cdot s \cdot TeV}$.

4.10.7 Leeds L2 Trigger Inefficiency Correction

In order to test the accuracy of the Leeds L2 simulation model, special simulations were produced and used to analyze Crab Nebula data from the 2010-2011 observing season. The Leeds L2 trigger was in operation during this entire season; the simulations were produced using an array configuration that reflected the T1 relocation of 2009. In order to study the effect of the Leeds inefficiency on the instrument's effective area, a set of 10 million showers were

[22] Because the cosmic ray spectrum obeys a power law with index -2.7, the smaller size cut allows for additional cosmic ray events. A larger ring size will of course allow for more events from the irreducible background

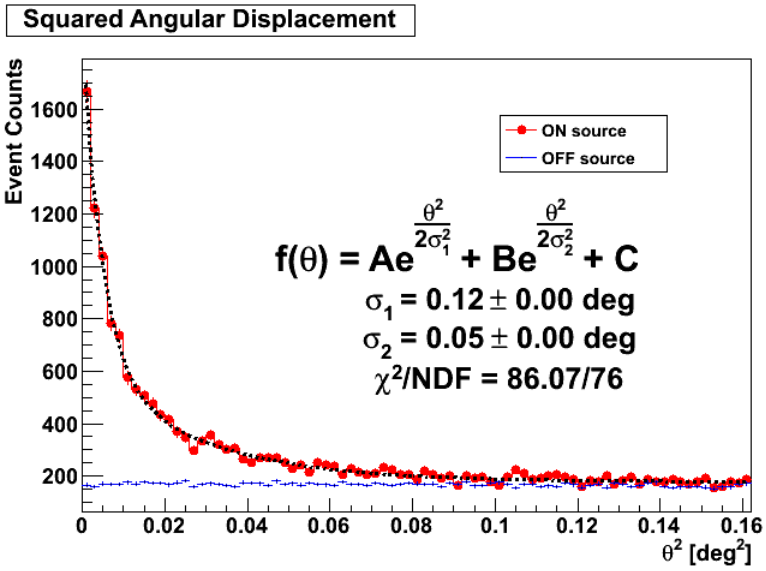

Figure 4.27 *Squared angular distribution of events in the soft cuts Crab Nebula analysis from the 2011-2012 data sample.*

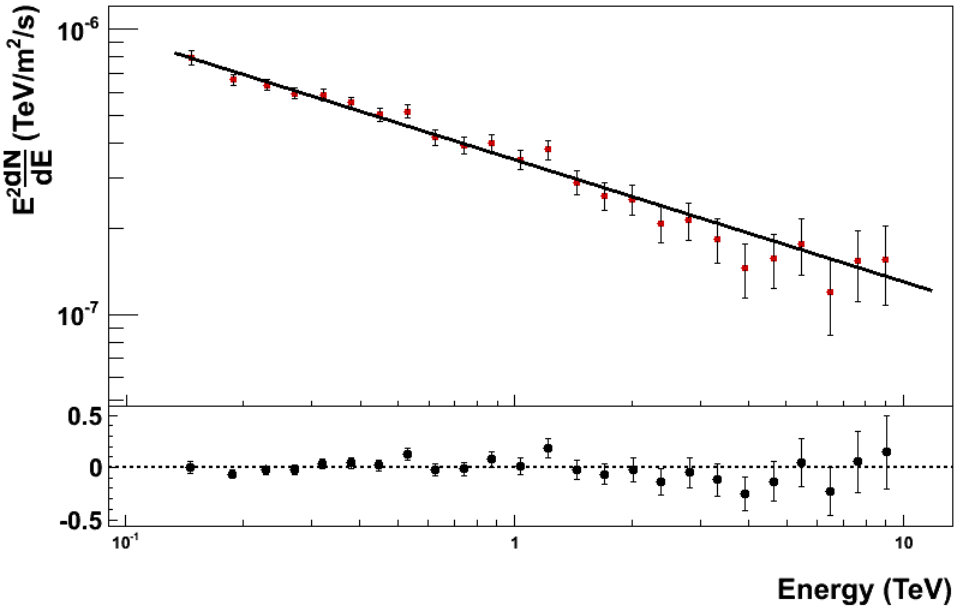

Figure 4.28 *Spectrum of the Crab Nebula from 2011-2012 data taken with the ANL/ISU trigger, analyzed with soft cuts. Notice that the lowest energy flux point is reconstructed at 147 GeV.*

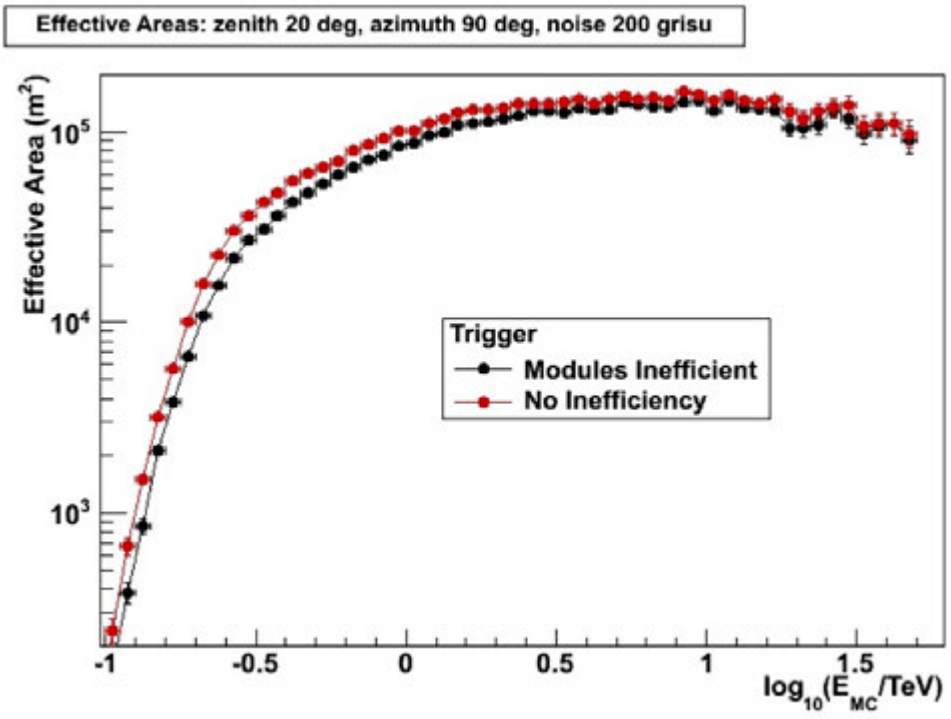

Figure 4.29 *Effective areas derived from detector models using the Leeds (inefficient) and ANL triggers.*

generated at a single zenith angle and azimuth, and simultaneously passed through detector simulations including the Leeds and ANL triggers, respectively.

Figure 4.29 shows effective areas from both trigger configurations. While the Leeds trigger consistently causes a lower effective area, the difference is more pronounced at lower energies. The cause for this effect is the inefficiency pattern[23] shown in Figure 3.26. Small images incident upon the camera, which contain very few sets of three contiguous pixels, may fail the L2 trigger criterion due to the inefficiency. Larger images, on the other hand, will tend to pass the trigger criterion even if certain contiguous CFD triggers fail to pass the L2, because there are many more sets of three contiguous pixels in these images. Therefore, we expect data taken with the Leeds trigger to underestimate the γ-ray flux at low energies. To confirm this, the same 10 million showers used to create the Leeds effective area in Figure 4.29 were analyzed with

[23]The shape of the inefficiency pattern itself is due to the topology of the Leeds L2 trigger, folded with the trigger's module inefficiency.

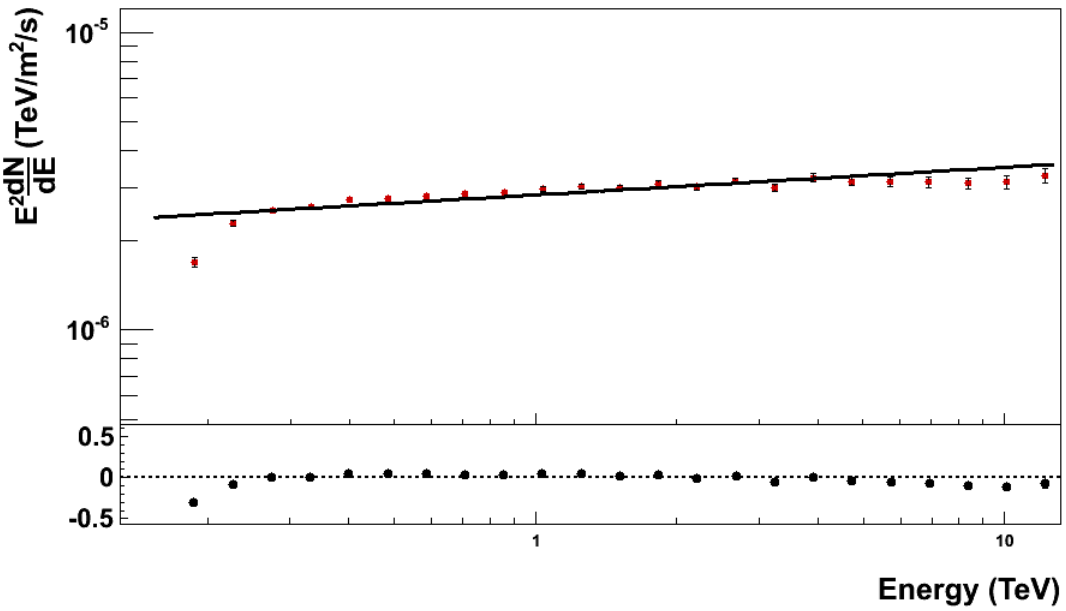

Figure 4.30 *Leeds simulations at 20° zenith angle and 90° azimuth, reconstructed with tables from the OAWG simulations.*

VEGAS, and events were reconstructed with lookup tables and effective areas from the OAWG simulations (which essentially model the ANL trigger).

The reconstructed spectrum from the Leeds simulations is shown in Figure 4.30. Notice that the spectrum is artificially hardened. Although the simulations were generated with a spectral index of Γ = -2.0, the fit to the spectrum gives an index of -1.92 ± 0.01. The ANL simulations were also analyzed; the spectral fit is -2.00 ± 0.01, demonstrating that VEGAS will properly reconstruct a spectrum if the detector model used to produce the lookup tables and effective areas is accurate. We thus expect data taken with the Leeds trigger to exhibit artificial spectral hardening due to an underestimation of low energy fluxes, unless the trigger inefficiency is modeled in the simulations used to produce the lookup tables and effective areas. To that end, Leeds simulations were produced at zenith angles up to 40° with random azimuth, and were analyzed at the same noise levels used to analyze the OAWG simulations. 30 million showers were produced at 0° zenith, and 65 million showers were produced at all other zenith angles[24]. Lookup tables and effective areas were produced, and the 2010-2011 Crab Nebula

[24]This is larger than the number of showers produced by the OAWG. More showers were produced for the

data sample was analyzed.

4.10.8 Spectrum from the 2010-2011 Data Sample

The spectrum of the Crab Nebula was reconstructed between 220 GeV and 10 TeV from Leeds-era data using 8.6 hours of observations. Table 4.12 lists all runs used in the analysis; no time cuts were applied. Event reconstruction and spectral unfolding were performed using the standard OAWG simulations, therefore no correction has been made for the Leeds trigger inefficiency. The spectrum is fit by the power law function given in 4.8 with a χ^2 of 40.4 and 20 degrees of freedom. The result is shown in Figure 4.31.

$$\Phi(\mathrm{E}) = (4.50 \pm 0.08) \cdot 10^{-7} \frac{\mathrm{ph}}{\mathrm{m}^2 \cdot \mathrm{s} \cdot \mathrm{TeV}} \left(\frac{\mathrm{E}}{1\ \mathrm{TeV}} \right)^{-2.34 \pm 0.02} \tag{4.8}$$

As expected based on the spectral analysis of the Leeds simulations, the index of this spectrum is harder than the result from data taken with the ANL/ISU trigger. The dataset was re-analyzed with the lookup tables and effective areas produced from the Leeds simulations. The spectrum is given by the power law in Equation 4.9, which fits the data with a χ^2 of 37.3 and 20 degrees of freedom. The result is shown in Figure 4.31.

$$\Phi(\mathrm{E}) = (4.76 \pm 0.09) \cdot 10^{-7} \frac{\mathrm{ph}}{\mathrm{m}^2 \cdot \mathrm{s} \cdot \mathrm{TeV}} \left(\frac{\mathrm{E}}{1\ \mathrm{TeV}} \right)^{-2.46 \pm 0.02} \tag{4.9}$$

The difference in spectral index between the uncorrected and corrected results is significant. Specifically, modeling the Leeds inefficiency results in an artificial spectral hardening of $\Delta\Gamma = 0.12 \pm 0.028$, corresponding to 4.24σ. It should be noted that the Crab is an especially strong source, and spectral analyses on weaker sources produce spectral fits with larger error bars. Therefore the effect of the Leeds inefficiency is likely to be far less significant on the vast majority of VERITAS spectral analyses. However, the significant hardening in the spectrum of the Crab demonstrates the importance of properly modeling the Leeds trigger. The spectral hardening in the 2010-2011 Crab spectrum is larger than the systematic error on the 2011-2012 Crab spectrum derived from data taken with the ANL/ISU trigger.

Leeds simulations to account for the smaller number of showers which pass the trigger criterion.

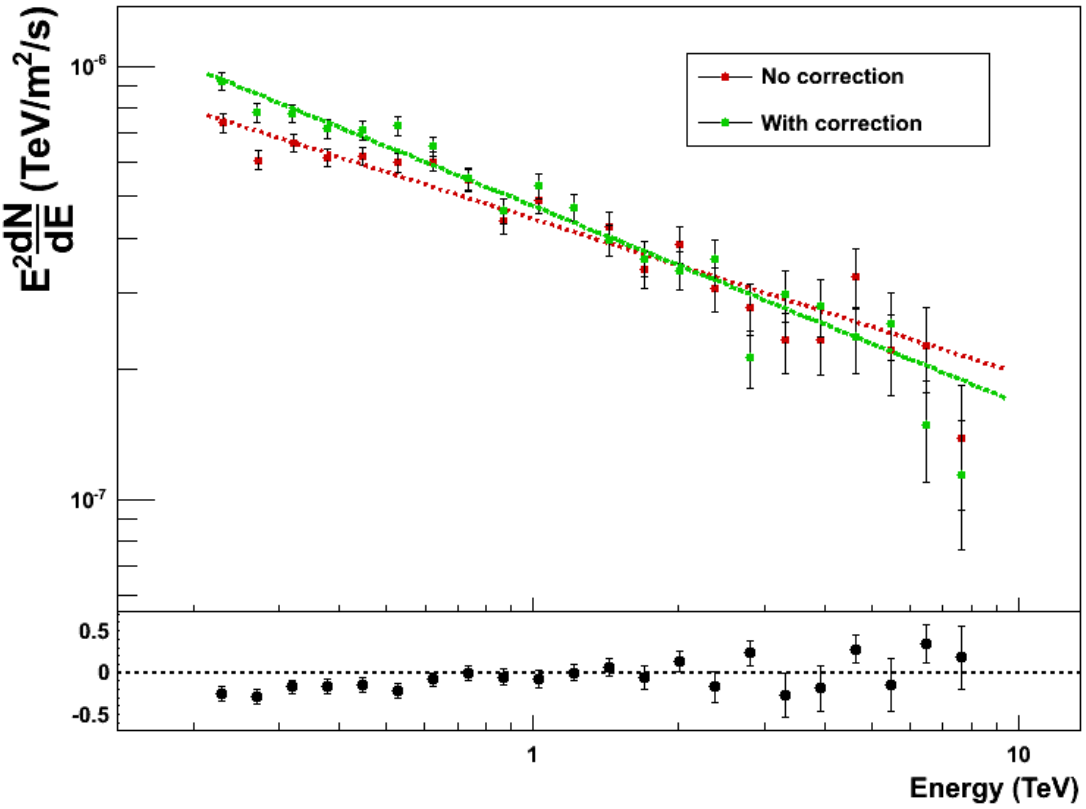

Figure 4.31 *Spectra of the Crab Nebula from 2010-2011 data taken with the Leeds L2 trigger. The spectra were analyzed with both standard simulations, and special Leeds simulations. Note the artificial spectral hardening introduced when spectra are not corrected.*

Table 4.11 Flux Points from "Soft Cuts" Crab Analysis.

Energy (TeV)	Flux	Error on Flux
0.1466	$3.69 \cdot 10^{-5}$	$2.19 \cdot 10^{-6}$
0.1882	$1.88 \cdot 10^{-5}$	$8.21 \cdot 10^{-7}$
0.2296	$1.21 \cdot 10^{-5}$	$5.4 \cdot 10^{-7}$
0.2713	$8.1 \cdot 10^{-6}$	$3.72 \cdot 10^{-7}$
0.3206	$5.73 \cdot 10^{-6}$	$2.66 \cdot 10^{-7}$
0.3789	$3.85 \cdot 10^{-6}$	$1.87 \cdot 10^{-7}$
0.4478	$2.5 \cdot 10^{-6}$	$1.3 \cdot 10^{-7}$
0.5291	$1.84 \cdot 10^{-6}$	$9.73 \cdot 10^{-8}$
0.6252	$1.07 \cdot 10^{-6}$	$6.61 \cdot 10^{-8}$
0.7388	$7.17 \cdot 10^{-7}$	$4.78 \cdot 10^{-8}$
0.873	$5.22 \cdot 10^{-7}$	$3.63 \cdot 10^{-8}$
1.032	$3.28 \cdot 10^{-7}$	$2.58 \cdot 10^{-8}$
1.219	$2.55 \cdot 10^{-7}$	$1.99 \cdot 10^{-8}$
1.441	$1.4 \cdot 10^{-7}$	$1.33 \cdot 10^{-8}$
1.702	$8.99 \cdot 10^{-8}$	$9.8 \cdot 10^{-9}$
2.012	$6.26 \cdot 10^{-8}$	$7.49 \cdot 10^{-9}$
2.377	$3.68 \cdot 10^{-8}$	$5.32 \cdot 10^{-9}$
2.809	$2.71 \cdot 10^{-8}$	$4.1 \cdot 10^{-9}$
3.319	$1.67 \cdot 10^{-8}$	$2.92 \cdot 10^{-9}$
3.922	$9.47 \cdot 10^{-9}$	$2.04 \cdot 10^{-9}$
4.635	$7.31 \cdot 10^{-9}$	$1.57 \cdot 10^{-9}$
5.477	$5.89 \cdot 10^{-9}$	$1.31 \cdot 10^{-9}$
6.472	$2.87 \cdot 10^{-9}$	$8.59 \cdot 10^{-10}$
7.648	$2.63 \cdot 10^{-9}$	$7.37 \cdot 10^{-10}$
9.037	$1.91 \cdot 10^{-9}$	$5.88 \cdot 10^{-10}$
10.68	$1.14 \cdot 10^{-9}$	$4.00 \cdot 10^{-10}$

Table 4.12 Selected Runs for 2010-2011 Crab Nebula Analysis.

Date	Run	Flasher Run
20101007	52390	52371
20101007	52391	52371
20101009	52446	52440
20101009	52447	52440
20101009	52448	52440
20101009	52449	52440
20101009	52450	52440
20101010	52477	52474
20101010	52478	52474
20101010	52479	52474
20101010	52480	52474
20101010	52481	52474
20101011	52507	52495
20101011	52508	52495
20101014	52592	52581
20101014	52593	52581
20101014	52594	52581
20101106	53047	53023
20101106	53048	53023
20101106	53049	53023
20101107	53075	53079
20101108	53109	53103
20101108	53110	53103
20101108	53111	53103
20101108	53112	53103
20101110	53166	53160
20101110	53167	53160
20101110	53168	53160
20101110	53169	53160

CHAPTER 5. SPECTRAL ANALYSIS OF BLAZAR SOURCES

In this section analyses are presented on five blazar sources that have been approved by the VERITAS collaboration for long-term study. The primary objective is to achieve a statistically significant detection of each source, derive its VHE γ-ray spectrum, and look for emission in the optically-thick regime of the EBL. The spectrum of each source is de-absorbed with assumed EBL SEDs. In each case the SEDs of Dominguez et al. (2011) (hereafter referred to as DPR, referring to Dominguez, Primack, and Rosario) and Orr et al. (2011) (hereafter referred to as OKD, referring to Orr, Krennrich, and Dwek) are used. The DPR SED is a reverse evolution EBL model, however, the OKD SED is a "best fit" to observational data.

Great care must be taken when comparing observations from the Fermi satellite with ground-based IACT observations. Whereas Fermi monitors γ-ray sources continuously and produces a single integrated result, IACT observations are taken over considerably shorter time intervals. Because AGNs can exhibit variability, an IACT observation may not reflect the source's mean integrated flux. To account for this, each source's TeV emission was de-absorbed with the OKD SED as well as the 2σ upper and lower bounds on this fit, and the absolute flux of the TeV emission was treated as a free parameter. The GeV and TeV data were then fit with a single, continuous power law function. By treating the absolute flux as a free parameter, we remove the effect of short-term variability from the study of these sources. We do not account for the systematic errors in the VERITAS detector, because this would also require a thorough systematic error analysis of the Fermi instrument.

5.1 1ES1218+304

1ES1218+304 is a high-frequency peaked BL Lac object located at a redshift of $z = 0.182$ (see Acciari et al. (2009b) for the VERITAS detection and Albert et al. (2006) for original MAGIC discovery). The dataset from observations of 1ES1218+304 is very large, with more observation hours taken on this source than any other blazar presented in this work. Data from the analysis presented in Acciari et al. (2010) were included here, as well. 1ES1218+304 is also a very bright source, with a quiescent flux of 8% of the Crab Nebula. Due to the abundance of photon statistics it was possible to reconstruct a spectrum with very small statistical errors, in which the dominant error arises from systematic uncertainty.

5.1.1 Run selection

A total of 126 hours of A/B weather data were taken on 1ES1218+304 between December 2008 and May 2013. 17 hours were removed for reasons including the use of moon filters or reduced high voltage, as well as CFD thresholds different from the nominal values modeled in the OAWG simulations. Also included in these cut hours are 15 runs which were removed due to unloaded L2 pixel delays. A 109 hour dataset remained for analysis. The data sample is given in table 5.1.

5.1.2 Analysis Results

1ES1218+304 was analyzed with standard cuts from the Crab Nebula analysis, as shown in table 4.6. 109.2 hours remain after run selection and time cuts. A total of 3086.7 excess events were detected, corresponding to a statistical significance of 44.1 standard deviations above the background. A number of runs missing telescopes 1, 2, 3, or 4 were included in the analysis, and the appropriate effective areas were derived from simulations. The results from the standard cuts sky analysis are shown in Figure 5.2, and the results from the soft cuts sky analysis are shown in Figure 5.3.

Table 5.1 1ES1218+304 Data Sample.

Season	Exposure Hours	Live Time Hours
2008-2009	34.4	30.3
2009-2010	–	–
2010-2011	34.5	31.1
2011-2012	26.6	26.6
2012-2013	10.4	8.6
Total	109.2	97.0

Table 5.2 Results from the analysis of 1ES1218+304 (**standard cuts**).

ON	6206 events
OFF (total)	3119.3 events
Significance	44.1σ
Signal rate	$0.53\pm 0.01\gamma$/min
Background rate	0.54 events/min
Excess	3086.7 events
Live time	97.0 hours

5.1.3 Spectrum

The spectrum of 1ES1218+304 from a standard cuts analysis was reconstructed between 230 GeV and 4.5 TeV, and is shown in Figure 5.1; the flux points from this analysis are given in table B.1 (fluxes in units of $\mathrm{ph/m^2 \cdot s \cdot TeV}$). The spectrum is fit by the following power-law function,

$$\Phi(\mathrm{E}) = (1.38 \pm 0.07) \cdot 10^{-8} \frac{\mathrm{ph}}{\mathrm{m^2 \cdot s \cdot TeV}} \left(\frac{\mathrm{E}}{1\ \mathrm{TeV}} \right)^{-3.12 \pm 0.05} \tag{5.1}$$

with $\chi^2/\mathrm{N.D.F.} = 26.61/15$. The integral flux of this source from the standard cuts spectrum is 7.8% of the Crab Nebula flux.

The spectrum of 1ES1218+304 from a soft cuts analysis is shown in 5.2; the flux points from this analysis are given in table B.2 (fluxes in units of $\mathrm{ph/m^2 \cdot s \cdot TeV}$). The spectrum is fit by the following power-law function,

Table 5.3 Results from the analysis of 1ES1218+304 (**soft cuts**).

ON	46097 events
OFF (total)	38155.4 events
Significance	36.3σ
Signal rate	$1.36\pm 0.04\gamma$/min
Background rate	6.53 events/min
Excess	7941.6 events
Live time	97.0 hours

$$\Phi(\mathrm{E}) = (1.74 \pm 0.09) \cdot 10^{-8} \frac{\mathrm{ph}}{\mathrm{m}^2 \cdot \mathrm{s} \cdot \mathrm{TeV}} \left(\frac{\mathrm{E}}{1\ \mathrm{TeV}} \right)^{-2.94 \pm 0.05} \tag{5.2}$$

with χ^2/N.D.F. = 32.63/14. The spectrum appears to turn over at ∼230 GeV. A fit above this energy gives a spectral index of Γ = -3.14 ± 0.07. This deviates from the fit over the whole range by 0.2, corresponding to the 2.3σ confidence interval.

5.1.4 EBL De-Absorption

The spectrum of 1ES1218+304 was de-absorbed using EBL SEDs of (Dominguez et al., 2011) and (Orr et al., 2011). The EBL de-absorption from the standard cuts analysis is shown in Figure 5.3, and from the soft cuts analysis is shown in Figure 5.4, and in both cases is compared to the HE spectrum from the Fermi Gamma Ray Space Telescope. Both analyses show the least disagreement in spectral shape between the Fermi spectrum and the de-absorbed VHE spectrum under the assumption of a DPR EBL SED. The spectral indices differ by 0.07, corresponding to a significance of 0.08σ. The standard cuts spectrum was also de-absorbed with the OKD 2σ upper and lower bounds, with the absolute flux being treated as a free parameter. The result is shown in Figure 5.5. The fit to the HE spectrum and fit to the combined HE and VHE spectra differ by 0.1, corresponding to a 1.3σ disagreement between the Fermi spectrum and the joint fit.

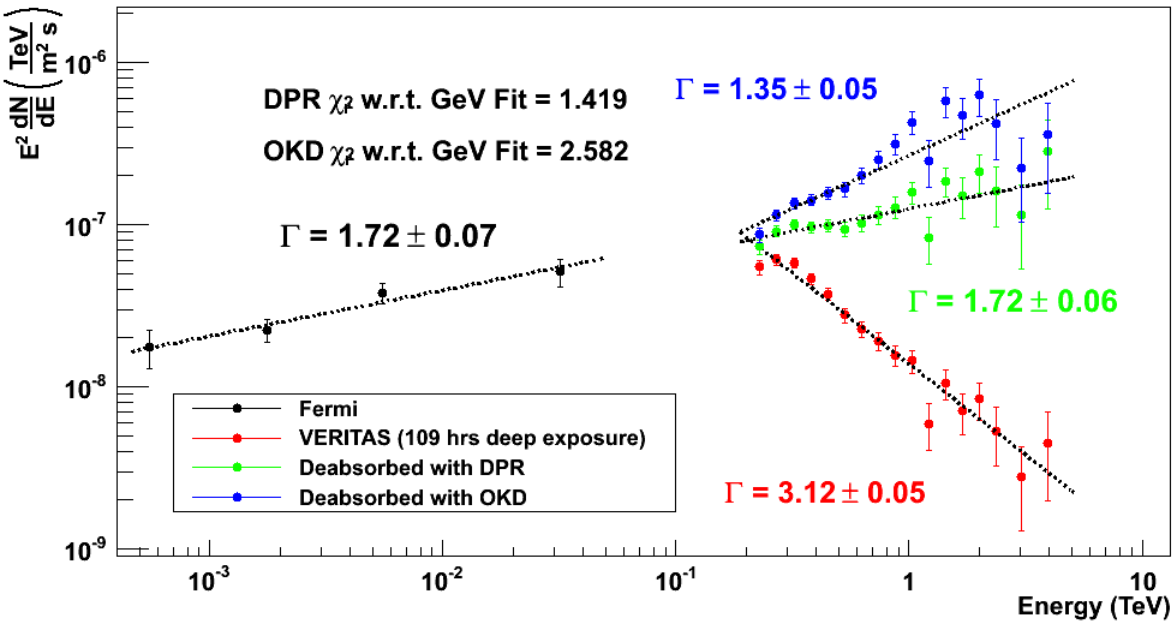

Figure 5.1 *Spectrum of 1ES1218+304. Analyzed with* ***standard cuts****.*

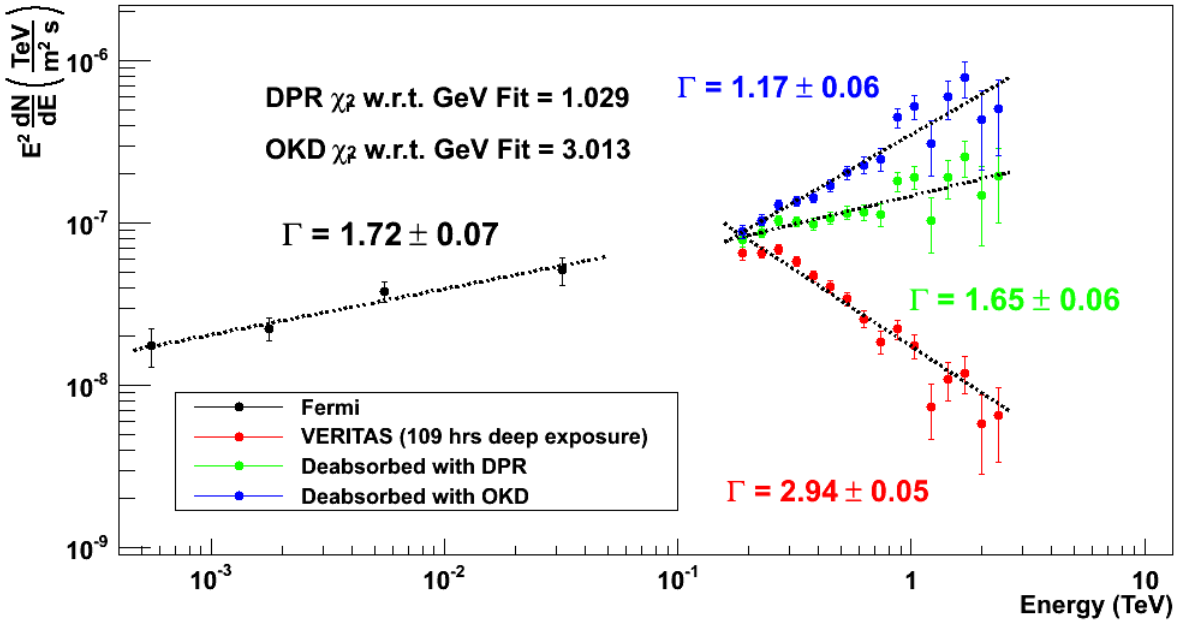

Figure 5.2 *Spectrum of 1ES1218+304. Analyzed with* ***soft cuts****.*

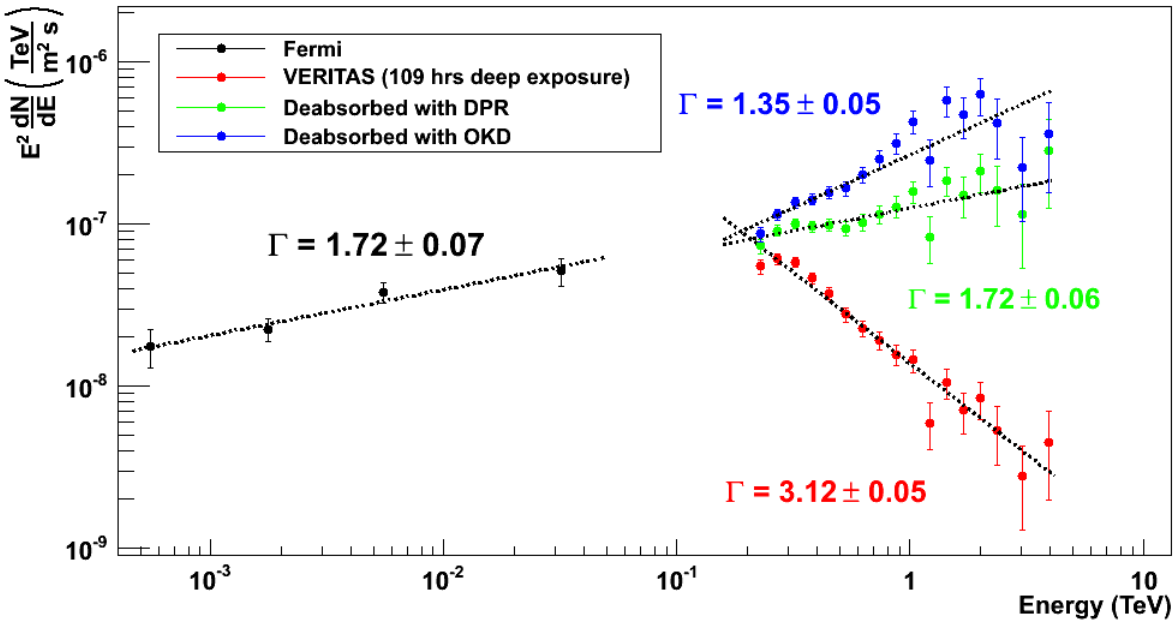

Figure 5.3 *EBL de-absorption of the VHE spectrum of 1ES1218+304 (analyzed with* ***standard cuts****) using the DPR and OKD EBL SEDs.*

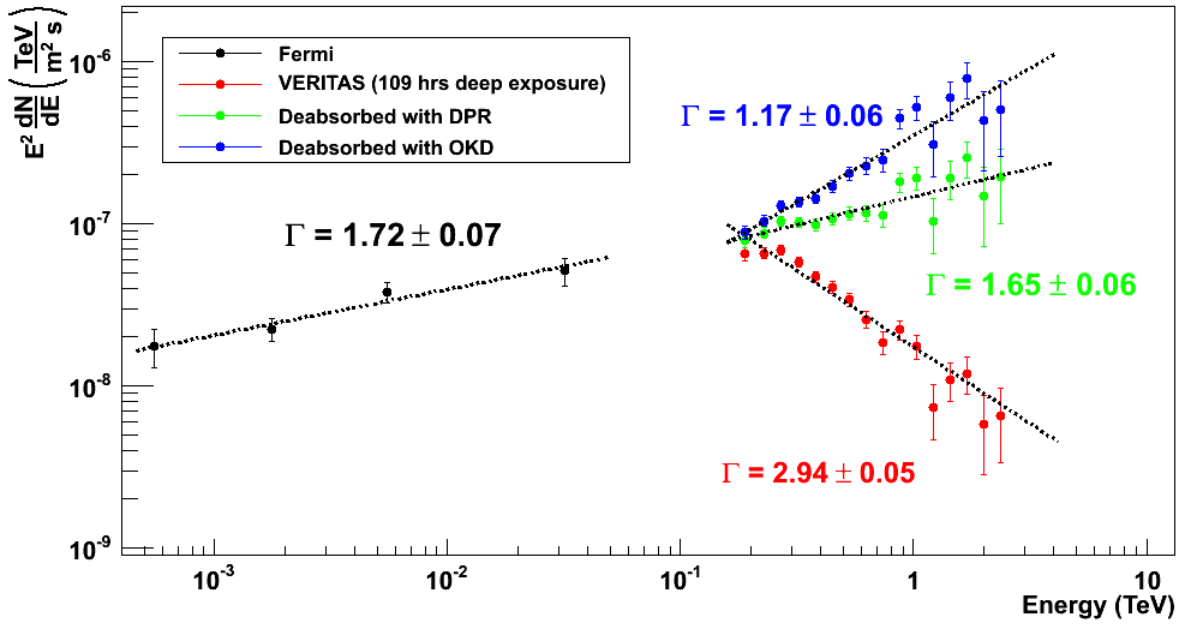

Figure 5.4 *EBL de-absorption of the VHE spectrum of 1ES1218+304 (analyzed with* ***soft cuts****) using the DPR and OKD EBL SEDs.*

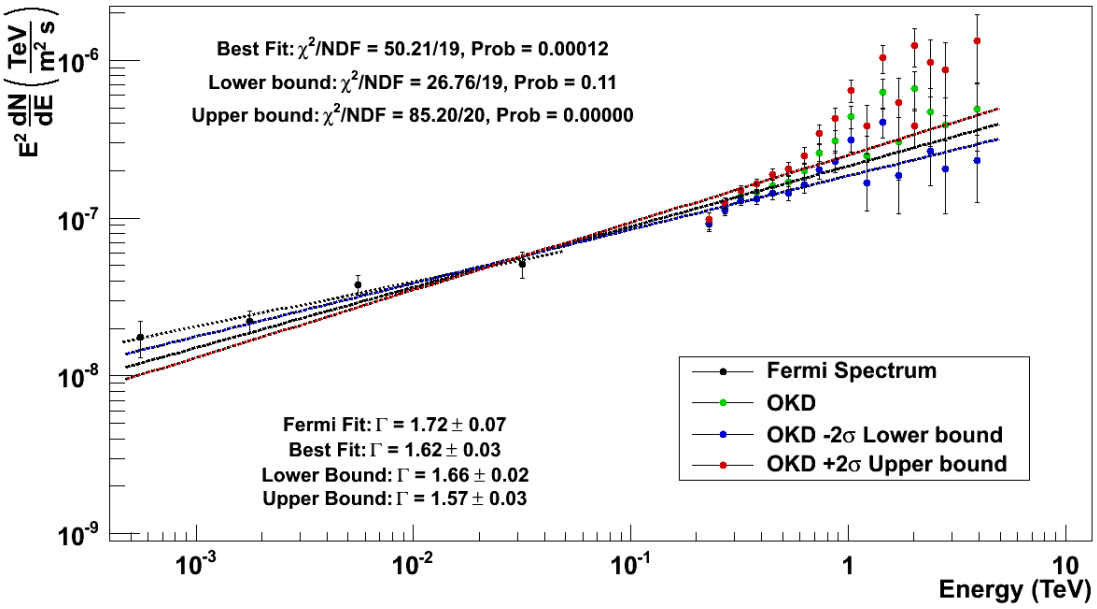

Figure 5.5 *EBL de-absorption of the VHE spectrum of 1ES1218+304 (analyzed with **standard cuts**) in which the VHE spectral points include absolute flux as a free parameter in order to account for possible short term variability.*

5.1.5 Systematics

Table B.3 contains the results of the systematic error analysis on the standard cuts spectrum of 1ES1218+304, with flux normalizations given in units of $10^{-8}\frac{\text{ph}}{\text{m}^2\cdot\text{s}\cdot\text{TeV}}$. Throughput, cut efficiency, and γ-ray PSF were investigated using identical assumptions to those described in Section 4.10.5. As in the case of the Crab analysis, the throughput uncertainty dominates the systematics analysis. However, in order to maintain consistency with the other blazar analyses all errors were added in quadrature. The spectrum is given by Equation 5.3.

The error band derived from these analyses is shown in Figure 5.6. Here, systematic errors were calculated point-by-point, and contributions from each source of systematic uncertainty was added in quadrature.

$$\Phi(E) = \left(1.38 \pm 0.08_{stat}\,(+0.74 - 0.49)_{sys}\right)\cdot 10^{-8}\frac{\text{ph}}{\text{m}^2\cdot\text{s}\cdot\text{TeV}}\left(\frac{E}{1\ \text{TeV}}\right)^{-3.13\pm 0.05_{stat}(+0.21-0.07)_{sys}} \tag{5.3}$$

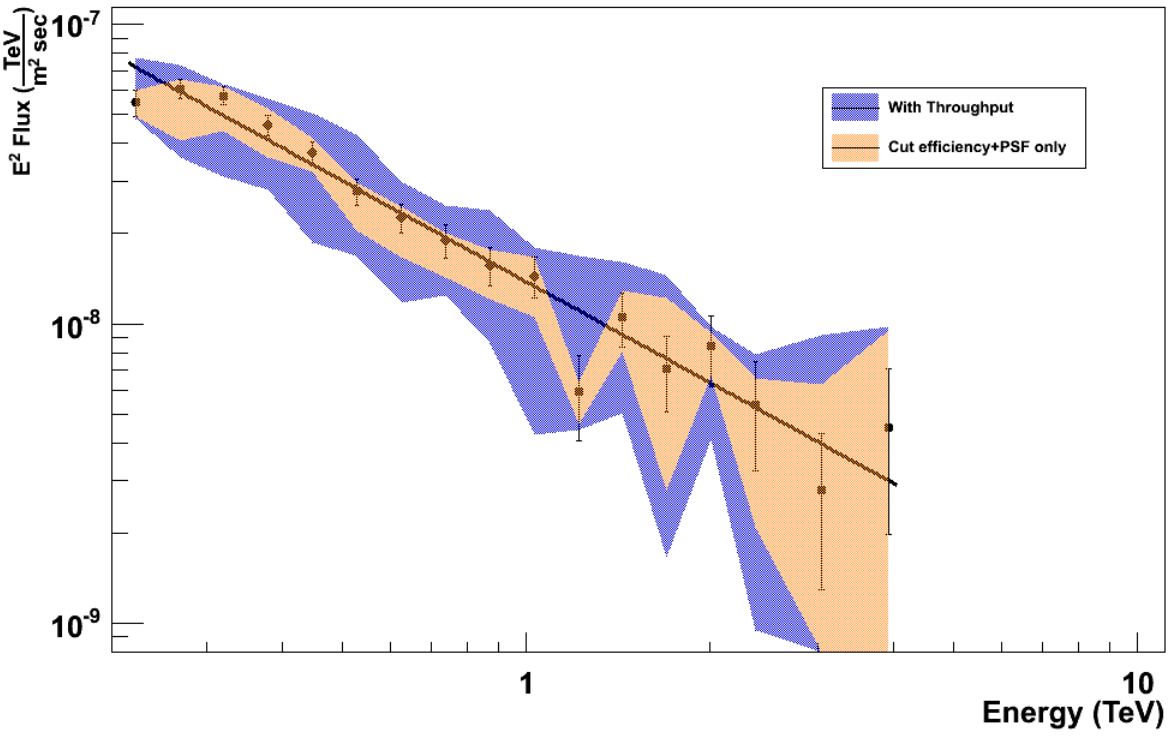

Figure 5.6 *Systematic error band on the spectrum of 1ES1218+304. Error bars are statistical.*

Table 5.4 Results of systematics analysis on 1ES1218+304.

	Φ_0 min	Φ_0 max	Γ min	Γ max	$\Delta\Phi$ min	$\Delta\Phi$ max	$\Delta\Gamma$ min	$\Delta\Gamma$ max
Size	0.79	1.87	3.06	3.31	0.61	.47	0.07	0.18
MSL	1.13	1.30	3.14	3.16	0.27	–	–	0.03
MSW	1.11	1.27	3.16	3.20	–	–	–	0.07
Ring	1.36	1.39	3.14	3.14	0.04	–	–	0.01
Q-Sum					0.66	.47	0.07	0.20

5.1.6 Comparison to Flare Analysis

Acciari et al. (2010) presents an analysis of the time averaged spectrum of 1ES1218+304 from the 2008-2009 dataset, consisting of 27 hours of exposure time. This spectrum[1] is compared to the deep exposure presented in this work. Comparisons to the standard and soft cuts analyses are shown, respectively, in Figure 5.7 and 5.8. The spectrum from standard cuts agrees well with the Acciari et al. (2010) result. The soft cuts spectrum disagrees by a spectral index difference of 0.22 at the 2.1σ confidence interval. This is due to the apparent low energy turnover at ∼189 GeV. The fit above 230 GeV gives a spectral index of Γ = -3.14±0.07, in good agreement with the standard cuts and Acciari et al. (2010) results.

5.2 1ES0229+200

1ES0229+200 is high-frequency peaked BL Lac object located at a redshift of $z = 0.14$, and Aliu et al. (2013a) describes an analysis of 54.3 livetime-corrected hours of earlier VERITAS observations. These data are included in the analysis presented in this work, as are new data including 6 livetime-corrected hours of observations taken with the upgraded VERITAS II cameras.

5.2.1 Run selection

A total of 77.9 hours of A/B weather data were taken on 1ES0229+200 between October 2009 and January 2013. 7.7 hours were removed for reasons including the use of reduced high

[1]Spectral points obtained from Imran (2010)

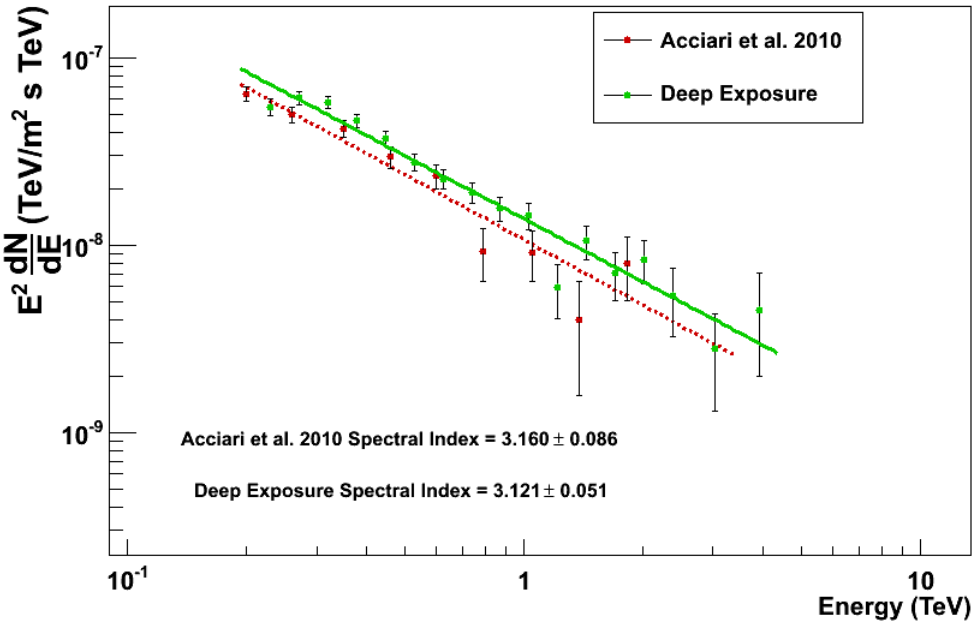

Figure 5.7 *Comparison of Acciari et al. (2010) to* ***standard cuts*** *analysis of 1ES1218+304. Additional exposure time provides for smaller statistical errors and spectral reconstruction to higher energies.*

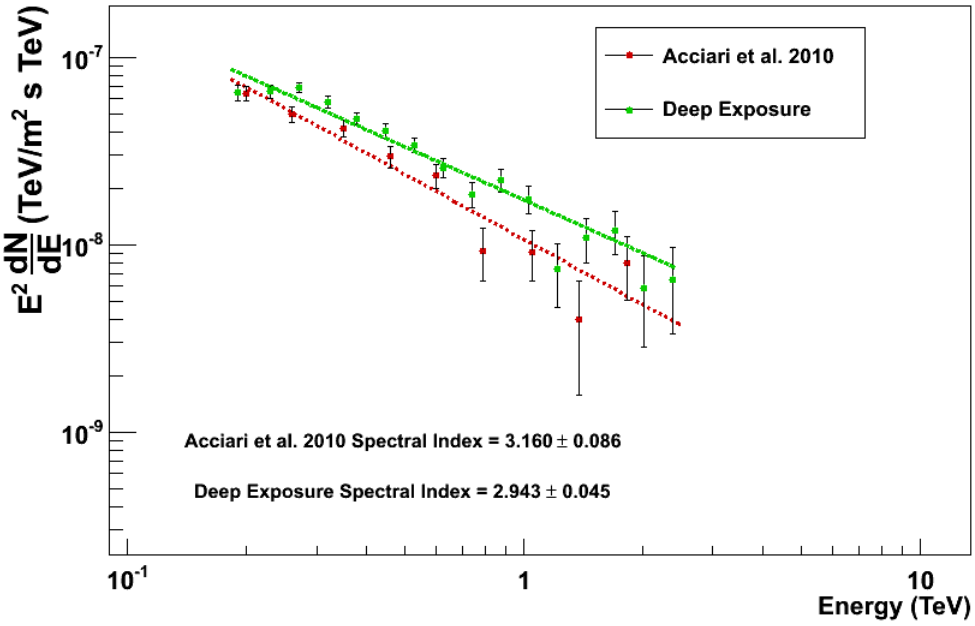

Figure 5.8 *Comparison of Acciari et al. (2010) to* ***soft cuts*** *analysis of 1ES1218+304. The choice of cuts allows for spectral reconstruction at slightly lower energies. Although the spectrum appears to turn over below 200 GeV, it should be noted that the soft cuts analysis is still consistent with the standard cuts spectrum to within the systematic errors.*

Table 5.5 1ES0229+200 Data Sample.

Season	Exposure Hours	Live Time Hours
2009-2010	31.9	27.9
2010-2011	20.2	18.0
2011-2012	10.8	9.2
2012-2013	7.2	6.0
Total	70.2	61.1

Table 5.6 Results from the analysis of 1ES0229+200 (**standard cuts**).

ON	3152 events
OFF (total)	2649.3 events
Significance	8.7σ
Signal rate	$0.14\pm 0.02\gamma$/min
Background rate	0.72 events/min
Excess	502.7 events
Live time	61.1 hours

voltage or CFD thresholds different from the nominal values modeled in the OAWG simulations. A 70.2 hour dataset remained for analysis. The data sample is given in table 5.5.

5.2.2 Analysis Results

1ES0229+200 was analyzed with standard cuts from the Crab Nebula analysis, as shown in table 4.6. 29.4 hours remain after deadtime correction and time cuts. With standard cuts, a total of 502.7 excess events were detected, corresponding to a statistical significance of 8.7 standard deviations above the background. The soft cuts analysis results in 758.8 excess events, with a statistical significance of 6.5 standard deviations above the background. Distributions of events in squared angular displacement, from standard and soft cuts, are given in figures 5.9 and 5.10.

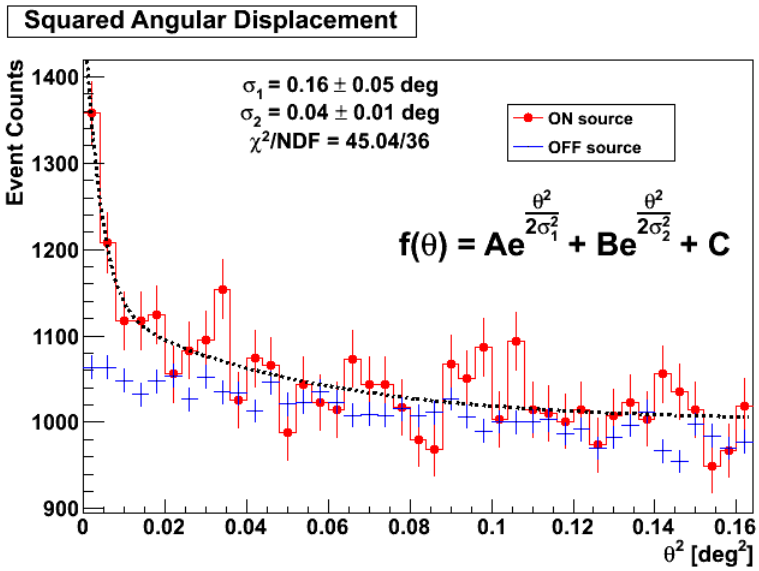

Figure 5.9 *Distribution of events in squared angular displacement from* ***standard cuts*** *analysis of 1ES0229+200.*

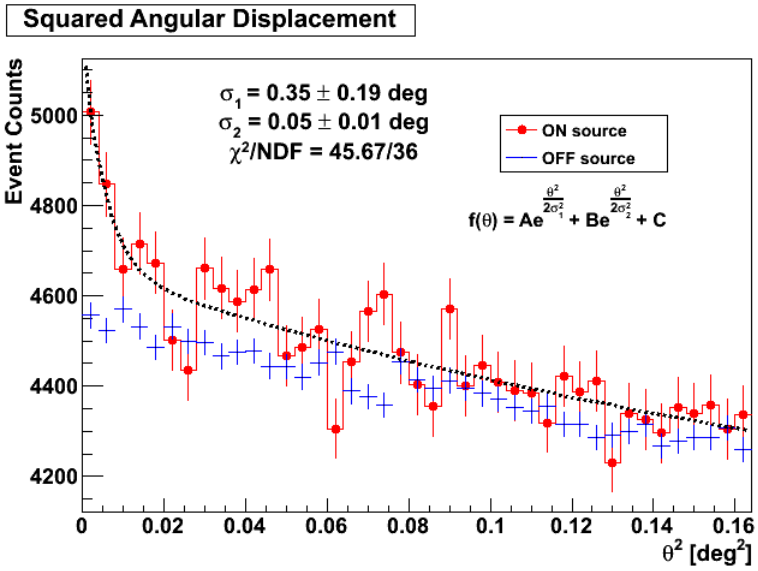

Figure 5.10 *Distribution of events in squared angular displacement from* ***soft cuts*** *analysis of 1ES0229+200.*

Table 5.7 Results from the analysis of 1ES0229+200 (**soft cuts**).

ON	12126 events
OFF (total)	11367.2 events
Significance	6.5σ
Signal rate	$0.21\pm 0.03\gamma$/min
Background rate	3.1 events/min
Excess	758.8 events
Live time	61.1 hours

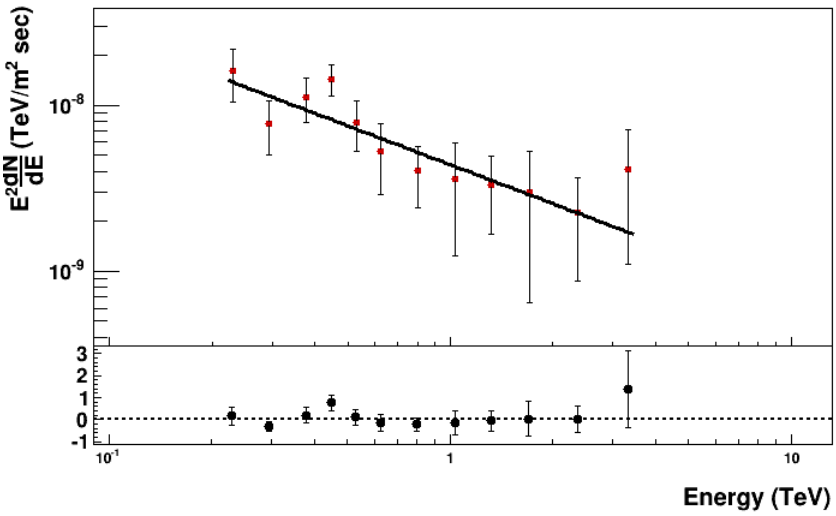

Figure 5.11 *Spectrum of 1ES0229+200 derived from a **standard cuts** analysis.*

5.2.3 Spectrum

The spectrum of 1ES0229+200 from an analysis with standard cuts was reconstructed between 230 GeV and 3.3 TeV, and is shown in Figure 5.11. The flux points from this analysis are given in table B.4. The spectrum is fit by the following power-law function,

$$\Phi(\mathrm{E}) = (4.38 \pm 0.74) \cdot 10^{-9} \frac{\mathrm{ph}}{\mathrm{m}^2 \cdot \mathrm{s} \cdot \mathrm{TeV}} \left(\frac{\mathrm{E}}{1\ \mathrm{TeV}} \right)^{-2.78\pm0.19} \tag{5.4}$$

with $\chi^2/\mathrm{N.D.F.} = 7.96/10$. The integral flux of this source from the standard cuts spectrum is 1.7% of the Crab Nebula flux.

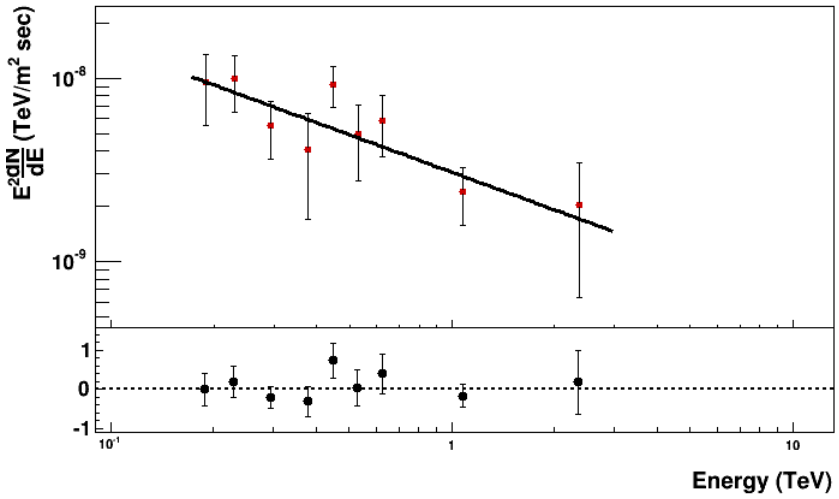

Figure 5.12 *Spectrum of 1ES0229+200. Analyzed with* ***soft cuts****.*

The spectrum of 1ES0229+200 from a soft cuts analysis was reconstructed between 190 GeV and 2.3 TeV, and is shown in 5.12; the flux points from this analysis are given in table B.5 (fluxes in units of ph/m$^2 \cdot$ s $\cdot$ TeV). The spectrum is fit by the following power-law function,

$$\Phi(\mathrm{E}) = (3.06 \pm 0.65) \cdot 10^{-9} \frac{\mathrm{ph}}{\mathrm{m}^2 \cdot \mathrm{s} \cdot \mathrm{TeV}} \left(\frac{\mathrm{E}}{1\ \mathrm{TeV}} \right)^{-2.68 \pm 0.20} \tag{5.5}$$

with χ^2/N.D.F. = 5.31/7.

5.2.4 EBL De-Absorption

The spectrum of 1ES0229+200 was de-absorbed using the DPR and OKD SEDs. The EBL de-absorption from the standard cuts analysis is shown in Figure 5.14, and from the soft cuts analysis is shown in Figure 5.14, and in both cases is compared to the HE spectrum from the Fermi Gamma Ray Space Telescope. Both analyses show the least disagreement in spectral shape between the Fermi spectrum and the de-absorbed VHE spectrum under the assumption of an OKD EBL SED. The spectral shapes differ by an index of 0.06, corresponding to a 0.2σ statistical significance. The standard cuts spectrum was also de-absorbed with the OKD 2σ upper and lower bounds, with the absolute flux being treated as a free parameter. The result is shown in Figure 5.15. The fit to the HE spectrum and fit to the combined HE and VHE

Table 5.8 Flux Points from 1ES0229+200 **soft cuts** analysis.

Energy (TeV)	Flux	Error on Flux
0.1892	2.66e-07	1.11e-07
0.2294	1.89e-07	6.43e-08
0.2937	6.42e-08	2.23e-08
0.3786	2.83e-08	1.65e-08
0.4475	4.61e-08	1.17e-08
0.5288	1.77e-08	7.86e-09
0.6248	1.51e-08	5.56e-09
1.079	2.07e-09	7.20e-10
2.354	3.67e-10	2.52e-10

spectra differ by 0.01, corresponding to a 0.04σ disagreement between the Fermi spectrum and the joint fit.

5.2.5 Systematics

Table B.6 contains the results of the systematic error analysis on the standard cuts spectrum of 1ES0229+200, with flux normalizations given in units of $10^{-9}\frac{\text{ph}}{\text{m}^2\cdot\text{s}\cdot\text{TeV}}$. Throughput, cut efficiency, and γ-ray PSF were investigated using identical assumptions to those described in Section 4.10.5. Errors from all analyses performed in the systematics study are added in quadrature. The spectrum is given by Equation 5.6

The error band derived from these analyses is shown in Figure 5.16. Here, systematic errors were calculated point-by-point, and contributions from each source of systematic uncertainty was added in quadrature.

$$\Phi(E) = \left(4.38 \pm 0.74_{stat}\,(+0.50 - 1.41)_{sys}\right)\cdot 10^{-8}\frac{\text{ph}}{\text{m}^2\cdot\text{s}\cdot\text{TeV}}\left(\frac{E}{1\text{ TeV}}\right)^{-2.78\pm 0.19_{stat}(+0.14-0.02)_{sys}} \tag{5.6}$$

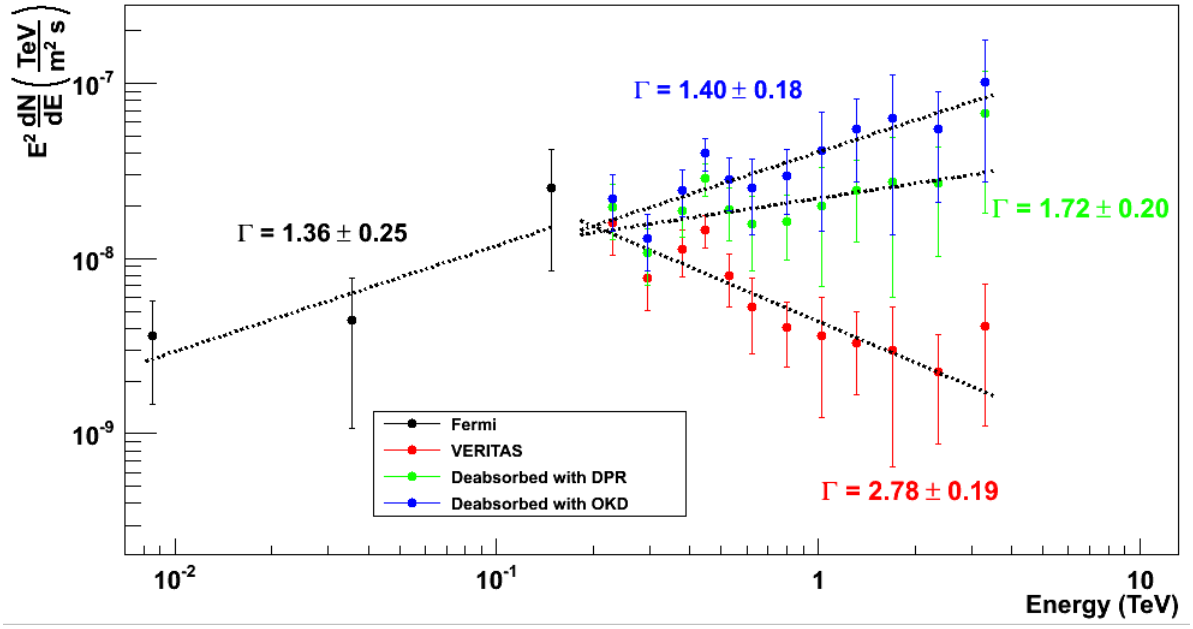

Figure 5.13 *EBL de-absorption of the VHE spectrum of 1ES0229+200 (analyzed with* ***standard cuts****) using the DPR and OKD EBL SEDs.*

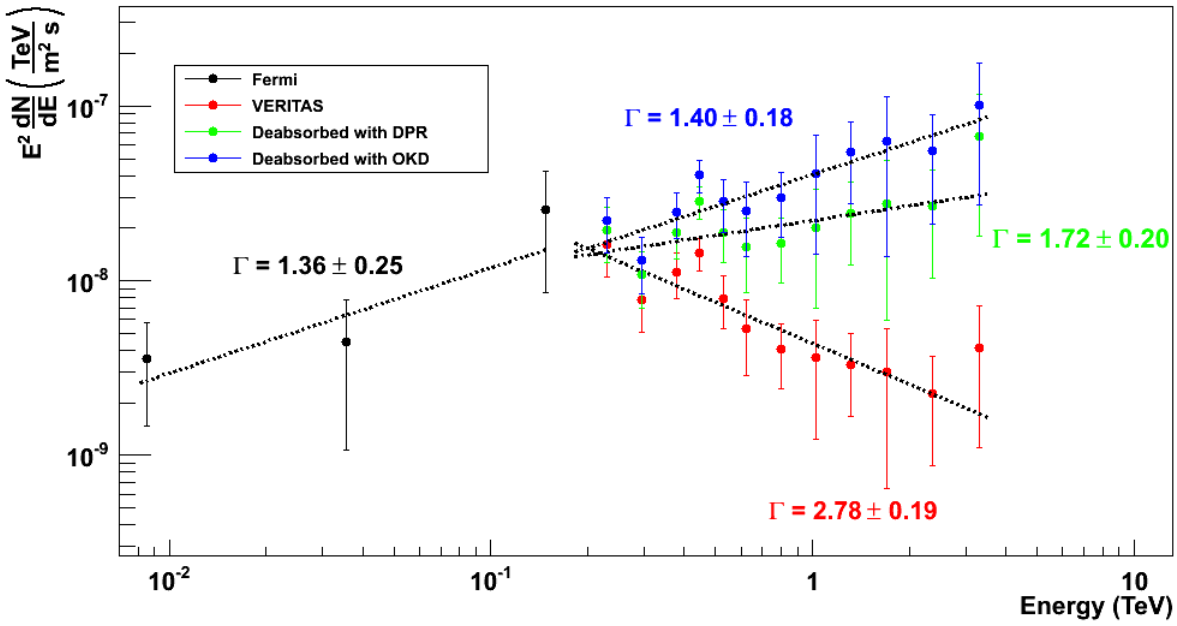

Figure 5.14 *EBL de-absorption of the VHE spectrum of 1ES0229+200 (analyzed with* ***soft cuts****) using the DPR and OKD EBL SEDs.*

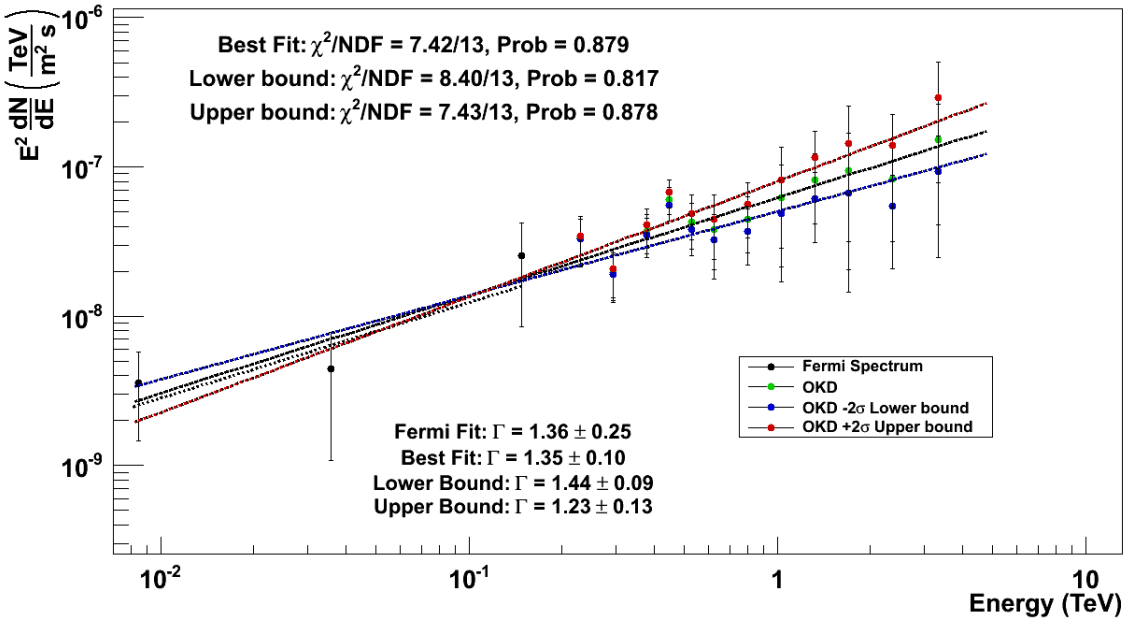

Figure 5.15 *EBL de-absorption of the VHE spectrum of 1ES0229+200 (analyzed with **standard cuts**) in which the VHE spectral points include absolute flux as a free parameter in order to account for possible short term variability.*

5.3 H1426+428

H1426+428 is a hard-spectrum blazar with a redshift of $z = 0.129$. This source was observed by Whipple; an analysis by Petry et al. (2002) found that the VHE spectrum of H1426+428 obeyed a power law with a spectral index of Γ = -3.50 ± 0.35. The analysis presented in this work shows a much harder spectrum with an index between approximately -2.5 and -2.7.

5.3.1 Run selection

A total of 36 hours of A/B weather data were taken on H1426+428 between March 2009 and June 2013. 4 hours were removed for reasons including the use of moon filters or reduced high voltage, as well as CFD thresholds different from the nominal values modeled in the OAWG simulations. 6 runs were removed due to unloaded L2 pixel delays. A 31.8 hour dataset remained for analysis. The data sample is given in table 5.9.

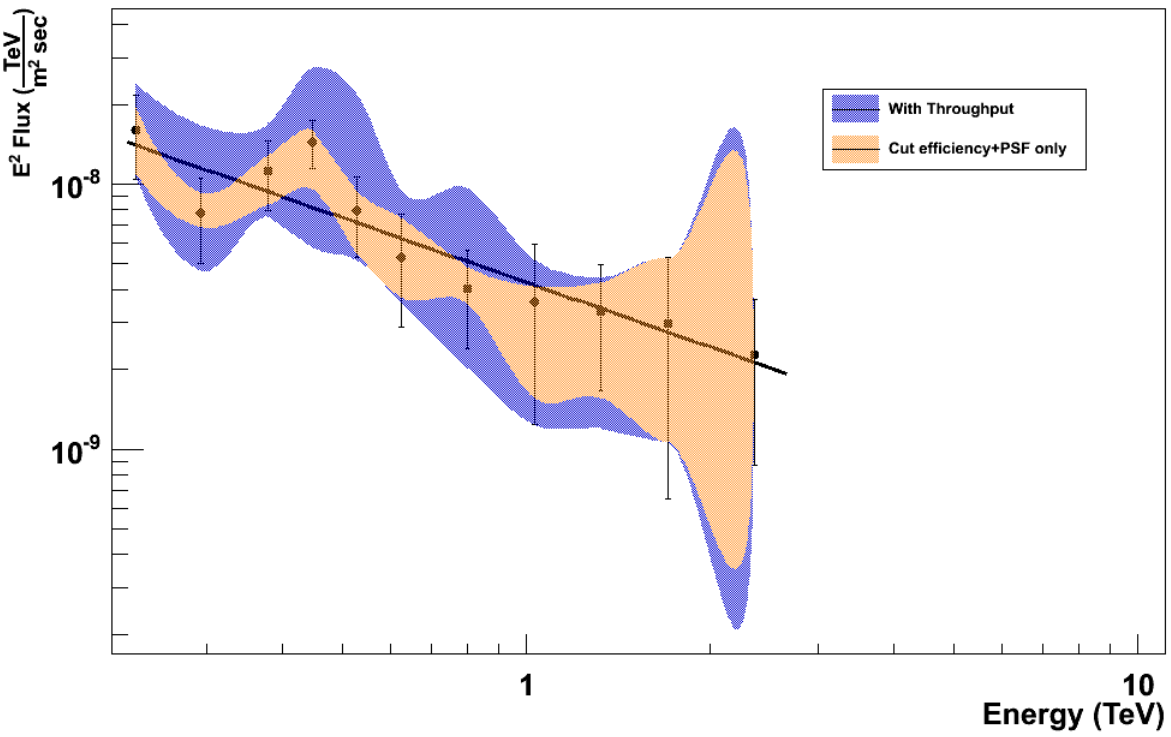

Figure 5.16 *Systematic error band on the spectrum of 1ES0229+200. Error bars are statistical.*

Table 5.9 H1426+428 Data Sample.

Season	Exposure Hours	Live Time Hours
2008-2009	0.33	0.29
2009-2010	6.83	6.23
2010-2011	6.95	6.43
2011-2012	16.02	14.94
2012-2013	1.67	1.51
Total	31.8	29.4

Table 5.10 Results from the analysis of H1426+428 (**standard cuts**).

ON	1132 events
OFF (total)	900.5 events
Significance	6.8σ
Signal rate	$0.13\pm 0.02\gamma$/min
Background rate	0.51 events/min
Excess	231.5 events
Live time	29.4 hours

5.3.2 Analysis Results

H1426+428 was analyzed with standard cuts from the Crab Nebula analysis, as shown in table 4.6. 29.4 hours remain after deadtime correction and time cuts. With standard cuts, a total of 231.5 excess events were detected, corresponding to a statistical significance of 6.8 standard deviations above the background. The soft cuts analysis leaves a more generous 665.5 excess events, with a statistical significance of 5.9 standard deviations above the background. Distributions of events in squared angular displacement, from standard and soft cuts, are given in figures 5.17 and 5.18.

5.3.3 Spectrum

The spectrum of H1426+428 from an analysis with standard cuts was reconstructed between 230 GeV and 4 TeV, and is shown in Figure 5.19. The flux points from this analysis are given in table B.7. The spectrum is fit by the following power-law function,

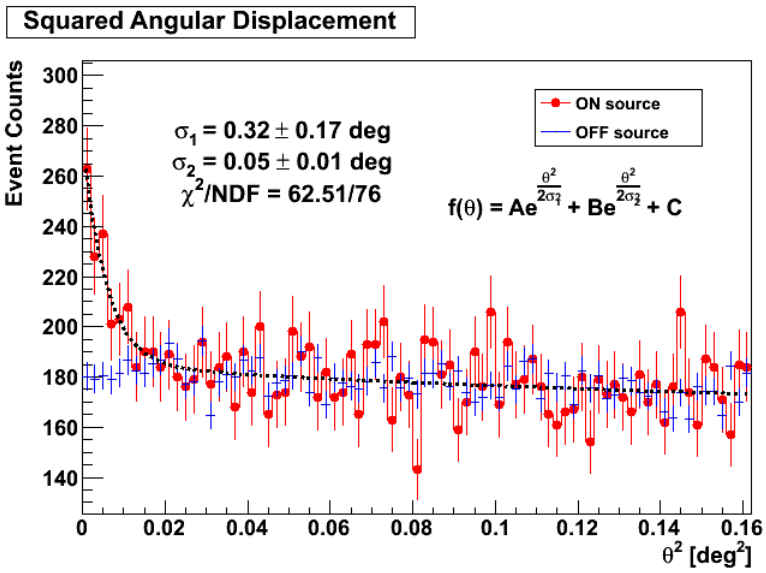

Figure 5.17 *Distribution of events in squared angular displacement from* ***standard cuts*** *analysis of H1426+428.*

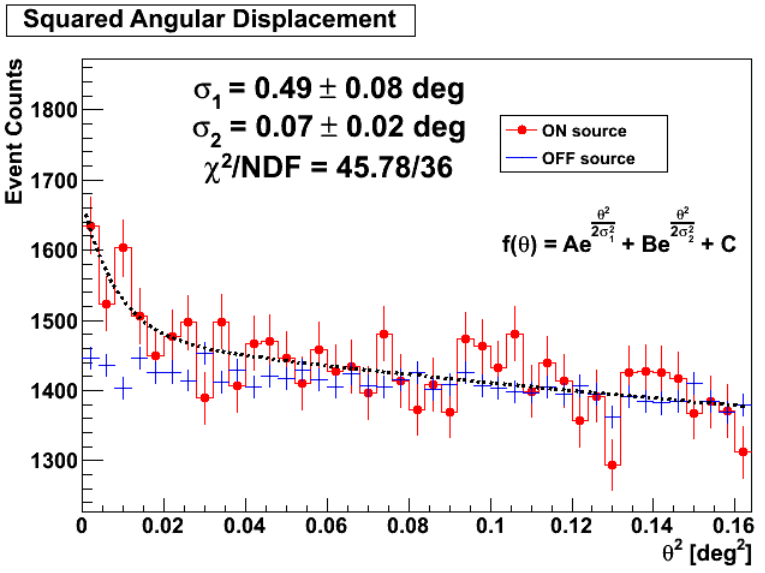

Figure 5.18 *Distribution of events in squared angular displacement from* ***soft cuts*** *analysis of H1426+428.*

Table 5.11 Results from the analysis of H1426+428 (**soft cuts**).

ON	11379 events
OFF (total)	10713.5 events
Significance	5.9σ
Signal rate	$0.38\pm 0.06\gamma$/min
Background rate	6.07 events/min
Excess	665.5 events
Live time	29.42 hours

Table 5.12 Flux Points from H1426+428 **soft cuts** analysis.

Energy (TeV)	Flux	Error on Flux
0.1894	$5.91{\cdot}10^{-7}$	$3.37{\cdot}10^{-7}$
0.2296	$4.78{\cdot}10^{-7}$	$1.91{\cdot}10^{-7}$
0.2714	$1.89{\cdot}10^{-7}$	$1.13{\cdot}10^{-7}$
0.3484	$1.44{\cdot}10^{-7}$	$3.85{\cdot}10^{-8}$
0.4479	$7.28{\cdot}10^{-8}$	$2.83{\cdot}10^{-8}$
0.5292	$3.08{\cdot}10^{-8}$	$1.87{\cdot}10^{-8}$
0.6254	$1.92{\cdot}10^{-8}$	$1.29{\cdot}10^{-8}$
0.8027	$1.57{\cdot}10^{-8}$	$5.62{\cdot}10^{-9}$
1.1510	$4.99{\cdot}10^{-9}$	$2.47{\cdot}10^{-9}$

$$\Phi(\mathrm{E}) = (6.31 \pm 1.01) \cdot 10^{-9} \frac{\mathrm{ph}}{\mathrm{m}^2 \cdot \mathrm{s} \cdot \mathrm{TeV}} \left(\frac{\mathrm{E}}{1\ \mathrm{TeV}} \right)^{-2.55 \pm 0.21} \tag{5.7}$$

with $\chi^2/\mathrm{N.D.F.} = 3.28/10$. The integral flux of this source from the standard cuts spectrum is 1.9% of the Crab Nebula flux.

The spectrum of H1426+428 from a soft cuts analysis was reconstructed between 190 GeV and 1.2 TeV, and is shown in 5.20; the flux points from this analysis are given in table B.8 (fluxes in units of $\mathrm{ph/m^2 \cdot s \cdot TeV}$). The spectrum is fit by the following power-law function,

$$\Phi(\mathrm{E}) = (7.35 \pm 2.04) \cdot 10^{-9} \frac{\mathrm{ph}}{\mathrm{m}^2 \cdot \mathrm{s} \cdot \mathrm{TeV}} \left(\frac{\mathrm{E}}{1\ \mathrm{TeV}} \right)^{-2.71 \pm 0.28} \tag{5.8}$$

with $\chi^2/\mathrm{N.D.F.} = 1.58/7$.

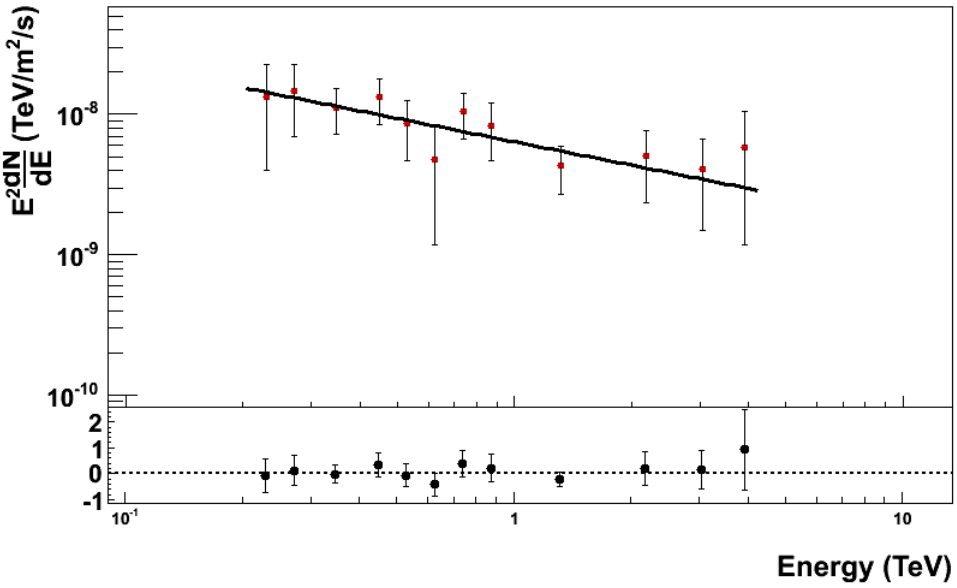

Figure 5.19 *Spectrum of H1426+428 derived from a* ***standard cuts*** *analysis.*

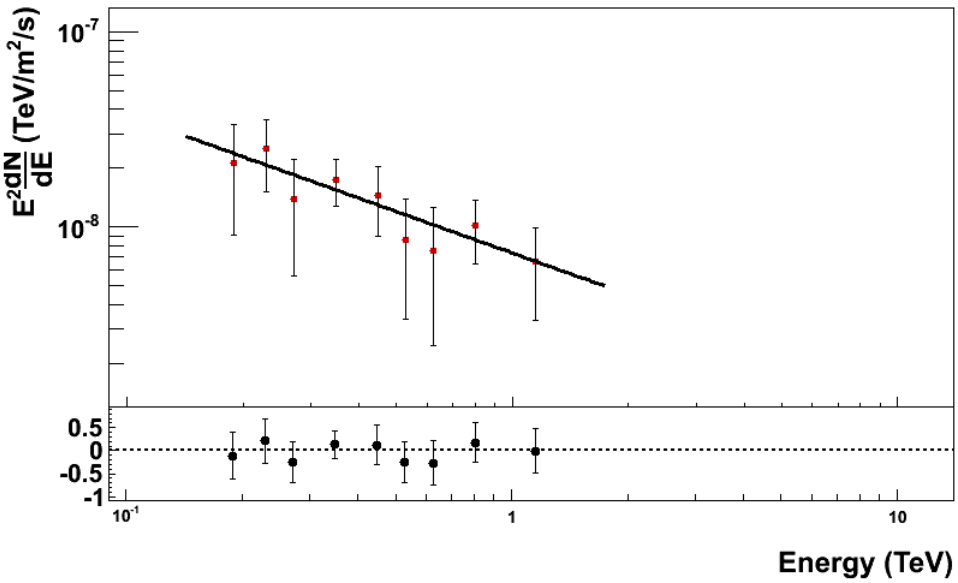

Figure 5.20 *Spectrum of H1426+428. Analyzed with* ***soft cuts****.*

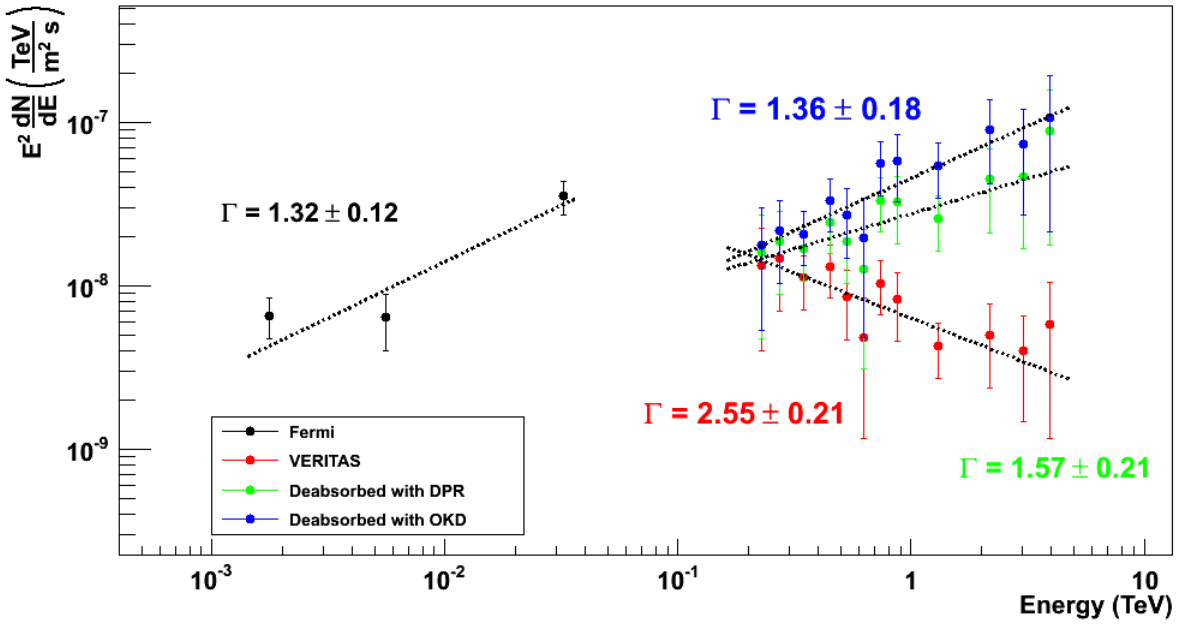

Figure 5.21 *EBL de-absorption of the VHE spectrum of H1426+428 (analyzed with **standard cuts**) using the DPR and OKD EBL SEDs.*

5.3.4 EBL De-Absorption

The spectrum of H1426+428 was de-absorbed using the DPR and OKD SEDs. The EBL de-absorption from the standard cuts analysis is shown in Figure 5.21, and from the soft cuts analysis is shown in Figure 5.22, and in both cases is compared to the HE spectrum from the Fermi Gamma Ray Space Telescope. Both analyses show the least disagreement in spectral shape between the Fermi spectrum and the de-absorbed VHE spectrum under the assumption of an OKD EBL SED. The spectral shapes differ by an index of 0.04, corresponding to 0.2σ. However, the absolute flux of the de-absorbed spectrum appears to be underestimated. The standard cuts spectrum was also de-absorbed with the OKD 2σ upper and lower bounds, with the absolute flux being treated as a free parameter. The result is shown in Figure 5.23. The fit to the HE spectrum and fit to the combined HE and VHE spectra differ by 0.01, corresponding to a 0.02σ disagreement between the Fermi spectrum and the joint fit.

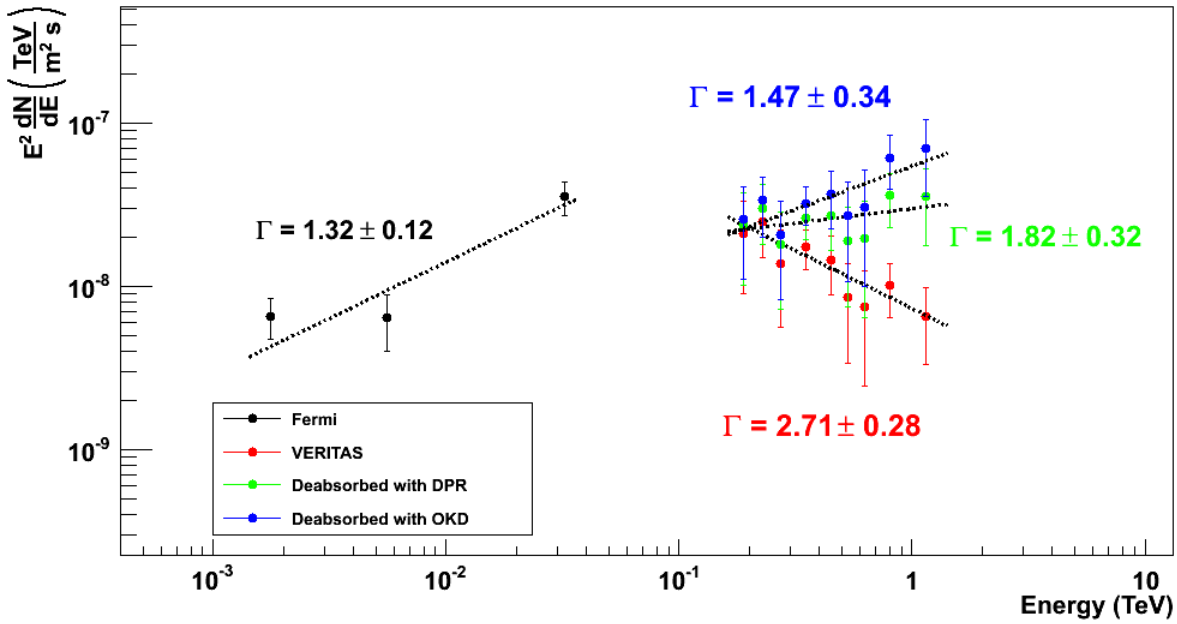

Figure 5.22 *EBL de-absorption of the VHE spectrum of H1426+428 (analyzed with **soft cuts**) using the DPR and OKD EBL SEDs.*

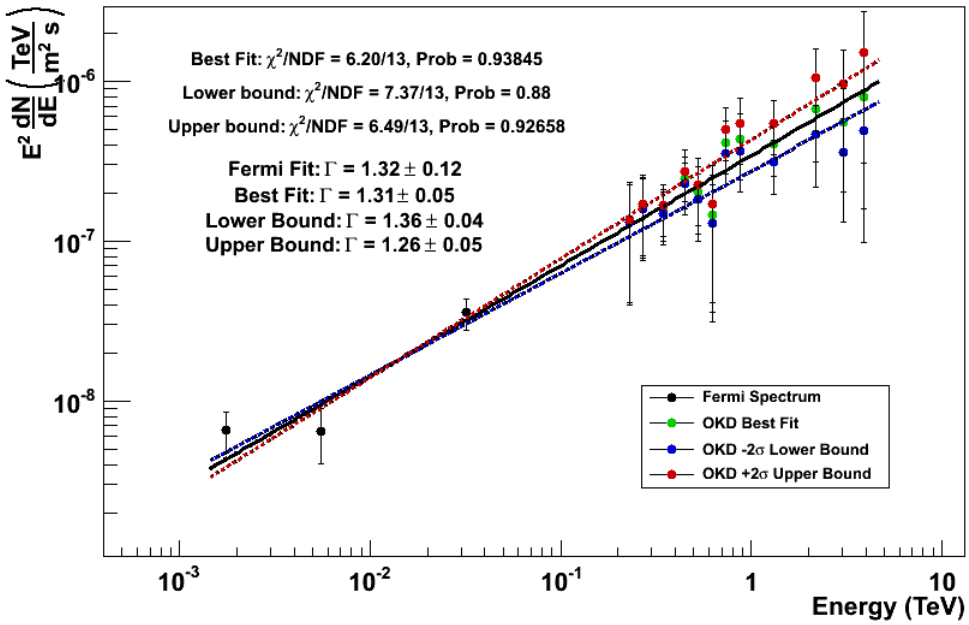

Figure 5.23 *EBL de-absorption of the VHE spectrum of H1426+428 (analyzed with **standard cuts**) in which the VHE spectral points include absolute flux as a free parameter in order to account for possible short term variability.*

Table 5.13 Results of systematics analysis on H1426+428.

	Φ_0 min	Φ_0 max	Γ min	Γ max	$\Delta\Phi$ min	$\Delta\Phi$ max	$\Delta\Gamma$ min	$\Delta\Gamma$ max
Size	3.84	8.31	2.72	2.83	2.47	2.00	–	0.11
MSL	5.61	5.93	2.50	2.55	0.7	–	0.05	0
MSW	4.89	6.98	2.58	2.75	1.42	0.67	–	0.2
Ring	6.35	6.36	2.55	2.57	–	0.05	0	0.02
Q-Sum					2.93	2.1	0.05	0.23

5.3.5 Systematics

Table B.9 contains the results of the systematic error analysis on the standard cuts spectrum of H1426+428, with flux normalizations given in units of $10^{-9}\frac{\text{ph}}{\text{m}^2\cdot\text{s}\cdot\text{TeV}}$. Throughput, cut efficiency, and γ-ray PSF were investigated using identical assumptions to those described in Section 4.10.5. The spectrum is given by Equation 5.9.

The error band derived from these analyses is shown in Figure 5.24. Here, systematic errors were calculated point-by-point, and contributions from each source of systematic uncertainty was added in quadrature.

$$\Phi(E) = \left(6.31 \pm 1.01_{stat}\,(+2.1 - 2.93)_{sys}\right)\cdot 10^{-9}\frac{\text{ph}}{\text{m}^2\cdot\text{s}\cdot\text{TeV}}\left(\frac{E}{1\text{ TeV}}\right)^{-2.55\pm0.21_{stat}(+0.23-0.05)_{sys}} \tag{5.9}$$

5.3.6 Comparison to Whipple Data

H1426+428 was previously observed by HEGRA (Horns et al., 2003) and by Whipple (Petry et al., 2002). Petry et al. (2002) details an analysis of Whipple data resulting in the spectrum,

$$\Phi\,(E) = 10^{-7.31\pm0.15}\left(\frac{E}{\text{TeV}}\right)^{-3.50\pm0.35}\frac{\text{ph}}{\text{m}^2\cdot\text{s}\cdot\text{TeV}} \tag{5.10}$$

In order to quantify the difference between the results of this work and the earlier Whipple observations, a spectrum with index -3.5±0.35 was imposed on the soft cuts spectrum (the flux constant was ignored because we are interested in spectral variability rather than absolute flux variability). The result, shown in Figure 5.25, is a fit with $\chi^2/N.D.F.$ of 7.86/7. This

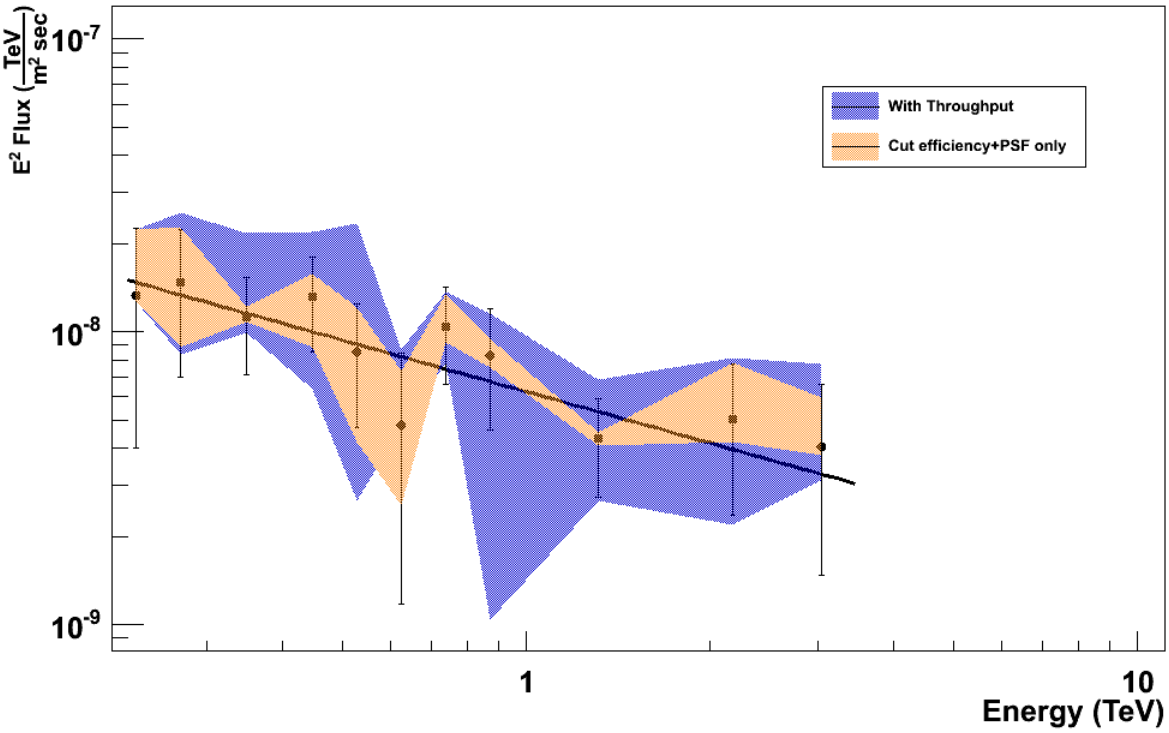

Figure 5.24 *Systematic error band on the spectrum of H1426+428. Error bars are statistical.*

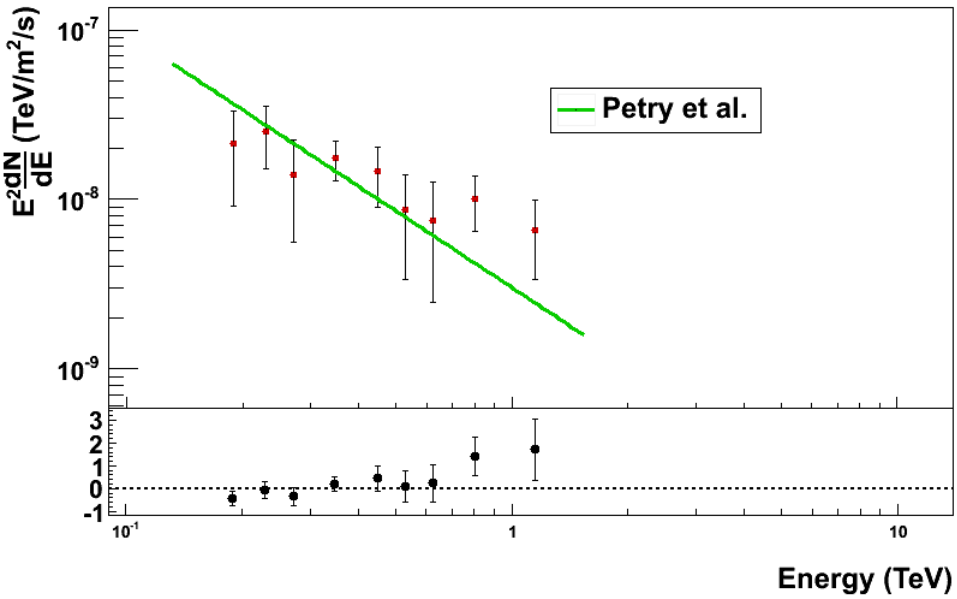

Figure 5.25 *The VERITAS flux points from a **soft cuts** analysis, with the spectral shape of the Whipple spectrum imposed upon the fit.*

corresponds to a fit probability of 34 %, as opposed to the 98% fit probability obtained from the fit without any constraint imposed on the fitted spectral index.

5.4 RGBJ0710+591

RGBJ0710+591 is a blazar located at a redshift of $z = 0.125$ (Giommi et al. (1991)). This source has been previous observed by VERITAS, as reported by Acciari et al. (2010b), and was detected at a statistical significance of 5.5 standard deviations above the background with a spectral index of Γ = -2.69 $\pm$ 0.26.

5.4.1 Run selection

A total of 94.6 hours of A/B weather data were taken on RGBJ0710+591 between January 2009 and March 2013. 12.2 hours were removed for reasons including the use of moon filters or reduced high voltage, as well as CFD thresholds different from the nominal values modeled in the OAWG simulations. A 82.4 hour dataset remained for analysis. The data sample is given

Table 5.14 RGBJ0710+591 Data Sample.

Season	Exposure Hours	Live Time Hours
2008-2009	20.9	19.0
2009-2010	9.9	9.0
2010-2011	12.8	11.3
2011-2012	15.7	13.7
2012-2013	23.1	19.7
Total	82.4	72.6

Table 5.15 Results from the analysis of RGBJ0710+591 (**standard cuts**).

ON	2413 events
OFF (total)	2042.7 events
Significance	7.34σ
Signal rate	$0.08\pm 0.01\gamma$/min
Background rate	0.47 events/min
Excess	370.3 events
Live time	72.6 hours

in table 5.14.

5.4.2 Analysis Results

RGBJ0710+591 was analyzed with standard cuts from the Crab Nebula analysis, as shown in table 4.6. 72.6 hours remain after deadtime correction and time cuts. With standard cuts, a total of 370.3 excess events were detected, corresponding to a statistical significance of 7.34 standard deviations above the background. The soft cuts analysis provides 1142.5 excess events for a statistical significance of 6.8 standard deviations above the background. Distributions of events in squared angular displacement, from standard and soft cuts, are given in figures 5.26 and 5.27.

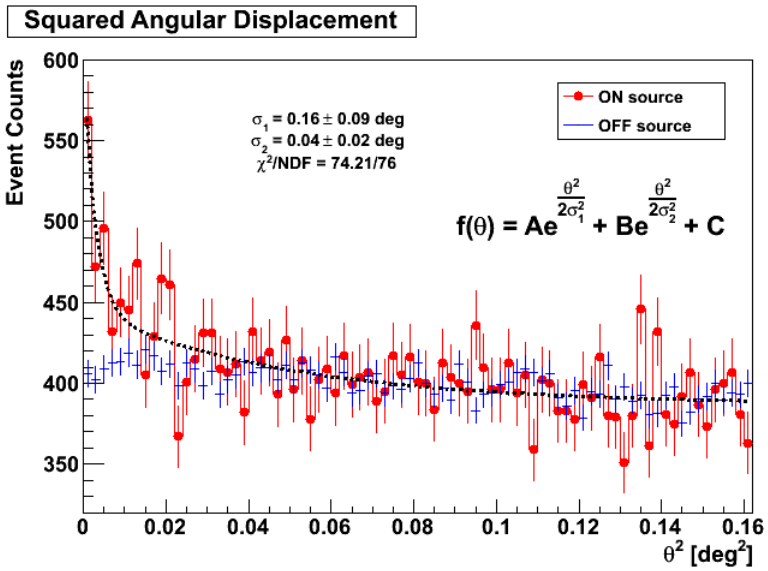

Figure 5.26 *Distribution of events in squared angular displacement from* ***standard cuts*** *analysis of RGBJ0710+591.*

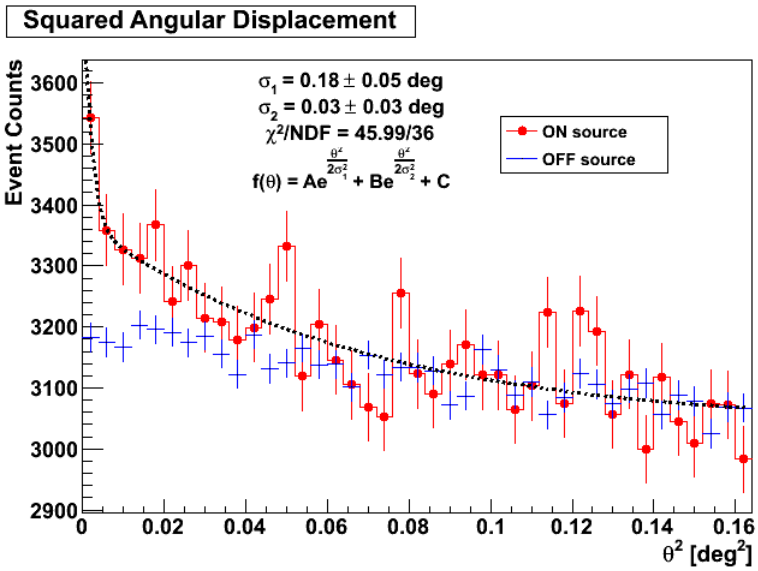

Figure 5.27 *Distribution of events in squared angular displacement from* ***soft cuts*** *analysis of RGBJ0710+591.*

Table 5.16 Results from the analysis of RGBJ0710+591 (**soft cuts**).

ON	24565 events
OFF (total)	23417.7 events
Significance	6.9σ
Signal rate	$0.26\pm 0.04\gamma$/min
Background rate	5.37 events/min
Excess	1147.3 events
Live time	72.6 hours

5.4.3 Spectrum

The spectrum of RGBJ0710+591 from an analysis with standard cuts was reconstructed between 345 GeV and 6.8 TeV, and is shown in Figure 5.28. The flux points from this analysis are given in table B.10. The spectrum is fit by the following power-law function,

$$\Phi(\mathrm{E}) = (6.20 \pm 0.91) \cdot 10^{-9} \frac{\mathrm{ph}}{\mathrm{m}^2 \cdot \mathrm{s} \cdot \mathrm{TeV}} \left(\frac{\mathrm{E}}{1\ \mathrm{TeV}} \right)^{-2.76\pm0.18} \tag{5.11}$$

with χ^2/N.D.F. = 5.57/5. The integral flux of this source from the standard cuts spectrum is 2.3% of the Crab Nebula flux.

The spectrum of RGBJ0710+591 from a soft cuts analysis was reconstructed between 280 GeV and 1.5 TeV, and is shown in 5.29; the flux points from this analysis are given in table B.11 (fluxes in units of ph/m$^2 \cdot$ s $\cdot$ TeV). The spectrum is fit by the following power-law function,

$$\Phi(\mathrm{E}) = (7.09 \pm 1.35) \cdot 10^{-10} \frac{\mathrm{ph}}{\mathrm{m}^2 \cdot \mathrm{s} \cdot \mathrm{TeV}} \left(\frac{\mathrm{E}}{1\ \mathrm{TeV}} \right)^{-2.62\pm0.26} \tag{5.12}$$

with χ^2/N.D.F. = 5.94/6.

5.4.4 EBL De-Absorption

The spectrum of RGBJ0710+591 was de-absorbed using the DPR and OKD SEDs. The EBL de-absorption from the standard cuts analysis is shown in Figure 5.31, and from the soft cuts analysis is shown in Figure 5.32, and in both cases is compared to the HE spectrum from the Fermi Gamma Ray Space Telescope. Both analyses show the least disagreement in spectral

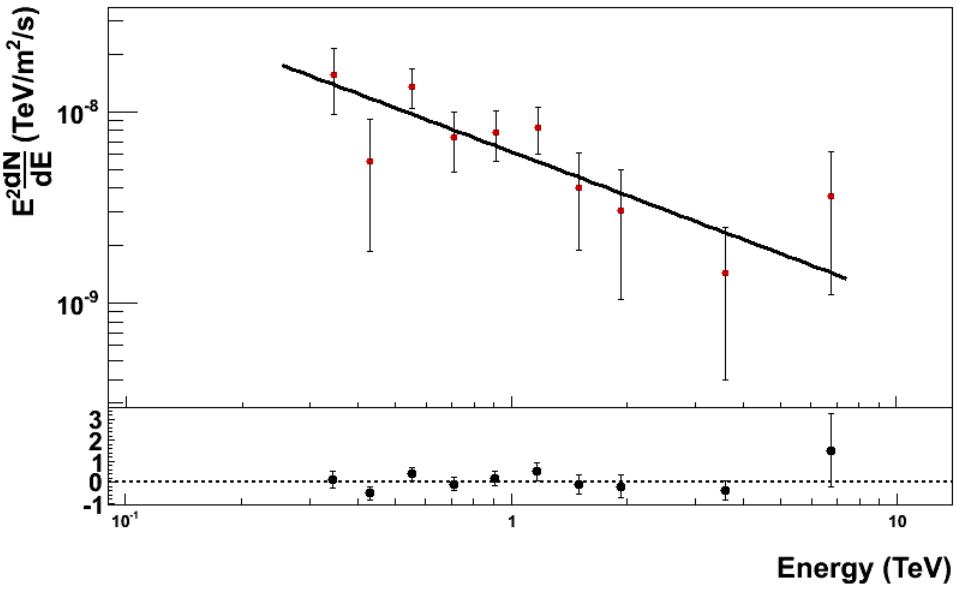

Figure 5.28 *Spectrum of RGBJ0710+591 derived from a* ***standard cuts*** *analysis.*

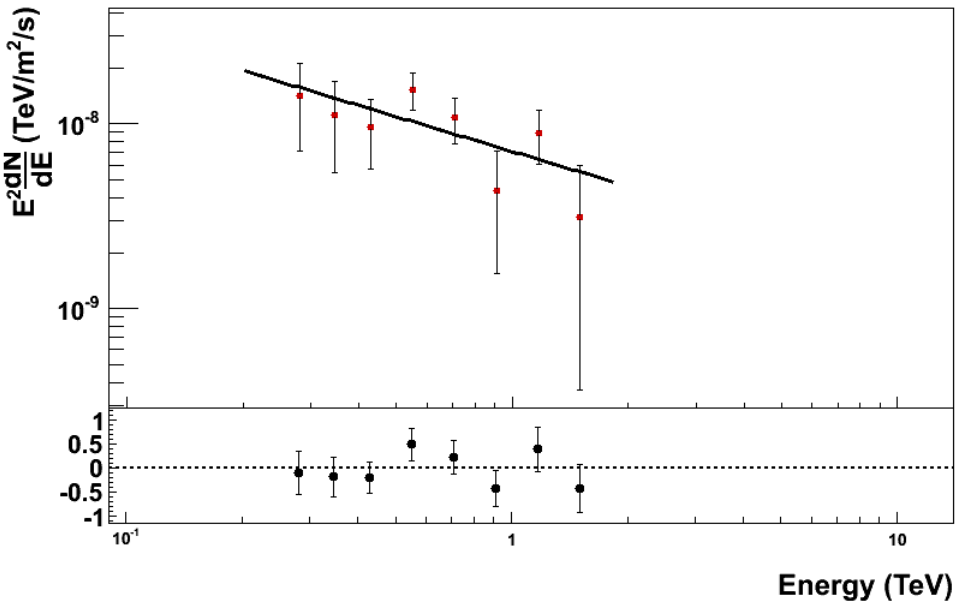

Figure 5.29 *Spectrum of RGBJ0710+591 derived from a* ***soft cuts*** *analysis.*

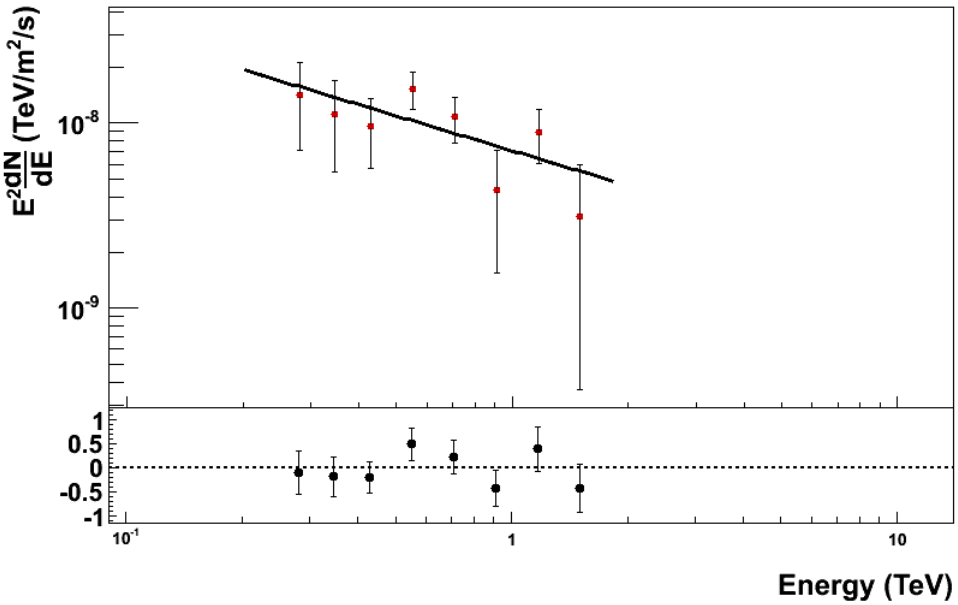

Figure 5.30 *Spectrum of RGBJ0710+591. Analyzed with* ***soft cuts****.*

shape between the Fermi spectrum and the de-absorbed VHE spectrum under the assumption of a DPR EBL SED. The standard cuts spectrum was also de-absorbed with the OKD 2σ upper and lower bounds, with the absolute flux being treated as a free parameter. The result is shown in Figure 5.23. The fit to the HE spectrum and fit to the combined HE and VHE spectra differ by 0.04, corresponding to a 0.3σ disagreement between the Fermi spectrum and the joint fit.

5.4.5 Systematics

Table B.12 contains the results of the systematic error analysis on the standard cuts spectrum of RGBJ0710+591, with flux normalizations given in units of $10^{-9}\frac{\text{ph}}{\text{m}^2\cdot\text{s}\cdot\text{TeV}}$. Throughput, cut efficiency, and γ-ray PSF were investigated using identical assumptions to those described in Section 4.10.5. The spectrum is given by Equation 5.13.

The error band derived from these analyses is shown in Figure 5.34. Here, systematic errors were calculated point-by-point, and contributions from each source of systematic uncertainty was added in quadrature.

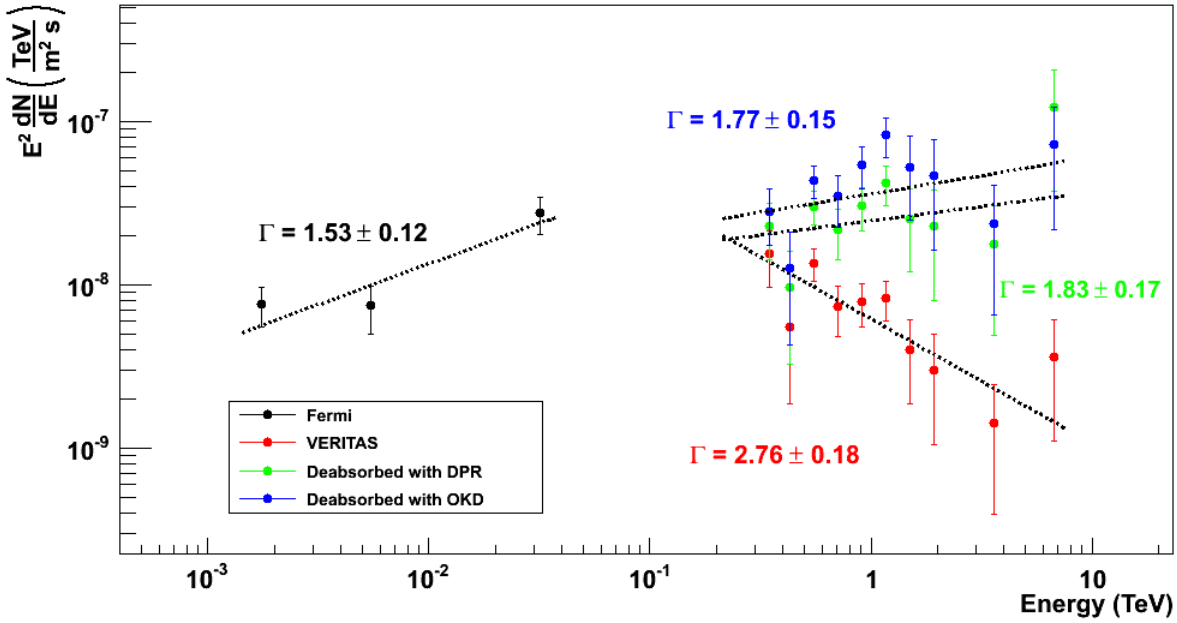

Figure 5.31 *EBL de-absorption of the VHE spectrum of RGBJ0710+591 (analyzed with* ***standard cuts****) using the DPR and OKD EBL SEDs.*

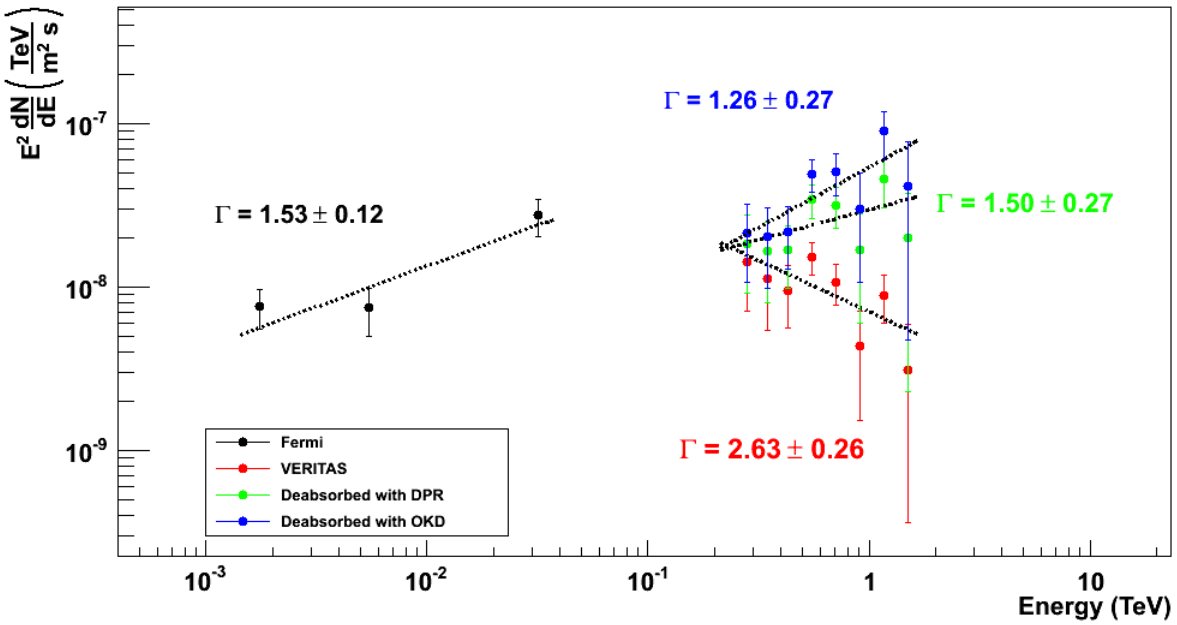

Figure 5.32 *EBL de-absorption of the VHE spectrum of RGBJ0710+591 (analyzed with* ***soft cuts****) using the DPR and OKD EBL SEDs.*

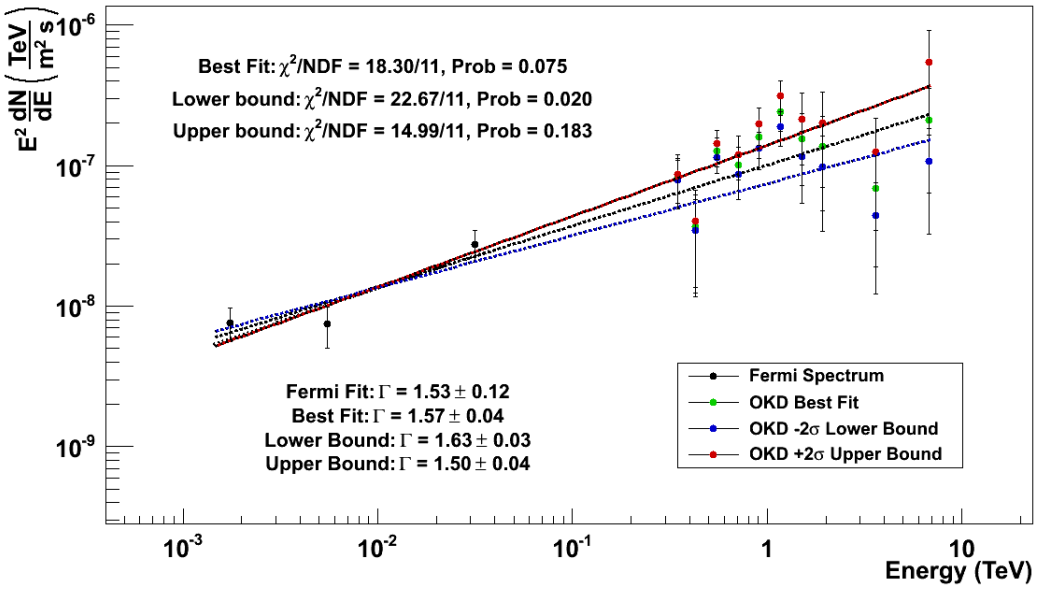

Figure 5.33 *EBL de-absorption of the VHE spectrum of RGBJ0710+591(analyzed with* ***standard cuts****) in which the VHE spectral points include absolute flux as a free parameter in order to account for possible short term variability.*

$$\Phi(E) = \left(6.20 \pm 0.91_{stat}\,(+1.57 - 2.30)_{sys}\right)\cdot 10^{-9}\frac{\text{ph}}{\text{m}^2\cdot\text{s}\cdot\text{TeV}}\left(\frac{E}{1\text{ TeV}}\right)^{-2.76\pm 0.18_{stat}(+0.10-0.55)_{sys}} \tag{5.13}$$

5.5 1ES 0414+009

1ES0414+009 is a high-frequency peaked BL Lac located at a redshift of $z = 0.287$. Aliu et al. (2012) described previous observations by VERITAS between January 2008 and February 2011 for a total of 56.2 livetime-corrected hours, resulting in a detection of 6.4 standard deviations above the background and a VHE spectral index of Γ = -3.4 $\pm$ 0.3_{stat}. Here we include additional data taken until March 2013.

5.5.1 Run selection

A total of 83.7 hours of A/B weather data were taken on 1ES0414+009 between January 2008 and March 2013. 3.5 hours were removed for reasons including hardware pathologies and

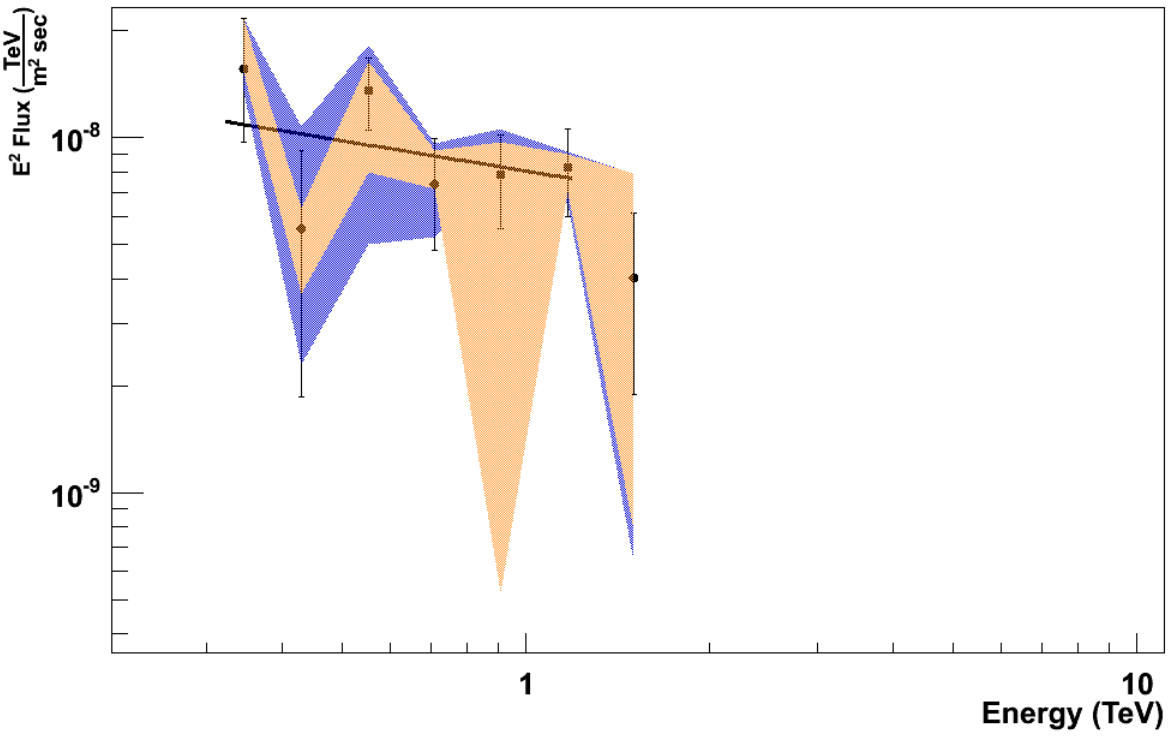

Figure 5.34 *Systematic error band on the spectrum of RGBJ0710+591. Error bars are statistical.*

Table 5.17 1ES0414+009 Data Sample.

Season	Exposure Hours	Live Time Hours
2007-2008	12.0	10.8
2008-2009	1.6	1.4
2009-2010	38.3	34.7
2010-2011	11.8	10.6
2011-2012	7.5	6.5
2012-2013	8.3	6.5
Total	79.5	70.5

the use as CFD thresholds different from the nominal values modeled in the OAWG simulations. Telescope 4 was cut from 20 runs due to a pathology in the L2 trace from one of the FADC crates, however data from the other three telescopes was included in the analysis. A 80.2 hour dataset remained for analysis. The data sample is given in table 5.17.

5.5.2 Analysis Results

1ES0414+009 was analyzed with a custom set of cuts. 70.5 hours remain after deadtime correction and time cuts. Because of the weak and soft nature of this source, neither the standard nor soft cuts were used in the analysis. Instead, all events (including upgrade data) were reconstructed with a size cut of 400 dc; the final sky analysis and spectral analysis were performed with a ring size of 0.1°[2]. The distribution of events in squared angular displacement is shown in Figure 5.35.

5.5.3 Spectrum

The spectrum of 1ES0414+009 from an analysis with standard cuts was reconstructed between 280 GeV and 600 GeV, and is shown in Figure 5.36. The flux points from this analysis are given in table B.13. The spectrum is fit by the following power-law function,

[2]This cut set was used to analyze 1ES0414+009 prior to settling on the standard and soft cuts for other sources. Because this analysis was done *a priori*, no trials factor has been included when citing the detection significance.

Table 5.18 Results from the analysis of 1ES0414+009.

ON	2774 events
OFF (total)	2474.5 events
Significance	5.5 σ
Signal rate	0.07± 0.01γ/min
Background rate	0.58 events/min
Excess	299.5 events
Live time	70.5 hours

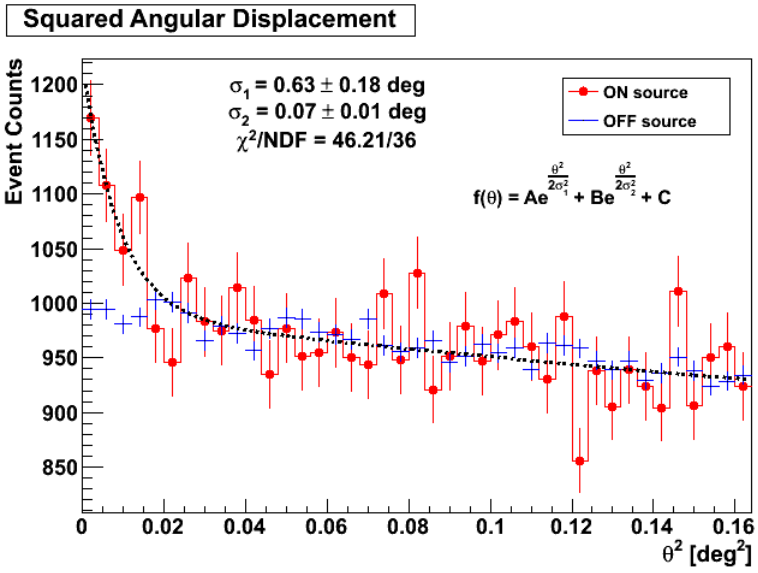

Figure 5.35 *Distribution of events in squared angular displacement from the analysis of 1ES0414+009.*

$$\Phi(\mathrm{E}) = (1.34 \pm 0.32) \cdot 10^{-7} \frac{\mathrm{ph}}{\mathrm{m}^2 \cdot \mathrm{s} \cdot \mathrm{TeV}} \left(\frac{\mathrm{E}}{300\ \mathrm{GeV}} \right)^{-4.64 \pm 0.90} \tag{5.14}$$

with χ^2/N.D.F. = 1.56/2. The integral flux of this source from the spectrum is 1.9% of the Crab Nebula flux.

5.5.4 EBL De-Absorption

The spectrum of 1ES0414+009 was de-absorbed using the DPR and OKD SEDs. The EBL de-absorption of the spectrum is shown in Figure 5.37, and is compared to the HE spectrum

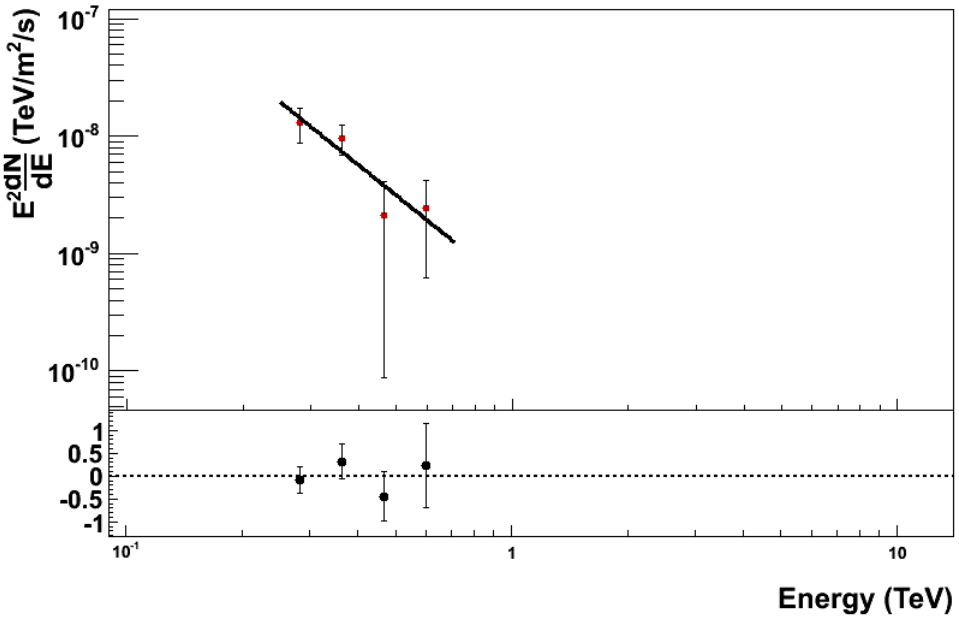

Figure 5.36 *Spectrum of 1ES0414+009 derived from an analysis with custom cuts.*

from the Fermi Gamma Ray Space Telescope. The spectrum was also de-absorbed with the Orr 2σ upper and lower bounds, with the absolute flux being treated as a free parameter. The result is shown in Figure 5.38. The fit to the HE spectrum and fit to the combined HE and VHE spectra differ by 0.03, corresponding to a 0.2σ disagreement between the Fermi spectrum and the joint fit.

5.5.5 Systematics

Table B.14 contains the results of the systematic error analysis on the standard cuts spectrum of 1ES0414+009, with flux normalizations given in units of $10^{-9}\frac{\text{ph}}{\text{m}^2\cdot\text{s}\cdot\text{TeV}}$, at 300 GeV. Throughput, cut efficiency, and γ-ray PSF were investigated using identical assumptions to those described in Section 4.10.5. The spectrum is given by Equation 5.15.

The error band derived from these analyses is shown in Figure 5.39. Here, systematic errors were calculated point-by-point, and contributions from each source of systematic uncertainty was added in quadrature.

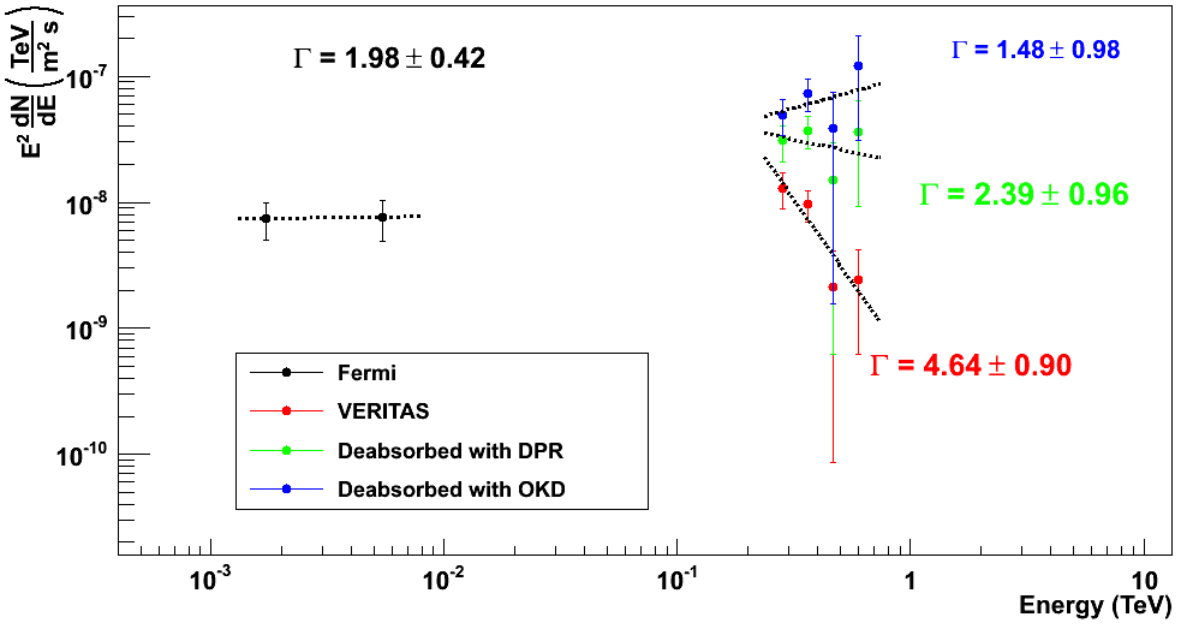

Figure 5.37 *EBL de-absorption of the VHE spectrum of 1ES0414+009 using the DPR and OKD EBL SEDs.*

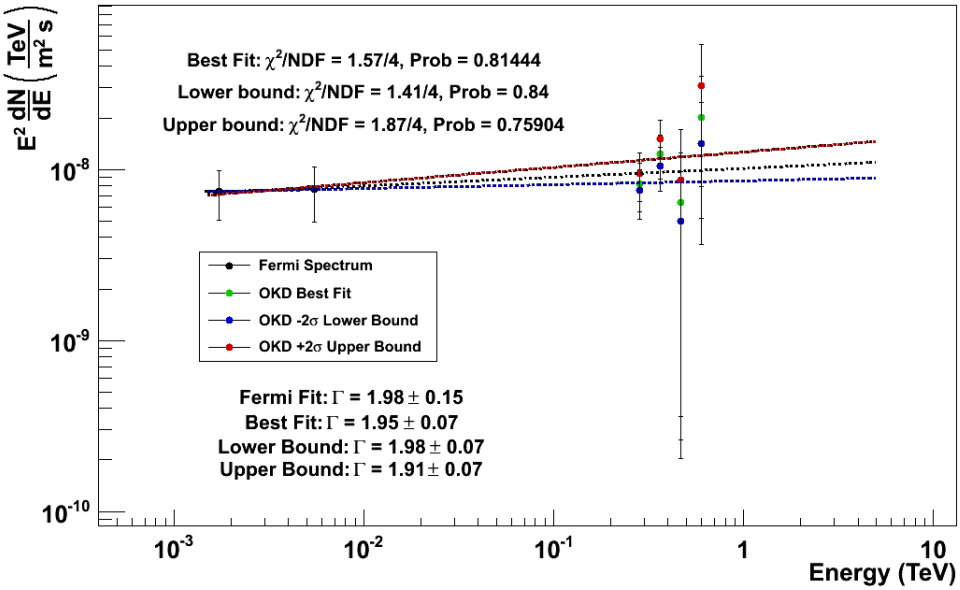

Figure 5.38 *EBL de-absorption of the VHE spectrum of 1ES0414+009 (analyzed with* ***standard cuts****) in which the VHE spectral points include absolute flux as a free parameter in order to account for possible short term variability.*

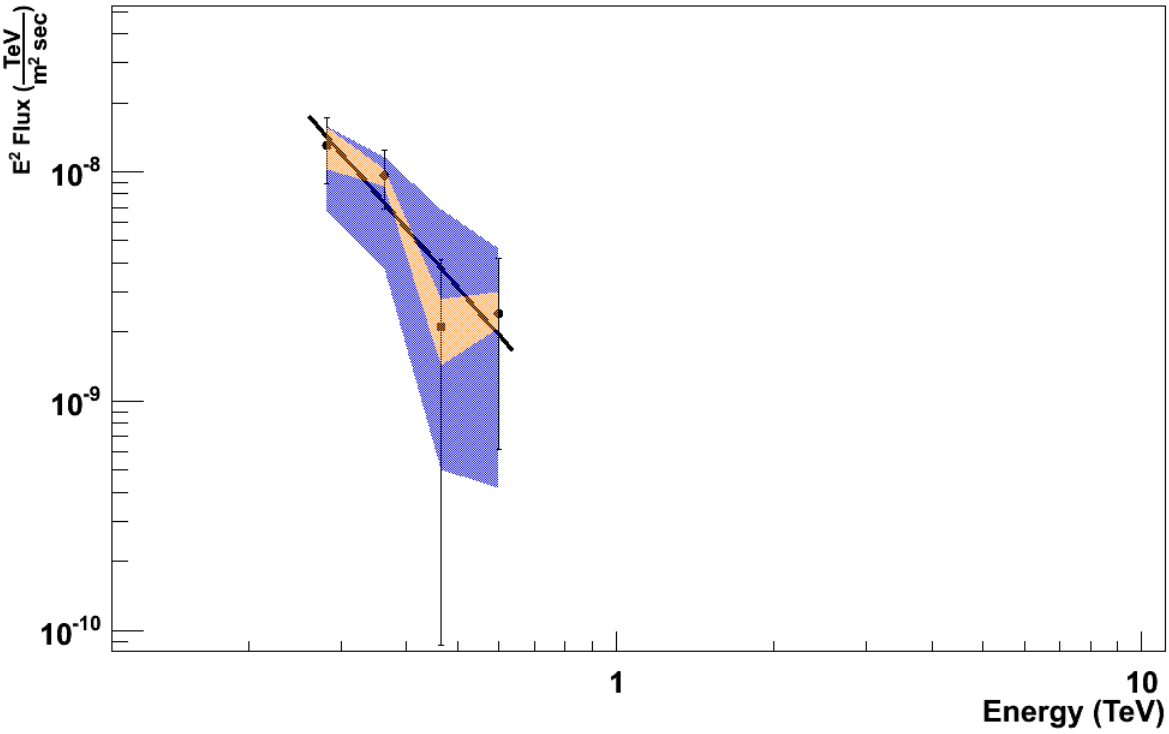

Figure 5.39 *Systematic error band on the spectrum of 1ES0414+009 Error bars are statistical.*

$$\Phi(E) = \left(1.34 \pm 0.32_{stat}\,(+0.74 - 0.13)_{sys}\right) \cdot 10^{-9} \frac{\text{ph}}{\text{m}^2 \cdot \text{s} \cdot \text{TeV}} \left(\frac{E}{300\ \text{GeV}}\right)^{-4.64 \pm 0.90_{stat}(+0.93-1.49)_{sys}} \tag{5.15}$$

CHAPTER 6. DISCUSSION AND CONCLUSIONS

The blazars analyzed in this work all possess GeV spectra with emission harder than $\Phi(E) = \Phi_0 \left(\frac{E}{E_0}\right)^{-2.0}$, as observed by the Fermi satellite. In this energy regime, the optical depth curves shown in Figure 2.5 demonstrate that EBL absorption is negligible. It is likely that these sources are also hard in the transition region between the Fermi and VERITAS measurements. All blazars emit detectable γ-rays into the optically-thick regime of the EBL, with the exception of 1ES0414+009. All sources, even the latter, can be de-absorbed to compare TeV and GeV data, and thus estimate the efficacy of the EBL model in reproducing the (assumed) intrinsic source emission. Orr et al. (2011) employ two methods of blazar spectrum analysis in order to arrive at the "best fit" EBL SED. The first is a comparison between the overall shapes (i.e. spectral indices) of the GeV and TeV spectra. The fundamental assumption here is that the intrinsic spectra do not harden between the Fermi and VERITAS energy regimes, and that the observed softening can be used to derive a solid upper limit on TeV photon absorption due to the EBL. Though the intrinsic emission could in principle steepen in the transition region, it is unlikely that this is the case for all of the blazar sources. Thus, any upper limits derived from this method are likely also a good estimate of the absolute intensity of the EBL. The second method employed by Orr et al. (2011) involves fitting each spectrum with a broken power law. Because the near IR peak of the EBL is at a wavelength of 1.6 μm, Equation 2.2 suggests that the inflection energy of this broken power law should be fixed at 1.3 TeV. It should also be noted that this method yields a strong constraint on the ratio of the near- to mid-IR EBL flux, requiring a near-IR flux that is consistent with the result from the extrapolation of GeV data.

GeV-TeV Spectral Shape Method

Each blazar has been de-absorbed with the EBL. GeV spectral indices were compared with TeV indices from the de-absorptions performed with the Dominguez and Orr Best Fit SEDs. In order to account for the fact that the data were not taken contemporaneously and thus may reflect different flux states, the flux of the TeV data points was taken as a free parameter. The spectra were de-absorbed with the Orr Best Fit SED, as well as its 2σ upper and lower bounds, and the combined GeV and TeV data points were fit.

When treating the TeV flux of each source as a free parameter, a combined fit can be performed on every blazar which very closely reproduces the spectral shape of the Fermi observations. With the exception of 1ES1218+304, the combined fit yields a power law fit probability greater than 7%.

In principle, the sources presented here could have intrinsic curvature in their GeV-TeV spectra. This can occur if the Klein-Nishina cutoff in the VHE spectrum occurs at energies where the γ-ray spectrum has been reconstructed. A power law fit to such data will result in the appearance of a softer spectrum. The blazars studied in this work are unlikely to possess strong intrinsic curvature between a few GeV and 1 TeV, since their spectra extend well into the multi-TeV regime (with the exception of 1ES0414+009).

To make certain that the blazars studied in this work do not possess intrinsic curvature, 18 blazars from the TeVCat website were compiled which have measured GeV and TeV data. A plot of the GeV-TeV spectral break vs. redshift is shown in Figure 6.1, and is fit with a linear function. Blazars which fall significantly below this fit may possess intrinsic curvature. Figure 6.1 shows that only three blazars are significantly below the fit: and PKS 2005-489 (z=0.071), PKS 2155-304 (z=0.116), and RX J0648.7+151 (z=0.179). All of the blazars studied in this work intercept the fit line, thus increasing our confidence that they do not possess intrinsic curvature.

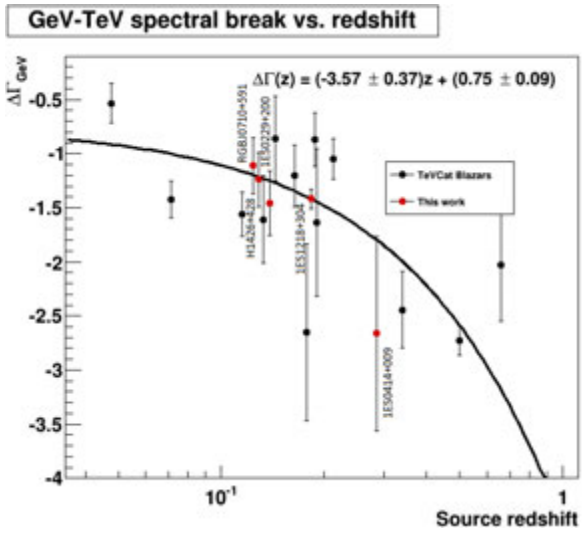

Figure 6.1 *Spectral break between GeV and* ***absorbed*** *TeV spectra. Points below the fit line may have intrinsic curvature (and may be responsible for the non-zero intercept).*

TeV Spectral Break Method

TeV spectral breaks are obtained by fitting γ-ray spectra with a continuous, broken power law. For a break energy of E_b, the broken power law function is given by Equation 6.1; note that this equation imposes the condition of continuity on the spectrum. The blazar spectra derived from *standard cuts* were fit with this function, where $E_b = 1.3TeV$. Figure 6.2 shows an example of a broken power law fit to the spectrum of 1ES0229+200. We define the spectral break as $\Delta\Gamma = \Gamma_1 - \Gamma_2$.

$$\Phi(E) = \begin{cases} \Phi_0 \left(\frac{E}{E_b}\right)^{-\Gamma_1} \\ \Phi_0 \left(\frac{E}{E_b}\right)^{-\Gamma_2} \end{cases} \tag{6.1}$$

Table 6.1 lists the spectral break calculated from each blazar. 1ES0414+009 was excluded because it does not exhibit detectable γ-ray emission at the break energy. The spectral breaks from this work were combined with the breaks from the blazars compiled by Orr et al. (2011). These blazars are: 1ES2355+514, 1ES1959+650, PKS0548-322, PKS2005-489, RGBJ0152+017, PKS2155-304, 1ES1101-232, and 1ES0347-121. The blazars 1ES1218+304, 1ES0229+200, H1426+428, and RGBJ0710+591 were also studied by Orr et al. (2011). The

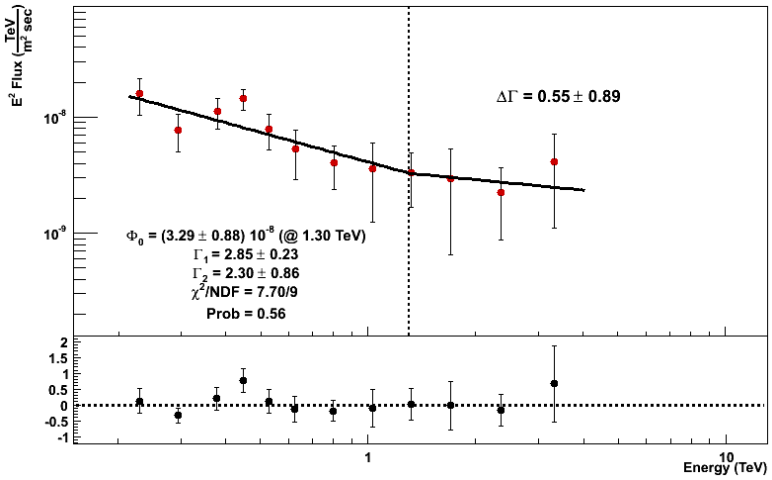

Figure 6.2 *The spectral break obtained from a piecewise power law fit to the spectrum of 1ES0229+200. The inflection energy is set at 1.3 TeV.*

results from these sources were updated with the values derived in this work

The redshift dependent spectral break is derived from a linear fit to these data with a floating y-intercept, as well as with a y-intercept fixed at 0. The result from a floating intercept is given by Equation 6.2. The result with an intercept fixed at zero is 6.3. The data were also fit with $\Gamma(z) = 0$ under the assumption of no spectral break.

$$\Delta\Gamma\,(\mathrm{z}) = (2.72 \pm 4.21)\,\mathrm{z} + (0.11 \pm 0.63) \qquad \chi^2/\mathrm{ndf} = 12.30/11 \tag{6.2}$$

$$\Delta\Gamma\,(\mathrm{z}) = (3.44 \pm 1.24)\,\mathrm{z} \qquad \chi^2/\mathrm{ndf} = 12.34/12 \tag{6.3}$$

$$\Delta\Gamma\,(\mathrm{z}) = 0)\mathrm{z} \qquad \chi^2/\mathrm{ndf} = 20.04/12 \tag{6.4}$$

These results can be compared to the fit derived by Orr et al. (2011).

$$\Delta\Gamma\,(\mathrm{z}) = (8.68 \pm 5.37)\,\mathrm{z} + (0.24 \pm 0.71) \tag{6.5}$$

$$\Delta\Gamma\,(\mathrm{z}) = (6.94 \pm 1.65)\,\mathrm{z} \tag{6.6}$$

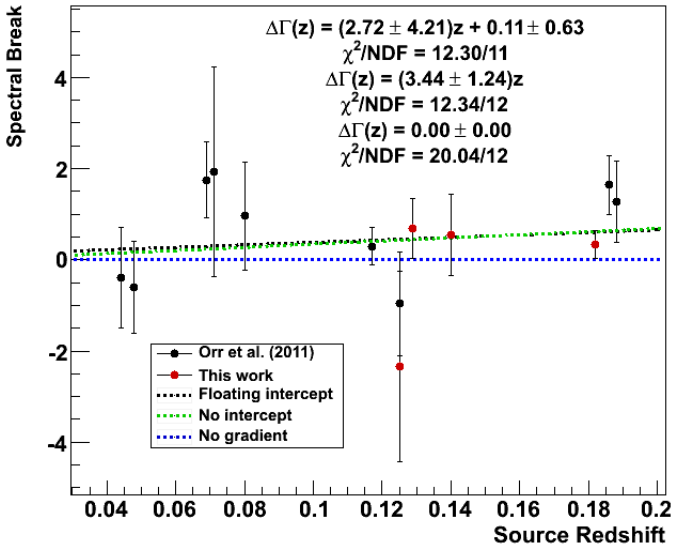

Figure 6.3 *Spectral breaks as a function of redshift.*

Table 6.1 Spectral breaks at 1.3 TeV.

Source	Redshift	Spectral Break	Error
RGBJ0710+591	0.125	-2.34	2.09
H1426+428	0.129	0.63	0.64
1ES0229+200	0.140	0.55	0.89
1ES1218+304	0.182	0.33	0.31
1ES0414+009	0.287	–	–

An F-test was performed on Equations 6.4 and 6.2. The hypothesis of no spectral break in the blazar data is excluded at the 3.1σ confidence interval. This is only marginally less than the 3.2σ obtained by Orr et al. (2011).

Conclusions and Potential Future Work

In this work, TeV energy spectra were derived for five blazars over a range of redshifts from 0.1 to 0.3. All of these blazars show emission consistent with a power law function and show γ-ray emission into the optically thick regime of the EBL. De-absorptions with the EBL model of Dominguez produce VHE spectra that are comparable to the Fermi HE spectra. A

TeV spectral break analysis was combined with additional blazar data, and revealed a trend consistent with the value derived by Orr et al. (2011). By performing similar studies of redshift-dependent spectral breaks for EBL models, it is possible to use this trend to impose constraints on the spectrum of the EBL. Additionally, the addition of higher redshift sources to the blazar sample, as well as a larger number of blazar sources, will allow for better measurements of TeV spectral breaks. Further deep exposures of these sources also increases the probability of observing a source during a flare; such an observation could provide sufficient statistics to even resolve a spectral break from a single source. The results presented here make a compelling case for further studies of hard-spectrum blazars at HE and VHE energies. By obtaining γ-ray spectra of these sources over a variety of redshifts, it is possible to further elucidate the energy-dependent effect of γ-ray absorption by the EBL.

APPENDIX A. Calculation of Shower Maximum in the VEGAS Analysis Package

A.1 Introduction

Electrons from γ-ray induced air showers follow a coma-shaped distribution. The peak of this distribution represents the largest number of electrons, and is referred to as the shower maximum (*showermax*). When the Cherenkov image of an air shower is projected onto the focal plane of the VERITAS cameras, the major axis of the ellipse corresponds to the longitudinal development of the shower, and the image centroid approximately gives the position of the shower maximum. The *showermax* parameter, along with reconstructed direction of the shower on the sky and its core location in the array's mirror plane, represents the three dimensional structure of the shower.

A.2 Energy dependence of the shower maximum

As air showers develop, successive generations of e^+e^- pairs are less energetic. According to the Heitler toy model, in which the electromagnetic cascade is described by simple branching as described in Figure A.1, an air shower will develop until the current generation of electrons reaches the critical energy E_c (Gaisser, 1990) of approximately 80 MeV.

The critical energy is the point on the electrons' energy loss curve at which ionization losses become dominant over bremsstrahlung losses. Consider a shower induced by a primary γ-ray of energy E_0. Assuming an electron mean free path λ, the number of particles at shower depth X is given by,

$$N(X) = 2^{\frac{X}{\lambda}}$$

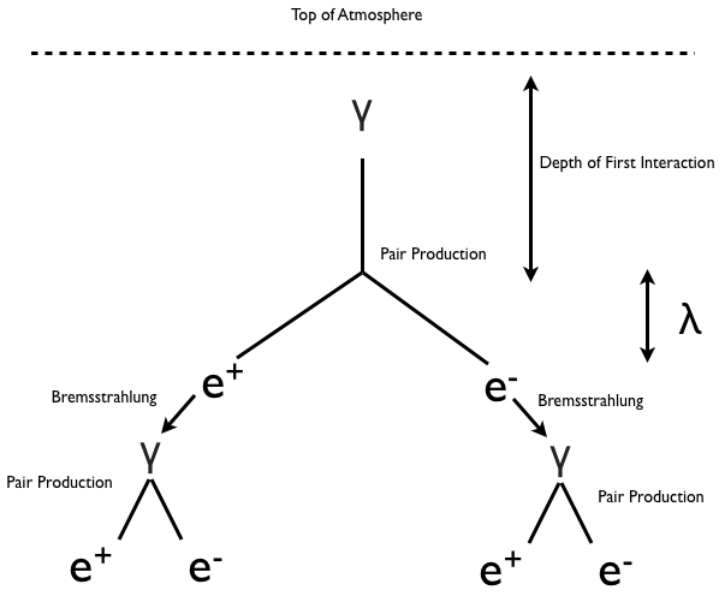

Figure A.1 *Illustration of the Heitler toy model. Here, the air shower is modeled by a branching process. After the first interaction, the electrons travel a length λ before emitting bremsstrahlung photons, which again pair produce to produce the next generation of electrons. The process continues until ionization losses become dominant.*

Table A.1 Shower maxima predicted by the toy model.

Energy	Shower Max Depth (gm/cm^2)	Altitude (km)
200 GeV	406	9.9
1 TeV	490	9.1
10 TeV	610	7.9

We can further assume that the energy from the primary γ-ray is evenly distributed amongst particles, so that the energy per particle is given by,

$$E(X) = \frac{E_0}{N(X)} = E_0 \cdot 2^{-\frac{X}{\lambda}}$$

If the depth of the shower max, X_0 occurs when the energy per particle is reduced to the critical energy E_c, then the shower maximum is given by,

$$X_0 = \lambda \, log_2 \left(\frac{E_0}{E_c} \right) = \lambda \, \frac{ln\,(E_0/E_c)}{ln\,(2)}$$

We thus expect the shower maximum to depend on the logarithm of the primary particle energy. Assuming an interaction length of $\lambda = 36 gm/cm^2$, critical energy $E_c = 80 MeV$, first interaction at 14 km, and atmospheric density of $\rho = 10^{-3} gm/cm^3$, table A.2 gives the predicted shower maxima for three primary γ-ray energies.

Monte Carlo simulations can be used to verify the effect predicted by the toy model. Figure A.2 shows distributions of Cherenkov photon emission heights for γ-ray showers with primary energies of 200 GeV, 1 TeV, and 10 TeV. Each distribution was constructed from multiple events to account for random variations in the depth of the first interaction. The maxima of higher energy showers tend to occur closer to the ground than those of lower energy showers. This effect serves as an important cross-check to ensure that reconstructed shower maxima are properly calculated.

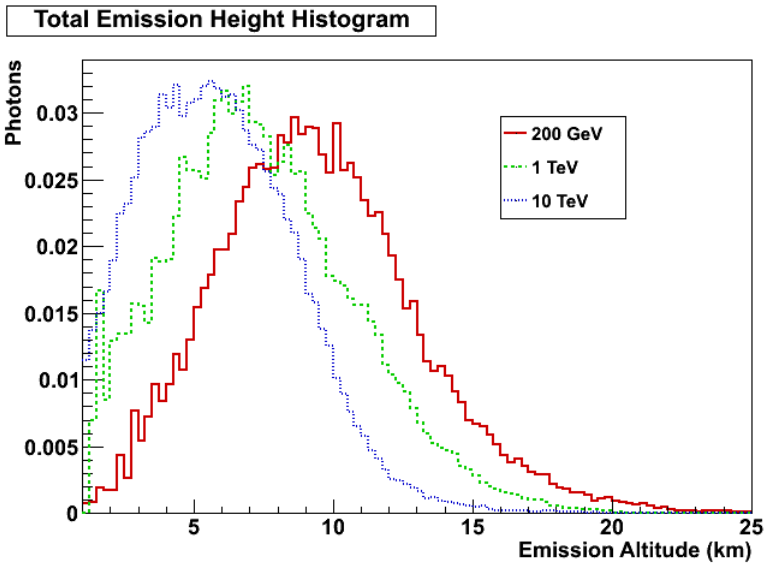

Figure A.2 *Distributions of Cherenkov photons by emission height for simulated γ-ray induced showers with primary energies of 200 GeV, 1 TeV, and 10 TeV. Multiple events were used to average over random variation in depth of the first interaction. Air shower simulation done with Kascade and Cherenkf. The cutoff at ≈1 km is due to the simulated observatory altitude.*

A.3 Reconstructing the shower maximum

A.3.1 Current incorrect method

As of release version 2.4.2., stage4 of the VEGAS analysis package calculates the shower maximum using the angular difference between pairs of images, as illustrated in Figure A.3. A triangle is formed between all pairs of participating telescopes and the shower. The distance between the centroids of the two telescope's Cherenkov images in the focal plane is taken to be the angular separation θ between the telescopes' lines of sight to the shower. Using a small angle approximation, the known distance between telescopes L is used to derive the shower maximum. We then take the mean between all pairs of participating telescopes,

$$h = \frac{1}{n_{pairs}} \sum_{i=0}^{n_{pairs}} \left(\frac{L_{i,j}}{\theta_{i,j}} \right)$$

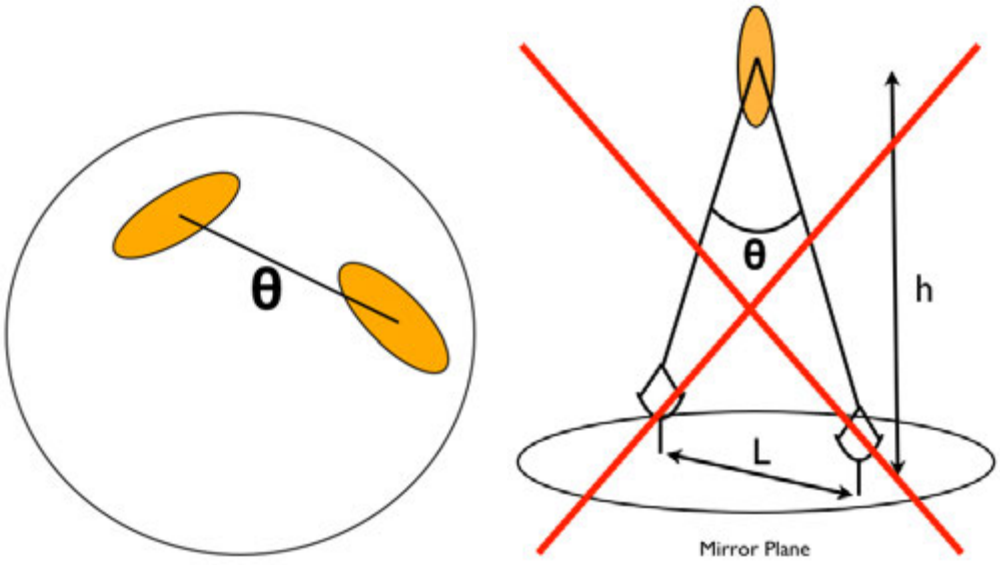

Figure A.3 *Current VEGAS method of determining the shower maximum. The angle θ shown in the camera plane is in fact not equal to the angular displacement of the two telescopes from the air shower. This results in incorrect calculation of showermax.*

Unfortunately, this method does not properly reconstruct the shower maximum. Figure A.4 shows that the reconstructed shower maxima have no energy dependence in the regime where analysts typically reconstruct spectra (200 GeV to 50 TeV). This is because the centroid

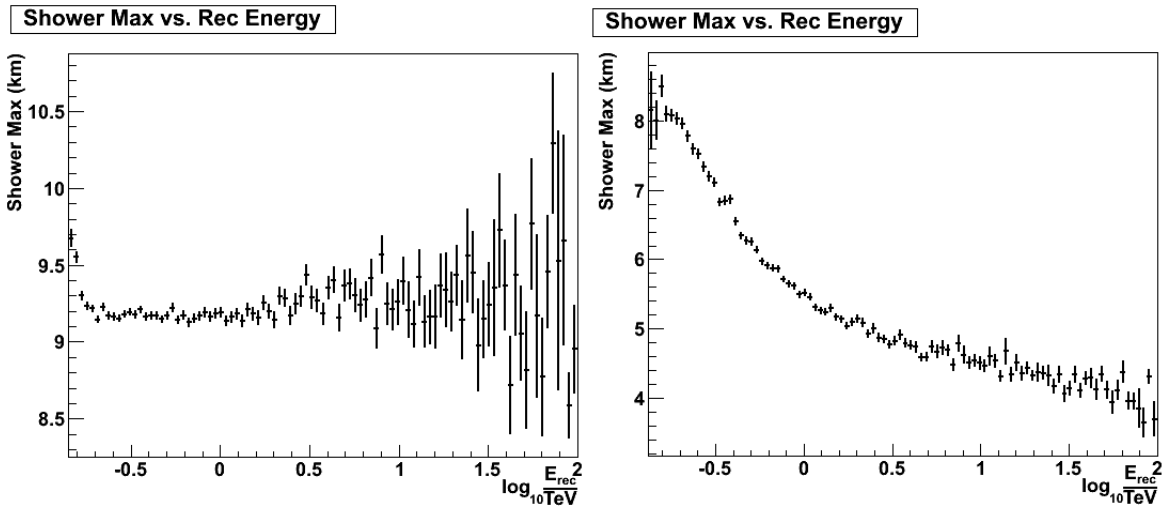

Figure A.4 *(left) Correlation plot of averaged shower max and energy shows no energy dependence using the old method of shower maximum calculation. (right) The alternate method restores the expected dependence of shower maximum with energy. Both distributions created from the November 2010 simulations at 0° zenith and 0.5° wobble offset at 100 grisu units noise level.*

displacement between two images does not in fact equal the angular separation between the telescopes with respect to the shower. The centroid displacement between two images will vary not only with the shower maximum, but also with the Cherenkov angle. Therefore it is impossible to calculate the shower maximum without additional information beyond the angular separation between images.

A.3.2 Correct method using centroid displacement from shower direction and core location

Calculation of the shower maximum requires knowledge of the core impact position in the telescope mirror plane. Because this parameter is calculated during event reconstruction, evaluation of the shower maximum is also possible. Consider a shower whose axis is parallel to the tracking position of the telescopes (this amounts to an observation with the source at the center of the field of view). If the shower core is located at a distance of R in the mirror plane from any given telescope and has a centroid displacement θ from the center of the field of view,

then the right triangle construction shown in Figure A.5 can be used to calculate *showermax* for a γ-ray induced shower.[1]

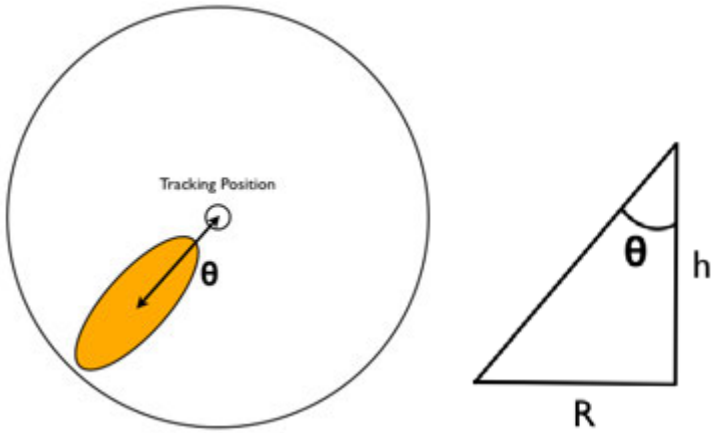

Figure A.5 *Right triangle construction used to calculate a shower core from the single telescope centroid parameters and the array-reconstructed shower core.*

This method is valid for ON source observations of point sources, but adjustments must be made to account for showers whose longitudinal axes are not parallel to the array tracking direction. During wobble observations, most γ-ray shower directions are displaced from the tracking position by 0.5°. When observing an extended source, *most* showers will have directions other than the camera center or even the putative source location. In these situations, it is helpful to work in so-called shower core coordinates, i.e. the coordinate system whose xy plane is parallel to the longitudinal axis of the shower (here, $z = 0$ still corresponds to the telescope location). The parameter of interest, h, is the perpendicular distance of the shower maximum to the telescope, *not* the distance between the shower maximum and the array plane or ground plane. We choose this parameter because it best represents the column depth traversed by the electromagnetic cascade, and will have the greatest energy-dependence.

Given a shower with distance L from a telescope with offset angle β, the projection of the shower core location in the shower plane has length $R = \frac{L}{cos(\beta)}$. We can then use the

[1]This method will fail to locate the shower maximum of cosmic ray induced showers because their wider lateral distribution of electrons creates less compact images in the camera plane. The Hillas parameterization of these images will usually result in incorrect shower core locations, thus causing an incorrect shower maximum to be calculated.

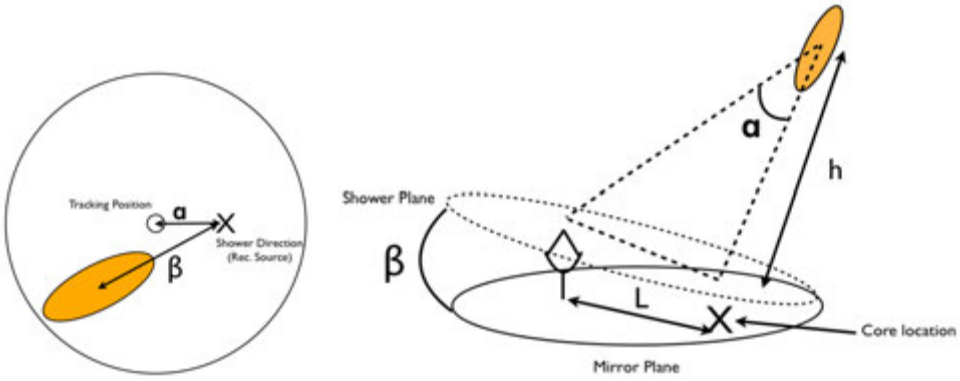

Figure A.6 *Correct method of determining the shower maximum using the reconstructed core location.*

construction shown in Figure A.5 and average over all telescopes to obtain the expression for the shower maximum,

$$h = \frac{1}{n_{tel}} \sum_{i=0}^{n_{tel}} \left(\frac{L_i}{cos\,(\beta_i)\,tan\,(\alpha_i)} \right)$$

Figure A.4 shows that this method produces the expected dependence between shower maximum and energy. The shower maximum algorithm described here will correctly derive *showermax* for wobble and extended source observations.

A.4 Use of the shower maximum in γ/hadron separation

The shower maximum is currently used in VEGAS analysis as a γ/hadron separation cut (*showermax* $>$ 7 km for moderate spectrum sources, *showermax* $>$ 8 km for soft spectrum sources). The new shower maximum algorithm was used to calculate *showermax* for the analysis of 406 minutes of Crab Nebula data. All data was taken during the 2011-2012 observing season. Figure A.7 shows no obvious signal to background separation in the shower maximum distribution, suggesting that it is not an appropriate variable for γ/hadron separation.

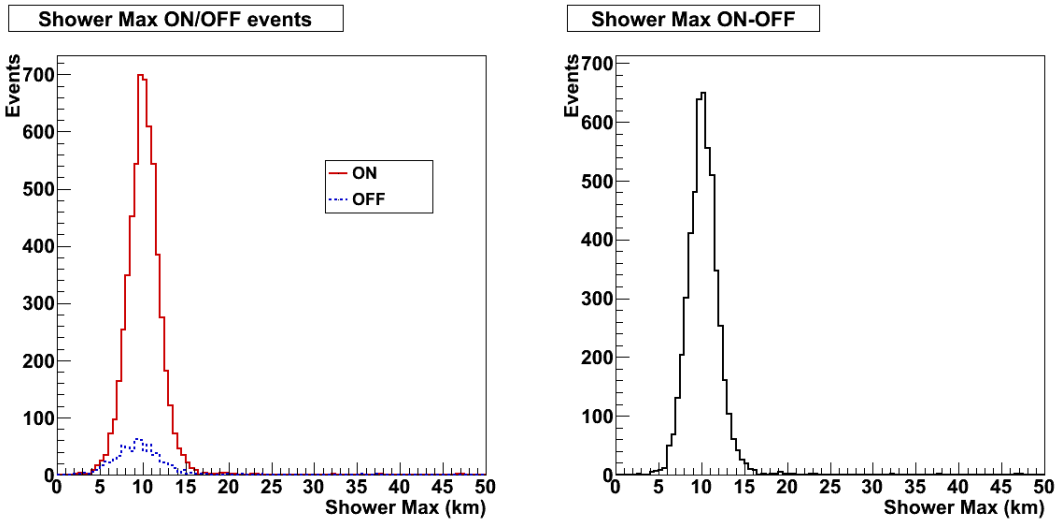

Figure A.7 *Distributions of shower maximum from Crab Nebula data. These plots were created from a 406 minute exposure, with all data taken in the 2011-2012 observing season after the ANL/ISU trigger upgrade. Here the mean scaled cuts have been applied.*

A.5 Conclusions

The current method of shower maximum calculation in VEGAS has been replaced with a new algorithm that takes advantage of the reconstructed shower core to estimate the distance of γ-ray induced air showers from the telescopes. Unlike the current algorithm, this method gives us the correct value of *showermax* and shows the expected correlation between shower maximum and reconstructed energy. This variable does not appear to be an effective means of γ/hadron separation. However, the energy dependence of the shower maximum suggests that it would have value in improving energy estimation. It has been shown that adding the shower maximum as a dimension to the lookup tables can improve energy resolution by approximately 3%.Duke (2010) However, the addition of table dimensions requires the simulation of many additional events, since each table is filled with a smaller fraction of the total number of available showers. The shower maximum may, however, be used as a correction on the *size* parameter prior to referencing the current lookup tables. A γ-ray shower's depth of first interaction is subject to random variation, therefore two otherwise identical showers may develop at different heights, and thus may have different lateral distributions of photons on the ground. The *size*

calculated by a participating telescope is effectively a measurement of the shower's photon density sampled at the telescope's location. If reconstructed energy is treated solely as a function of *size* and shower core distance, the random variations in depth of first interaction can cause mis-estimation of a shower's energy. This effect is one contributor to the VERITAS array's energy resolution. By correcting an image's *size* prior to energy estimation, it may be possible to improve the array's energy resolution.

APPENDIX B. Spectral Points and Details of Systematic Errors from Blazar Analyses

This appendix provides the flux points from spectral analyses of all blazar sources studied in this work. Spectra from standard and soft cuts analyses are shown for all spectra except 1ES0414+009. In the case of 1ES0414+009 only a relaxed size cut is applied, because the soft cuts analysis does not produce a detection greater than the required 5σ.

The results of the systematic error analyses are also presented. All systematic studies were performed using standard cuts, varied as specified in section 4.10.5. The flux normalizations and spectral indices resultingng from variation of each specified parameter are given in the tables. Flux normalizations are specified in the same units given in the spectral fits (e.g. values in table B.3 are in units of $10^{-8}\frac{\mathrm{ph}}{\mathrm{m}^2\cdot\mathrm{s}\cdot\mathrm{TeV}}$). Deviations from the values derived from the spectral fits are also specified, as are the quadrature sums which constitute the final systematic errors on the spectra. In any case where a "–" appears in a cell, both positive and negative variations of a parameter resulted in a spectral fit parameter change in the same direction. In this case, only the larger deviation is given, and is used to calculate the quadrature sum of systematic errors.

Table B.1 Flux Points from 1ES1218+304 **standard cuts** analysis.

Energy (TeV)	Flux	Error on Flux	Excess Counts	Significance (σ)
0.2294	$1.04 \cdot 10^{-6}$	$1.08 \cdot 10^{-7}$	242.33	11.23
0.2711	$8.29 \cdot 10^{-7}$	$6.34 \cdot 10^{-8}$	405.17	15.92
0.3204	$5.63 \cdot 10^{-7}$	$3.97 \cdot 10^{-8}$	400.5	17.34
0.3786	$3.22 \cdot 10^{-7}$	$2.47 \cdot 10^{-8}$	334.0	16.57
0.4474	$1.86 \cdot 10^{-7}$	$1.56 \cdot 10^{-8}$	264.5	15.05
0.5287	$9.91 \cdot 10^{-8}$	$9.96 \cdot 10^{-9}$	190.0	12.27
0.6247	$5.79 \cdot 10^{-8}$	$6.47 \cdot 10^{-9}$	152.33	11.18
0.7382	$3.49 \cdot 10^{-8}$	$4.42 \cdot 10^{-9}$	120.5	9.81
0.8723	$2.06 \cdot 10^{-8}$	$3.07 \cdot 10^{-9}$	88.17	8.08
1.031	$1.36 \cdot 10^{-8}$	$2.16 \cdot 10^{-9}$	73.17	7.54
1.218	$4.01 \cdot 10^{-9}$	$1.28 \cdot 10^{-9}$	29.0	3.54
1.439	$5.09 \cdot 10^{-9}$	$1.05 \cdot 10^{-9}$	46.17	5.89
1.701	$2.45 \cdot 10^{-9}$	$6.96 \cdot 10^{-10}$	26.83	4.06
2.01	$2.08 \cdot 10^{-9}$	$5.5 \cdot 10^{-10}$	27.83	4.44
2.375	$9.52 \cdot 10^{-10}$	$3.79 \cdot 10^{-10}$	15.5	2.87
3.039	$3.02 \cdot 10^{-10}$	$1.62 \cdot 10^{-10}$	12.0	1.92
3.919	$2.94 \cdot 10^{-10}$	$1.65 \cdot 10^{-10}$	8.17	2.04

Table B.2 Flux Points from 1ES1218+304 **soft cuts** analysis.

Energy (TeV)	Flux	Error on Flux	Excess Counts	Significance (σ)
0.1892	$1.81 \cdot 10^{-6}$	$1.64 \cdot 10^{-7}$	1111.25	11.92
0.2295	$1.25 \cdot 10^{-6}$	$9.93 \cdot 10^{-8}$	934.68	14.1
0.2712	$9.4 \cdot 10^{-7}$	$6.12 \cdot 10^{-8}$	933.48	17.16
0.3205	$5.63 \cdot 10^{-7}$	$3.89 \cdot 10^{-8}$	726.56	15.95
0.3787	$3.28 \cdot 10^{-7}$	$2.53 \cdot 10^{-8}$	570.28	14.48
0.4475	$2.03 \cdot 10^{-7}$	$1.69 \cdot 10^{-8}$	459.8	13.41
0.5288	$1.22 \cdot 10^{-7}$	$1.14 \cdot 10^{-8}$	361.7	11.98
0.6249	$6.59 \cdot 10^{-8}$	$7.72 \cdot 10^{-9}$	248.1	9.3
0.7384	$3.4 \cdot 10^{-8}$	$5.31 \cdot 10^{-9}$	164.87	6.88
0.8726	$2.91 \cdot 10^{-8}$	$3.96 \cdot 10^{-9}$	177.46	8.12
1.031	$1.65 \cdot 10^{-8}$	$2.69 \cdot 10^{-9}$	127.38	6.72
1.218	$4.99 \cdot 10^{-9}$	$1.87 \cdot 10^{-9}$	46.11	2.66
1.44	$5.26 \cdot 10^{-9}$	$1.4 \cdot 10^{-9}$	62.26	3.93
1.701	$4.13 \cdot 10^{-9}$	$1.05 \cdot 10^{-9}$	59.04	4.14
2.011	$1.44 \cdot 10^{-9}$	$7.33 \cdot 10^{-10}$	25.28	1.99
2.376	$1.15 \cdot 10^{-9}$	$5.58 \cdot 10^{-10}$	24.7	2.21

Table B.3 Results of systematics analysis on 1ES1218+304.

	Φ_0 min	Φ_0 max	Γ min	Γ max	$\Delta\Phi$ min	$\Delta\Phi$ max	$\Delta\Gamma$ min	$\Delta\Gamma$ max
Size	0.79	1.87	3.05	3.31	0.59	.49	0.07	0.19
MSL	1.13	1.30	3.14	3.16	0.25	–	–	0.04
MSW	1.11	1.27	3.16	3.20	0.27	–	–	0.08
Ring	1.13	1.30	3.14	3.16	0.25	–	–	0.02
Q-Sum					0.74	.49	0.07	0.21

Table B.4 Spectral points (**standard cuts**) from the analysis of 1ES0229+200.

Energy (TeV)	Flux	Error on Flux	Excess Counts	Significance (σ)
0.2295	$3.05{\cdot}10^{-7}$	$1.07{\cdot}10^{-7}$	66.5	3.09
0.2940	$9.02{\cdot}10^{-8}$	$3.20{\cdot}10^{-8}$	76.17	2.90
0.3787	$7.82{\cdot}10^{-8}$	$2.30{\cdot}10^{-8}$	54.5	3.56
0.4476	$7.22{\cdot}10^{-8}$	$1.51{\cdot}10^{-8}$	73.0	5.39
0.5289	$2.84{\cdot}10^{-8}$	$9.54{\cdot}10^{-9}$	36.67	3.14
0.6249	$1.36{\cdot}10^{-8}$	$6.23{\cdot}10^{-9}$	23.5	2.3
0.8006	$6.29{\cdot}10^{-9}$	$2.54{\cdot}10^{-9}$	32.5	2.64
1.031	$3.39{\cdot}10^{-9}$	$2.22{\cdot}10^{-9}$	13.0	1.66
1.321	$1.90{\cdot}10^{-9}$	$9.43{\cdot}10^{-10}$	18.83	2.05
1.702	$1.03{\cdot}10^{-9}$	$8.06{\cdot}10^{-10}$	7.33	1.35
2.359	$4.07{\cdot}10^{-10}$	$2.51{\cdot}10^{-10}$	13.17	1.77
3.318	$3.76{\cdot}10^{-10}$	$2.75{\cdot}10^{-10}$	5.5	1.5

Table B.5 Flux Points from 1ES0229+200 **soft cuts** analysis.

Energy (TeV)	Flux	Error on Flux	Excess Counts	Significance (σ)
0.1892	$2.66{\cdot}10^{-7}$	$1.11{\cdot}10^{-7}$	115.67	2.27
0.2294	$1.89{\cdot}10^{-7}$	$6.43{\cdot}10^{-8}$	98.67	2.96
0.2937	$6.42{\cdot}10^{-8}$	$2.23{\cdot}10^{-8}$	98.33	2.83
0.3786	$2.83{\cdot}10^{-8}$	$1.65{\cdot}10^{-8}$	33.17	1.71
0.4475	$4.61{\cdot}10^{-8}$	$1.17{\cdot}10^{-8}$	72.83	4.20
0.5288	$1.77{\cdot}10^{-8}$	$7.86{\cdot}10^{-9}$	34.83	2.27
0.6248	$1.51{\cdot}10^{-8}$	$5.56{\cdot}10^{-9}$	39.33	2.88
1.079	$2.07{\cdot}10^{-9}$	$7.20{\cdot}10^{-10}$	50.33	3.04
2.354	$3.67{\cdot}10^{-10}$	$2.52{\cdot}10^{-10}$	17.83	1.02

Table B.6 Results of systematics analysis on 1ES0229+200.

	Φ_0 min	Φ_0 max	Γ min	Γ max	$\Delta\Phi$ min	$\Delta\Phi$ max	$\Delta\Gamma$ min	$\Delta\Gamma$ max
Size	3.43	4.88	2.76	2.81	0.95	.50	0.02	0.03
MSL	3.50	3.97	2.83	2.86	0.88	–	–	0.08
MSW	3.81	4.01	2.81	2.89	0.57	–	–	0.11
Ring	4.16	4.39	2.74	2.75	0.01	–	–	0.01
Q-Sum					1.41	.50	0.02	0.14

Table B.7 Spectral points (**standard cuts**) from the analysis of H1426+428.

Energy (TeV)	Flux	Error on Flux	Excess Counts	Significance (σ)
0.2296	$2.53{\cdot}10^{-7}$	$1.77{\cdot}10^{-7}$	17.83	1.48
0.2713	$2.00{\cdot}10^{-7}$	$1.05{\cdot}10^{-7}$	28.33	2.21
0.3478	$9.27{\cdot}10^{-8}$	$3.36{\cdot}10^{-8}$	43.0	2.86
0.4477	$6.6{\cdot}10^{-8}$	$2.35{\cdot}10^{-8}$	28.17	3.21
0.529	$3.06{\cdot}10^{-8}$	$1.38{\cdot}10^{-8}$	18.0	2.53
0.6251	$1.23{\cdot}10^{-8}$	$9.30{\cdot}10^{-9}$	9.83	1.44
0.7387	$1.91{\cdot}10^{-8}$	$6.95{\cdot}10^{-9}$	20.17	3.2
0.8729	$1.09{\cdot}10^{-8}$	$4.82{\cdot}10^{-9}$	15.33	2.63
1.313	$2.50{\cdot}10^{-9}$	$9.27{\cdot}10^{-10}$	24.83	2.96
2.182	$1.06{\cdot}10^{-9}$	$5.64{\cdot}10^{-10}$	9.83	2.05
3.047	$4.36{\cdot}10^{-10}$	$2.77{\cdot}10^{-10}$	5.83	1.69
3.922	$3.79{\cdot}10^{-10}$	$3.03{\cdot}10^{-10}$	3.5	1.49

Table B.8 Spectral points (**soft cuts**) from the analysis of H1426+428.

Energy (TeV)	Flux	Error on Flux	Excess Counts	Significance (σ)
0.1894	$5.91{\cdot}10^{-7}$	$3.37{\cdot}10^{-7}$	79.83	1.61
0.2296	$4.78{\cdot}10^{-7}$	$1.91{\cdot}10^{-7}$	95.5	2.65
0.2714	$1.89{\cdot}10^{-7}$	$1.13{\cdot}10^{-7}$	53.67	1.77
0.3484	$1.44{\cdot}10^{-7}$	$3.85{\cdot}10^{-8}$	125.33	3.91
0.4479	$7.28{\cdot}10^{-8}$	$2.83{\cdot}10^{-8}$	45.5	2.56
0.5292	$3.08{\cdot}10^{-8}$	$1.87{\cdot}10^{-8}$	28.67	1.83
0.6254	$1.92{\cdot}10^{-8}$	$1.29{\cdot}10^{-8}$	22.17	1.57
0.8027	$1.57{\cdot}10^{-8}$	$5.62{\cdot}10^{-9}$	48.33	2.77
1.1510	$4.99{\cdot}10^{-9}$	$2.47{\cdot}10^{-9}$	31.17	2.07

Table B.9 Results of systematics analysis on H1426+428.

	Φ_0 min	Φ_0 max	Γ min	Γ max	$\Delta\Phi$ min	$\Delta\Phi$ max	$\Delta\Gamma$ min	$\Delta\Gamma$ max
Size	3.84	8.31	2.72	2.83	2.47	2.00	–	0.11
MSL	5.61	5.93	2.50	2.55	0.7	–	0.05	0
MSW	4.89	6.98	2.58	2.75	1.42	0.67	–	0.2
Ring	6.35	6.36	2.55	2.57	–	0.05	0	0.02
Q-Sum					2.93	2.1	0.05	0.23

Table B.10 Flux points (**standard cuts**) from the analysis of RGBJ0710+591.

Energy (TeV)	Flux	Error on Flux	Excess Counts	Significance (σ)
0.3456	$1.31 \cdot 10^{-7}$	$4.98 \cdot 10^{-8}$	58.5	2.98
0.4296	$3.00 \cdot 10^{-8}$	$1.99 \cdot 10^{-8}$	30.83	1.52
0.5518	$4.47 \cdot 10^{-8}$	$1.03 \cdot 10^{-8}$	78.5	4.51
0.7088	$1.47 \cdot 10^{-8}$	$5.08 \cdot 10^{-9}$	41.33	2.88
0.9105	$9.47 \cdot 10^{-9}$	$2.77 \cdot 10^{-9}$	48.17	3.92
1.17	$6.04 \cdot 10^{-9}$	$1.66 \cdot 10^{-9}$	43.17	4.03
1.502	$1.78 \cdot 10^{-9}$	$9.43 \cdot 10^{-10}$	17.67	1.9
1.93	$8.14 \cdot 10^{-10}$	$5.31 \cdot 10^{-10}$	11.67	1.53
3.6	$1.11 \cdot 10^{-10}$	$8.03 \cdot 10^{-11}$	17.83	1.63
6.75	$8.00 \cdot 10^{-11}$	$5.57 \cdot 10^{-11}$	6.0	1.75

Table B.11 Flux Points from RGBJ0710+591 **soft cuts** analysis.

Energy (TeV)	Flux	Error on Flux	Excess Counts	Significance (σ)
0.2806	$2.04 \cdot 10^{-7}$	$9.26 \cdot 10^{-8}$	187.83	2.62
0.3456	$1.03 \cdot 10^{-7}$	$4.92 \cdot 10^{-8}$	105.67	2.17
0.4296	$5.56 \cdot 10^{-8}$	$2.17 \cdot 10^{-8}$	99.67	2.30
0.5518	$5.24 \cdot 10^{-8}$	$1.16 \cdot 10^{-8}$	165.33	4.65
0.7087	$2.25 \cdot 10^{-8}$	$6.18 \cdot 10^{-9}$	108.67	3.74
0.9104	$5.53 \cdot 10^{-9}$	$3.45 \cdot 10^{-9}$	44.33	1.82
1.17	$6.48 \cdot 10^{-9}$	$2.16 \cdot 10^{-9}$	69.33	3.21

Table B.12 Results of systematics analysis on RGB J0710+591.

	Φ_0 min	Φ_0 max	Γ min	Γ max	$\Delta\Phi$ min	$\Delta\Phi$ max	$\Delta\Gamma$ min	$\Delta\Gamma$ max
Size	4.83	8.03	2.34	2.72	1.78	1.42	0.30	0.08
MSL	5.39	7.20	2.47	2.68	1.22	0.59	0.17	0.04
MSW	5.84	6.95	2.69	2.70	0.77	0.34	–	0.05
Ring	6.39	6.58	2.59	2.65	0.22	0.03	0.05	0.01
Q-Sum					2.30	1.57	0.55	0.10

Table B.13 Flux Points from 1ES0414+009 analysis.

Energy (TeV)	Flux	Error on Flux	Excess Counts	Significance (σ)
0.2822	$1.63{\cdot}10^{-7}$	$5.21{\cdot}10^{-8}$	78.83	3.42
0.3625	$7.37{\cdot}10^{-8}$	$2.11{\cdot}10^{-8}$	97.67	4.0
0.4657	$9.72{\cdot}10^{-9}$	$9.32{\cdot}10^{-9}$	22.33	1.16
0.5982	$6.76{\cdot}10^{-9}$	$5.03{\cdot}10^{-9}$	19.33	1.22

Table B.14 Results of systematics analysis on 1ES0414+009.

	Φ_0 min	Φ_0 max	Γ min	Γ max	$\Delta\Phi$ min	$\Delta\Phi$ max	$\Delta\Gamma$ min	$\Delta\Gamma$ max
Size	0.68	1.20	3.20	5.53	0.66	–	1.44	0.89
MSL	1.17	1.36	4.34	4.37	0.18	0.02	0.30	–
MSW	1.04	1.17	4.39	4.40	0.30	–	0.25	–
Ring	1.44	1.47	4.77	4.93	–	0.13	–	0.29
Q-Sum					0.74	0.13	1.49	0.93

BIBLIOGRAPHY

Abdo, A.A. et al. *Fermi Large Area Telescope Observations of the Crab Pulsar and Nebula.* ApJ. **708**:1254. 2009.

Abdo, A.A. et al., 2010, *Fermi Large Area Telescope Observations of the Crab Nebula and Pulsar.* ApJ. **708**:1254-1267.

Abdo, A.A. et al., 2011, *Gamma-ray flares from the Crab Nebula*, Science. **331**, 739.

Acciari, V.A. et al. *VERITAS Observations of the γ-ray Binary LS I +61 303.* APJ. **679**:1427-1432. 2008.

Acciari, V.A. et al. *Radio Imaging of the Very-High-Energy γ-Ray Emission Region in the Central Engine of a Radio Galaxy.* Science. **325**:444-448. 2009.

Acciari, V.A., et al. *Observation of Extended VHE Emission from the Supernova Remnant IC 443 with VERITAS* ApJ Letters. **698**:L133-137. 2009.

Acciari, V.A. et al. *VERITAS Observations of the BL Lac Object 1ES 1218+304.* ApJ. **695**:1370-1375. 2009.

Acciari, V.A. et al. *A connection between star formation activity and cosmic rays in the starburst galaxy M82.* Nature. **462**:770-772. 2009.

Acciari, V.A. et al. *Discovery of Variability in the Very High Energy γ-ray Emission of 1ES 1218+304 with VERITAS.* ApJ. **709**, L163, 2010.

Acciari, V.A. et al. *The Discovery of γ-Ray Emission from the Blazar RGB J0710+591.* ApJ. **715**:L49-L55, 2010.

Acciari, V.A. et al. *Discovery of TeV Gamma-Ray Emission from* Tycho's *Supernova Remnant.* ApJ Letters. **730**:L20. 2011.

Aguilar et al. *First Result from the Alpha Magnetic Spectrometer on the International Space Station: Precision Measurement of the Positron Fraction in Primary Cosmic Rays of 0.5350 GeV.* Phys. Rev. Lett. **110**:141102. 2013.

Aharonian, F.A. et al. (H.E.S.S. collaboration), and S. Johnston, J.G. Kirk, O. Skjaeraasen. *Discovery of the binary pulsar PSR B1259-63 in very-high-energy gamma rays around periastron with H.E.S.S.* A&A. **442**:1-10. 2005.

Aharonian, F.A. et al. *Discovery of very high energy gamma rays associated with an X-ray binary.* Science. **309**:746-749. 2005.

Aharonian, F., et al. *An Exceptional VHE Gamma-Ray Flare of PKS 2155-304.* ApJ Letters. **664**:L71. 2007.

Aharonian, F., et al. *Observations of the Crab Nebula with HESS.* A&A. **421**:529. 2012.

Albert, J. et al. *Discovery of Very High Energy Gamma Rays from 1ES 1218+30.4.* ApJ Letters. **642**:L119-L122. 2006.

Aliu, E. et al. *Multiwavelength Observations of the AGN 1ES 0414+009 with VERITAS, Fermi-LAT, Swift-XRT, and MDM.* ApJ. **755**:118. 2012.

Aliu, E. et al. *A Three-Year Multi-Wavelength Study of the Very High Energy ?-ray Blazar 1ES 0229+200.* Submitted to ApJ. 2013.

Aliu, E. et al., *A search for enhanced very-high-energy gamma-ray emission from the March 2013 Crab Nebula flare*, Submitted to ApJ. 2013.

Amenomori, M. et al. *New Estimation of the Spectral Index of High-Energy Cosmic Rays as Determined by the Compton-Getting Anisotropy.* ApJ Letters. **672**:1. 2008.

Baldini, L. and Tibaldo, L. *Science highlights from the Fermi Large Area Telescope,* in Proc. to Les Rencontres de Physique de la Vall. arXiv:1106.3416v1. 2011.

Berge, D., Funk, S., and Hinton, J. *Background modelling in very-high-energy γ-ray astronomy.* Astron. & Astrophys. **466**:3. 2007.

Biller, S.D., et al. *New Limits to the IR Background: Bounds on Radiative Neutrino Decay and on VMO Contributions to the Dark Matter Problem.* Phys. Rev. Letters. **80**:2992-2995. 1998.

Blandford, R.D. Proc. Heidelberg Conf. Physics of AGN, ed. W.J. Duschl and S.J. Wagner. Berlin: Springer, 3. 1991

Bloom, S.D., and Marscher, A.P. *An Analysis of the Synchrotron Self-Compton Model for the MultiWave Band Spectra of Blazars* ApJ. **461**:657. 1996.

Böttcher, M., Reimer, A., Sweeney, K., and Prakash, A. *Leptonic and Hadronic Modeling of Fermi-Detected Blazars.* Accepted for Publication in ApJ. 2013.

Bradbury, S.M. & Rose, H.J. *Pattern recognition trigger electronics for an imaging atmospheric Cherenkov telescope* Nucl. Instrum. Meth., A481:521-528, 2002

Breit, G. and Wheeler, J. *Collision of Two Light Quanta.* Phys. Rev. **46**:1087-1091. 1934.

Butt, Y. *Beyond the myth of the supernova-remnant origin of cosmic rays.* Nature. **460**:701-704. 2009.

Catanese, M., et al. *Multiwavelength Observations of a Flare from Markarian 501* ApJ Letters. **487**:L143-146. 1997.

Chary, R., and Elbaz, D. *Interpreting the Cosmic Infrared Background: Constraints on the Evolution of the Dust-Enshrouded Star Formation Rate* ApJ. **556**:562-581. 2001.

Cherenkov, P. A. *Visible Radiation Produced by Electrons Moving in a Medium with Velocities Exceeding that of Light.* Phys. Rev. **52**:378-379. 1937.

Cogan, P. *An Overview of The VERITAS Prototype Telescope And Camera.* Proceedings of the Conference "The Multiwavelength Approach to Unidentified Sources." arXiv:astro-ph/0408155. 2004.

Davies, J.M., Cotton, E.S. *J. Solar Energy Sci. and Eng.* **1**:16. 1957.

Dominguez, A., et al. *Extragalactic Background Light Inferred from AEGIS Galaxy SED-type Fractions.* MNRAS. **000**:1-25. 2011.

Donnarumma, I., et al. *The June 2008 Flare of Markarian 421 from Optical to TeV Energies.* ApJ. **691**:13. 2009.

Drury, L. O'C., Aharonian, F. A., and Voelk, H. J. *The gamma-ray visibility of supernova remnants. A test of cosmic ray origin.* A&A. **287**:959-971. 1994.

Duke, C. et al., *VERITAS Memo: Estimating Energies with Higher-Dimensional Lookup Tables and Artifical Neural Networks.* January, 2010.

Dwek, E. *The Evolution of the Elemental Abundances in the Gas and Dust Phases of the Galaxy.* ApJ. **501**:643-665. 1998.

Dwek, E., and Krennrich, F. *Simultaneous Constraints on the Spectrum of the Extragalactic Background Light and the Intrinsic TeV Spectra of Markarian 421, Markarian 501, and H1426+428.* ApJ. **618**:657-674. 2005.

Dwek, E., and Krennrich, F. *The extragalactic background light and the gamma-ray opacity of the universe.* Astropar. Phys. **43**:112-133. 2013.

Evenson, P. *Cosmic Ray Electrons.* Space Sci. Series of ISSI. **3**:63-73. 1998.

Fixen, D.J. et al. *The Spectrum of the Extragalactic Far-Infrared Background from the COBE* FIRAS Observations.* ApJ. **508**:123-128. 1998.

Frank, I. M. and Tamm, Ig., C. R. Ac. Sci. USSR. **14**:109. 1937.

Funk, B. et al. *An Upper Limit on the Infrared Background Density from HEGRA data on Mkn 501.* Astropart. Phys. **9**:97-103. 1998.

Gaisser, T. *Cosmic Rays and Particle Physics.* Cambridge: Cambridge University Press. 1990.

Galbraith, W. and Jelley, J.V. *Light Pulses from the Night Sky associated with Cosmic Rays.* Nature. **171**: 349-350. 1953.

Giommi, P. et al. *The* EXOSAT *High Galactic Latitude Survey.* ApJ. **378**:77-92. 1991.

Gould, R. J., and Schréder, G. P. *Opacity of the Universe to High-Energy Photons*, Phys. Rev. **155**:1404-1407

Greisen, K. *Cosmic Ray Showers.* Ann. Rev. Nucl. Part. Sci. **10**:63. 1960.

Grieder, P.K.F. *Extensive Air Showers.* Heidelberg: Springer-Verlag. 2010.

Hartman, R.C. et al. *The Third EGRET Catalog of High-Energy Gamma-Ray Sources.* ApJ. Supplemental Series **123**:79-202. 1999.

Hauser, M. et al. *The COBE Diffuse Infrared Background Experiment Search for the Cosmic Infrared Background. I. Limits and Detections.* ApJ. **508**:25. 1998.

Hauser, M. and Dwek, E. *The Cosmic Infrared Background: Measurements and Implications.* Ann. Rev. Astron. Astrophys. **39**:249-307. 2001

Hays, E. for the VERITAS Collaboration. *VERITAS Data Acquisition.* Proc. to 2007 ICRC. 2007.

Hester, J. J. *The Crab Nebula: An Astrophysical Chimera.* Ann. Rev. Astron. Astrophys. **46**:127-155. 2008.

Hillas, A. M. (1982) *The sensitivity of Cherenkov radiation pulses to the longitudinal development of cosmic-ray showers.* J. Phys. G, 8, p 1475, 1982.

Hillas, A. M. *Electromagnetic and muonic structure of showers initiated by gamma-rays and by hadrons*, Proc. 19th ICRC (La Jolla). **3**:445. 1985.

Holder, J. for the VERITAS Collaboration *VERITAS: Status and Highlights.*. Proc. to 2011 ICRC. 2011.

Holder, J. *Summary of Optical Filter Tests*. Internal Memo for the VERITAS Collaboration. 2011.

Horns, D. et al. *TeV observations of H1426+428 with HEGRA*. New Astron. Rev. **48**:387-390. 2003.

Horiuchi, S. Beacom., and Dwek, E. *Diffuse supernova neutrino background is detectable in Super-Kamiokande*. Phys. Rev. D. **79**:083013. 2009.

Imran, A. *Analysis of variable VHE gamma-ray emission from the hard spectrum blazar 1ES 1218+304*. Ph.D Thesis, Iowa State University, Ames, IA. 2010.

Jelley, J.V. *Cherenkov Radiation and its Applications*. London: Pergamon Press. 1958.

Jelly, J. G., and Porter, N. A. *Cherenkov Radiation from the Night Sky, and its Application to γ-Ray Astronomy*. Quart. J. R. Astron. Soc. **4**:275. 1963.

Kashlinsky, A. *Cosmic Infrared Background and Early Galaxy Evolution*. Physics Reports. **409**: 361-438. 2005.

Kitchin, C. *Galaxies in Turmoil* London:Springer-Verlag. 2006.

Krennrich, F., and Orr, M. *The Extragalactic Background Light (EBL): A Probe of Fundamental Physics and a Record of Structure Formation in the Universe*. Input for Snowmass. 2013.

Kusunose. M, and Takahara, F. *A structured Leptonic Jet Model of the "Orphan" TeV Gamma-Ray Flares in TeV Blazars* ApJ. **651**:113-119. 2006.

Le Bohec, S. and Sleege, G. *Design of the Preamplifier for VERITAS*. Internal Memo for the VERITAS Collaboration.

Lafferty, G.D. and Wyatt, T.R. *Where to Stick your Data Points: The Treatment of Measurements Within Wide Bins*. Nuclear Instruments and Methods. **272**:317. 1983.

Li, T.P. and Ma, Y.Q., *Analysis Methods for Results in Gamma-Ray Astronomy*. ApJ. **355**:541-547. 1983.

Lin, Y.C. et al. *Detection of High-Energy Gamma-Ray Emmission from the BL Lacertae Object Markarian 421 by the EGRET Telescope on the Compton Observatory*. ApJ. **401**: L61. 1992.

Lorimer, D.R. *Binary and Millisecond Pulsars*. Living Rev. Relativity. **11**:8. 2008.

Macchetto, F. et al. *The Supermassive Black Hole of M87 and the Kinematics of its Associated Gaseous Disk*. ApJ. **489**:579. 1997.

Madau, P., and Pozzetti, L. *Deep galaxy counts, extragalactic background light and the stellar baryon budget*. MNRAS. **312**: L9-15. 2000.

Malkov, M.A. and Drury, L. O'C. *Nonlinear theory of diffusive acceleration of particles by shock waves*. Rep. Prog. Phys. **64**:429-481. 2001.

Marscher, A.P. et al. *Observational evidence for the accretion-disk origin for a radio jet in an active galaxy*. Nature. **417**:625-627. 2002.

Meier, D.L., Koide, S., and Uchida, Y. *Magnetohydrodynamic Production of Relativistic Jets*. Science. **291**:84. 2001.

Meier, G. *Monte Carlo Studies of the first VERITAS telescope*. Proceedings of the 29th ICRC. 2005.

Mirzoyan, R. and Lorenz, E. *Measurement of the Night Sky Light Background at La Palma*. MPI-PhE/94-35. 1994.

Mohanty, G., et al. *The Very High Energy Photon Spectrum of Markarian 421.* Proceedings of the 23rd ICRC. 1993.

Mohanty, G., et al. *The Spectrum of TeV Gamma Rays from the Crab Nebula.* ApJ. **503**:744-759. 1998.

Moralejo, A., et al (2009). *Status of Magic-II*, in Proc. to 2009 Fermi Symposium, arXiv:0912.3673v1. 2009.

Orr, M., Krennrich, F., and Dwek, E. *Strong New Constraints on the Extragalactic Background Light in the Near- to Mid-IR.* ApJ. **733**:77. 2011.

Otte, A. N. for the VERITAS Collaboration, et al. *The Upgrade of VERITAS with High Efficiency Photomultipliers* in Proceedings of the 32nd ICRC. 2011.

D. Petry et al. *The TeV Spectrum of H1426+428.* ApJ. **580**:104-109. 2002.

Pohl, M. and Schlickeiser, R. *On the conversion of blast wave energy into radiation in active galactic nuclei and gamma-ray bursts.* A&A. **354**:395. 2000.

Puget, J.L. et al. A&A. **308**:L5. 1996.

Rando, R. on behalf of the Fermi LAT collaboration. *Post-launch performance of the Fermi Large Area Telescope.* in Proceedings of the 31st ICRC. 2009.

Raue, M and Meyer, M. *Probing the peak of the star formation rate density with the extragalactic background light.* MNRAS. **426**: 2, 1097-1106. 2012.

Renaud, M. *Latest results on Galactic sources as seen in VHE γ-rays.* Proceedings of 44th Recontres de Moriond. 2009.

Schroedter, M., et al. *A Topological Trigger System for Imaging Atmospheric-Cherenkov Telescopes.* Proceedings of the 31st ICRC. 2009.

Schlegel, D.J., Finkbeiner, D.P., and Davis, M. *Maps of Dust Infrared Emission for Use in Estimation of Reddening and Cosmic Microwave Background Radiation Foregrounds*. ApJ. **500**:525. 1998.

Seo, E.S. et al. *Cosmic-ray energetics and mass (CREAM) balloon project*. Adv. Space Research. **33**:1777-1785. 2004.

Stecker, F.W. and De Jager, O.C. *New Upper Limits on Intergalactic Infrared Radiation from High-Energy Astrophysics*. ApJ. **415**:L71-L73. 1993.

Swordy, S. *The Energy Spectra and Anisotropies of Cosmic Rays*. Space Sci. Rev. **99**:85-94. 2001.

Urry, C.M. and Padovani, P. *Unified Schemes for Radio-Loud Active Galactic Nuclei*. Publications of the Astronomical Society of the Pacific. **107**:803. 1995.

Vassiliev, V. V., et al. *VERITAS CFDs*. Proc. to ICRC. 5, 2851. 2003.

Weekes, T.C. et al. *Observation of TeV Gamma Rays from the Crab Nebula Using the Atmospheric Cherenkov Imaging Technique*. ApJ. **342**:379-395. 1989.

Weekes, T.C. et al. *Very high energy gamma-ray astronomy*. Bristol: Institute of Physics Publishing. 2003.

Weinstein, A. for the VERITAS Collaboration. *The VERITAS Trigger System*. Proc. of the 30th ICRC. 2007.

Woosley, S. and Janka, T. *The physics of core-collapse supernovae*. Nature Physics. **1**:147-154. 2005.

Zanin, R. et al. *MAGIC measurement of the Crab Nebula spectrum over three decades in energy*. Proc. of the 32nd ICRC. 2011.